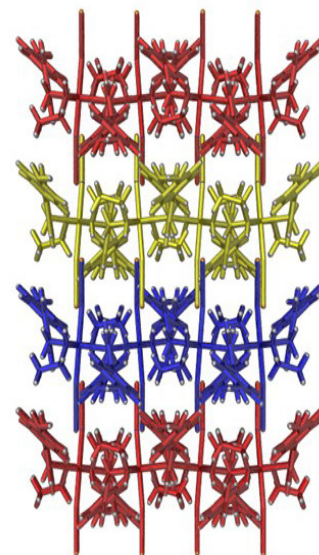
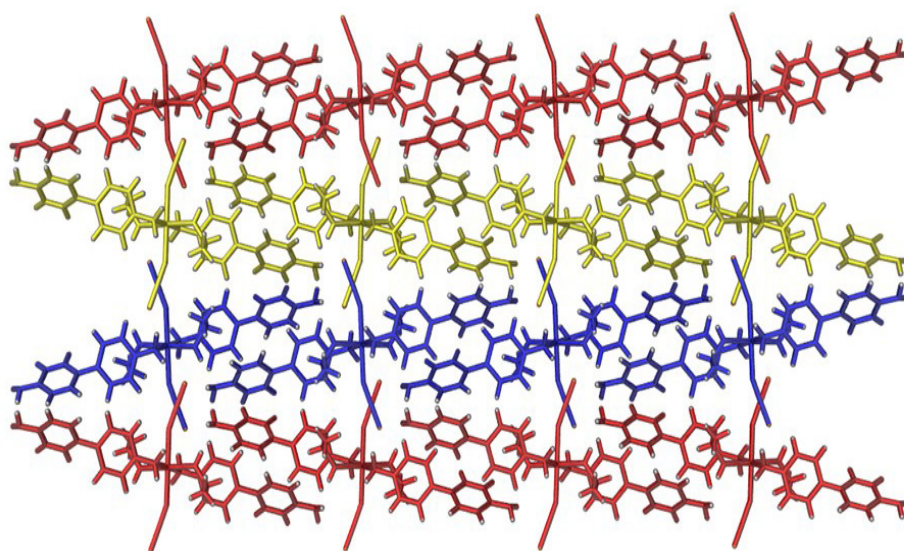




STUDIA UNIVERSITATIS
BABEŞ-BOLYAI



UNIVERSITATEA BABEŞ-BOLYAI
BABEŞ-BOLYAI TUDOMÁNYEGYETEM
BABEŞ-BOLYAI UNIVERSITÄT
BABEŞ-BOLYAI UNIVERSITY
TRADITIO ET EXCELLENTIA



CHEMIA

1/2025

STUDIA UNIVERSITATIS BABEȘ-BOLYAI CHEMIA

1/2025

ISSN (print): 1224-7154;
ISSN (online): 2065-9520; ISSN-L: 1224-7154

© STUDIA UBB CHEMIA

Published by Babeș-Bolyai University

EDITORIAL BOARD OF STUDIA UNIVERSITATIS BABEȘ-BOLYAI CHEMIA

ONORARY EDITOR:

IONEL HAIDUC – Member of the Romanian Academy

EDITOR-IN-CHIEF:

LUMINIȚA SILAGHI-DUMITRESCU

EXECUTIVE EDITOR:

CASTELIA CRISTEA

ASSOCIATE EDITOR:

ALEXANDRU LUPAN

EDITORIAL BOARD:

PAUL ȘERBAN AGACHI, Babeș-Bolyai University, Cluj-Napoca, Romania

LIVAIN BREAU, UQAM University of Quebec, Montreal, Canada

HANS JOACHIM BREUNIG, Institute of Inorganic and Physical Chemistry,
University of Bremen, Bremen, Germany

JEAN ESCUDIE, HFA, Paul Sabatier University, Toulouse, France

ION GROSU, Babeș-Bolyai University, Cluj-Napoca, Romania

EVAMARIE HEY-HAWKINS, University of Leipzig, Leipzig, Germany

FLORIN DAN IRIMIE, Babeș-Bolyai University, Cluj-Napoca, Romania

FERENC KILAR, University of Pecs, Pecs, Hungary

BRUCE KING, University of Georgia, Athens, Georgia, USA

ANTONIO LAGUNA, Department of Inorganic Chemistry, ICMA, University of
Zaragoza, Zaragoza, Spain

JURGEN LIEBSCHER, Humboldt University, Berlin, Germany

KIERAN MOLLOY, University of Bath, Bath, UK

IONEL CĂTĂLIN POPESCU, Babeș-Bolyai University, Cluj-Napoca,
Romania

CRISTIAN SILVESTRU, Babeș-Bolyai University, Cluj-Napoca, Romania

YEAR
MONTH
ISSUE

Volume 70 (LXX) 2025
March
1

PUBLISHED ONLINE: 2025-03-20
PUBLISHED PRINT: 2024-04-30
ISSUE DOI: 10.24193/subbchem.2025.1

S T U D I A

UNIVERSITATIS BABEȘ-BOLYAI

CHEMIA

1

CONTENT/ SOMMAIRE/ INHALT/ CUPRINS

Marian-Iosif FRÎNCU, Gabriele-Mario BOGDAN, Sorin-Aurel DORNEANU, Selective Electroextraction of Base Metals from Leaching Solutions Obtained During the Recycling of Waste Printed Circuit Boards. III. Preliminary Tests for Iron, Nickel and Zinc Electroextraction	7
Miron RANCEA, Ovidiu NEMEȘ, Liliana BIZO, Thermal Behaviour of Composite Materials Obtained from Recycled Tetra Pak® by Thermoplasting Forming	23
Baocheng WU, Ye XING, Yande CAO, Haichao LI, Synthesis of N-doped Carbon Materials with Ultra-microporous by Activative Rubidium Chloride	35
Madalina Anca UJICA, Ionel MANG, Ossi HOROVITZ, Aurora MOCANU, Maria TOMOAI A-COTISEL, Gold Nanoparticles Functionalized with Anticancer Biocompounds	47
Madalina Anca UJICA, Ionel MANG, Ossi HOROVITZ, Olga SORITAU, Gheorghe TOMOAI A, Aurora MOCANU, Horea-Rares-Ciprian BENE A, Viorica RAISCHI, Csaba VARHELYI, George BORODI, Maria TOMOAI A-COTISEL, The Effect of Gold Nanoparticles Synthesized by Sodium Citrate and Functionalized with Anticancer and Natural Compounds on Cancer Cell Lines.....	65

Adriana-Maria ANDREICA, Mihaela Cecilia VLASSA, Rahela CARPA, Ioan PETEAN, Green Synthesis of Silver Nanoparticles Using <i>Galium Verum</i> L. Aqueous Extract and Evaluation of Its Antimicrobial Activity	87
Radu F. SEMENIUC, Tiffany M. Smith PELLIZZERI, The Molecular and Supramolecular Structure of $Mn(4,4'$ -diaminobiphenyl) $_2(NCS)_2(EtOH)_2$	101
Mohammed Larbi Ben AMOR, Elhafnaoui LANEZ, Yahia BEKKAR, Aicha ADAIKA, Touhami LANEZ, Kaouther NESBA, Lazhar BECHKI, Evaluation of Ferrocenylmethylnucleobases Derivatives Interacting with DNA: Insights From Electrochemical, Spectroscopic, DFT Calculation, Molecular Docking and Molecular Dynamic Simulations	111
Lucian DORDAI, Marius ROMAN, Levente LEVEL, Assessment of Greenhouse Gas (GHG) Emissions Associated with Rapeseed Farming in Romania.....	133
Andra TĂMAȘ, Laura COCHECI, Lavinia LUPA, Xanthan Gum and Guar Gum – Potential Green Inhibitors for Scale Formation	147
Fatma A. A. AL ANI, Azhar S. HAMODY, Ruaa M. MAHMOOD ^a , Nahla A. ALASSAF, Dhafir T.A. AL-HEETIMI, Green Spectrophotometric Method for Concurrent Estimation of Piroxicam and Mefenamic Acid Mixture	159
Ruxandra ȘTEFĂNESCU, Robert-Alexandru VLAD, Silvia IMRE, Amelia TERO-VESCAN, Bianca-Eugenia ÓSZ, Dan-DRAGOȘ SITA, Lénárd FARCZÁDI, Development and Validation of an LC-MS/MS Method for the Quantification of Six Cannabinoids in Commercial Products.....	173
Nicoleta MATEI, Semaghiul BIRGHILA, Simona DOBRINAS, Alina SOCEANU, Ana-Maria ILIE, Viorica POPESCU, Method Validation for Copper Determination in Human Hair Samples Through Graphite Furnace Atomic Absorption Spectrometry	191
Erdal DİNÇ, Burak ARI, Eda BÜKER, Dorina CASONI, Chemometric Smart Approaches Using Artificial Neural Networks and Continuous Wavelet Transform for Simultaneous Quantitative Analysis of Ciprofloxacin-Ornidazole Tablets.....	203
Farid SOUAS, Abdelhamid SAFRI, Ahmed Salah Eddine MEDDOUR, Rheological Characterization of Algerian Crude Oils.....	221

Studia Universitatis Babes-Bolyai Chemia has been selected for coverage in Thomson Reuters products and custom information services. Beginning with V. 53 (1) 2008, this publication is indexed and abstracted in the following:

- Science Citation Index Expanded (also known as SciSearch®)
- Chemistry Citation Index®
- Journal Citation Reports/Science Edition

SELECTIVE ELECTROEXTRACTION OF BASE METALS FROM LEACHING SOLUTIONS OBTAINED DURING THE RECYCLING OF WASTE PRINTED CIRCUIT BOARDS.

III. PRELIMINARY TESTS FOR IRON, NICKEL AND ZINC ELECTROEXTRACTION

Marian-Iosif FRÎNCU^{a,b} , Gabriele-Mario BOGDAN^a ,
Sorin-Aurel DORNEANU^{a,b,*} 

ABSTRACT. This paper presents the results of our research concerning the feasibility of the Fe, Ni and Zn electroextraction from partially treated spent leaching solutions resulting from the waste printed circuit boards recycling process using the bromine/bromide system. The first tests, performed in a real sample of spent leaching solution and using a Pt Fisher type cathode, led to unacceptable results due to the intensive hydrogen evolution. To find a feasible industrial solution, systematic preliminary tests were performed by hydrodynamic cyclic voltammetry in synthetic solutions using small diameter (3 mm) rotating disk electrodes (RDEs) of carbon paste (CP) and 304 type stainless steel (304 SS), resulting in theoretical current efficiencies of up to 95.8%. Further, to prove the feasibility of the pure Zn and Zn alloys electroextraction, long duration (0.15÷8 h) experiments were done by potentiostatic chronoamperometry using RDEs on CP and 304 SS of large diameters (38 and 29 mm, respectively). The obtained results proved that, depending on the electrolyte's composition and pH, and on the imposed potential, high purity Zn (over 98%) or Zn-Fe-Ni alloy deposits can be obtained at current efficiencies between 20 and 96% and specific energy consumptions between 2 and 17 kWh/kg of alloy.

Keywords: waste printed circuit boards recycling, selective electroextraction, iron, nickel and zinc recovery, iron-nickel-zinc alloy electrodeposition

^a Babeş-Bolyai University, Faculty of Chemistry and Chemical Engineering, Department of Chemical Engineering, 11 Arany Janos Street, Cluj-Napoca, RO-400028, Romania

^b Babeş-Bolyai University, Interdisciplinary Research Institute on Bio Nano Sciences, 42 Treboniu Laurian Street, Cluj-Napoca, RO-400271, Romania

* Corresponding author: sorin.dorneanu@ubbcluj.ro



INTRODUCTION

During the last decades, due to the environmental and economic implications, intensive research has been carried out regarding the development and optimization of technologies for the recovery of metals and other materials from the waste printed circuit boards (WPCBs). [1-4] As an alternative to the traditional pyrometallurgical methods [5,6], exhaustive studies concerning the valuable metals leaching by hydrometallurgical [7,8], bio-hydrometallurgical [9, 10], and electrochemical [11,12] processes have been conducted. For the latter, electrochemically regenerable leaching systems based on the $\text{Fe}^{3+}/\text{Fe}^{2+}$ [13], $\text{Cu}^{2+}/\text{Cu}^+$ [14] or Br_2/Br^- [15] redox couples can be successfully used, requiring only minimal pre-treatment of the WPCBs. Noticeably, compared to the chloride containing systems, the Br_2/Br^- one is extremely efficient, allowing a fast leaching of the base metals (BM, e.g. Cu, Sn, Pb, etc.) [16] or even noble metals (e.g. Ag, Au) [17], and the complete recovery of other WPCBs components.

From another point of view, it's worth noting that, in the great majority of published studies, the recovery of leached metals from WPCBs is focused only on metals with a high market value or those with high toxicity, applying methods such as cementation [18], precipitation, extraction [19,20] or electrodeposition. [21,22] Unfortunately, the recovery of the other metals left in the solution, such as Zn, Al, Fe, Ni, is extremely little discussed [23,24] because of their low market value and high extraction costs. [25,26] A possible solution to these problems can be the electrodeposition of binary and/or ternary alloys of Zn, Fe and Ni. This process has been intensively studied on various cathode materials, both in potentiostatic [27] or galvanostatic [28] mode, but the main goal of these studies was to obtain films with good mechanical and anti-corrosion properties. [29-31] Generally, to improve the quality of the obtained deposits, different additives (e.g., acidity correctors, leveling agents, gelatin, etc.) were used. [32,33] Unfortunately, the presence of these additives in the solutions used for leaching metals from WPCBs can interfere significantly with the recovery of target metals and with the reagent's electrochemical regeneration processes.

In the previously mentioned context, this paper presents our main results concerning the feasibility of Fe, Ni and Zn electroextraction from leaching solutions obtained during the process of BM electrochemical recovery from WPCBs. The first set of measurements, performed in a real sample of spent leaching solution and using a traditional Pt Fisher electrode, revealed that Pt is inadequate because it favors the hydrogen evolution reaction (HER). Consequently, the next experiments were performed using rotating disc electrodes (RDE), made of carbon paste (CP) and 304 type stainless steel (304 SS). The results obtained by hydrodynamic cyclic voltammetry (HCV)

and potentiostatic chronoamperometry (PCA) confirmed the possibility of advanced and efficient recovery of these metals, as well as the creation of premises for the total recovery of the initial leaching solution.

RESULTS AND DISCUSSION

Electroextraction test on Pt Fisher electrode

Aiming to rigorously evaluate the quantities of Fe, Ni and Zn that can be extracted from the leaching solutions obtained during the BM recovery from WPCBs, a series of experiments were started using as catholyte the solution resulted after the previous tests concerning the potentiostatic selective electroextraction of Cu, Sn and Pb.[22] Moreover, the same experimental setup (equipped with the Pt Fisher electrode) was used and similar protocols were applied. The evolutions of electrolyte pH and of the main electrical parameters recorded during these tests are presented in Figure 1, whereas a summary of the main experimental parameters and results is presented in Table 1. Also, three examples of the obtained deposits photographs, indicated in Table 1, are presented in Figure 2.

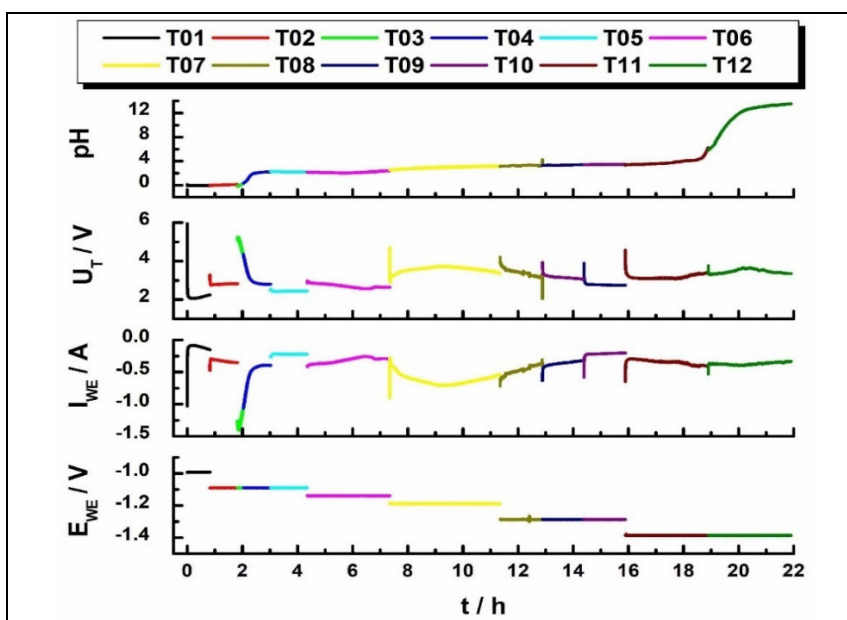


Figure 1. Evolutions of the electrolyte pH and of the main electrical parameters during the potentiostatic electrodeposition of Fe, Ni and Zn from a real sample of leaching solution using the Pt Fisher type electrode

Table 1. Main experimental conditions and results for the tests of Fe, Ni and Zn potentiostatic electrodeposition from a real sample of leaching solution on the Pt Fisher type electrode

Test	Deposit	E _{WE} (V/RE)	t (h)	pH _M	m _D (mg)	[Fe] (%)	[Ni] (%)	[Zn] (%)	[Imp] (%)	C.E. (%)	W _s (kWh/kg)
T01	D1	-1.00	0.8	-0.05	131	1.37	1.93	75.0	21.7	93.4	1.96
T02÷04	D2	-1.10	2.2	0.62	127	0.21	0.17	69.7	30.0	6.74	42.4
T05	D3	-1.10	1.3	2.22	70	10.8	1.63	52.3	35.2	13.0	16.0
T06	D4	-1.15	3.0	2.16	112	51.1	0.47	36.4	12.0	9.37	26.2
T07	D5	-1.20	4.0	2.94	112	27.7	0.56	7.34	64.4	1.49	224
T08÷10	D6	-1.30	4.5	3.35	503	14.4	2.21	0.17	83.2	5.07	60.1
T11	D7	-1.40	2.0	3.86	1464	6.69	0.69	0.06	92.6	13.3	30.5
T12	D8	-1.40	4.0	11.5	17	18.7	3.64	0.57	77.1	0.17	971

In Figure 1, E_{WE} represents the potential of the working electrode (WE) in respect to the reference electrode (RE) of Ag/AgCl/KCl_{SAT} type, I_{WE} is the current through the WE and U_T represents the voltage at the terminals of the electrochemical reactor (ECR). Also, in Table 1, t is the duration of each successive test (T01 to T12), pH_M represents the mean value of the electrolyte pH, m_D is the mass of the obtained deposits (D1 to D8), [Fe], [Ni] [Zn] and [Imp.] represent the percentages of metals and impurities in the deposit (calculated based on flame atomic absorption spectrometry analysis), and C.E. and W_s are the current efficiency and the specific electricity consumption, respectively. The last two parameters were calculated using the relations:

$$C.E. = \frac{z \cdot F \cdot m_D \cdot \left(\frac{[Fe]}{A_{Fe}} + \frac{[Ni]}{A_{Ni}} + \frac{[Zn]}{A_{Zn}} \right)}{1000 \cdot \int_0^t I_{WE} \cdot dt} \quad [\%] \quad (1)$$

$$W_s = \frac{1000 \cdot \int_0^t I_{WE} \cdot U_T \cdot dt}{36 \cdot m_D \cdot ([Fe] + [Ni] + [Zn])} \quad [kWh/kg] \quad (2)$$

where z is the number of transferred electrons (2 in the case of Fe, Ni and Zn), F is the Faraday constant (96480 A*s/E_g), and A_{Fe}, A_{Ni} and A_{Zn} represent the atomic masses of the metals, respectively.

As can be seen from Figure 1, at the start of Test 1 (T01), conducted at E_{WE} of -1.0 V/ER, we observed a very large current impulse, corresponding to HER, which is highly favored by the Pt cathode matrix and the electrolyte's

acidity. Fortunately, as the Fisher electrode is increasingly covered with a Zn layer, HER is strongly inhibited and Zn deposition is subsequently favored, resulting in a smooth and compact deposit (see picture D1 in Figure 2).

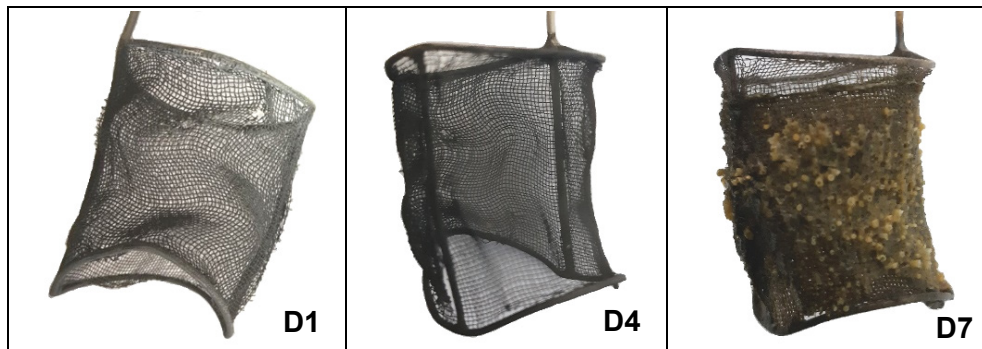


Figure 2. Examples of deposits obtained on the Pt Fisher type electrode

Correlating the data from Table 1 and Figures 1 and 2, it can be observed that, by using a relatively low E_{WE} (-1.0 V/ER), Zn can be extracted with an acceptable purity (over 95%), with an overall C.E. of approximately 93% and a W_S value less than 2 kWh/kg of deposit.

From the data acquired and the performance parameters evaluated from tests T02 – T04, we can conclude that the attempting to speed up the electrodeposition process by increasing the E_{WE} value to -1,1 V/ER has a negative effect on the metals' electroextraction, achieving C.E and W_S values under 6.7% and over 42 kWh/kg, respectively. Additionally, the massive hydrogen evolution during test T04 led to a significant pH rise, over the value of 2. In these new conditions, during T05 and T06, Fe and Ni start to be co-deposited together with Zn as adherent and compact deposits as exemplified in picture D4 from Figure 2.

The following tests (T07 – T12), performed at increasingly negative potentials (between -1,2 and -1,4 V/ER) have shown pronounced pH rises and apparent increases of the deposit's masses. Analyzing the obtained deposits, we found that, in fact, the evaluated quantities of Zn, Fe and Ni were very low, leading to extremely low C.E. and exaggerated W_S values. This paradox can be attributed to the fact that, at elevated pH values, the deposits attached to the Fisher electrode (see Picture D7 from Figure 2) consist preponderantly in oxy-hydroxides of the BM present in the WPCBs leaching solutions, where, besides Fe, Ni and Zn, we also detected high amounts of Cr, Al, Bi and Mn.

The results of this first set of tests suggest that, by using an inadequate cathodic matrix and unoptimized process parameters, we cannot obtain promising results regarding the possibility of Fe, Ni and Zn electroextraction from WPCBs leaching solutions. Consequently, we decided to perform additional tests aimed at finding technical solutions able to ensure the more advanced electroextraction of Fe, Ni and Zn from leaching solutions.

Preliminary electroextraction tests by HCV using small diameter RDE of CP and 304 SS

Before starting new long duration electroextraction test, we decided to perform preliminary HCV experiments to evaluate the electrochemical behavior of other candidates (CP and 304 SS) as cathodic material. Concretely, to evaluate the feasibility to recover Fe, Ni and Zn from synthetic ternary solutions (2 M KBr + 0.5 M HBr + 10 g/L Fe + 10 g/L Zn + 1 g/L Ni), at different pH values (adjusted to 0, 1, 2 or 3), and returning potentials (E_{RET}), two small diameter (3 mm) RDEs of CP and 304 SS were used, a few examples from the recorded curves being presented in Figure 3.

As can be observed in Figure 3.A and 3.B, at pH = 0, on both materials, the electrodeposition of Fe-Ni-Zn alloys is strongly inhibited, the shape of the anodic redissolution peaks indicating that the obtained deposits, at all tested E_{RET} values, are predominantly composed of Zn. Contrarily, at pH = 2 (Figures 3.C and 3.D), the obtained deposits start to include increasing amounts of Fe and Ni in parallel with the progressive shift of E_{RET} to more negative values. The phenomenon is less evident for CP due to its low electrical conductivity, which leads to significant voltage drops and, implicitly, pronounced alteration of the imposed voltage at the WE's surface.

To find the optimal conditions for Fe, Ni and Zn electroextraction, we evaluated, for all tested conditions, the electrodeposition efficiency (E.E.) as the ratio between the electrical charges recorded during the anodic and cathodic processes, the calculated values being presented in Table 2.

The data presented in Table 2 reveals that, for both materials and at all tested pH values, an E_{RET} value of -1.0 V/RE is too positive to start de electrodeposition process and values more negative than -1.1 V/RE are required. Further, for CP and 304 SS, the maximal E.E. values, of 95.8 and 86.8%, are obtained at pH values of 3 and 2, and E_{RET} values of -1.3 and -1.2 V/RE, respectively. These E.E. values revealed that, theoretically, by adequately choosing the electrode material, solution pH and applied potential, Fe, Ni and Zn can be efficiently extracted by electrodeposition from the spent leaching solutions resulting from the WPCBs recycling process.

SELECTIVE ELECTROEXTRACTION OF BASE METALS FROM LEACHING SOLUTIONS OBTAINED DURING THE RECYCLING OF WASTE PRINTED CIRCUIT BOARDS. III.

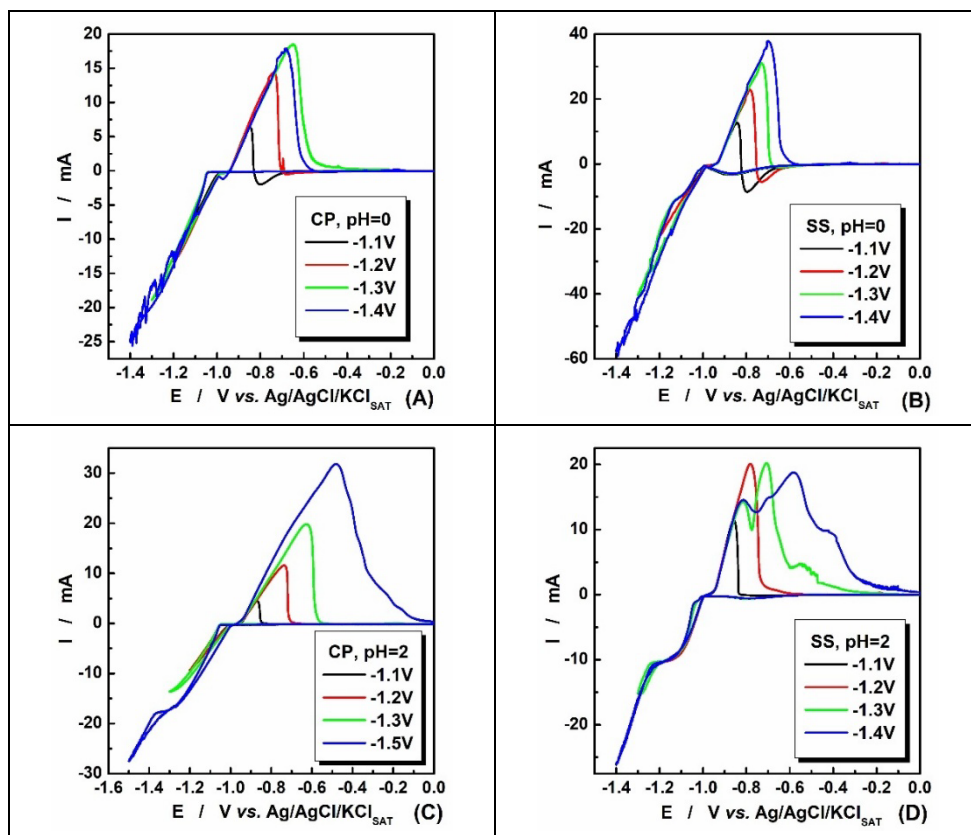


Figure 3. Examples of voltammograms recorded using HCV on RDE of CP (A and C) and 304 SS (B and D) in synthetic ternary solution (2 M KBr + 10 g/L Fe + 10 g/L Zn + 1 g/L Ni) for different values of E_{RET} (indicated in legends) and pH values of 0 (A and B) and 2 (C and D) ($\omega = 1000$ rpm; $v = 10$ mV/s)

Table 2. Electrodeposition efficiency (%) evaluated through HCV for the Fe, Ni and Zn electrodeposition on RDE of CP and 304 SS in the ternary synthetic solution (2 M KBr + 10 g/L Fe + 10 g/L Zn + 1 g/L Ni) for different E_{RET} and pH values

E_{RET} (V/RE)	WE = CP				WE = 304 SS			
	pH=0	pH=1	pH=2	pH=3	pH=0	pH=1	pH=2	pH=3
-1	0	0	0	0	0	0	0	0
-1.1	47.6	51.9	38.9	72.1	32.8	63.5	68.2	73.4
-1.2	66.5	86.5	81.4	89.1	39.4	81.2	86.8	80.8
-1.3	66.6	87.6	90.8	95.8	32.7	68.6	84.4	85.8
-1.4	30.9	80.1	91.1	95.5	27.0	67.5	81.2	72.7

Long-duration PCA tests on RDE of CP and 304 SS

The first sets of long duration electroextraction tests by PCA were performed in an original compartmented ECR (see Experimental section), using a CP RDE of 38 mm diameter and ternary synthetic solutions (2 M KBr + 0.5 M HBr + 10 g/L Fe + 10 g/L Zn + 1 g/L Ni), at different pH and E_{WE} values. The corresponding evolutions of pH and main electrical parameters are presented in Figure 4, a synthesis of the main experimental parameters and the obtained results is presented in Table 3, and a few examples of the obtained deposits photographs are presented in Figure 5.

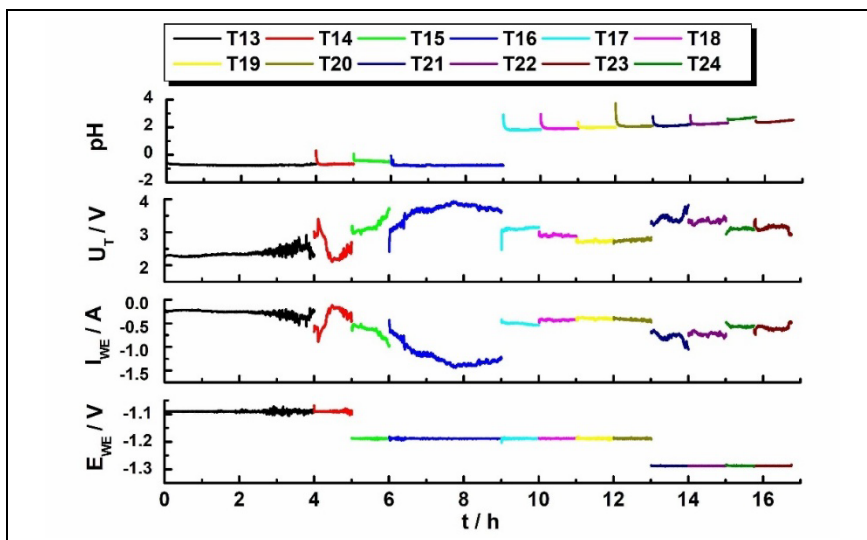


Figure 4. Evolution of the pH and main electrical parameters during the potentiostatic electrodeposition of Fe, Ni and Zn from samples of synthetic leaching solution (2 M KBr + 0.5 M HBr + 10 g/L Fe + 10 g/L Zn + 1 g/L Ni) using the CP RDE of 38 mm diameter

Very interestingly, as can be seen from Figure 4 and the first four lines of Table 3 (T13 ÷ T16), the pH recorded in the ternary solution of metals (Fe + Zn + Ni) containing 2 M KBr and 0.5 M HBr presented exaggerated negative values (generally, under -0.5 pH units). We also recorded this abnormal behavior in similar solutions, even without the BM ions [34], most probably due to the ions' interactions in solutions with very high ionic strength. [35,36] In these conditions, as can be seen from the first two lines of Table 3 (T13 and T14), when the CP RDE was polarized at -1.1 V/ER, no deposits were obtained. Contrarily, in the same solution, decreasing the E_{WE} to -1.2V/ER (T15 and T16)

allows the deposition of high purity Zn with an C.E. of around 50% and W_s of 6 kWh/kg. Moreover, as can be seen in Figure 5, deposit D12 is relatively compact, allowing it to be easily detached and analyzed. These first two experiments prove the fact that, by choosing the adequate polarizing potential, Zn can be recovered from the leaching solution without diminishing its acidity, which allows for the direct recirculation of the leaching solution in the process.

Table 3. The main experimental parameters and obtained results for the PCA electrodeposition tests of Fe, Ni and Zn from synthetic ternary solutions (2 M KBr + 0.5 M HBr + 10 g/L Fe + 10 g/L Zn + 1 g/L Ni) using the CP RDE of 38 mm diameter

Tests	Deposit	E_{WE} (V/RE)	t (h)	pH _M	m_D (mg)	[Fe] (%)	[Ni] (%)	[Zn] (%)	[Imp.] (%)	C.E. (%)	W_s (kWh/kg)
T13	D9	-1.1	4	-0.74	-	-	-	-	-	-	-
T14	D10	-1.1	1	-0.66	-	-	-	-	-	-	-
T15	D11	-1.2	1	-0.45	560	0.05	0.18	68.8	31.4	48.1	5.53
T16	D12	-1.2	3	-0.76	2450	0.12	0.04	89.8	10.1	50.6	6.02
T17	D13	-1.2	1	1.84	590	1.08	0.14	83.0	16.0	80.3	3.20
T18	D14	-1.2	1	1.93	500	1.34	0.20	84.8	14.0	83.4	2.88
T19	D15	-1.2	1	1.98	420	1.92	0.18	94.7	3.59	84.5	2.68
T20	D16	-1.2	1	2.10	500	5.45	0.52	80.8	14.3	85.8	2.69
T21	D17	-1.3	1	2.13	960	17.9	1.55	63.3	20.3	86.1	3.42
T22	D18	-1.3	1	2.25	940	29.4	3.35	45.1	28.8	88.5	3.31
T23	D19	-1.3	1	2.42	790	35.5	3.85	37.2	31.1	89.9	3.11
T24	D20	-1.3	0.75	2.62	670	44.2	4.32	13.7	46.5	91.2	3.14

Further tests, conducted at pH values of around 2, indicate the fact that, depending on the imposed E_{WE} and the depletion degree of the leaching solution, mixed deposits of Fe-Ni-Zn in varying proportions can be obtained, with C.E. values between 80 and 91% and W_s values between 2.7 and 3.4 kWh/kg. Additionally, as can be seen from the example included in Figure 5 (D14), the deposits are compact, facilitating their removal.

The results of the long-duration PCA tests, performed on the CP RDE at pH = 2, suggest the fact that, when the leaching solution is almost entirely spent (excessively loaded with Fe, Ni, Zn and other metals), the operator can opt for the advanced electroextraction of Fe, Ni and Zn, followed by the strong alkalization of the solution for complete removal of BM ions and total regeneration of the leaching solution.

Encouraged by the previously obtained results and conclusions, we decided to perform another set of measurements, using once again a 304 SS RDE, but with an increased diameter of 29 mm, which is going to allow the advanced electroextraction of Fe, Ni and Zn from highly acidic spent

leaching solutions (pH under 0). The evolution of pH as well as the main electrical parameters recorded during this new set of experiments is presented in Figure 6, and a synthesis of the main experimental parameters and obtained results is presented in Table 4.

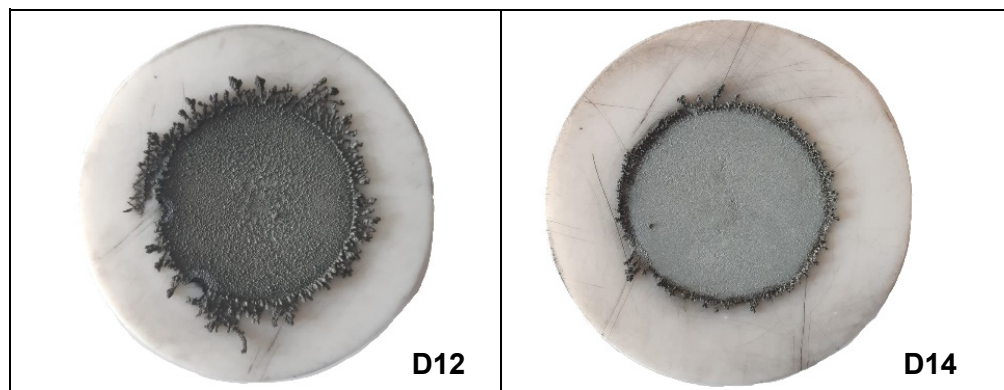


Figure 5. Examples of the Fe-Ni-Zn deposit pictures (see Table 3) obtained by PCA on CP RDE with a diameter of 38 mm in synthetic ternary solutions (2 M KBr + 0.5 M HBr + 10 g/L Fe + 10 g/L Zn + 1 g/L Ni).

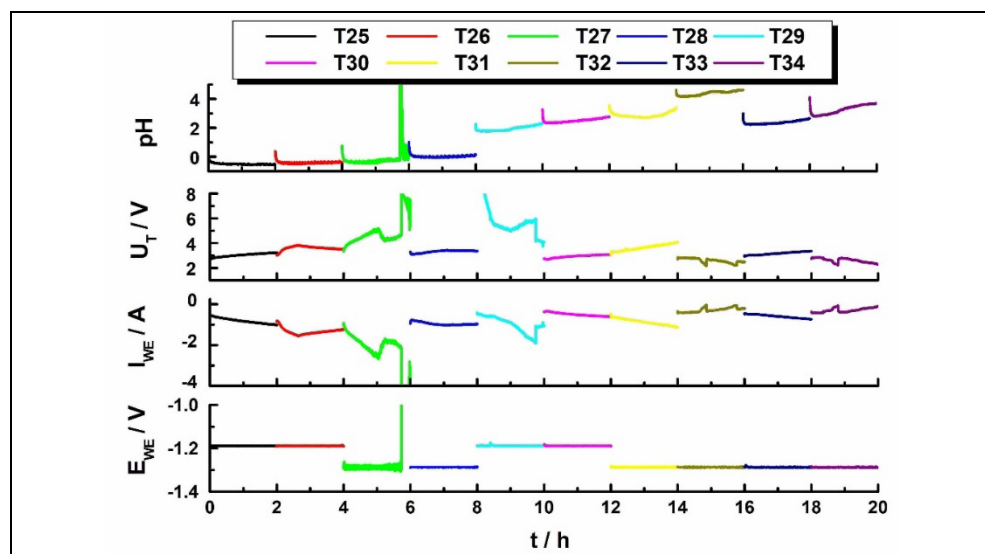


Figure 6. Evolution of the pH and the main electrical parameters during the electrodeposition of Fe, Ni and Zn from samples of synthetic spent leaching solution (2 M KBr + 0.5 M HBr + 10 g/L Fe + 10 g/L Zn + 1 g/L Ni) using the 304 SS RDE with a diameter of 29 mm

As can be seen from the first two lines of Table 4 (T25, T26), when the 304 SS RDE was polarized at -1.2 V/ER in the ternary solution of pH under 0, there is the risk that HER will dominate, which is going to lead to the impossibility of forming a Zn film on the electrode and, implicitly, the impossibility of forming a deposit.

Table 4. Experimental parameters and obtained results during the electrodeposition of Fe, Ni and Zn from samples of synthetic spent leaching solution (2 M KBr + 0.5 M HBr + 10 g/L Fe + 10 g/L Zn + 1 g/L Ni) using the 304 SS RDE with a diameter of 29 mm

Tests	Deposit	E_{WE} (V/RE)	t (h)	pH_M	m_D (mg)	[Fe] (%)	[Ni] (%)	[Zn] (%)	[Imp.] (%)	C.E. (%)	W_s (kWh/kg)
T25	D21	-1.2	2	-0.49	800	0.04	0.04	99.12	0.79	41.6	6.07
T26	D22	-1.2	2	-0.42	1	1.53	1.53	20.67	76.28	0.01	40737
T27	D23	-1.3	2	-0.11	1780	3.39	3.39	74.06	19.16	26.3	16.8
T28	D24	-1.3	2	0.03	360	3.45	4.08	81.93	10.54	20,8	13.6
T29	D25	-1.2	2	1.95	590	1.25	0.15	91.39	7.20	27.8	16.7
T30	D26	-1.2	2	2.50	500	1.74	0.20	94.91	3.15	54.0	4.52
T31	D27	-1.3	2	2.87	420	1.44	0.18	95.03	3.35	26.4	11.5
T32	D28	-1.3	2	4.39	500	5.45	0.52	89.78	4.25	73.3	3.02
T33	D29	-1.3	2	2.37	960	17.49	1.55	74.12	6.84	76.7	3.52
T34	D30	-1.3	2	3.26	94	29.35	3.35	27.05	40.25	88.1	2.71

On the contrary, in the same solution, decreasing the E_{WE} to -1.3V/ER (T27, T28) allows for the deposition of mixed Zn-Fe-Ni with a modest C.E. (under 26%) and W_s of 13 kWh/kg. In these conditions, as can be seen in Figure 7, the D23 deposit has a granular and dendritic structure, with weak adherence to the cathodic matrix, which allows its facile extraction from the reactor as a powder.

The subsequent tests were performed starting from an initial pH of 2 and for identical durations (120 minutes), with imposed E_{WE} of -1.2 and -1.3 V/ER (T29-T34). Using these parameters, a series of mixed Fe-Ni-Zn deposits were obtained, with acceptable C.E. and W_s values of 26 and 88% and 2.7 and 16.7 kWh/kg, respectively.

Regarding the structure of the obtained deposits, as can be seen in the example D27 from Figure 7, they have a pronounced granular and powdery aspect, with weak mechanical properties and an accentuated tendency of fragmentation and detachment from the electrode. This apparent disadvantage can be exploited for the continuous detachment of the deposit from the electrode by using a scraper fixed in the proximity of the electrode's surface if it's of RDE or rotating cylinder electrode (RCE) type.

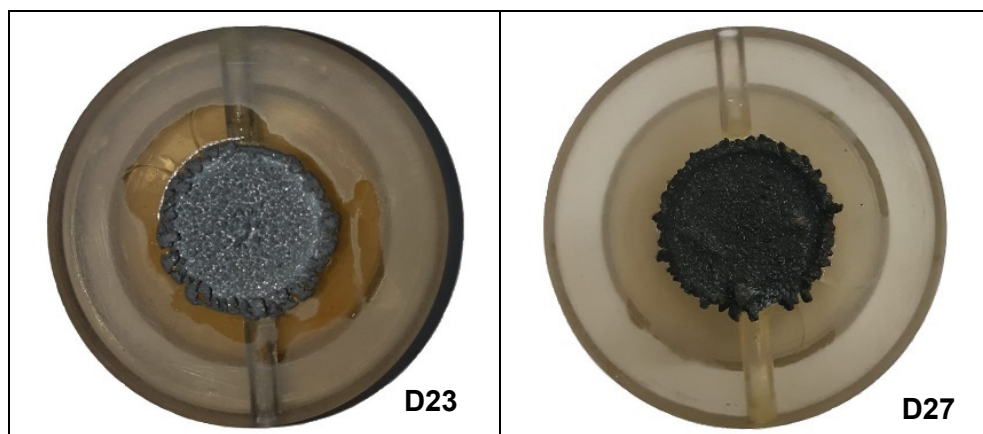


Figure 7. Examples of the Fe-Ni-Zn deposits obtained by PCA on CP RDE (D12/D14) and examples of Fe-Ni-Zn deposits obtained by PCA on 304 SS RDE with a diameter of 29mm in synthetic ternary solutions (2 M KBr + 0.5 M HBr + 10 g/L Fe + 10 g/L Zn + 1 g/L Ni)

From another point of view, the highly dispersed values of the deposit composition, C.E. and W_s can be associated with uncontrolled pH variations due to the HER and due to the proton migration through the ceramic membrane. Considering these factors, we appreciated that the electroextraction process of Fe, Ni and Zn can be significantly improved by the constantly monitoring and adjusting of pH. Additionally, the implementation of analytical techniques able of permanently monitoring the concentration of metallic ions in solutions is crucial when it comes to making a decision regarding the continuation of the electroextraction process or moving on to the complete purification of the leaching solutions by alkalization and removal of the resulting precipitates.

CONCLUSIONS

Literature provides an extremely large number of research articles regarding the recovery of metals from WPCBs, but most of these papers are focused only on the recovery of precious metals (Au, Pt, Ag, Pd etc.) and of those with a high market value (Cu, Sn, Pb etc.). Unfortunately, the separation, extraction and valorization of other metals which are found in smaller quantities or have a lower market value (Fe, Ni, Zn, Al etc.) but which are present, regardless, in the specific fluxes of WPCBs recycling processes, is insufficiently studied. In this context, our studies focused on evaluating the feasibility of the electroextraction process of Fe, Ni and Zn, both from synthetic and real

leaching solutions corresponding to the final steps of BMs recovery process from WPCBs. The performed experiments and the obtained results allowed us to draw the following conclusions:

- Using a Pt Fisher electrode is inadequate for the sequential electroextraction of Fe, Ni and Zn from real samples because of the intense HER on this substrate.

- The tests performed by HCV in synthetic solutions and using RDEs with a reduced diameter (3 mm) made of CP and 304 SS, indicate the fact that, by carefully selecting the pH and the imposed cathode potential, Zn can be selectively electroextracted, as well as its alloys with Fe and Ni, with hypothetical C.E. values between 17.5 and 95.8%.

- The long-duration (0,15 ÷ 8 h) experiments, performed by PCA in synthetic samples and using large diameter RDEs on CP ($\varnothing = 38$ mm) and 304 SS ($\varnothing = 29$ mm), have shown that, by adequately polarizing the cathode and carefully adjusting the solution pH, high purity Zn deposits (>98%) can be obtained, as well as Fe-Ni-Zn alloys.

- Even though CP RDEs are extremely useful and versatile in laboratory studies, their exploitation at an industrial level is not feasible. A potential solution to this deficiency is using 304 SS cathodic matrices, which led to extremely promising results.

- The composition of the Fe-Ni-Zn alloys is highly dependent on experimental parameters, as the electrolyte solution composition and imposed E_{WE} , the obtained C.E. and W_s values varying between 20 and 96% and 2 and 17 kWh/kg of alloy, respectively.

- Using a 304 SS RDE allows the selective electroextraction of Zn (even from highly acidic solutions), and their direct recirculation in the process.

- A pH value of 2 creates the conditions needed for the advanced recovery of Fe, Ni and Zn as alloys and allows for the easy and total regeneration of the leaching solutions.

EXPERIMENTAL SECTION

Reagents

Reactants such as KBr, HBr, KOH, Fe, NiO, ZnO were purchased from Fluka and Sigma-Aldrich.

As pointed in our previous study[22], after the selective electrodeposition of Cu, Sn and Pb, the concentration of the main metallic ions left in the real leaching solution were: 3 mg/L Cu; 20 mg/L Sn; 14 mg/L Pb; 0.2 g/L Cr; 7.5 g/L Zn; 5.1 g/L Fe; 0.62 g/L Ni; 6.9 g/L Al. This solution was used as catholyte for the electroextraction experiments that used the Pt Fisher type electrode.

For all other experiments, the synthetic solutions used as catholyte were prepared by dissolving adequate amounts of Fe, NiO and ZnO in a KBr 2 M + HBr 0.5 M solution. Where necessary, the pH of the solutions was adjusted to the required values by adding 10 M KOH or 48% HBr. The anolyte was prepared by dissolving 238 g KBr in double-distilled water and adding HBr until the pH reached 2, for a final volume of 1L. Main metal concentrations in the synthetic ternary solution were 30 g/L Fe, 3 g/L Ni and 30 g/L Zn.

Equipment and methods

For the tests concerning the selective potentiostatic electrodeposition of Fe, Ni and Zn from the real spent leaching solution using the Pt Fisher type electrode, the experimental setup already presented in our previous paper [22] was used. Moreover, the same protocols were used for the cathode cleaning and weighing, and for the mineralization and analysis of obtained deposits.

The HCV experiments were performed using a computer-controlled multi-channel potentiostat (DXC240, Datronix Computer, Romania) and a glass electrochemical cell of 50 mL, equipped with a Pt wire ($\varnothing = 0,5$ mm, L = 10 cm) as counter-electrode, an Ag/AgCl/KCl_{SAT} system as reference electrode (RE) and the two small diameter ($\varnothing = 3$ mm) RDEs of CP and 304 SS. All HCV measurements were performed at a scan rate of 10 mV/s.

For the long-duration PCA experiments, as can be seen in Figure 8, to assure a uniform current distribution on the large diameter RED surface, an original ECR, divided with a horizontal ceramic membrane, was used.

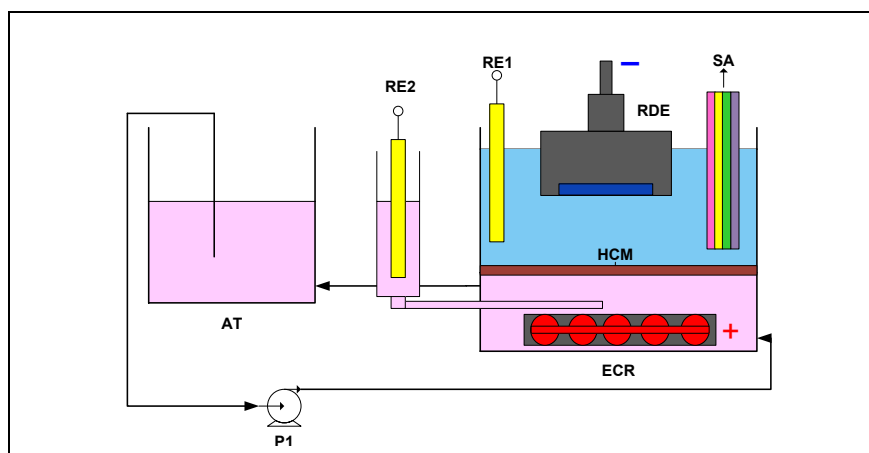


Figure 8. Schematic of the experimental setup used for the PCA experiments: AT – anolyte tank; ECR – electrochemical reactor; HCM – horizontal ceramic membrane; P1 – peristaltic pump; RE1,2 – Ag/AgCl/KCl_{SAT} reference electrodes; RDE – rotating disk electrode; SA – sensor array (pH and temperature).

0.75 L samples of 2 M KBr + 0.5 M HBr solution, adjusted at pH = 2, and 0.45 L samples of ternary synthetic leaching solutions were used as anolyte and catholyte, respectively. The ECR electrodes and the sensor array (pH and temperature) were connected to a computer controlled electrochemical station (DXC236, Datronix Computer, Romania).

At the end of the PCA experiments, all performed at a rotation speed of 400 rpm, the obtained deposits were detached from the RDE surface, cleaned, weighed and mineralized, and the resulting solutions were analyzed by flame atomic absorption spectrometry using an AVANTA-PM spectrometer (GBC, Australia).

ACKNOWLEDGEMENTS

Author Gabriele-Mario Bogdan is grateful for the financial support received from “Babeş-Bolyai” University of Cluj Napoca (Special scholarship for scientific activity).

REFERENCES

1. A. Abbadi, A. Rácz, L. Bokányi, *J. Mater. Cycles Waste Manag.*, **2024**, 26, 1326-1348.
2. Z. A. Cheshmeh, Z. Bigverdi, M. Eqbalpour, E. Kowsari, S. Ramakrishna, M. Gheibi, *J. Clean. Prod.*, **2023**, 389, 136132.
3. S. Deng, Z. Xiao, W. Zhang, A. Noble, S. Das, Y. Yih, J. W. Sutherland, *Resour. Conserv. Recycl.*, **2023**, 190, 106810.
4. S. Mir, N Dhawan, *Resour. Conserv. Recycl.*, **2022**, 178, 106027.
5. Z. Wang, Y. Liu, L. Meng, J. Qu, Z. Guo, *Process Saf. Environ. Prot.*, **2023**, 175, 554-564.
6. F. Faraji, R. Golmohammadzadeh, C. A. Pickles, *Environ Manage.*, **2022**, 316, 115242.
7. I. Birloaga, F. Veglio, *Environ Manage.*, **2022**, 307, 114567.
8. M. Gomez, S. Grimes, G. Fowler, *J. Clean. Prod.*, **2023**, 420, 138379.
9. A. Esmaeili, M. Arshadi, S. Yaghmaei, *Resour. Conserv. Recycl.*, **2022**, 177, 105976.
10. A. Trivedi, S. Hait, *J. Environ. Manage.*, **2024**, 349, 119565.
11. Q. Song, H. Sun, L. Zhang, Z. Xu, *J. Hazard. Mater.*, **2021**, 420, 126568.
12. S. Singh Siwal, H. Kaur, R. Deng, Q. Zhang, *Curr. Opin. Green Sustain. Chem.*, **2023**, 39, 100722.
13. S. Fogarasi, F. Imre-Lucaci, A. Egedy, Á. Imre-Lucaci, P. Ilea, *Waste Manage.*, **2015**, 40, 136-143.
14. C. Cocchiara, S. -A. Dorneanu, R. Inguanta, C. Sunseri, P. Ilea, *J. Clean. Prod.*, **2019**, 230, 170-179.

15. S. -A. Dorneanu, *Studia UBB Chemia*, **2017**, 62(3), 177-186.
16. S. Varvara, S. -A. Dorneanu, A. Okos, L. M. Muresan, R. Bostan, M. Popa, D. Marconi, P. Ilea, *Mater.*, **2020**, 13, 3630.
17. S. A. Dorneanu, A. A. Avram, A. H. Marincea, N. Cotolan, T. Frențiu, P. Ilea, *Studia UBB Chemia*, **2018**, 63(4), 147-158.
18. S. Gulliani, M. Volpe, A. Messineo, R. Volpe, *RSC Sustain.*, **2023**, 1(5), 1085-1108.
19. S. C. Chakraborty, M. W. U. Zaman, M. Hoque, M. Qamruzzaman, J. U. Zaman, D. Hossain, B. K. Pramanik, L. N. Nguyen, L. D. Nghiem, M. Mofijur, M. I. H. Mondal, J. A. Sithi, S. M. S. Shahriar, M. A. H. Jahir, M. B. Ahmed, *Environ. Sci. Pollut. Res.*, **2022**, 29, 32651-32669.
20. Q. Liang, J. Wang, S. Chen, S. Chen, L. Hu, J. Qin, Y. Han, X. Zeng, X. Li, Q. Guo, M. Chen, J. Shu, *J. Clean. Prod.*, **2023**, 409, 137223.
21. M. -I. Frîncu, E. Covaci, S. -A. Dorneanu, P. Ilea, *Studia UBB Chemia*, **2020**, 65(3), 33-44.
22. M. -I. Frîncu, E. Covaci, S. -A. Dorneanu, P. Ilea, *Studia UBB Chemia*, **2021**, 66(2), 137-149.
23. W. Liu, X. Hu, R. Jia, D. Zhang, L. Chen, T. Yang, *J. Clean. Prod.*, **2022**, 349, 131295.
24. Q. Xia, Q. Song, Z. Xu, *Waste Manage.*, **2023**, 158, 146-152.
25. H. Li, J. Eksteen, E. Oraby, *Resour. Conserv. Recycl.*, **2018**, 139, 122-139.
26. X. Li, Q. Gao, S. -Q. Jiang, C. -C. Nie, X. -N. Zhu, T. -T. Jiao, *J. Environ. Manage.*, **2023**, 348, 119288.
27. G. Roventi, R. Cecchini, A. Fabrizi, T. Bellezze, *Surf. Coat. Technol.*, **2015**, 276, 1-7.
28. R. P. Oliveira, D. C. Bertagnolli, E. A. Ferreira, L. da Silva, A. S. Paula, *Surf. Coat. Technol.*, **2018**, 349, 874-884.
29. Z. Liu, Y. Yang, X. Yang, B. Pan, *Surf. Coat. Technol.*, **2021**, 422, 127561.
30. S. Anwar, F. Khan, Y. Zhang, S. Caines, *J. Loss. Prev. Process. Ind.*, **2021**, 69, 104376.
31. R. S. Bhat, K. B. Munjunatha, S. I. Bhat, K. Venkatakrisna, A. C. Hegde, *J. Mater. Eng. Perform.*, **2022**, 31, 6819-6826.
32. A. C. Hegde, K. Venkatakrisna, N. Eliaz, *Surf. Coat. Technol.*, **2010**, 205, 2031-2041.
33. R. S. Bhat, M. K. Balakrishna, P. Parthasarathy, A. C. Hegde, *Coatings*, **2023**, 13(4), 772.
34. G. -M Bogdan, M. -I. Frîncu, S. -A. Dorneanu, *Studia UBB Chemia*, **2024**, 69(3), 177-191.
35. S. Lainela, I. Leito, A. Heering, G. Capitaine, B. Anes, F. Camões, D. Stoica, *Water*. **2021**; 13(18), 2522.
36. Y. Marcus, *Pure&Appl. Chem.*, **1989**, 61(6), 1133-1138.

THERMAL BEHAVIOUR OF COMPOSITE MATERIALS OBTAINED FROM RECYCLED TETRA PAK® BY THERMOPLASTING FORMING

Miron RANCEA^a, Ovidiu NEMEȘ^{a,*} , Liliana BIZO^{b,*} 

ABSTRACT. Tetra Pak® (TP) multilayer packaging consisting of paper, polyethylene (PE) and aluminum, are widely used as aseptic packages in the food and beverage industry. Consequently, large quantity of packaging waste is generated, and many efforts have been made for recycling. The aim of this work was to develop new composite materials from TP cartons waste by thermoplastic method at different temperatures ranging from 120 °C to 140 °C. The resulting material was characterized by thermogravimetric/differential thermal analyses (TG/DTA) and differential scanning calorimetry (DSC) measurements to establish the thermal behavior of the prepared composites. Based on these results, the degradation pathway of the composites obtained from TP waste was proposed. The results of the study show that the preparation of thermoplastic composites represents a promising recycling process. The thermal degradation temperature of the prepared composites establishes a limit for practical use, which prohibits the utilization of these materials at temperatures exceeding this threshold.

Keywords: *Tetra Pak® waste, recycling, composite materials, thermal degradation*

INTRODUCTION

Tetra Pak® (TP) packaging is widely recognized as an aseptic solution in the beverage and liquid food industry. TP cartons are particularly popular for containing milk, wine, juice, and soft drinks and enable products to be

^a *Technical University of Cluj-Napoca, Faculty of Materials and Environmental Engineering, 103-105 Muncii bld., RO-400641, Cluj-Napoca, Romania*

^b *Babeș-Bolyai University, Faculty of Chemistry and Chemical Engineering, 11 Arany Janos str., RO-400028, Cluj-Napoca, Romania*

* *Corresponding authors: ovidiu.nemes@imadd.utcluj.ro; liliana.bizo@ubbcluj.ro*



distributed without refrigeration for extended periods without spoiling. Additionally, TP containers help maintain the nutritional quality and hygiene of the contents [1-3]. The development of milk packaging began in 1943, led by Swedish engineer Ruben Rausing. The brand name Tetra Pak® was established in 1944, inspired by the tetrahedral shape of the cartons. TP cartons gained popularity due to their ability to efficiently transport and store milk foams. In 1961, TP introduced aseptic sterilization technology, enabling the production of bacteria-free milk. This technology further evolved to allow products to be stored for up to six months without refrigeration using the ultra-high temperature (UHT) pasteurization process [4].

It is known that TP consists mainly of three materials, namely paper, polyethylene (PE), and aluminum (Al) foil, organized into six-layers. The type of paper used in composite beverage cartons varies based on the packaged product, the region where it will be sold, and the manufacturing conditions. Generally, paper constitutes 75% of the total weight of the package, while PE accounts for 20%, and Al makes up the remaining 5% [5]. The primary function of the paper is to ensure the package maintains its rigid shape and to enhance material strength. The Al foil is included due to its excellent barrier properties, protecting against light, oxygen, water vapor, and microorganisms, whereas PE serves several purposes, it protects the paper layer from water, safeguards the Al layer from direct contact with the contents, bonds the layers together, and allows for heat sealing [6].

Packaging waste leads to significant environmental and financial impacts, prompting various efforts aimed at recycling. The concept of a circular economy seeks to prolong the life of products through strategies such as reuse, energy recovery, and recycling. Depending on the level of processing involved, the recycling process encompasses various stages, as production recycling, material and feedstock recycling. [4, 7-9].

In such circumstances, it is essential to establish a TP recycling system and explore effective technologies for recycling TP materials [10]. The first method used to recycle TP was the particle board method. In this process, the cartons were not separated into their components before being processed through thermal compression, resulting in boards that could be used in furniture, civil construction, and packaging industries. In subsequent years, a new recycling method known as hydro-pulping was developed. This method allowed for the recovery of paper fibres, which make up 75% of the TP cartons. After hydro-pulping, the remaining PE and Al parts are processed using various technologies, including plastic product transformation, energy recovery, pyrolysis, and plasma technologies. However, these processes are quite expensive and complex. Nowadays, the collected TP are either accumulated in certified collection and separation facilities, placed in landfill areas, or burned in cement plants [11].

One of the most promising applications of the TP recycled cellulose is the preparation of thermoplastic composites [12]. Many research groups have concentrated their efforts on the production of composite materials utilizing packaging waste in order to better validated such materials. Obtaining composite materials, particularly from TP waste, represent a valuable resource that can serve as an alternative for various structural and non-structural applications. The optimization of processing parameters for recycled TP is critical, as the properties of these composites are influenced by several factors, including material type, mixing ratio, mixing duration, material size, and the employed technology. A range of technologies is available to produce new composites, with compressive moulding being among the most prevalent. Research indicates that the Al layer present in TP can significantly minimize water absorption, while the high cellulose content in TP reduces the necessity for supplementary reinforcement materials. Furthermore, TP enhances multiple mechanical properties of composite materials, including density, thickness, swelling, elastic modulus, and compressive strength. Therefore, the development of new composite materials derived from packaging waste not only alleviates environmental pollution but also contributes to the reduction of waste management costs [13-15].

To enhance the utility and quality of composite materials derived from TP waste, it is crucial to study their thermal properties, as these determine potential applications. Due to their chemical composition, these materials are both thermally degradable and combustible. The characteristics of their thermal degradation significantly impact their performance and sustainability. The thermal degradation temperature establishes a definitive upper limit for practical use. Therefore, these materials cannot be utilized at temperatures beyond this threshold. Gaining a thorough understanding of thermal degradation behaviour is essential for various practical applications [16].

Many efforts are made to enhance the recycling capacity for carton packages across the European Union (EU), aligning with the proposed EU Packaging and Packaging Waste Regulation (PPWR), which are very important in facilitating the transition towards sustainable food packaging and to achieving greater material circularity. In this context, the novelty of this study consists in preparation and characterization of new composites materials obtained from TP waste by using an advantageous method with a low energy consumption and respecting the principles of the circular economy. Consequently, the aim of this work was to investigate the thermal behaviour of TP composite materials, and their production parameters influence on the critical temperatures and weight loss. Such approach gives important data for further establishing of these composites' application areas.

RESULTS AND DISCUSSION

In order to evaluate the thermal behavior of new composite materials based on TP waste as raw material, a series of samples were obtained using the methods developed in our research group [17]. The samples codes used in this study and the process parameters are presented in *Experimental section*.

Thermal analyses of the new composite materials were carried out under the same conditions to determine the thermal degradation behaviors. Thermogravimetry (TG), its derivative (DTG) and differential thermal analysis (DTA) profiles of composite materials prepared at different temperatures are displayed in Figures 2-6. TG, DTG and DTA curves of the composite thermoformed at 120 °C (S1-120.5) are shown in **Figure 1**. The initial weight loss between 24.21 and 97.75 °C was only about 3.39%, suggesting the moisture loss. The primary weight loss of 59.95% occurred within the temperature range 213.16 - 382.65 °C, with the maximum weight loss rate peak at 332.61 °C, which was caused by the decomposition of cellulose fibers from the composite material. About 25.34% of the initial weight was lost between 382.65 and 495.64 °C, with a weight loss peak at 448.83 °C, which was caused by the decomposition of the PE layers. It was expected that the char is formed mainly from the cardboard part of the packaging used in the composite preparation, so the residue after 500 °C probably consisted of the aluminum and the char formed. The results of the analysis were consistent with previously reported studies on TG analysis of waste TP packaging [18-20]. The behavior of the thermal decomposition of composite (S1-120.5) obtained from TP waste clearly shows two important different stages, with the maximum decomposition rates at 332.61 °C and 448.83 °C, in agreement with the results obtained by Haydary et al. [19]. The first stage corresponds with thermal decomposition of cellulose and hemicelluloses to an intermediate product and the second stage includes decomposition of low-density polyethylene (LDPE) and the intermediate product.

The decomposition profiles of the other composites (S2-125.5, S3-130.5, S4-135.5, S5-140.5) are quite similar (**Figures 2÷5**), following the 4 stages as revealed in **Table 1**. After the initial mass loss, which corresponds to the moisture loss, two important separate stages of mass loss were clearly observed, the first for the degradation of the cellulose fibers and the second for the decomposition of the PE from the composite plates.

DTA curves can be a viable source of information about energy absorption during the thermal conversion of different kinds of materials. The DTA curve of S1-120.5 sample can be seen in **Figure 1**. As is evident, the exothermic peaks at 250.29, 347.94 and 451.25 °C were caused by the decomposition of cellulose and PE, respectively, which were in accordance

with the DTG peaks. The melting of Al would lead to the presence of a very small weight loss peak on the DTG curve, it consequently created a weak endothermic peak at 660.28 °C. It should be noticed that temperatures used for the preparation of the materials do not show major differences between the behaviors of the TG, DTG and DTA curves (**Table 1**).

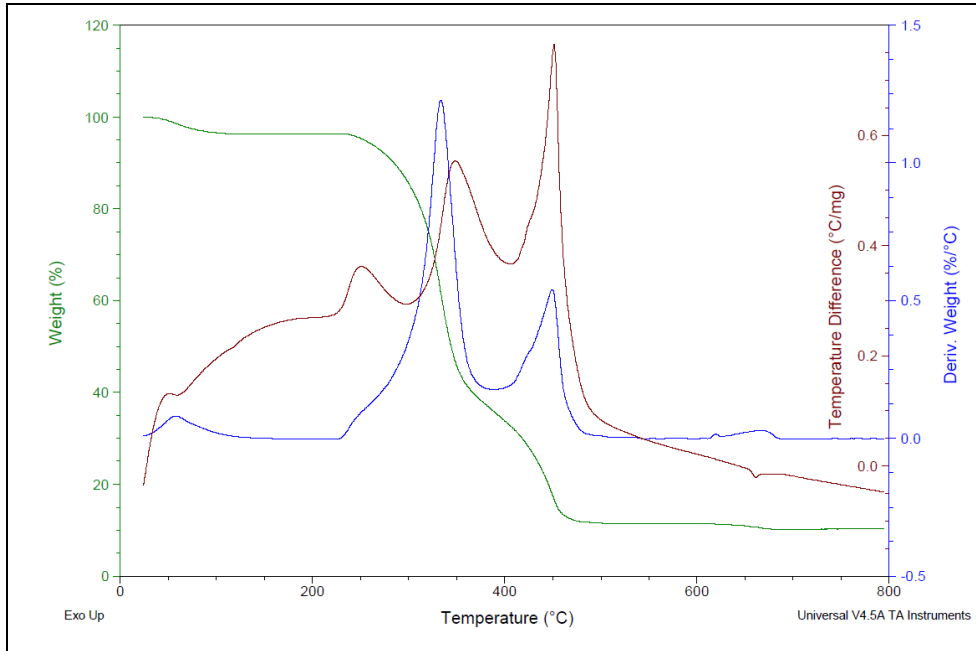


Figure 1. Thermogravimetry (TG- green), its derivative (DTG-blue) and differential thermal analysis (DTA- red) curves of sample S1-120.5

Table 1. Characteristic temperatures and mass losses for the thermal degradation reaction of the prepared composites from TP waste

Thermoforming temperature	S1-120.5 120 °C	S2-125.5 125 °C	S3-130.5 130 °C	S4-135.5 135 °C	S5-140.5 140 °C
Thermal steps	T_i-T_f (°C)	T_i-T_f (°C)	T_i-T_f (°C)	T_i-T_f (°C)	T_i-T_f (°C)
Moisture evaporation	24.21- 97.75	26.27- 117.12	26.72- 92.10	33.99- 92.10	28.34- 97.75
Step I	59.95- 382.65	60.52- 397.98	62.63- 397.98	63.53- 395.56	65.8- 410.09
Step II	25.34- 495.64	22.10- 515.82	24.83- 512.59	19.70- 498.87	17.78- 496.45
Step III	1.40- 694.99	1.95- 699.83	1.76- 703.06	2.06- 701.45	1.95- 708.71
Total mass lost	90.08	87.99	91.74	88.18	88.49

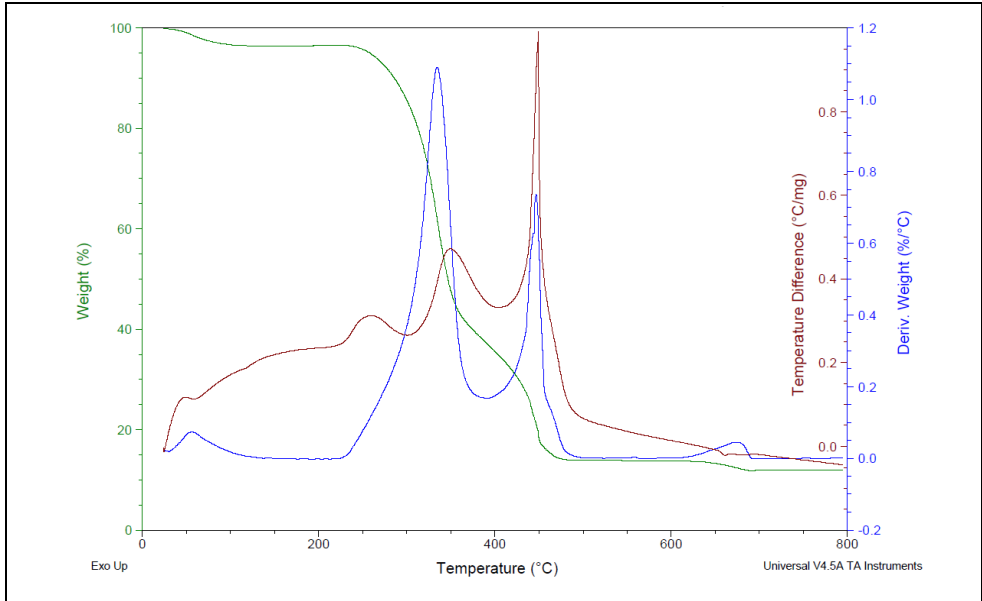


Figure 2. Thermogravimetry (TG- green), its derivative (DTG-blue) and differential thermal analysis (DTA- red) curves of S2-125.5 sample

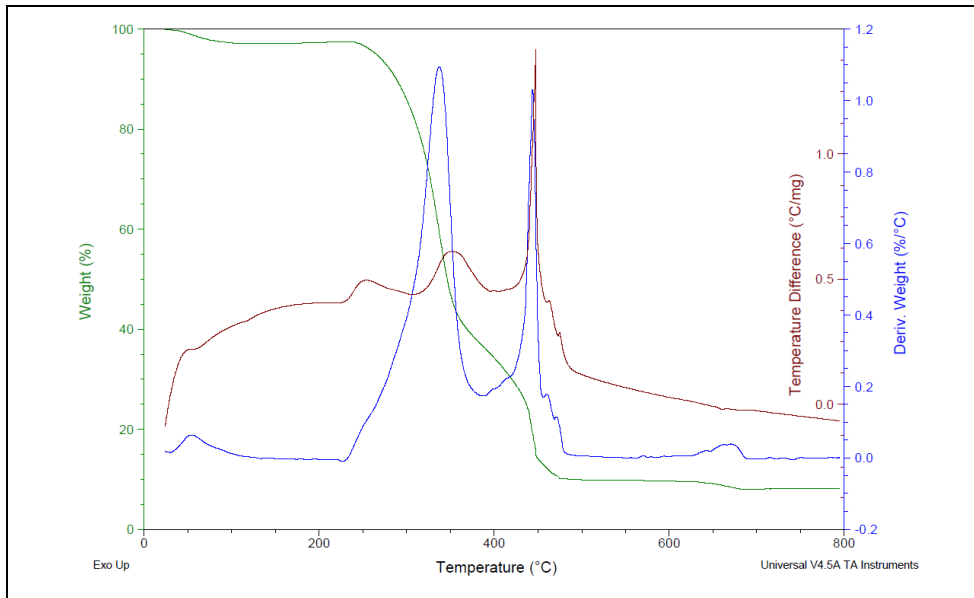


Figure 3. Thermogravimetry (TG- green), its derivative (DTG-blue) and differential thermal analysis (DTA- red) curves of S3-130.5 sample

THERMAL BEHAVIOUR OF COMPOSITE MATERIALS OBTAINED FROM RECYCLED TETRA PAK®
BY THERMOPLASTING FORMING

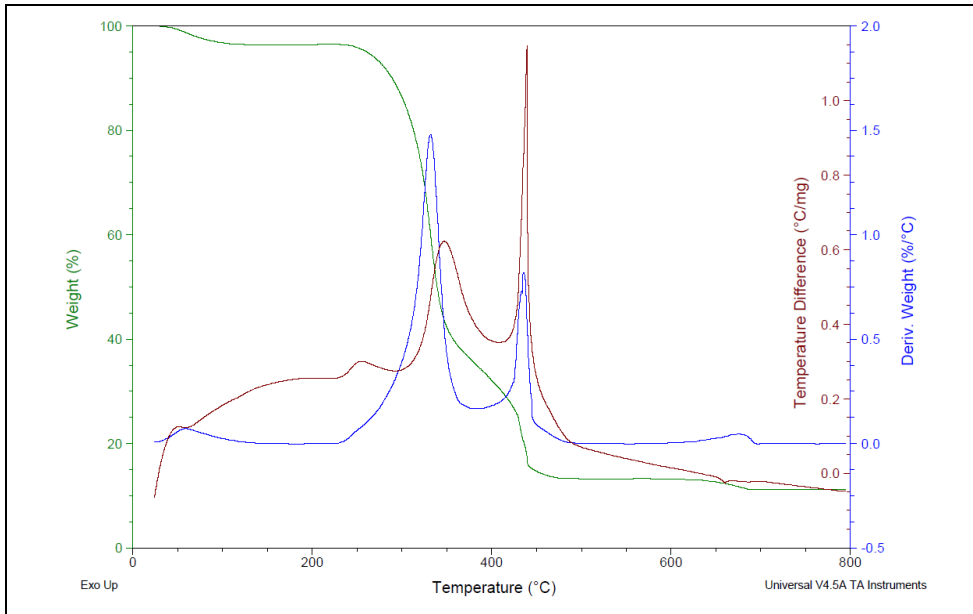


Figure 4. Thermogravimetry (TG- green), its derivative (DTG-blue) and differential thermal analysis (DTA- red) curves of S4-135.5 sample

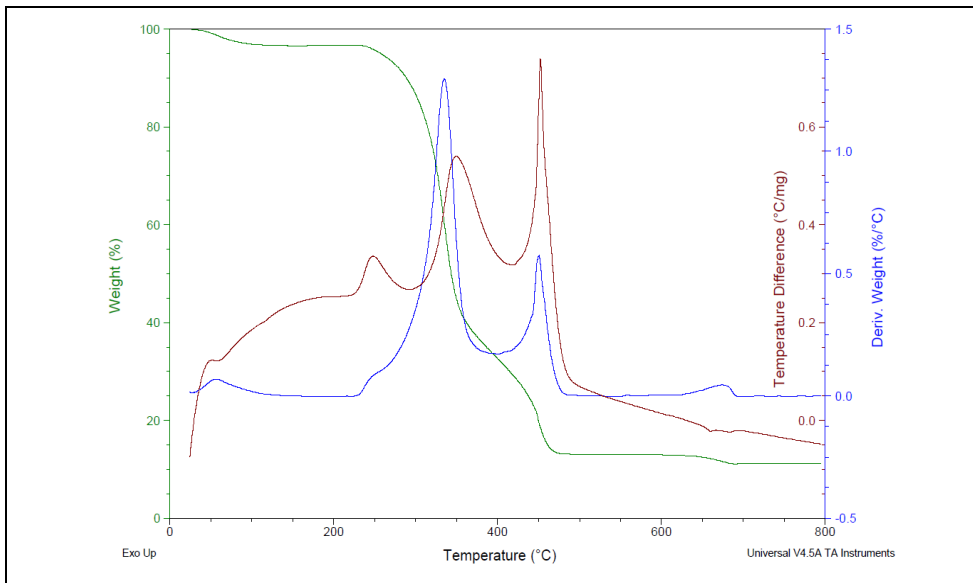


Figure 5. Thermogravimetry (TG- green), its derivative (DTG-blue) and differential thermal analysis (DTA- red) curves of S5-140.5 sample

Figure 6 shows the DSC curves of composite materials (S1-120.5, S2-125.5, S3-130.5, S4-135.5 and S5-140.5) obtained at different temperatures.

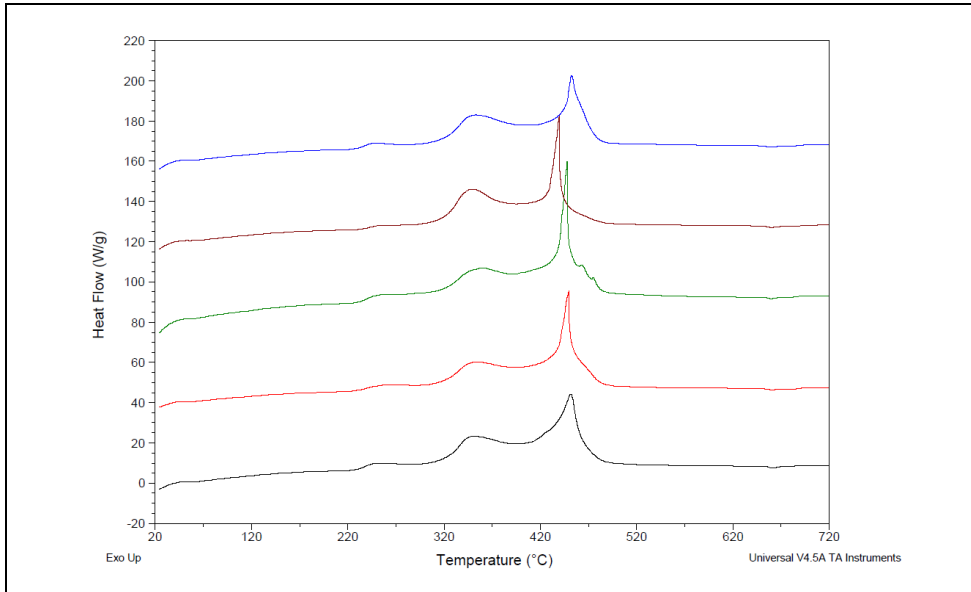


Figure 6. DSC curves of composites S1-120.5 (black), S2-125.5 (red), S3-130.5 (green), S4-135.5 (yellow), and S5-140.5 (blue), respectively.

All five DSC curves have three exothermic peaks between 220 °C and 450 °C. The first two exothermic peaks are attributed to the decomposition of cellulose. The third peak at ~ 480 °C showed the decomposition of low LDPE type PE polymer in the composites. Finally, the last peak ~ 660 °C was related to an endothermic process of fusion of aluminum in the samples. In general, the melting point of LDPE is lower than the linear low-density polyethylene (LLDPE).

The development of new materials with enhanced performance using various waste materials has gained significant attention in recent years, primarily due to environmental and socioeconomic benefits. In the study conducted by Yilgör et al., composite panels were manufactured from TP waste [20]. The thermal degradation properties of these panels were analyzed using TG/DTG methods. Their study demonstrated that it is possible to produce panels from TP waste without generating additional waste, in addition to utilizing them in the pulping process. The thermal degradation of the paper layer occurred at lower temperatures compared to the LDPE layer and the composite panel. Specifically, the thermal degradation of the paper layer began at temperatures

ranging from 200 °C to 350 °C, while the LDPE layer started degrading at 432 °C, in agreement with our results. Additionally, aluminum does not degrade during thermal treatment and melts at approximately 600 °C, indicating that it does not influence the TG and DTG profiles of the panels. These composite panels may have limited applications because of the hydrophilic nature of cellulose in their structure. However, they can be considered for indoor applications where there is a low risk of fungal decay, and the use of additives is not required [20]. In our study, the thermal degradation of the TP composites began at temperatures beginning from ~ 200 °C for any of the studied samples. Due to the different forming temperatures, ranging from 120 °C to 140 °C, which do not exceed the beginning of the degradation temperature, there is no influence on the higher critical decomposition temperatures.

In a recent study, Sergi et al. proposed the use of LDPE/Al mix obtained after the recovery of cellulose from multilayer aseptic packaging as a matrix for composite materials reinforced with short natural basalt fibers [21]. Consequently, an assessment of its thermal stability and the effects of the basalt fibers was necessary. A commercially available material, EcoAllene, which is obtained from the recycling of multilayer packaging, was reinforced with short natural basalt fibers at levels up to 30 wt.% using twin screw extrusion. The goal was to enhance the mechanical properties of this material and expand its potential applications. Thermal characterization through TG and DSC analysis revealed that the material is a complex mixture comprising LDPE, high-density polyethylene (HDPE), polypropylene (PP), and aluminum (Al). The addition of basalt fibers did not alter the melting and crystallization profiles, nor did it affect the overall degradation behavior of the composite. The EcoAllene, along with polyethylene and aluminum waste, exhibited a single-step degradation behavior with a maximum degradation temperature of approximately 485 °C, finding which agree with existing literature [22]. This degradation step could be attributed to the presence of LDPE, while the resulting residue indicates the Al content, which is expected to show no significant weight loss.

Cravero et al. included in their study the thermograms of a pure LDPE which exhibited a maximum degradation temperature around 474 °C [22]. In the work authored by Hidalgo-Salazar et al. [23], the authors reported a maximum degradation temperature around 470 °C. Recently, Georgiopoulou et al. [24] reported, for a LDPE/Al by-product recovered by a selective dissolution/precipitation process, a maximum degradation temperature of 482 °C, with an onset degradation temperature of 429 °C, which are in close agreement with the values obtained by Sergi et al. In our work, the maximum degradation temperature in all the samples studied was found to be ~ 450 °C, in close agreement with the other recent studies.

CONCLUSIONS

The recycling of waste TP packages composed of paper, LDPE, and Al is of great recycling significance. In the present work we have investigated the thermal degradation behavior of composites produced from TP waste without any significant recycling process, by thermoplastic forming. Thermal behavior of the resulting materials was studied and the results showed that thermal degradation consisted of two important distinct steps after the moisture evaporation: the first step was caused by the decomposition of cellulose fibers from the composite material and the second step corresponds to the degradation of LDPE. It's clear that the residue consists of char and aluminum after the thermal degradation of the composites. Results from the present study show that these low-cost thermoplastic composites show potential in many applications, respecting the decomposition temperature found to begin at ~ 200 °C as proposed by the thermal analysis, which prohibits the utilization of these materials at temperatures exceeding this threshold.

EXPERIMENTAL SECTION

Composites preparation

The composite materials were obtained from multi-layer packaging wastes, containing aluminum, paper and polyethylene terephthalate (e.g. juice packs, milk packs, etc.), using the procedure previously described in literature by our group [14]. The multi-layer packages have been carefully washed and cropped out into small pieces. Afterwards, the obtained material was compressed at different temperatures, 120 °C, 125 °C, 130 °C, 135 °C and 140°C, without any kind of bonding materials addition, with the obtaining of some plates, as illustrated in **Figure 7**. The composite material plates have been produced in a

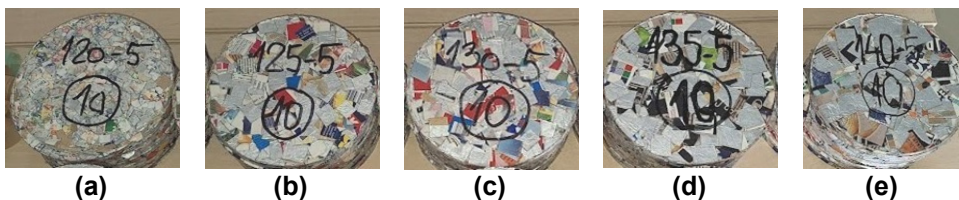


Figure 7. Composite plates obtained at (a) 120 °C, (b) 125 °C, (c) 135 °C and (d) 140 °C, respectively.

specific mold (**Figure 8**). To ensure the heating of the material, the mold was endowed with an electrical resistance, which guarantees the required forming temperature. The samples presented in **Figure 7**, have been named considering the forming temperature, as follows: S1-120.5, S2-125.5, S3-130.5, S4-135.5 and S5-140.5, respectively (see **Table 2**).



Figure 8. The mold used for the fabrication of composite plates.

Table 2. Samples codes and process parameters

Samples Code	Process parameters
S1-120.5	T = 120 °C, P= 5MPa
S2-125.5	T = 125 °C, P= 5MPa
S3-130.5	T = 130 °C, P= 5MPa
S4-135.5	T = 135 °C, P= 5MPa
S5-140.5	T = 140 °C, P= 5MPa

Thermal analyses

The TA Instruments SDT Q600 Thermogravimetric Analyzer (TGA) & Differential Scanning Calorimeter (DSC) was used for simultaneous measurement of weight change and differential heat flow on the composite samples from ambient to 800 °C. Data on thermogravimetry (TG), its derivative (DTG), differential thermal analysis (DTA), and differential scanning calorimetry (DSC)

curves, were simultaneously acquired under the following measurement conditions: heating from laboratory temperature to 800 °C at a heating rate of 10 °C/min, under normal air atmosphere, using alumina pans.

REFERENCES

1. I. Russell; J. Kellershohn; S.K. Panda; *Probiotic beverages*, Academic Press, Amsterdam, Netherlands, **2021**, pp. 441-466.
2. F. Lecheb; S. Bougherara; K. Delleci; L. Djoubani; M. Lazazi; B. Rahal; *Algerian J. Env. Sc. Technology*, **2022**, 8:3, 2569-25773.
3. A. Castro; J. Araújo; J. Carvalho; Proceedings paper "IMECE2014-38880," paper No: IMECE2014-38880, V014T11A025, pp. 1-6, **2017**.
4. M.I.P. Maduwantha; R.A. Jayasinghe; *Int. J. Eng. Sci.*, **2023**, 7(1), 1-9.
5. C.M.A. Lopes; M.I. Felisberti; *J. Appl. Polym. Sci.* **2006**, 101, 3183-3191.
6. J. Zawadiak; S. Wojciechowski; T. Piotrowski; A. Krypa; *Am. J. Chem. Eng.*, **2017**, 5(3), 37-42.
7. N.F. Da Cruz; P. Simões; R.C. Marques; *Resour. Conserv. Recycl.*, **2014**, 85, 1-4.
8. A.R. Elgie; S.J. Singh; J.N. Telesford; *Resour. Conserv. Recycl.* **2021**, 164, 105170.
9. A. Bartl; *Waste Manag. Res.*, **2014**, 32, 3-18.
10. H. Dong; F. Yu; Z. Bi; C. Zhang; X. Liu; Y. Geng; S. Ohnishi; H. Li; *Resour. Conserv. Recycl.*, **2024**, 202, 107355.
11. M. Karaboyaci; G.G. Elbek; M. Kilic; A. Sencan; *EJENS*, **2017**, 2(1), 126-129.
12. G. Martínez-Barrera; M. Martínez-López; N. González-Rivas; J.J. del Coz-Díaz; L. Ávila-Córdoba; J.M.L.d. Reis; O. Gencel; *Construct. Build. Mater.*, **2017**, 157, 1018-1023.
13. A.K. Figen; E. Terzi; N. Yilgör; S.N. Kartal; S. Pişkin; *Korean J. Chem. Eng.* **2013**, 30(4), 878-890.
14. S. Nishad; M. Ouederni; I. Krupa; *Energy Built Environ.* **2025**, 6(3), 455-465.
15. Y. Ciawi; S.G. Tonyes; N.M. Utami Dwipayanti; *Acad. Environ. Sci. Sustain.* **2025**, 2(1), 1-12.
16. A. Korkmaz; J. Yanik; M. Brebu; C. Vasile; *Waste Manag.*, **2009**, 29, 2836-2841.
17. A.M. Gomboş; O. Nemeş; V.F. Soporan; A. Vescan; *Studia UBB Chemia*, **2008**, 53(3), 81-88.
18. M. Irgolič; M. Čolnik; P. Kotnik; M. Škerget; *Polymers*, **2024**, 16, 1879.
19. J. Haydary; D. Susa; *Chem. Pap.* **2013**, 67(12) 1514-1520.
20. N. Yilgör; S.N. Kartal; C. Houtman; E. Terzi; A. Kantur; C. Köse; S. Piskin, <https://www.academia.edu/3389259/>, accessed on 20.02.2025.
21. C. Sergi; J. Tirillò; T. Valente; F. Sarasini; *J. Compos. Sci.*, **2022**, 6, 72.
22. F. Cravero; A. Frache; *Polymers*, **2020**, 12, 2357.
23. M.A. Hidalgo-Salazar; M.F. Munóz; J.H. Mina; *Int. J. Polym. Sci.*, **2015**, Article ID 386325, 1-8.
24. I. Georgiopoulou; G.D. Pappa; S.N. Vouyiouka; K. Magoulas; *Resour. Conserv. Recycl.*, **2021**, 165, 105268.

SYNTHESIS OF N-DOPED CARBON MATERIALS WITH ULTRA-MICROPOROUS BY ACTIVATIVE RUBIDIUM CHLORIDE

Baocheng WU^{a,b}, Ye XING^a, Yande CAO^{a,c}, Haichao LI^{a,*}

ABSTRACT. Activated carbon from quinoa straw, an agricultural waste, was prepared by chemical activation using a novel activator, rubidium chloride. The effects of time, temperature and amount of activator on the yield and adsorption properties of quinoa straw activated carbon were also investigated. The results showed that the optimal activation process for quinoa straw activated carbon was: activation temperature 700 °C, activation time 2 h, and RbCl-QS ratio 1:1. The quinoa straw activated carbon prepared under this process had a yield of 27.18%, an iodine adsorption value of 828.11 mg g⁻¹, a total pore volume of 0.303 cm³ g⁻¹, a major pore size of 0.58 nm, and a specific surface area of 635.59 m² g⁻¹. At room temperature and pressure, the H₂ desorption can reach 3.92 cm³ g⁻¹. quinoa straw activated carbon prepared using RbCl as activator has excellent adsorption and hydrogen storage properties.

Keywords: Ultra-microporous, Activated carbon, Hydrogen adsorption storage, *Chenopodium quinoa* Willd., rubidium chloride

INTRODUCTION

Hydrogen energy has significant advantages such as zero carbon, high efficiency, high calorific value, cleanliness and non-pollution. It can be used as an ideal substitute for fossil energy in the future. In recent years, with

^a Key Laboratory of Applied Physical Chemistry of Qinghai Province, Qinghai Minzu University, Xining 810007

^b China School of Chemical Engineering and Automation, Qinghai Vocational and Technical University, Xining 810016, China

^c Asia Silicon (Qinghai) Co., Ltd, Xining 810007, China

* Corresponding author: lihaichao@vip.163.com



the continuous research on hydrogen storage materials. Hydrogen storage materials have been widely used in the fields of transportation, industry and construction [1]. However, hydrogen being a chemically active gas, hydrogen storage technology is considered to be the key bottleneck limiting the large-scale commercial application of hydrogen energy [2]. Hydrogen storage materials have been widely studied, including metal complex hydride hydrogen storage materials, solid state hydrogen storage materials, and organic liquid hydrogen storage materials. However, metal complex hydride hydrogen storage materials have low storage pressure but poor cyclic stability [3]; Solid-state hydrogen storage materials are safe, do not require high pressure, and are easy to transport, but have harsh release conditions [4]; Organic liquid hydrogen storage materials have high hydrogen storage density, high safety, convenient storage and transportation, expensive cost and harsh reaction conditions limit their development [5]. In summary it is necessary to develop a new hydrogen storage material.

Quinoa is native to the middle and high altitude mountains of the Andes in South America. It is now widely planted in China's Qinghai, Gansu, Tibet and other provinces. Due to its high cold tolerance, high yield and short growth cycle. It has become one of the few specialty crops that can be grown in the Tibetan Plateau region [6,7]. The massive cultivation of quinoa has made the problem of quinoa straw treatment progressively more acute. Unsilaged quinoa straw cannot be eaten by cattle. Leaving it in the field will interfere with the following year's cultivation. In the past, burning was used in most of the treatments, which can pollute the environment. It is also a serious waste of resources [8]. Like most plant straws, quinoa straw's main components are lignin, cellulose and hemicellulose. In a previous study, activated carbon (AC) prepared from straw after activation had better adsorption and energy storage properties [9]. Most of the traditional activators used in the preparation of AC are zinc chloride, phosphoric acid and potassium hydroxide. Most of the activators are not recyclable and need to be pH-neutralized after activation, and even produce toxic gases [10]. The selection of activators has hindered the development of AC materials. The Tibetan Plateau region is rich in salt lakes. Chloride-type salts usually have high melting points [11,12]. It is considered as an activator for the preparation of AC materials, which is of great significance for the application of salt resources in Qinghai Province.

In this experiment QS was used as a carbon source and RbCl as an activator. The activation of quinoa straw by the chemical activation method allowed the complete recovery of RbCl at the end of the experiment.

RESULTS AND DISCUSSION

The fixed activation temperature was 700 °C and the activation RbCl-QS ratio was 1:1. The effect of activation time (0-3 h) on the yield of QSAC and the adsorption performance of iodine value was investigated. As can be seen from Figure 1(a), the iodine adsorption value of QSAC increases with the increase of activation time from 0 to 2 h. The yield (27.18%), iodine adsorption value (765.35 mg g⁻¹) of QSAC at 2h was greater than the values obtained at other activation times. At 3 h, the yield and iodine adsorption value were significantly reduced compared with that at 2 h. Therefore, 2.0 h was selected as the optimal time.

The fixed activation time was 2 h, and the activation RbCl-QS ratio was 1:1. To investigate the effect of activation temperature (500~800 °C) on the yield of QSAC and iodine adsorption value. From Figure 1(b), it can be seen that the QSAC yield decreased from 33.81% to 17.37% with the increase of activation temperature. The iodine adsorption value increased continuously, and at 700 °C the iodine adsorption value (794.21mg g⁻¹). The iodine adsorption value decreased when the temperature reached 800 °C, when the yield (17.37%) and iodine adsorption value (574.43 mg g⁻¹) were the lowest. Therefore, 700 °C is selected as the optimal temperature.

The activation temperature was fixed at 700 °C and the activation time was 2 h. To investigate the effect of activated RbCl-QS ratio on QSAC yield as well as iodine adsorption value. From Figure 1(c), it can be seen that at a RbCl-QS ratio of 0.5:1 (18.33%), the QSAC yield was the lowest compared to 1:1 (27.09%) and 1:2 (29.46%). At RbCl-QS ratio 2:1, there was no remarkable increase in QSAC yield and iodine adsorption values compared to 1:1. The optimal RbCl-QS ratio was chosen to be 1:1 from the economic point of view. Higher iodine adsorption values of activated carbon will result in better performance. In summary, an activation time of 2 h, an activation temperature of 700 °C and a RbCl-QS ratio of 1:1 was chosen as the characterization samples in the following experiments.

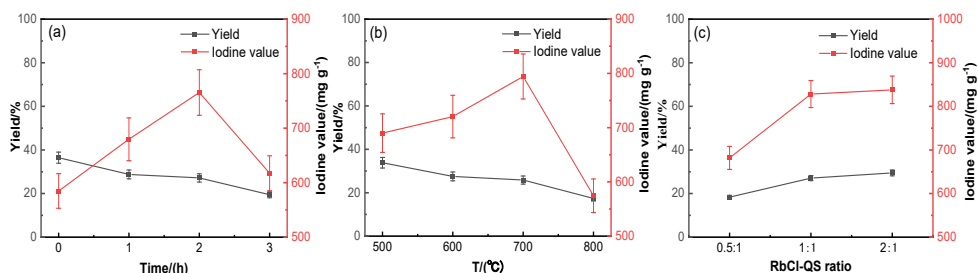


Figure 1. Effect of activation parameters on QSAC yield and adsorption performance

STRUCTURAL CHARACTERISTICS

The original image of RbCl is shown in Figure 2(a) reveal boulder like particles of RbCl with diameters of about 5 – 15 μm . The carbonised samples do not evidence such large particles indicating that the RbCl remains after carbonisation should be nanostructured, such a fact can be proved by the XRD patterns applying the Scherrer formula on the RbCl peaks. The surface of uncarbonised quinoa straw as shown in Figure 2(b) is smooth, compact and fewer pores. As shown in Figure 2(c), without adding any activator, the surface of quinoa straw carbon (QSC) was rough and the plant tissues were severely damaged. As shown in Figure 2(d-f), the pores on the surface of carbonised QS increased significantly. As the RbCl-QS ratio gradually increased, the vascular bundles and basic tissues of QSAC were more intact, the surface was smoother and less porous, and most of the vascular bundles were hardly broken and collapsed.

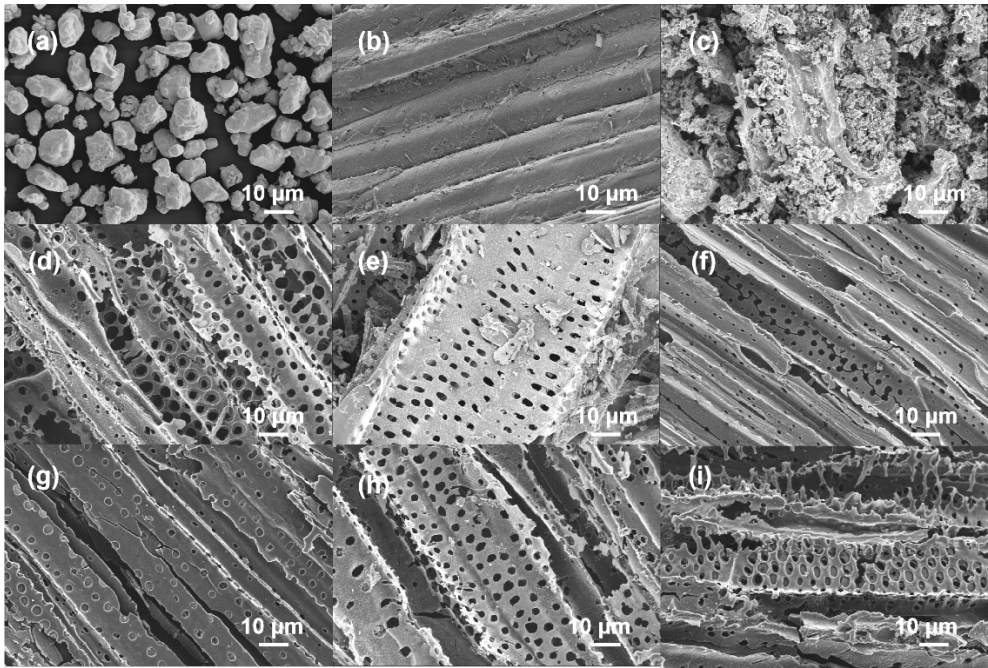


Figure 2. SEM image of the samples. (a) RbCl; (b) Quinoa Straw; (c) QSC700; (d) RbCl-QS ratio 0.5:1 QSAC700; (e) RbCl-QS ratio 1:1 QSAC700; (f) RbCl-QS ratio 2:1 QSAC700; (g) RbCl-QS ratio 1:1 QSAC500; (h) RbCl-QS ratio 1:1 QSAC600; (i) RbCl-QS ratio 1:1 QSAC800

As shown in Figure 2 (g-i), the number of pores increases significantly with increasing carbonation temperature. Compared to QSC, the surface of QSAC maintains the basic characteristics of the plant's microstructure. At higher temperatures and less RbCl, part of the microporous structure was damaged, leading to a decrease in the specific surface area of QSAC. The surface of QSAC is smooth and becomes more microporous, which has a larger specific surface area as well as better hydrogen adsorption capacity compared to QSC. It may be due to the addition of RbCl as an activator, which acts as a flame retardant and slows down the release of gaseous small molecules such as aromatic hydrocarbons, allowing the microstructure of the plant to be preserved. At the same time, during the gradual increase in temperature, small molecules such as aromatic hydrocarbons are slowly released, creating a large number of ultra-micropores [13].

As shown in Figure 3(a), the AC adsorption-desorption isotherm conforms to type I according to the IUPAC New Code-2015 Physical Adsorption Isotherm Classification method, which shows that the QSAC has a very high adsorption value of N₂, as high as 196.13 cm³ (STP) g⁻¹ [14]. The adsorption isotherm has a larger slope in the low relative pressure region, especially in the low-pressure part ($P/P_0 < 0.01$) of the adsorption. N₂ adsorption tends to equilibrate with increasing relative pressure. This is mainly due to stronger interactions, indicating that QSAC is dominated by micropores. According to the BET method, the total pore volume of QSAC700 was 0.303 cm³ g⁻¹, an overall distribution concentrated in the range of 0.58-0.73 nm, and a specific surface area of 635.59 m² g⁻¹. The results of the nitrogen adsorption-desorption curves are further corroborated from the pore size distribution plot in Figure 3(b). The QSAC700 dominant pore size distribution is at 0.58 nm. According to the IUPAC New Specification-2015 Code it can be determined that QSAC700 is a new type of ultra-microporous carbon material.

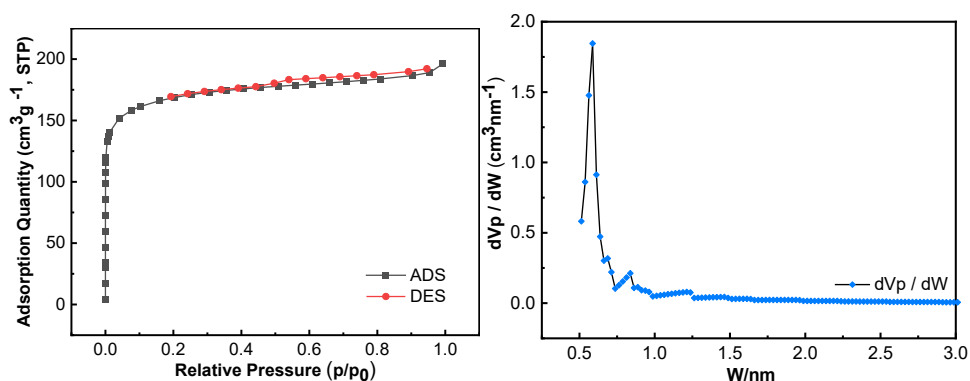


Figure 3. (a) N₂ adsorption-desorption isotherms, (b) Pore size distribution of QSAC700

The grey, blue and green XRD patterns in Figure 4(a) have a less intense and broadened peak at 27.15° which belongs to RbCl according to PDF 89-3623. The QSC700 does not have any peak at 27.15° . The intensity of peak at 27.15° is small in the grey pattern corresponding to less amount of RbCl and it progressively increases for the blue and green patterns due to the increased amount of RbCl. The peak at 27.15° is slightly broadened for all grey, blue and green patterns indicating that RbCl remains in the carbonised samples are nanostructured, that's why they are not visible on the SEM images. Applying Scherrer formula to the mentioned peaks; according to my calculations it results the following diameters for the RbCl nanoparticles: Grey pattern 25 nm, Blue pattern 60 nm, Green pattern 90 nm. Meanwhile, the structural orderliness of QSAC700 was analysed by XRD, as shown in Figure 4(a). It can be seen that all samples had distinct characteristic diffraction spectrum of carbon. The (002) crystal plane and the (100) crystal plane have typical amorphous carbon characteristics at 2θ of about 26° and 43° . The d_{002} graphite layer spacings of QSC and QSAC at different RbCl:QS ratios of 2:1, 1:1, and 0.5:1 were calculated from Bragg's formula to be 0.350 nm, 0.426 nm, 0.354 nm, 0.387 nm, which is larger than the layer spacing of fully non-graphitised carbon (0.344 nm). It can be demonstrated that the prepared QSAC are in the amorphous carbon stage, which can be graphitised by increasing the temperature. As shown in Figure 4(b), the presence of distinct D, G and 2D band in QSAC700 is typical of amorphous carbon. The intensity ratio of the D and G bands (I_D/I_G) has long been considered a key parameter for analyzing graphitization levels [15]. The calculated I_D/I_G ratio of AC700 is 0.9263, which indicates that the prepared QSAC possesses some degree of graphitization [16]. This indicates that the interior of QSAC is transforming from a graphite disordered layer structure to an ordered one, and the microcrystalline defects are gradually reduced. The slightly bulged 2D band near 2700 cm^{-1} also confirms that there are still some defects purely in the graphite layered structure.

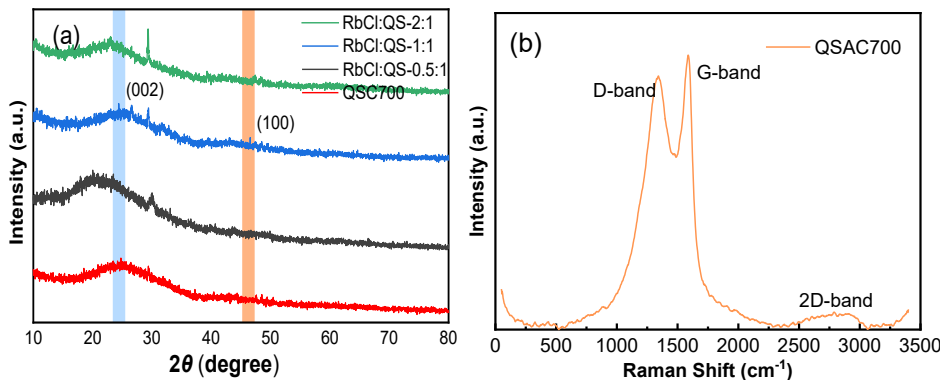


Figure 4. (a) XRD spectra and (b) Raman spectra of the samples

As can be seen in Figure 5, the characteristic peak shapes of QSC and QSAC infrared spectra are almost identical. The peaks around wave number $3\ 412\ \text{cm}^{-1}$ are attributed to the O-H and N-H stretching vibrations; $2\ 525\ \text{cm}^{-1}$ for the methylene and amino stretching vibration peak; The peak with a wave number near $1\ 808\ \text{cm}^{-1}$ is caused by the stretching vibration of the C=C bond of the benzene ring; The peak at $1\ 464\ \text{cm}^{-1}$ is associated with the C-N stretching vibrational mode; The peaks at $1\ 001\ \text{cm}^{-1}$ are those of C-O-C, C-O stretching vibrations and O-H bending vibrations in carboxylates, phenols or alcohols; The peak at $877\ \text{cm}^{-1}$ is an out-of-plane deformation vibrational peak of the aromatic ring; The $718\ \text{cm}^{-1}$ peak is a bending vibration in the C-C=O plane. It can be seen that the main structure of QSAC consists of multiple aromatic rings. The aromatic ring may also have functional groups such as $-\text{CH}_3$, $-\text{CH}_2$, $-\text{COOH}$ and $-\text{OH}$. The absorption peaks of QSAC at $3\ 412\ \text{cm}^{-1}$ and $1\ 001\ \text{cm}^{-1}$ were significantly broader than those of QSC, suggesting that the QSAC may contain more oxygen-containing functional groups dominated by C-O and O-N bonds. This is due to the increase in the content of highly substituted aromatic rings as a result of the polycondensation of QS by the carbonisation process. Meanwhile, the peak at $1\ 464\ \text{cm}^{-1}$ and $3\ 412\ \text{cm}^{-1}$ can characterise QSAC as a typical nitrogen doped carbon material. Addition of RbCl activator reduces the breakage of chemical bonds connecting the carbon network. It indicates that the prepared QSAC contains sufficient carbon framework and abundant organic functional groups, which in turn makes the QSAC exhibit strong adsorption properties [17].

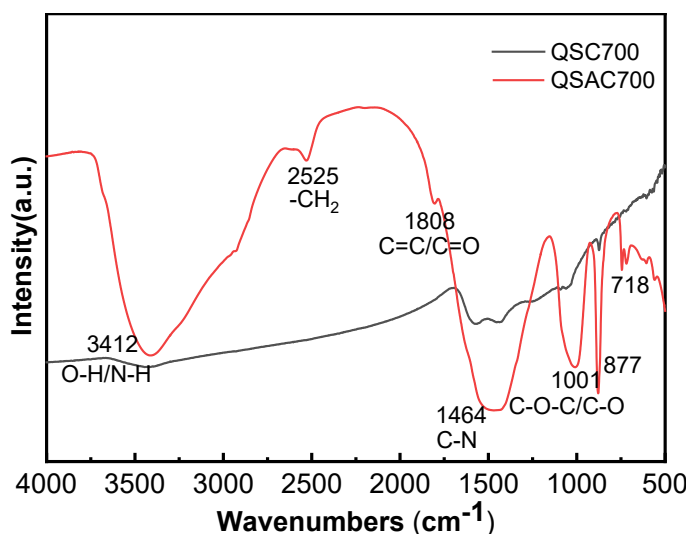


Figure 5. FT-IR spectra of QSC700 and QSAC700

X-ray photoelectron spectroscopy is commonly used to characterise the chemical structure of material surfaces. Figure 6 shows that QSAC700 contains C, N and O elements. From Figure 6 (b) to 6 (d), the C1s spectrum splits into three peaks. It is shown that there are five possible bonding forms of C, namely C=C (284.8 eV), C-O/C=N (286.4 eV) and C-O/C-N (288.4 eV); O1s split into 3 peaks, O-C=O (532.3 eV), C-O (530.8 eV) and C=O (529.5 eV); N1s then splits into 3 peaks, pyridine N (397.2 eV) pyrrole N (398.8 eV) and graphitised N (400.6 eV). Both XPS and FTIR data indicated the presence of O and N in the sample, suggesting that the prepared QSAC700 is N-doped amorphous carbon [18].

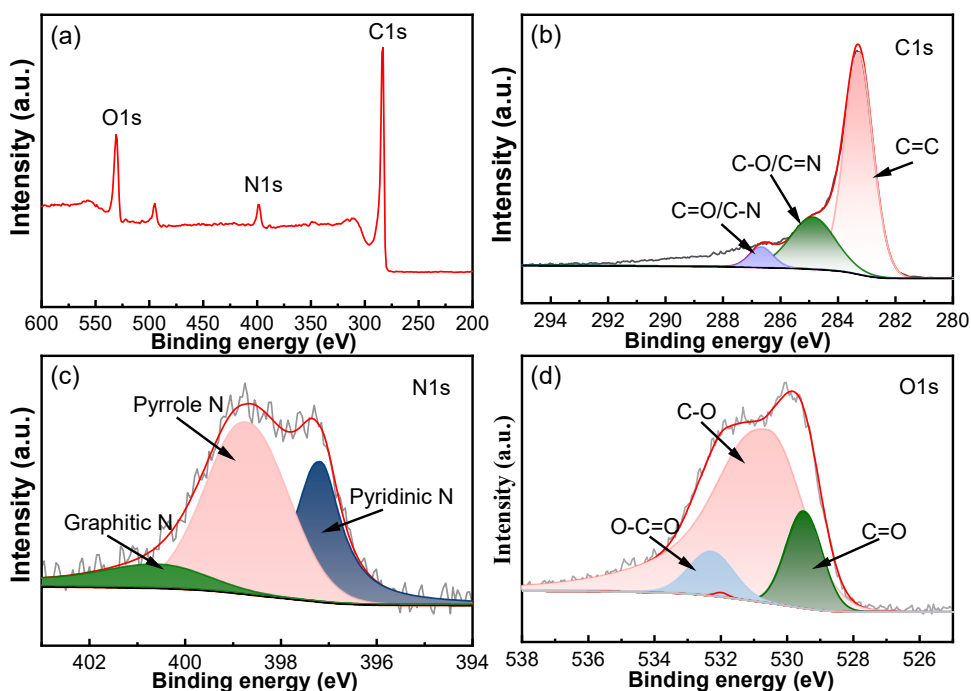


Figure 6. XPS survey (a) and fitted spectra of C1s (b), O1s (c) and N1s (d) of QSAC700

Theoretical calculations and experiments have shown that the physical adsorption of hydrogen on nanomaterials under low-temperature liquid nitrogen conditions depends on the microporous volume and microporous size distribution, especially the microporous volume size is closely related [19]. This is due to the fact that hydrogen molecules are smaller, so their adsorption efficiency is higher on micropores than on mesopores. In general, there is a

good linear relationship between hydrogen storage and microporous pore volume, i.e., the larger the microporous pore volume, the larger the hydrogen storage. S. Schaefer demonstrated that pores with widths ranging from 0.5 to 0.7 nm are best suited for hydrogen storage at 298 K, independent of pressure [20]. Based on this, it is hypothesised that QSAC700 should be a good material for hydrogen storage. The atmospheric pressure hydrogen adsorption and desorption curves for QSAC700 under cryogenic liquid nitrogen conditions are shown in Figure 7. As can be seen from the results in Figure 7, the adsorption capacity of hydrogen reaches $3.92 \text{ cm}^3 \text{ g}^{-1}$ at 298 K and 101.3 KPa, which is higher than the 0.59 wt% reported in literature [20]. It is shown that the QSAC700 microporous structure has excellent hydrogen storage capacity. It is also important to note that QSAC has excellent reversibility as a hydrogen storage material. As the pressure drops, the physically adsorbed hydrogen can be completely and reversibly desorbed without hysteresis loops. With the same specific surface area, the hydrogen storage capacity is higher than that of AC based on rice husk [21], corn kernel [22], bamboo and other raw materials [23], which has a greater application prospect.

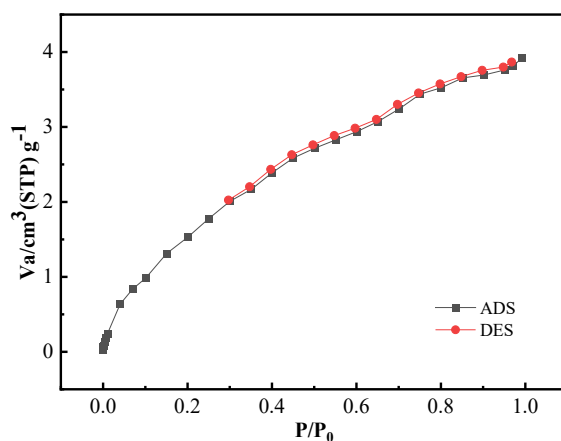


Figure 7. Hydrogen storage capacity of QSAC700

CONCLUSIONS

In the paper, quinoa straw was used as the raw material and RbCl was employed as the activator at 700 °C. QSAC with nitrogen-doped ultra-micropores was prepared by a one-step carbonisation method. The optimal process for the preparation of QSAC was determined by single factor

experiment method as: The activation temperature was 700 °C, the activation time was 2 h and the RbCl-QS ratio was 1:1. The specific surface area of QSAC reached 635.59 m² g⁻¹ with a pore volume of 0.303 cm³ g⁻¹ and a dominant pore size of 0.58 nm. Among the carbon materials with the same specific surface area biomass AC, it has a higher percentage of micropores and higher surface nitrogen and oxygen heteroatom content. The adsorption capacity of hydrogen reaches 3.92 cm³ g⁻¹ at room temperature and pressure, which has excellent hydrogen storage capacity. It was demonstrated that RbCl could be used as a novel activator for the activation of quinoa straw for the preparation of N-doped ultra-microporous activated carbon. It provides new ideas for solving the problem of agricultural waste occupying arable land in highland areas and diversified utilization of salt lakes products.

EXPERIMENTAL SECTION

QS was obtained from cultivated land in Haixi Prefecture, Qinghai Province (situated at 37°23'N 97°22'E). Rubidium chloride (RbCl), Iodine (I₂), Potassium iodide (KI), Starch soluble and Sodium thiosulfate (Na₂S₂O₃) were purchased from Shanghai Aladdin Biochemical Science and Technology Co., Ltd. and were analytically pure, and the reagent was used directly without special treatment.

QS removed from the plowed fields was washed to remove soil and dried in an oven for 12 hours. After crushing in a pulverizer, it passes through a 200mesh sieve. Using the single factor experiment method, 10 g of QS powder and RbCl were mixed in a crucible in the ratios of 0.5:1, 1:1, and 2:1, respectively, and deionised water was added until it exceeded the QS powder. Due to the non-contact and non-reaction between the solids, RbCl amount is dissolved by the deionised water and fills the pores of quinoa straws and further re-crystallises after heating at 70 C. After removal, the crucible was placed in a muffle furnace. The temperature was increased to 500, 600, 700 and 800 °C at a rate of 10 °C min⁻¹ in an air atmosphere. The carbonisation products were obtained by holding the temperature for 1h, 2h, 3h, 4h respectively. The activated samples were then filtered, dried, and ground in a mortar for further study.

SEM: The microstructural features of quinoa straw activated carbon (QSAC) were observed using a Gemini 500 scanning electron microscope from Zeiss, Germany. XRD: Diffraction spectra obtained using a Shimadzu XRD-7000 diffractometer were tested to characterise the microcrystalline structure of QSAC. The XRD investigation was effectuated with Cu K α radiation with a scan rate of 3 (°)/min in the range of 10–80°. Raman: Used for Raman determination

via Thermo Fisher Scientific DxR2XI, USA. The Raman spectrum of QSAC was obtained at an excitation wavelength of 532 nm, and the Raman detection can be used to obtain the degree of graphitization of carbon materials. BET: N₂ adsorption/desorption isotherms for QSAC at 77 K were obtained using BELSORPmax from MicrotracBEL Japan, Inc. Specific surface area and micropore volume were based on the Brunauer-Emmett-Teller (BET) method, respectively. Estimation of pore size distribution by Horvath-Kawazoe (HK) model. The adsorption and desorption of H₂ was carried out at 298K. FTIR: The QSAC powder was mixed and ground with KBr powder and then pressed into discs, which were examined Thermo Fisher NICOLET IS20.USA. XPS: Surface functional groups were analysed by X-ray photoelectron spectroscopy with the ESCALAB 250XI model from Thermo Fisher Scientific, USA. Each photoelectron spectral region was scanned several times to obtain a good signal ratio. The C1s peak was set to 284.6 eV and used as an internal standard for the other peaks. The iodine adsorption value is determined according to GB/T 12496.8-2015 "Test methods of wooden activated carbon-Determination of iodine number".

ACKNOWLEDGMENTS

This work was supported by the Key R&D and Transformation Program of Qinghai (2022-QY-210).

REFERENCES

1. J. W. Ren; N. M. Musyoka; H. W. Langmi; M. Mathe; S. J. Liao; *Int. J. Hydrog. Energy*, **2017**, 42, 289-311.
2. M. Ayvaz; S. İ. Ayvaz; İ. Aydin; *Int. J. Hydrog. Energy*, **2018**, 43, 20271-20283.
3. C. G. Michael; S. K. Eustathios; S. M. Sofoklis; K. Konstantinos; N. P. Efstratios; *Comput. Chem. Eng.*, **2009**, 33, 1077-1090.
4. A. Kumar; P. Muthukumar; P. Sharma; E. A. Kumar; *Sustain. Energy Technol. Assess.*, **2022**, 52, 102204.
5. P. C. Rao; Y. S. Kim; H. Kim; Y. H. Son; Y. Y. Choi; K. Na; M. Y. Yoon; *ACS Sustainable Chem. Eng.*, **2023**, 11, 12656-12666.
6. Y. M. Tang; Y. Z. Liu; Y. H. Zhang; Y. N. Cao; P. P. Song; L. M. Hou; L. X. Peng; *Food Sci. Nutr.*, **2024**, 1-13.
7. N. Wang; F. X. Wang; C. Shock; F. B. Fritschi; L. Gao; Z. J. Huang; J. Y. Zhao; *Agric. For Meteorol.*, **2022**, 323, 109084.
8. X. L. Zhao; F. Wang; Y. Fang; D. W. Zhou; S. P. Wang; D. Q. Wu; L. X. Wang; R. Z. Zhong; *BioResources*, **2020**, 312, 123512.

9. D. Abril; V. Ferrer; G. Y. Mirabal; B. G. Cabrera; C Segura.; A. Marican; A. Pereira; E. F. Durán-Lara; O. Valdés; *Materials*, **2022**, 15, 4898.
10. C. L. Zhang; H. C. Li; Z. Z. Lin; B. X. Du; X. P. Zhang; *Carbon Trends*, **2024**, 14, 100322.
11. R. S. DeFever; H. M. Wang; Y. Zhang; E. J. Maginn; *J. Chem. Phys.*, **2020**, 153, 011101.
12. E. Çetingürbüz; A. Turkyilmaz; *Ind. Crops Prod.*, **2023**, 203, 117171.
13. S. Hao; Q. Zhang; Y. Shi; Q. Guo; P. Li; J. Huang; *Biomass Conv. Bioref.*, **2024**, 14, 9581–9594.
14. S. Lee; M. E. Lee; M. Y. Song; S. Y. Cho; Y. S. Yun; H. Jin; *Carbon Letters*, **2016**, 20, 32-38.
15. D. Guo; Y. Fu; F. Bu; H. Liang; L. Duan; Z. Zhao; C. Wang; A. M. ElToni; W. Li; D. Zhao; *Small Methods*, **2021**, 5, 2001137.
16. C. Zhou; S. Geng; X. W. Xu; T. H. Wang; L. Q. Zhang; X. J. Tian; F. Yang; H. T. Yang; Y. F. Li; *Carbon*, **2016**, 108 234-241.
17. Y. Gao; Q. Yue; B. Gao; Y. Sun; W. Wang; Q. Li; Y. Wang; *Chem. Eng. J.*, **2013**, 217 345-353.
18. B. X. Du; H. C. Li; C. L. Zhang; Q. S. Ji; *Heliyon*, **2024**, 10, e27585.
19. W. Zhao; V. Fierro; N. Fera'ndez-huerta; M. T. Izquierdo; A. Celzard; *Int. J. Hydrog. Energy*, **2012**, 37, 14278-14284.
20. S. Schaefer; V. Fierro; M. T. Izquierdo; A. Celzard, *Int. J. Hydrog. Energy*, **2016**, 41, 12146-12156.
21. B. K. Kizilduman; Y. Turhan; M. Doğan; *Adv. Powder Technol.*, **2021**, 32, 4222-4234.
22. T. T. Qin; M. K. Song; K. K. Jiang; J. W. Zhou; W. Zhuang; Y. Chen; D. Liu; X. C. Chen; H. J. Ying; J. L. Wu; *RSC Adv.*, **2017**, 7, 37112-37121.
23. H. S. Jang; J. Y. Mun; W. G. Hong; S. M. Lee; J. W. Jeon; C. Y. Lee; H. J. Kim; B. H. Kim; *Int. J. Hydrog. Energy*, **2020**, 45, 10516-10522.

DEDICATED TO THE MEMORY OF
Associated Professor MARIUS IULIU SĂLĂJAN (1952-2004)

GOLD NANOPARTICLES FUNCTIONALIZED WITH ANTICANCER BIOCOMPOUNDS

Madalina Anca UJICA^a, Ionel MANG^a , Ossi HOROVITZ^a ,
Aurora MOCANU^a , Maria TOMOAI A-COTISEL^{a,b,*} 

ABSTRACT. The focus of this work is on the functionalization of gold nanoparticles, GNPs, with doxorubicin, D, an anticancer drug, both in the absence and in the presence of natural adjuvant biomolecules, like piperine, P, resveratrol, R, resveratrol-piperine, RP, complex, and icariin, I, which are therapeutic molecules with demonstrated anticancer and anti-inflammatory activity, to form highly stabilized colloidal dispersions. The green syntheses of GNPs, as cores, loading self-assemblies of various selected biomolecules, adsorbed on their surface, as shells, was confirmed by observing surface plasmon resonance at about 538 nm. Further, gold nanoparticles stabilized by resveratrol, GNP-R, are functionalized with various concentrations of selected biomolecules: D, P, R, RP, and I, resulting in different D/P/R/RP/I@GNPs-R composite nanoparticles for various compositions. Another series of stabilized colloidal dispersions is generated as GNP-R1, where the initial GNP-R is centrifuged and washed and then it is dispersed in aqueous solutions and further functionalized with said selected biomolecules. This study proves the functionalization of GNPs, as composite nanoparticles of high stability, in the presence of phosphate buffer saline, PBS, as confirmed by UV-Vis spectra of their colloidal aqueous dispersions.

Keywords: *gold nanoparticles, doxorubicin, adjuvant anticancer molecules, UV-Vis spectroscopy, surface plasmon resonance*

^a Babeş-Bolyai University, Research Center of Excellence in Physical Chemistry, Faculty of Chemistry and Chemical Engineering, 11 Arany Janos St., 400028, Cluj-Napoca, Romania

^b Academy of Romanian Scientists, 3 Ilfov St., 050044 Bucharest, Romania

* Corresponding author: mcotisel@gmail.com; maria.tomoaia@ubbcluj.ro



INTRODUCTION

Gold nanoparticles, GNPs, are regularly used in cancer treatment due to their capability to carry drugs and therapeutic adjuvants to designated targeting tumors, while reducing the drug side effects [1, 2] and also improving the efficiency of pharmaceuticals with low water solubility [3--5]. The production and characterization of gold nanoparticles have generated a distinctive progress in the field of cancer treatment [6-8]. Firstly, the synthesis of spherical GNPs was initiated by Turkevich [9]; HAuCl₄ is treated with citric acid in boiling alkaline aqueous solution, in which sodium citrate acts as both reducing agent and stabilizing agent. Later, Frens [10] revealed that different proportions of HAuCl₄ and citrate can be used to produce spherical GNPs of controllable size, which is still in use today. The GNPs provide a large surface area, easily to be functionalized and ability for translocation into the cells, achieving varied functions for many uses [11]. The GNPs allow controlled release of therapeutic constituents, while enhancing the efficiency of cancer treatment [1, 2, 11].

Therapeutic adjuvant substances, such as curcumin and flavonoids [12,13], as well as carotenoids [14,15] play a crucial role as antioxidants, anti-inflammatory and anticancer compounds. It is also demonstrated that carotenoids, such as astaxanthin [14] and canthaxanthin [15] are able to induce apoptosis in various tumor cells. This effect is due to their remarkable electronic and optical characteristics [16] and to their molecular orientation at biological interfaces [17], as well as to their interaction with various lipids from cell membrane as the Langmuir lipid layers [18-20].

Therapeutic medicine, such as doxorubicin, D, is considered as an effective anticancer drug used in chemotherapy of various types of cancer, e.g., leukemias, breast, ovarian, and lung cancer [21]. Its mechanism of action is based on doxorubicin intercalation with DNA, and finally blocking the DNA and RNA synthesis and leading to cell death. Accordingly, doxorubicin inhibits DNA and RNA production, by impeding an enzyme known as topoisomerase 2, leading to cell death. However, like other anticancer drugs, its administration is accompanied by an induced adverse effect which can be associated to neurotoxicity [21, 22], and/or cardiotoxicity [23] in a dose dependent manner, which limits the usefulness of doxorubicin.

Recently, an additional strategy is proposed namely to use natural adjuvant compounds as inducers of immunogenic cell death, which might activate immune cells to fight cancer cells and develop the cancer immunotherapy [24]. Further research is needed to investigate doxorubicin side effects at various doxorubicin doses and increase its activity on diverse cancer cells, including drug resistance cells, specifically MCF-7 cells [25] and ovarian cancer cells [26]. Novel core-shell nanoparticles (i.e., nanocomplexes or nanocomposites)

need to be designed to bind doxorubicin that might serve as efficient doxorubicin carriers to overcome the drug resistance mechanism in cancer cells, due to P-glycoprotein, PGP, which might be over expressed and can mediate export of doxorubicin from intracellular to cellular exterior [26]. Alternatively, some cancer cells might be expressing an array of genes that could confer intrinsic resistance.

For the first time, we developed a new strategy to effectively use a therapeutical agent, trans-resveratrol, R, to mediate the effects of doxorubicin in two human cervical tumor cell lines, specifically HeLa and CaSki [27]. Resveratrol is a polyphenol produced by plants and can form complexes with GNPs [27-29] whose biocompatibility has been demonstrated, making it a good candidate for drug delivery [30-33] and as an anti-oxidant for clinical implications [33].

Several studies have demonstrated the beneficial effects of resveratrol on the living organism, for instance, the anti-inflammatory action, modulation of lipid metabolism and inhibition of platelet aggregation [30, 34-36]. Resveratrol might have the therapeutic potential against emerging respiratory vital infections [36]. Even alone, resveratrol has a slight anticancer action [37].

Piperine, P, is an alkaloid obtained by extraction from *Piper longum* and *Piper nigrum*, which has been used for a long time [38, 39] for its antioxidant, anti-inflammatory and immunomodulatory effects, with a potential role in cancer prevention [40] and cancer treatment [41]. Piperine has the ability to modulate the bioactivity and bioavailability of resveratrol [42]. Piperine in combination with resveratrol, either as a physical mixture, R:P, or as a RP co-crystal, jointly enhance radiosensitivity of tumor cells, increasing cellular death through apoptosis [43].

Icariin is a natural flavonoid with pharmacological activities [44], anti-inflammatory and immunoregulatory effects [45], and a drug for anticancer treatment.[46] Icariin is presented as an active participant in the increased intracellular accumulation of doxorubicin in hepatocellular carcinoma [47], inducing immunogenic cell death. Moreover, icariin enhances the cytotoxicity of doxorubicin in human multidrug-resistant osteosarcoma cells [48]. Icariin has a broad inhibitory effect on breast cancer, colon cancer and hepatocellular carcinoma.

This study presents the green synthesis of gold nanoparticles [49, 50], under alkaline conditions [27], and the strategy of their functionalization with doxorubicin, in the absence and the presence of said natural biomolecules. Further, these new formulations containing functionalized GNPs are used in various cell cultures to evaluate *in vitro* conditions the anticancer activity of doxorubicin in the presence of the selected adjuvant biomolecules.

RESULTS AND DISCUSSION

UV-VIS characterization of GNPs colloidal solutions obtained by reduction with resveratrol

The procedure described by Mohanty et al. [29] was followed, but for the HAuCl_4 concentration indicated by the authors (4 mM) we did not obtain a colloidal gold solution. The color of the mixture turned rapidly to red, and after 30 min an absorption peak at 551 nm was observed; but then a yellowish-brown muddy suspension resulted (Fig. 1a). Therefore, a more diluted HAuCl_4 solution (10^{-3} M) was used [27]. The color of the reaction mixture changed rapidly to red, signifying the formation of gold nanoparticles, GNPs, with their surface coated by resveratrol molecules, denoted GNP-R or as GNP_R, and the maximum absorbance increases during the first hour. The absorption maximum is observed at about 538 nm (Fig. 1b). This GNP-R colloidal solution was stable for more than a year (Fig. 1c).

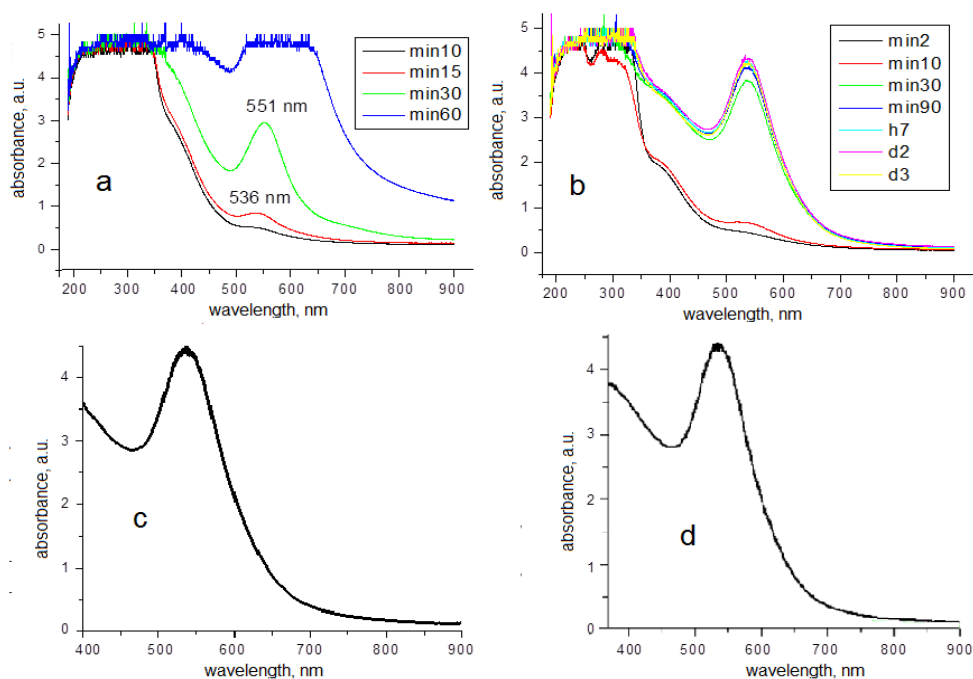


Fig. 1. Time evolution of the UV-Vis spectrum for a mixture of 4 mM HAuCl_4 and resveratrol, in NaOH solution (pH 12) at room temperature (a); the 1 mM HAuCl_4 solution and resveratrol (b); UV-Vis spectrum of GNP-R solution after 1 year (c); UV-Vis spectrum of GNP-R1 solution at 1 year (d)

By centrifugation and washing with ultrapure water, a concentrated gold colloidal solution was obtained, without residual resveratrol or its oxidation products. After dilution for 70 times with ultrapure water, the maximum intensity of the absorption peak (at 535-538 nm) is similar to that of the initial GNPs solution (Fig. 1d).

Assuming a total reduction of Au(III) to Au(0), the GNPs concentration in the two solutions, namely GNP-R initially synthesized in aqueous alkaline solution, and GNP-R1 finally obtained, after its centrifugation, and dispersed in deionized water was 0.91 mM (179 mg/L), as presented in Table 1.

Interaction of GNP-R with PBS solution

Since *Dulbecco's phosphate buffered saline* (DPBS, noted also PBS) solution was later used for the preparation of all solutions, and further utilized in cell cultures, its interaction with the GNP-R solution was also investigated by UV-Vis as shown in Fig. 2.

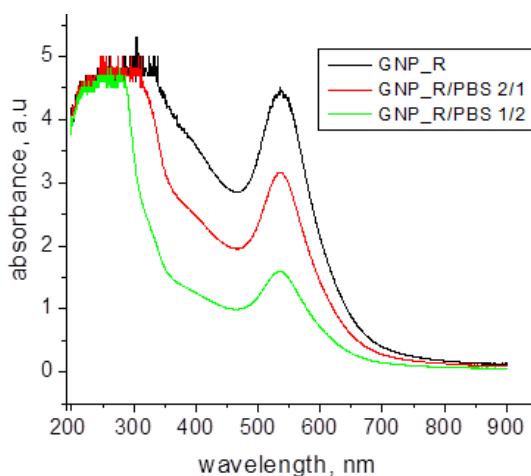


Fig. 2. UV-VIS spectrum of GNP-R (179 mg Au/L) mixed with *Dulbecco's phosphate buffered saline* (PBS) in different volume ratios (v/v) as given in the insert.

In the presence of PBS, as shown in Fig. 2, the surface plasmon resonance (SPR), namely the maximum of absorption band of the GNP-R, does not modify its position, only a decrease of absorbance with increasing dilution is observed.

Functionalization of GNP-R with doxorubicin hydrochloride, D

At physiological pH 7.4, the doxorubicin molecule is mainly protonated at the N atom (positively charged cationic form), while resveratrol molecule is almost non ionized, but at higher pH, resveratrol is negatively ionized (anionic forms).

Adding to the colloidal GNP-R solution (179 mg Au/L, which is equivalent to $0.91 \cdot 10^{-3}$ M) increasing amounts of doxorubicin ($7.2 \cdot 10^{-5}$ M (D) aqueous solution, containing 42 mg/L doxorubicin hydrochloride, as shown in Table 1, causes a slight shift of the absorption maximum from 538 to 542 nm, but for a higher D content in the GNP-R-D (i.e., D@GNP-R) mixture the nanoparticles aggregate in time and finally precipitate. For the GNP-R/D, volume/volume ratio 2, after 5 days the sedimentation is almost complete (Fig. 3a). For a lower D content (GNP-R/D = 6.25/1, v/v; or D@GNP-R = 1/6.25 v/v) the colloidal system is stable at least for 5 days (Fig. 3b).

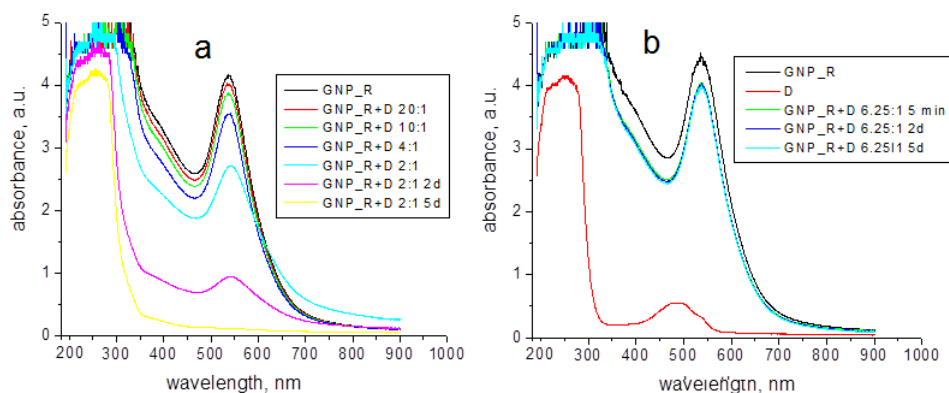


Fig. 3. UV-Vis spectra of GNP-R (179 mg Au/L) aqueous dispersion, and its mixtures with doxorubicin hydrochloride (D, 42 mg/L) aqueous solution, in deionized water, for different volume ratios as given in the insert, and the time evolution, immediately after preparation (at about 5 min), as well as at 2 and 5 days, as shown in the insert (a); UV-Vis spectra for GNP-R dispersion, D solution, and their GNP-R/D mixture for v/v, 6.25 mL: 1mL ratio, at different times after mixing (b), as shown in the insert

For the GNP-R/D volume/volume ratio 2, after 5 days, the GNP peak practically disappears (yellow curve is at the bottom in Fig. 3a), due to the almost complete sedimentation of constituent particles. For a lower D content, such as GNP-R/D = 6.25/1, v/v; or D@GNP-R = 1/6.25, v/v, the colloidal system is stable at least for 5 days (Fig. 3b).

The mixtures of the three solutions for, GNP-R with PBS and D, were unstable and deposited gold sediment was observed, for higher than 4 mg/L, of D content. Therefore, many different systems were tested to discover the optimum quantity of Au, requested for the high stability of the GNP-R functionalized with doxorubicin, also noted as D@GNP-R nanocomposite in aqueous dispersion.

Lastly, a mixture of GNP-R solution (12.5 mL), PBS (25 mL) and D solution (4 mL), with an Au content of 54 mg/L and D content of 4 mg/mL, was identified to be stable for several months (Fig. 4a).

Accordingly, the most stable colloidal solution was identified, as given in Fig. 4, and subsequently it was used *in vitro* research on various cancer cells (unpublished results).

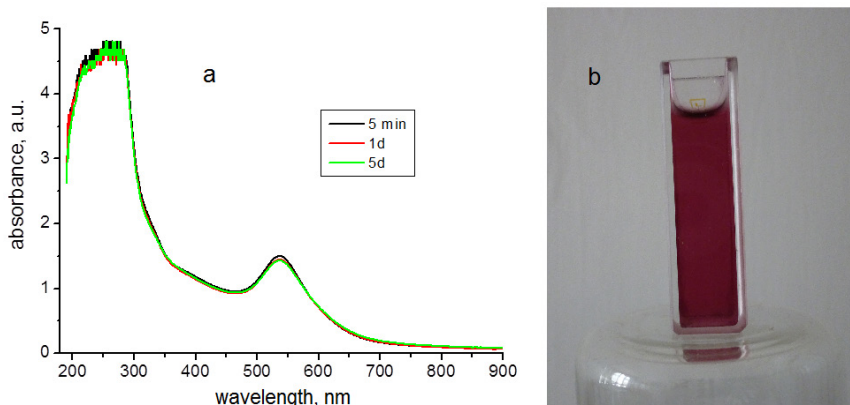


Fig. 4. UV-Vis spectrum of a dispersion, containing GNP-R functionalized with D, symbolized as D@GNP-R nanocomposite in PBS, obtained in a mixture of 12.5 mL of diluted GNP-R (Au 54 mg/L) and 4 mL of D (4 mg/L) solution and 25 mL PBS, measured in time (a), and a photo of this colloidal solution (b)

Thus, the surface functionalization of GNP-R with anticancer drugs, such as doxorubicin, is leading to one of the most favorable D@GNP-R nanocomposites with a high stability, as demonstrated in Fig. 4, having a strong shell formed of doxorubicin mixed with resveratrol, which is covering the core of GNPs, and is capable of resisting to the required washing steps and incubation conditions, especially in biological studies for biomedical applications.

This functionalization is realized by noncovalent interactions, particularly through electrostatic interactions, hydrogen bonds, and van der Waals forces. The advantage of this steady self-assembled layer of biomolecules covering the GNPs core of composite nanoparticles consists of the fact that these

biomolecules are not attached by various chemical modifications to the GNPs core and thus, are easier released in the interior of cancer cells. Certainly, the binding core-shell needs to be strong enough to produce stable shell surfaces capable of surviving during biological studies in cell cultures.

After functionalization, the new structure, spherical core (GNP)-shell (adsorbed as outer coating) of biomolecules, is realized particularly by electrostatic interactions, which leads to a non-covalent modification of the GNP surface and might have the great potential to be optimized and stabilized for various drug delivery systems [27].

On the other hand, the treatment with doxorubicin can increase reactive oxygen species and other adverse effects potentially leading to neurotoxicity and/or cardiotoxicity. In these situations, natural compounds with therapeutic activity are selected for use to reduce the cellular oxidative stress and inflammatory effects and simultaneously enhance the anticancer activity of doxorubicin.

In agreement with the therapeutic properties of resveratrol, piperine and resveratrol-piperine complex, and icariin, I, these biocompounds are used in achieving innovative composites in the presence of GNPs, obtained by reduction of HAuCl_4 with resveratrol, namely further resulting gold nanoparticles coated by a layer of resveratrol, GNP-R (also noted as GNP_R) and followed by centrifugation and redispersion in deionized water or in PBS, resulting in GNP-R1 (noted as well GNP_R1).

The surface of GNP-R and GNP-R1 nanoparticles is further functionalized with anti-cancer drug, e.g., doxorubicin, and various therapeutic adjuvant biomolecules, such as resveratrol, piperine, resveratrol-piperine complex, and icariin. The concentration of each component in solution is given in Table 1, as mg/L and mmol/L.

Functionalization of GNP-R with resveratrol-piperine, RP, complex

The UV-Vis spectra of resveratrol (R, saturated solution in PBS comprising 30 mg/L), piperine (P, saturated solution in PBS containing 40 mg/L) and of the resveratrol-piperine (RP) complex (50 mg/L) are compared in Fig. 5a. The concentration of these biocompounds in PBS solutions is shown in Table 1.

The addition of the resveratrol-piperine complex solution in PBS (50 mg/L) to the GNP-R colloidal solution (Au 179 mg/L), in the GNP-R/RP = 2/1 (v/v) ratio does not shift the absorption band of the GNP-R (Fig. 5b).

Also adding small amounts of doxorubicin solution, D (42 mg/L) in the volume ratios GNP-R/RP/D = 6/3/1 (v/v/v) did not modify the UV-Vis spectrum

(Fig. 5b). Thus, the mixtures of GNP-R with RP complex and with doxorubicin are leading to D/RP@GNP-R nanocomposite significantly stable, but color change and sedimentation occur after 8 days.

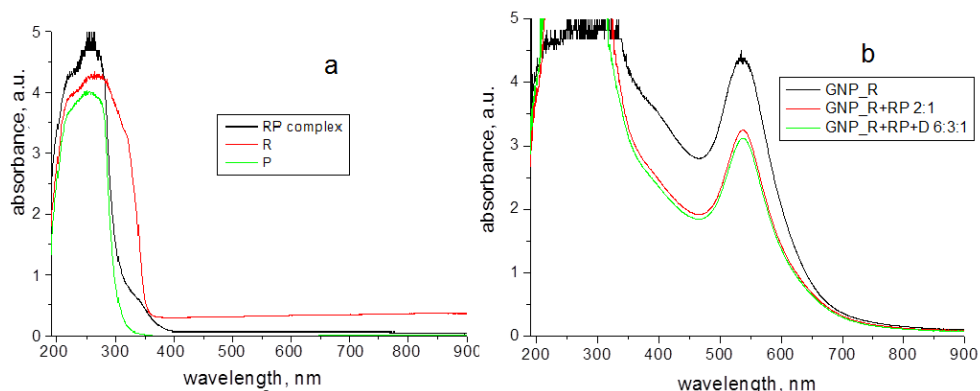


Fig. 5. (a) UV-Vis spectrum of the resveratrol-piperine, RP, complex (50 mg/L) in PBS, of a saturated piperine (40 mg/L) solution in PBS, and of a saturated resveratrol (30 mg/L) solution in PBS; (b) UV-Vis spectra of GNP-R dispersion (Au 179 mg/L), of RP@GNP-R nanocomposite in PBS dispersion (GNP-R: RP, 2:1 v/v ratio), and of GNP-R (Au 179 mg/L) mixed with resveratrol-piperine (RP) complex (50 mg/L), and with doxorubicin (D 42 mg/L) solutions at the volume v/v ratios of 6:3:1 as given in the insert of Figure 5b, resulting in stable D/RP@GNP-R nanocomposites in PBS dispersion.

This investigation aimed to determine the effect of a combination of doxorubicin and resveratrol-piperine complex, which contains piperine as a bioenhancer of resveratrol activity, and jointly adsorbed on the surface of GNP-R, and also improve required stability of D/RP@GNP-R nanocomposite in aqueous dispersions.

Functionalization of GNP-R with icariin, I

The UV-Vis spectra of DMSO, and of icariin (I, 100 mg/L) dissolved in DMSO and PBS (1mL/1mL, v/v ratio) mixture, recorded directly after mixing, and after 2 and 3 days are shown in Fig. 6a. The concentration of icariin in DMSO and PBS solution is shown in Table 1. After preparation, the resulted icariin (I, 100 mg/L) solution was stable and there were no UV-Vis spectra modifications.

Accordingly, the solution of *icariin* in DMSO and PBS (1:1, v/v ratio) mixture was stable the first day, after preparation and from day 2 a yellow sediment appeared.

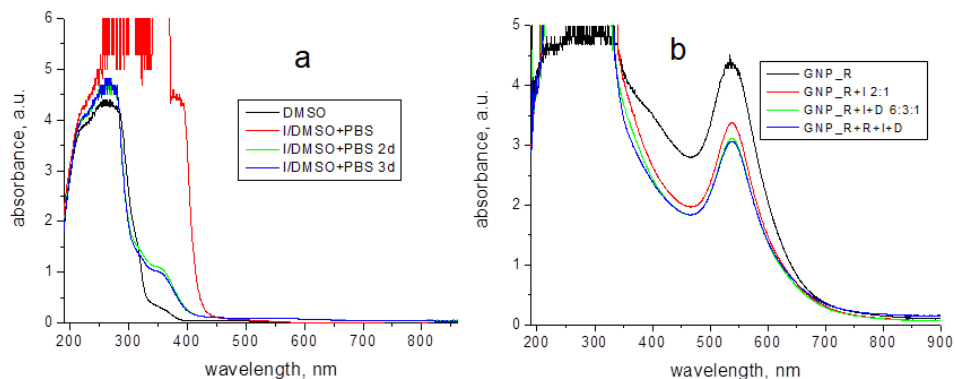


Fig. 6. UV-Vis spectra of DMSO, and of icariin (I, 100 mg/L) solution in the DMSO and PBS (1 mL/1 mL, v/v ratio) mixture, recorded directly after mixing, and after 2 and 3 days (a); UV-Vis spectra of GNP-R dispersion (Au 179 mg/L), of I@GNP-R nanocomposite in PBS dispersion (GNP-R: I for 2:1 v/v ratio), and of GNP-R (Au 179 mg/L) mixed with I (100 mg/L) solution and D (42 mg/L) solution, at the volume v/v ratios of 6:3:1 as given in the insert of Figure 6b, resulting in D/I@GNP-R nanocomposites in PBS dispersion as well as for GNP-R (1.8 mL) + R (0.4 mL) + I (0.5 mL) + D (0.3 mL) resulting in D/I/R@GNP-R nanocomposite in PBS dispersion.

The addition of this icariin (I, 100 mg/L) fresh solution in the GNP-R (179 mg Au/L) colloidal solution for GNP-R:I = 2:1 (v/v) ratio, does not change the absorption band of the GNP-R (Fig. 6b). The addition of doxorubicin solution, D (42 mg/L) in the volume ratios GNP-R/I/D = 6/3/1 (v/v/v) did not initially affect the UV-Vis spectra; neither did the addition of resveratrol (30 mg/L) in PBS solution to the mixture of GNP-R, I and D resulting in GNP-R (1.8 mL) + R (0.4 mL) + I (0.5 mL) + D (0.3 mL) change the spectrum just after mixing (Fig. 6b). Additionally, the evolution in time, after the first day of the D/I/R@GNP-R composite preparation, shows that the functionalized gold nanoparticles are rather stable for a week, when particles started to aggregate and precipitate.

This investigation is the first to assess the combinatorial effect of icariin, resveratrol and doxorubicin, together in functionalization of GNP-R, resulting in D/I/R@GNP-R nanocomposite stable in PBS dispersions. So, the self-assembled layer of these biomolecules is adsorbed on the surface of gold nanoparticles, GNP-R1, exemplified through SPR in UV-Vis spectroscopy, reaching a good stability of this nanocomposite, designed as a potential drug delivery system (Fig. 6b).

Functionalization of GNP-R1 with various biomolecules

The GNP-R was centrifugated and then diluted with bidistilled deionized water resulting in GNP-R1 (also noted GNP_R1) colloidal solution (of the same concentration in gold as in GNP-R initially synthesized in aqueous dispersion, as revealed in Fig. 1b. Both colloidal solutions of GNP-R and GNP-R1 have a very high stability as shown in Fig. 1c and Fig. 1d, respectively.

Moreover, the GNP-R1 colloidal solution displays a behaviour similar to that of GNP-R colloidal solution, in its interaction with solutions of various drugs, but the resulting mixtures with GNP-R1 are more stable in time. Therefore, several examples regarding the functionalization of GNP-R1 with resveratrol, piperine, resveratrol-piperine complex and doxorubicin are presented

The strongest effect on the absorption band is manifest for piperine (P) solution, and for the complex resveratrol-piperine (RP), both initially in PBS solutions. The UV-Vis spectra of mixtures formed of GNP-R1 colloidal solution and various solutions of resveratrol (R), doxorubicin (D), piperine (P) and/or resveratrol-piperine (RP) complex, at different volume ratios, are given in Figure 7. The concentration of these biocompounds in used solutions, is shown in Table 1.

The present study aimed to determine the effect of a combinative effect of doxorubicin and resveratrol as well as doxorubicin and resveratrol-piperine complex versus resveratrol, piperine, resveratrol-piperine complex, or doxorubicin effect on the stability of functionalized GNP-R1 in PBS dispersions.

The results confirmed a good stability for almost all studied systems, but the P@GNP-R1 nanocomposite appears to show a large maximum (of low absorbance) which probably denotes a stronger interaction among components.

The current investigation was hence proposed to study the combined effect of doxorubicin and several selected adjuvant biomolecules, adsorbed on the surface of GNPs, on the stability of functionalized GNPs designed for future drug delivery systems to be employed *in vitro* and *in vivo*. The most stable aqueous solutions (dispersions) will be employed later on as advanced models for their anticancer examination on different cancer cells, and thus, for establishing their potential therapeutic effect on various human cancers.

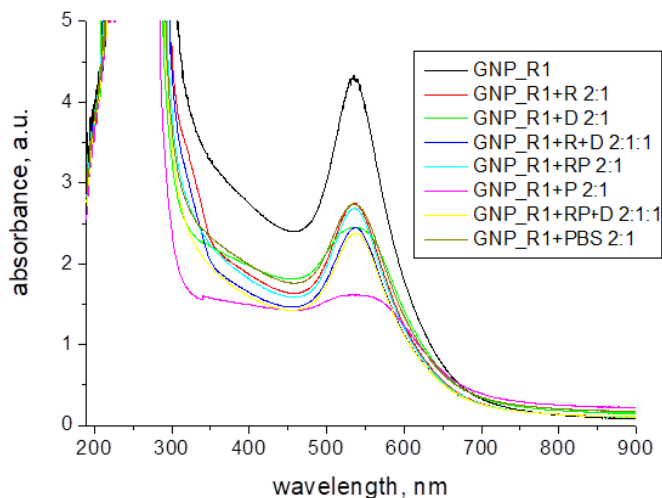


Fig. 7. UV-Vis spectra of GNP-R1 (Au 179 mg/L) aqueous dispersion; of R@GNP-R1 nanocomposite obtained from GNP-R1: R, with R (30 mg/L) in PBS solution, at 2:1 v/v ratio; of D@GNP-R1 nanocomposite for GNP-R1: D, with D (42 mg/L) aqueous solution, at 2:1 v/v ratio; of D/R@GNP-R1 nanocomposite for GNP-R1: R, with R (30 mg/L) in PBS solution, and D, with D (42 mg/L) aqueous solution, at 2:1:1 v/v/v ratio; of RP@GNP-R1 dispersion for GNP-R1: RP, with RP (50 mg/L) in PBS solution, at 2:1 v/v ratio; of P@GNP-R1 nanocomposite for GNP-R1: P, with P (40 mg/L) in PBS solution at the volume v/v ratio of 2:1; of D/RP@GNP-R1 nanocomposite for GNP-R1 mixed with RP (50 mg/L) in PBS solution and D (42 mg/L) aqueous solution at the volume v/v/v ratio of 2:1:1; and GNP-R1 (Au 179 mg/L) aqueous dispersion and PBS solution for volume v/v ratio, 2:1; altogether in final dispersions as given in the insert of Figure 7.

CONCLUSIONS

The GNP-R and GNP-R1 colloidal solutions obtained by the above green synthesis by reduction with resveratrol, were used together with doxorubicin, piperine, resveratrol, the resveratrol-piperine complex, and icariin, in the synthesis of multifunctional GNPs-anticancer drug composites, namely, D/P/R/RP/I@GNPs-R composites. These advanced composites, also named complexes, were made by self-assembly of biomolecules on the surface of gold nanoparticles, already stabilized with a coating layer of resveratrol. The UV-Vis study highlighted the interactions between these components and it is obviously to be further completed with other physico-chemical methods of characterization and with biological investigation on various cancer cells.

One major goal of this study was to optimize the functionalization of GNPs to be beneficial for achieving the union of multifunctional array and multi-therapeutic components, within the adsorbed shell on the surface of GNPs aimed at reaching a high stability in various aqueous dispersions, including cell cultures. The formation of self-assemblies of biomolecules might take advantage of electrostatic interaction as well as molecular changes by hydrogen bonds and intermolecular van der Waals forces among molecules.

As highlighted in this study, GNPs have a large ability to be easily functionalized with biomolecules as determined by surface plasmon resonance, SPR. The constructed multifunctional GNPs provide the colloidal solutions of high stability in various PBS conditions making them useful for biological investigation in various cell cultures, as tools for pharmaceutical and medical applications.

In the future research, the multifunctional GNPs will be used and further developed from their interaction with cancer cells and certainly new formulations will be tailored to obtain optimized therapeutic combinations, and thus, making them to support medical applications.

Moreover, the interaction among molecules adsorbed on GNPs might achieve highly ordered self-assemblies, which can also be preserved within the cells modifying the mechanism of doxorubicin action in cancer cells with resistance to anti-cancer drugs. Surely, the gold nanostructures should be evaluated *in vitro* and *in vivo* research for their efficiency.

EXPERIMENTAL SECTION

Materials and methods

Gold nanoparticles (GNPs) were obtained by the reduction of tetrachloroauric(III) acid, HAuCl_4 , with trans-resveratrol (R). The tetrachloroauric acid trihydrate ($\text{HAuCl}_4 \cdot 3\text{H}_2\text{O}$) 99.5% (Merck - Darmstadt, Germany), trans-resveratrol $\geq 99\%$ (HPLC assay, from Sigma-Aldrich, Buchs, Switzerland) and NaOH reagent grade $\geq 98\%$ (Merck KGaA, Darmstadt, Germany) were used in aqueous solutions prepared with bidistilled deionized water. Doxorubicin hydrochloride (about 98%) was purchased from Sigma-Aldrich Chemie GmbH (Munich, Germany). Piperine $\geq 98\%$ (HPLC assay), was obtained from AlfaAesar (Karlsruhe, Germany) and icariin, analytical standard ($\geq 94\%$) was obtained from Sigma-Aldrich (Steinheim, Germany). Resveratrol-Piperine complex was prepared in our Research Center of Physical Chemistry (*unpublished results*). Dimethyl sulfoxide (DMSO) for cell culture was purchased from Sigma-

Aldrich (Schnelldorf, Germany). Dulbecco's phosphate buffered saline (DPBS, noted also PBS), without CaCl_2 and MgCl_2 , (pH 7.4), was purchased from AlfaAesar (Karlshure, Germany).

Synthesis of GNPs

For the preparation of GNPs using trans resveratrol as reducing and stabilizing agent, by a modified method [29], we started with 100 mL 10^{-3} M aqueous HAuCl_4 solution; a freshly prepared solution obtained from 25 mg resveratrol dissolved in 10 mL 0.02 M NaOH solution was added under continuous stirring at 500 RPM, for 10 min at room temperature (about 22 °C). The initial resveratrol concentration was therefore 10^{-3} M and the pH about 12.

This GNP-R colloidal solution was concentrated by centrifugation (at about 14 000, RPM) for about 20 min, and the supernatant comprising the excess of resveratrol was removed. The obtained colloid gold particles, covered with a protective layer of resveratrol, from their initial colloidal solution, were washed with ultrapure water and dispersed in deionized water for further studies. The final solution was diluted for 70 times with ultrapure deionized water to attain the same gold concentration as in the initial colloidal solution (GNP-R), representing the GNP-R1 sample.

The GNP-R and GNP-R1 colloidal dispersions obtained by the above green synthesis were mixed in different proportions with anti-cancer drug solutions of doxorubicin hydrochloride, icariin, piperine, resveratrol and piperine-resveratrol complex to explore the functionalization of gold nanoparticles.

All used solutions in this study are given in Table 1. Since icariin is not soluble in water, it was solubilized in dimethyl sulfoxide (DMSO, 11 mg/ 10 mL) and then 100 mL PBS were added to the solution.

Table 1. Solutions used in this study

Solution	Solvent	Chemical formula	Molar mass (g/mol)	Concentration	
				mg/L	mmol/L
GNP-R, GNP-R1	Water	Au	197	179	0.91
Doxorubicin.HCl, D	water	$\text{C}_{27}\text{H}_{29}\text{NO}_{11} \cdot \text{HCl}$	580.0	42	0.072
Resveratrol, R	PBS	$\text{C}_{14}\text{H}_{12}\text{O}_3$	228.2	30	0.131
Piperine, P	PBS	$\text{C}_{17}\text{H}_{19}\text{NO}_3$	285.3	40	0.140
Resveratrol-Piperine, RP	PBS	$\text{C}_{14}\text{H}_{12}\text{O}_3 \cdot \text{C}_{17}\text{H}_{19}\text{NO}_3$	513.5	50	0.097
Icariin, I	DMSO, PBS	$\text{C}_{33}\text{H}_{40}\text{O}_{15}$	676.7	100	0.148

UV-Vis spectroscopy

The *UV-VIS absorption spectra* were measured with a Jasco UV/Vis V650 spectrophotometer, from 900 to 200 nm wavelength. The stability of the GNPs-R and GNPs-R1 and their further functionalization with various biomolecules, used as therapeutic adjuvants, was studied as function of PBS content, composition and time.

ACKNOWLEDGMENTS

This work was supported by a grant from the Ministry of Research, Innovation and Digitization, CNCS/CCCDI- UEFISCDI, project PN-III-P4-ID-PCE-2020-1910, project no. 186. The experimental facilities of excellence and the top equipment of the Scientific Research Center of Excellence in Physical Chemistry, part of STAR Institute, Babes-Bolyai University, were used in this study. The founder (2006) and director (2006–present) of this Research Center is Maria Tomoaia-Cotisel.

REFERENCES










1. H. Huang; R. Liu; J. Yang; J. Dai; S. Fan; J. Pi; Y. Wei; X. Guo; *Pharmaceutics*, **2023**, *15*, 1868
2. J. Lee; D. K. Chatterjee; M. H. Lee; S. Krishnan; *Cancer Lett.*, **2014**, *347*, 46-53
3. M. A. Ujica; G. A. Paltinean; A. Mocanu; M. Tomoaia-Cotisel; *Acad. Rom. Sci. Ann.-Ser. Biol. Sci.*, **2020**, *9*(1), 97-139
4. L. Kumari; Y. Choudhari; P. Patel; G. D. Gupta; D. Singh; J. M. Rosenholm; K. K. Bansal; B. D. Kurmi; *Life*, **2023**, *13*(5), 1099
5. I. R. S. Vieira; L. Tessaro; A. K. O. Lima; I. P. S. Velloso; C. A. Conte-Junior; *Nutrients*, **2023**, *15*, 3136
6. O. Horovitz; G. Tomoaia; A. Mocanu; T. Yupsanis; M. Tomoaia-Cotisel; *Gold Bull.*, **2007**, *40*(4), 295-304
7. M. A. Dheyab; A. A. Aziz; P. Moradi Khaniabadi; M. S. Jameel; N. Oladzadabbasabadi; S. A. Mohammed; R. S. Abdullah; B. Mehrdel; *Int. J. Mol. Sci.*, **2022**, *23*(13), 7400
8. M. Y. Kalashgrani; N. Javanmardi; *J. Adv. Appl. NanoBio. Tech.*, **2022**, *3*(3), 1–6
9. J. Turkevich; P. C. Stevenson; J. Hillier; *Discuss Faraday Soc.*, **1951**, *11*, 55–75
10. G. Frens; *Nat. Phys. Sci.*, **1973**, *241*, 20–22
11. H. Li; S. Pan; P. Xia; Y. Chang; C. Fu; W. Kong; Z. Yu; K. Wang; X. Yang; Z. Qi; *J. Biol. Eng.*, **2020**, *14*, 14

12. L. Z. Racz; C.-P. Racz; O. Horovitz; G. Tomoaia; A. Mocanu; I. Kacso; M. Sarkozi; M. Dan; S. Porav; G. Borodi; M. Tomoaia-Cotisel; *Stud. UBB Chem.*, **2022**, 67(3), 75-99
13. C.-P. Racz; L. Z. Racz; C. G. Floare; G. Tomoaia; O. Horovitz; S. Riga; I. Kacso; G. Borodi; M. Sarkozi; A. Mocanu; C. Roman; M. Tomoaia-Cotisel; *Food Hydrocoll.*, **2023**, 139, 108547
14. I. Faraone; C. Sinisgalli; A. Ostuni; M. F. Armentano; M. Carmosino; L. Milella; D. Russo; F. Labanca; H. Khan; *Pharmacol. Res.*, **2020**, 155, 104689
15. P. Palozza; N. Maggiano; G. Calviello; P. Lanza; E. Piccioni; F. O. Ranelletti; G. M. Bartoli; *Carcinogenesis*, **1998**, 19(2), 373–376
16. M. E. Orczyk; M. Samoc; J. Swiatkiewicz; N. Manickam; M. Tomoaia-Cotisel; P. N. Prasad; *Appl. Phys. Lett.*, **1992**, 60(23), 2837-2839
17. E. Chifu; J. Zsako; M. Tomoaia-Cotisel; *J. Coll. Interf. Sci.*, **1983**, 95(2), 346-354
18. M. Tomoaia-Cotisel; *Progr. Colloid Polym. Sci.*, **1990**, 83, 155-166
19. M. Tomoaia-Cotisel; J. Zsako; E. Chifu; *Ann. Chim. (Rome)*, **1981**, 71(3-4), 189-200
20. J. Zsako; M. Tomoaia-Cotisel; E. Chifu; *J. Coll. Interf. Sci.*, **1984**, 102(1), 186-205
21. K. Kaminska; A. Cudnoch-Jedrzejewska; *Neurotox. Res.*, **2023**, 41, 383–397
22. S. R. Kesler; D. W. Blayney; *JAMA Oncol.*, **2016**, 22(2), 185–92
23. A. N. Linders; I.B. Dias; T. Lopez Fernandez; C. G. Tocchetti; N. Bomer; P. Van der Meer; *npj Aging*, **2024**, 10, 9
24. L.-J. Yang; T. Han; R.-N. Liu; S.-M. Shi; S.-Y. Luan; S.-N. Meng; *Biomed. Pharmacother.*, **2024**, 177, 117099
25. K. Kudoh; M. Ramanna; R. Ravatn; A. G. Elkahloun; M. L. Bittner; P. S. Meltzer; J. M. Trent; W. S. Dalton; K.-V. Chin; *Cancer Res.*, **2000**, 60, 4161-4166
26. H. C. Arora; M. P. Jensen; Y. Yuan; A. Wu; S. Vogt; T. Paunesku; G. E. Woloschak; *Cancer Res.*, **2012**, 72(3), 769–778
27. G. Tomoaia; O. Horovitz; A. Mocanu; A. Nita; A. Avram; C.-P. Racz; O. Soritau; M. Cenariu; M. Tomoaia-Cotisel; *Colloid. Surface. B*, **2015**, 135, 726-734
28. O. Vesely; S. Baldovska; A. Kolesarova; *Nutrients*, **2021**, 13, 3095
29. R. K. Mohanty; S. Thennarasu; A. B. Mandal; *Colloid. Surface. B*, **2014**, 114, 138-143
30. L. Fremont; *Life Sci.*, **2000**, 66(8), 663-673
31. J. M. Lopez-Nicolas; F. Garcia-Carmona; *J. Agr. Food Chem.*, **2008**, 56, 7600-7605
32. M. Annaji; I. Poudel; S. H. S. Boddu; R. D. Arnold; A. K. Tiwari; R. J. Babu; *Cancer rep.*, **2021**, 4(3), 1353
33. C. Alarcon de la Lastra; I. Villegas; *Biochem. Soc. T.*, **2007**, 35(5), 1156-1160
34. D. Delmas; V. Aires; E. Limagne; P. Dutartre; F. Mazue; F. Ghiringhelli; N. Latruffe; *Ann. NY Acad. Sci.*, **2011**, 1215, 48-59
35. L. G. Carter; J. A. D’Orazio; K. J. Pearson; *Endocr.-Relat. Cancer*, **2014**, 21(3), 209-225
36. S. Filardo; M. Di Pietro; P. Mastromarino; R. Sessa; *Pharmacol. Ther.*, **2020**, 214, 107613
37. Z. Jiang; K. Chen; L. Cheng; B. Yan; W. Qian; J. Cao; J. Li; E. Wu; Q. Ma; W. Yang; *Ann. NY Acad. Sci.*, **2017**, 1403, 59-69

38. M. Zadorozhna; T. Tataranni; D. Mangieri; *Mol. Biol. Rep.*, **2019**, *46*, 5617-5629
39. A. K. Tripathi; A. K. Ray; S. K. Mishra; *Beni-Suef Univ. J. Basic. Appl. Sci.*, **2022**, *11*, 16
40. S. Benayad; H. Wahnou; R. El Kebbaj; B. Liagre; V. Sol; M. Oudghiri; E. M. Saad; R. E. Duval; Y. Limami; *Cancers*, **2023**, *15*, 5488
41. J. S. Lim; D. Y. Lee; J. H. Lim; W. K. Oh; J. T. Park; S. C. Park; K. A. Cho; *Front. Biosci. (Landmark Ed)*, **2022**, *27*(4), 137
42. J. J. Johnson; M. Nihal; I. A. Siddiqui; C. O. Scarlett; H. H. Bailey; H. Mukhtar; N. Ahmad; *Mol. Nutr. Food. Res.*, **2011**, *55*, 1169-1176
43. J. K. Tak; J. H. Lee; J.-W. Park; *BMB Rep.*, **2012**, *45*(4), 242-246
44. C. He; Z. Wang; J. Shi; *Adv. Pharmacol.*, **2020**, *87*, 197-203
45. Z. Bi; W. Zhang; X. Yan; *Biomed. Pharmacother.*, **2022**, *151*, 113180
46. Y. Liu; H. Yang; J. Xiong; J. Zhao; M. Guo; J. Chen; X. Zhao; C. Chen; Z. He; Y. Zhou; L. Xu; *Biomed. Pharmacother.*, **2023**, *157*, 113991
47. Z. Yu; J. Guo; M. Hu; Y. Gao; L. Huang; *ACS Nano*, **2020**, *14*, 4816-4828
48. Z. Wang; L. Yang; Y. Xia; C. Guo; L. Kong; *Biol. Pharm. Bull.*, **2015**, *38*(2), 277-284
49. A. Avram; G. Tomoaia; A. Mocanu; M. Tomoaia-Cotisel; *Acad. Rom. Sci. Ann., Ser. Phys. Chem*, **2020**, *5*(2), 23-64
50. A. Hossain; Md. T. Rayhan; Md. H. Mobarak; Md. I. H. Rimon; N. Hossain; S. Islam; S. M. A. Al Kafi; *Results Chem.*, **2024**, *8*, 101559

DEDICATED TO THE MEMORY OF
Associated Professor MARIUS IULIU SALAJAN (1952-2004)

THE EFFECT OF GOLD NANOPARTICLES SYNTHESIZED BY SODIUM CITRATE AND FUNCTIONALIZED WITH ANTICANCER AND NATURAL COMPOUNDS ON CANCER CELL LINES

Madalina Anca UJICA^a, Ionel MANG^{a,b} , Ossi HOROVITZ^{a*} ,
Olga SORITAU^c , Gheorghe TOMOAI^{b,d}, Aurora MOCANU^a ,
Horea-Rares-Ciprian BENE^a , Viorica RAISCHI^{a,e} ,
Csaba VARHELYI^a , George BORODI^f ,
Maria TOMOAI-COTISEL^{a,d*} 

ABSTRACT. Natural compounds, such as trans-resveratrol, R, piperine, P, and icariin, Ic, have antioxidant and anti-inflammatory properties, and potential anticancer activity. Gold nanoparticles, GNPs, are biocompatible and can be used as carriers for biomolecule delivery, improving their performance at a small dose. The aim of the present study was to synthesize GNPs with sodium citrate, noted GNP_C (or GNP-C), and enhancing their stability and anticancer activity by functionalization with R, P, Ic, asparagine, A, and doxorubicin, D, as a

^a Babeş-Bolyai University, Research Center of Excellence in Physical Chemistry, Faculty of Chemistry and Chemical Engineering, 11 Arany Janos Str., RO-400028, Cluj-Napoca, Romania

^b Department of Orthopedics and Traumatology, Iuliu Hatieganu University of Medicine and Pharmacy, 47 General Traian Moşoiu Str., RO-400132, Cluj-Napoca, Romania

^c Oncologic Institute Prof. Dr. I. Chiricuță, 20-26 Republicii Str., 400015 Cluj-Napoca, Romania

^d Academy of Romanian Scientists, 3 Ilfov Str., RO-050044, Bucharest, Romania

^e Institute of Physiology and SanoCreatology, State University of Moldova, Academy 1 Str., MD-2028, Chişinău, Moldova

^f National Research-Development Institute for Isotopic and Molecular Technologies, 67-103 Donath Str., RO-400293, Cluj-Napoca, Romania.

* Corresponding authors: mcotisel@gmail.com, ossihor@yahoo.com



standard drug. The obtained GNPs as cores, loading selected biomolecules, adsorbed on their surface as shells, were characterized by various methods, UV-Vis spectroscopy, XRD, AFM, TEM, and particle size analysis. The anticancer activity of functionalized GNP_C was evaluated using MTT assay in four human cell lines: breast cancer, MDA-MB-231 and MCF-7 cell lines, tumor stem cells (isolated from glioblastoma), a GM1 cell line, and a normal (healthy) stem cell line derived from a dental follicle, DF. GNP_C functionalized with R, P or Ic exhibited an anticancer activity comparable to GNP_C functionalized with doxorubicin for low concentrations in gold and in natural compounds, thus reducing side effects of anticancer drug. These promising results need further examination using various cell lines and animal models, to clinical applications.

Keywords: *functionalized gold nanoparticles, cytotoxicity and anticancer activity, cancer cell lines*

INTRODUCTION

Cancer is the second cause of death on Earth and requires a prompt identification (early cancer detection) and an efficient anti-cancer therapy [1]. The conventional chemotherapy and radiotherapy usually suffer from systemic toxicity. Moreover, cancer reappearance is too common, for example, in bone recurrence. Although huge efforts have been made, optimum treatment has not been achieved owing to the resistance of cancer cells to therapeutic treatment.

To overcome these difficulties, new biocompatible materials, like gold nanoparticles, GNPs, functionalized with anti-cancer drugs, have been developed as nanocarriers to kill cancer cells [2]. Gold nanoparticles can be synthesized by a variety of methods usually starting from tetrachloroauric acid as a precursor agent and using as a reducing agent either chemical substances, such as trisodium citrate, resveratrol and sodium borohydride, or plant extracts and microorganisms.

The typical synthesis of GNPs is the best known, which involves the chemical reduction of Au^{3+} ions from tetrachloroaurate to Au^0 atoms. This can only take place in the presence of a reducing agent, an agent that can sometimes also play the role of a stabilizing agent [2, 3]. This type of synthesis is well known since 1951, when Turkevich performed the first chemical synthesis of GNPs from a solution of chloroauric acid and sodium citrate [2, 4]. Although time has passed and many other reducing agents have been discovered, such as resveratrol, which creates a protective corona around the gold nanoparticle that not only stabilizes, but also potentiates the cytotoxic effect of GNPs in the fight against cancer cells [5]; however, the classic combination is still used.

Over time, scientists have developed and improved the classic synthesis method with the aim of better controlling the size and stability of the gold nanoparticles obtained. These changes mainly consist in varying the reaction conditions (temperature, pH, reaction time) or the concentrations of the reducing agent or the precursor [6]. In some cases, in addition to trisodium citrate, other substances are added, such as polyvinyl alcohol [7], carboxymethyl cellulose [8] or tannic acid [9, 10] with a role in directing the shape of the nanoparticle and co-encapsulation. In addition to chemicals, synthesis can also be aided by gamma ray irradiation [11]. Theoretical study [9] on the synthesis of GNPs, together with laboratory experiments, demonstrated that the variation of the reaction conditions helps control the synthesis of GNPs. Finally, it is demonstrated that anions of citrate are adsorbed on the surface of gold nanoparticles, GNP_C, through the central carboxylate groups [12].

Characterization methods play a very important role in establishing the efficiency of the synthesis. Thus, a variety of analysis methods are used, some of which we will review. UV-VIS spectroscopy shows the formation of the GNPs. [13, 14] Details on the formation of self-assembled layers on the surface of GNPs can be determined by TEM [15]. XRD confirms the crystalline nature of the nanoparticles of gold [16], and AFM reveals the morphology of GNPs self-assemblies. Besides these, other characterization techniques are also used, such as: FTIR, HR-TEM, SEM, Zeta potential and DLS.

To measure the effectiveness of GNP_C in cancer treatment, usually this is compared to the total inhibitor concentration that can reduce the cell viability with 50%, called IC50 [17]. Thus, over time, the cytotoxicity of GNP_C has been tested both on healthy cell lines, like BHK, L929 (fibroblasts), HDMEC (human dermal microvascular endothelial cell line) and hCMEC-D3 (human cerebral microvascular endothelial cells) [17-19] and on cancerous cell line, such as HeLa against healthy BHK cell line [18] and the results are somewhat agreeable. Other cancer lines [20-25] sensitive to gold nanoparticles synthesized with citrate were also used, for instance, ovarian carcinoma cell line [20] and human lung adenocarcinoma cell lines [23]. In the case of breast cancer cell lines [24, 25], of interest to us in this work are MCF-7 and MDA-MB-231 cell lines; the literature data show that there is an anticancer activity of GNP_C, but at rather high concentrations [25]. This made us determined to find the right functionalization of GNP_C to increase cytotoxicity, but lowering the dose of therapeutic drug, for example doxorubicin. In addition to high toxicity for cancer cells, the substances used in treatments must be biocompatible with healthy cells, and fortunately, GNP_C are toxic to these only at high concentrations [7, 26-29].

As a novelty in this study, the anticancer activity of GNP_C was extended for the first time towards their functionalization with different natural biomolecules, namely resveratrol, piperine or icariin in comparison with doxorubicin, a standard anti-cancer drug.

Trans resveratrol, R, is a polyphenol produced by plants, and can form complexes with GNPs, whose biocompatibility has been demonstrated, making it a good candidate for drug potentiation [30-33]. Even alone, R has a slight anticancer action and it reduces cellular oxidative stress and inflammation [5, 34].

Piperine, an alkaloid obtained by extraction from *Piper longum* and *Piper nigrum*, whose properties have been used by medicine for a long time [35] for its antioxidant, anti-inflammatory and immunomodulatory effects; its anticancer ability leads to a sensitization of cancer cells increasing cell death by apoptosis [5].

Icariin, the main active ingredient in a Chinese anti-inflammatory drug, which once ingested is mostly transformed into its metabolite – icaritin – [36], and it is presented [37, 38] as an active participant in the increased intracellular accumulation of doxorubicin in human multidrug-resistant osteosarcoma cells.

In accordance with the properties of icariin, piperine and resveratrol, these compounds are used to make innovative complexes with GNP_C, which are further used in two breast cancer (MDA-MB 231 and MCF-7) cell lines and on tumor stem cells derived from glioblastoma: GM1. Glioblastoma multiform stem cells have a high proliferative potential, despite chemotherapy and irradiation, and they have the ability to form spheroids in suspension [39]. MCF-7 cells retain several characteristics of differentiated mammary epithelium, including the cytoplasmic estrogen receptor. The commonly studied triple negative breast cancer (TNBC) MDA-MB-231 cell line was established in the 1970s from pleural effusion of a breast cancer patient. This cell line has the advantage of being a source of breast tumor cells with high viability and proliferation ability [40].

The growing interest in nanotechnology for increasing the clinical efficacy of natural products, is justified by necessity to increase the bioavailability of bio-active compounds, improving the biomolecule stability within biological systems and increasing the solubility and transport across biological membranes of these compounds [41-43]. Phytochemicals (e.g., resveratrol) adsorbed onto gold nanoparticles had an enhanced bioactivity against cancer, leading to an increased cellular uptake and anti-cancer activity compared to the phytochemicals alone [43].

Based on the above, the goal of our study is centered on the activity of gold nanoparticles synthesized with citrate, GNP_C, and functionalized with natural substances, resveratrol, piperine or icariin to be an innovation in anticancer research.

RESULTS AND DISCUSSION

Gold nanoparticles synthesis, functionalization and characterization

Gold nanoparticles were prepared by reduction of a tetrachloroauric acid (HAuCl_4), solution with a trisodium citrate ($\text{Na}_3\text{C}_6\text{H}_5\text{O}_7$) aqueous solution. The obtained nanoparticles were denoted as GNP_C. The calculated gold content in the obtained colloidal solution was $0.6 \cdot 10^{-3}$ M (118 mg/L Au). The presence of GNP_C in the final solution was revealed by the red color, due to the SPR absorption band of gold nanoparticles. The band appears in the visible range of the UV-Vis spectrum, with a maximum at 531 nm wavelength. Their spectrum is compared with that of gold nanoparticles obtained by reduction with resveratrol (GNP_R) [44] (Au content 179 mg/L) in Figure 1.

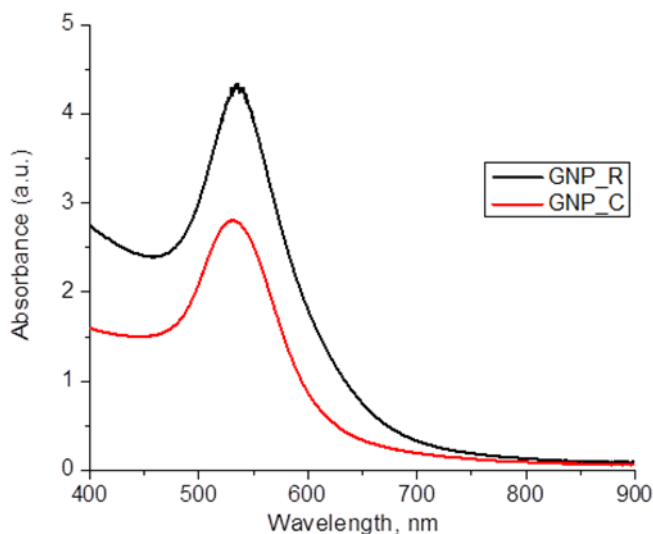


Figure 1. Comparison of UV-Vis (optical) spectra of GNPs solutions obtained by reduction with resveratrol (GNP_R) and with sodium citrate (GNP_C)

In Figure 2A, a TEM image for GNP_C is presented, and every nanoparticle is very well shown. From the diameters of a large number of GNPs (several hundred) measured in different TEM images for each sample, the histogram of size distribution in Figure 2B was obtained. The average diameter of synthesized GNP_C nanoparticles is 29.2 ± 4.8 nm.

The ξ -potential value measured on GNP_C is -31.5 mV, thus a stabilization by electrostatic repulsion can be assumed for their colloidal solution. The threshold value assuring electrostatic stability is considered to

be ± 30 mV [45]. The average diameter of particles measured by DLS is 31.64 nm, only slightly bigger than the diameter estimated from the TEM images. This suggests the presence of a rather thin organic coating of GNPs.

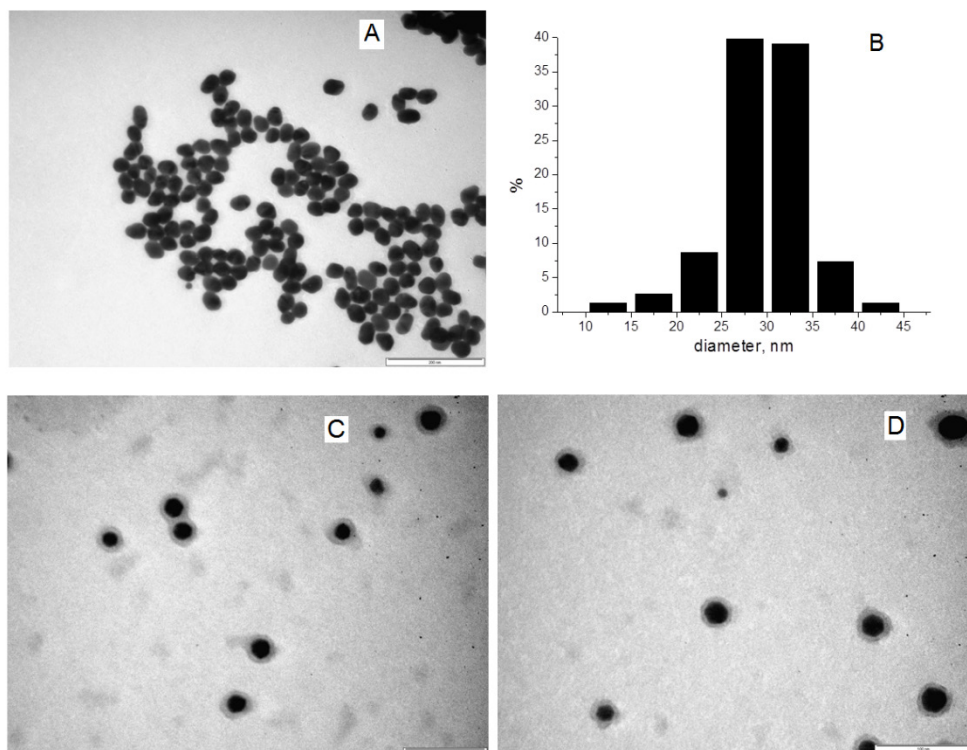


Figure 2. TEM image for synthesized GNP_C nanoparticles; the bar is 200 nm (panel A). Histogram of size distribution for GNP_C (panel B). TEM images for functionalized GNPs, used in sample 3 (Fig. 7) and sample 2 (Fig. 8), containing GNP-C 3.9 $\mu\text{g}/\text{mL}$, P 0.67 $\mu\text{g}/\text{mL}$ (panel C), and for sample 4 (Fig. 7) and sample 3 (Fig. 8) containing GNP-C/A 3.9 $\mu\text{g}/\text{mL}$, D 0.21 $\mu\text{g}/\text{mL}$ (panel D): the bar is 100 nm (panel C and panel D)

Figure 3 displays the morphology of the GNP-C layer adsorbed on glass from aqueous dispersion. The AFM images: 2D-topography image (A), phase image (B) and 3D-topography image (C) were obtained with atomic force microscope, operated in tapping mode. The nanoparticles of gold covered and stabilized by a layer of citrate, GNP_C, are well identified in every AFM image and they are well spread as a layer on glass showing a

rather small value of the surface roughness. However, the aggregated nanoparticles are also observed, particularly in the 3D-topography, where the height (the thickness of the GNP_C layer is rather high (about 56 nm), in comparison with the averaged diameter (around 30 nm) of NPs determined by TEM images. This aggregation might be related to a tendency of the formation of a double layer on GNP_C due to self-assemblies generation during the adsorption and drying process.

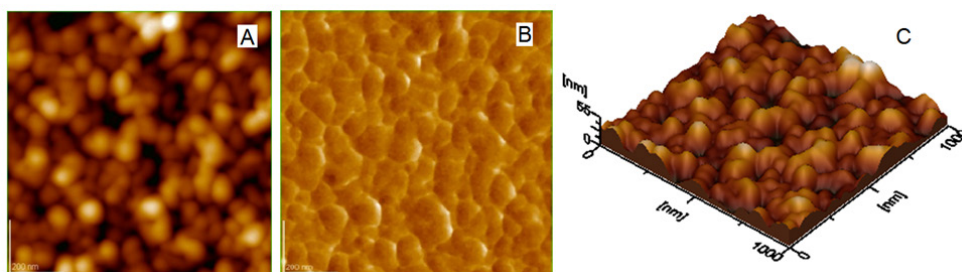


Figure 3. AFM images of gold nanoparticles synthesized and stabilized with citrate, GNP_C, as adsorbed layer on glass: 2D-topography (panel A); phase image (panel B); 3D-topography (panel C); scanned area $1 \mu\text{m} \times 1 \mu\text{m}$; surface roughness is given as root mean square, RMS, of about 4 nm

This situation might be caused by a strong interaction among the citrate covering layers on GNP_C justifying that the crystalline core of gold nanoparticle is very well covered by citrate layer as a stable shell.

The X-ray diffraction patterns for GNP are presented in Figure 4. Some characteristic peaks for gold are identified, at 2θ ($^\circ$) values: 38 (111 plane most intense signal); 44 (200); 65 (220); 78 (311). So, the presence of crystalline gold is evidenced. A peak also appears for NaCl, resulted from the synthesis reaction between HAuCl_4 and trisodium citrate ($\text{Na}_3\text{C}_6\text{H}_5\text{O}_7$).

The average size of GNP_C nanoparticles, obtained by Scherrer formula applied on the Au (111) diffraction peak in Figure 4, is about 15.6 nm, much smaller than the measured value by TEM images, given in Fig. 2. This is due to the fact that by XRD the size of crystalline domains is obtained within gold nanoparticles.

Adding positively charged doxorubicin (as water soluble doxorubicin hydrochloride, containing the cationic form of the therapeutic drug) to the negatively charged GNPs reduces their zeta-potential and thus, their stability against aggregation. For GNP_C, in the absence of a rather thick organic coating layer, the stability is mainly of electrostatic nature, thus we should

expect a significant destabilization of the aqueous colloidal system by doxorubicin, more important than for the GNP-R, already protected by a large layer of resveratrol [44]. The red color of the doxorubicin solution, due to its absorption band with a maximum at about 480 nm, is not visible at the low concentration used on cell lines, and does not interfere with the absorption band of the GNPs.

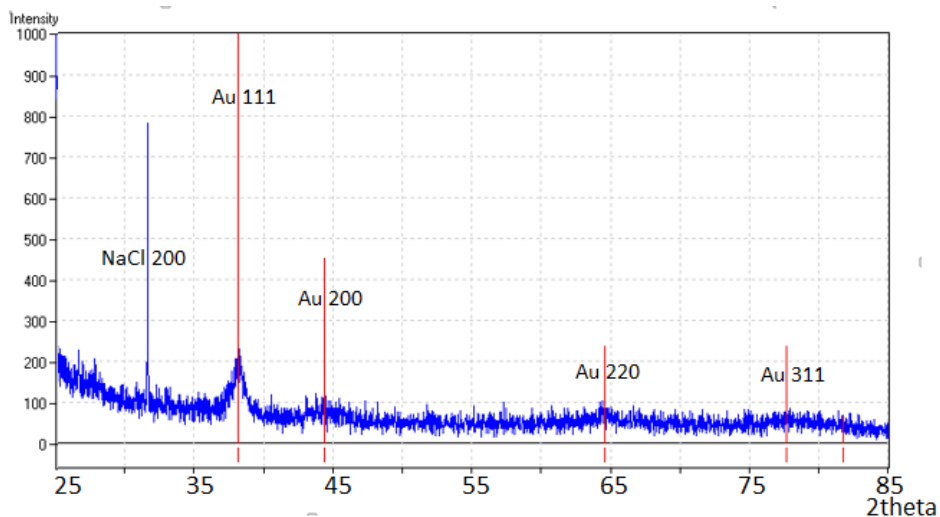


Figure 4. X-ray diffraction patterns for GNP_C nanoparticles. The red vertical bars give the positions of diffraction lines for crystalline gold domains

Therefore, GNP_C nanoparticles are highly sensitive towards the interaction with doxorubicin. Adding this compound, even in small amounts, changes almost immediately the color of the solution to violet and then to blue, followed by the sedimentation of GNPs aggregates. In the UV-Vis spectrum (Figure 5, panel A), the surface plasmon resonance, SPR, band characteristic for the GNPs is diminished and a new large band at higher wavelength (over 700 nm) appears, responsible for the change of color, and due to the formation of larger aggregates of particles. It is dominant both in the mixture 1 (mixt 1), of GNP_C and doxorubicin (D) solution (see Table 1) in the volume ratio 9:1 containing 106.2 mg/L Au and 4.2 mg/L D (mole ratio Au/D = 74/1, and flattens for a higher D content, as in mixture 2 (mixt 2) of the two solutions in the volume ratio 2:1, with: 78.7 mg/L Au; 14 mg/L D (mole ratio Au/D = 15.9/1), when the precipitation of the aggregates occurs.

THE EFFECT OF GOLD NANOPARTICLES SYNTHESIZED BY SODIUM CITRATE AND FUNCTIONALIZED WITH ANTICANCER AND NATURAL COMPOUNDS ON CANCER CELL LINES

The addition of resveratrol, R, solution, in the volume ratio GNP_C/R = 2:1 (Figure 5, panel B, mixture 3) does not affect the SPR band of GNP_C (black curve), while piperine, P, and icariin, Ic, solutions, in the same 2:1 v/v) ratio GNP_C/P (mixture 4) and respectively GNP_C/Ic (mixture 5) have both the same effect, a broadening and flattening of the GNP_C band. When doxorubicin is present, even in small amounts, together with resveratrol or piperine namely in the 5:4:1 volume ratio GNP_C: R: D (mixture 6), respectively GNP_C: P: Ic (mixture 7) of (Figure 5C), its effect is mostly the same as without R and P (Figure 5A).

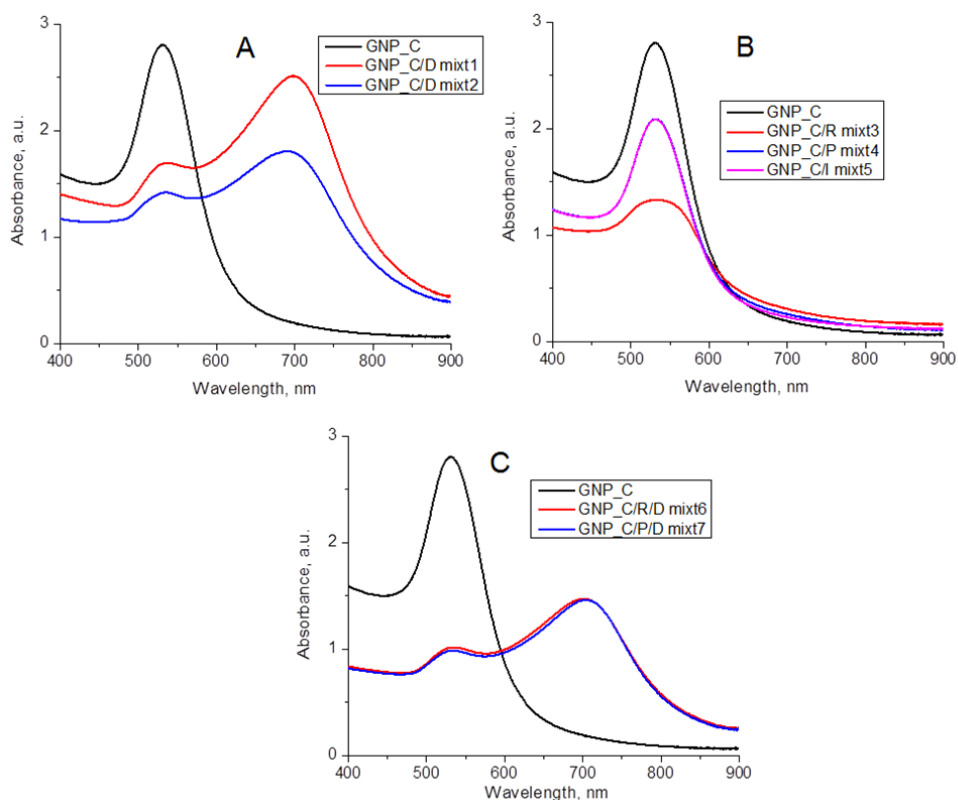


Figure 5. UV-Vis spectra of GNP_C (118 mg/L Au) mixtures with (panel A) doxorubicin (D), with contents (mg/L): mixt1: Au 106.2; D 4.2; mixt2: Au: 78.7; D 14 (B) resveratrol (R) - mixt 3: Au 39.3; R 10; piperine (P)- mixt 4: Au 78.7; P 13.3; and icariin (I)- mixt 5: Au: 78.7; I: 33.3; (C) resveratrol and doxorubicin – mixt6: Au 59; R 12; D 4.2; piperine and doxorubicin – mixt7: Au 58; P 10; D 4.2.

We had previously investigated the interaction between GNPs and asparagine, and found that asparagine binds to GNPs, resulting GNP_C/A nanoparticles, without causing their aggregation [4]. Therefore, we tried to protect the GNP_C against rapid aggregation by adding to their 0.6×10^{-3} mM colloidal solution a 10^{-3} M asparagine (A) solution. The colloidal GNP_C/A system is stable against increasing amounts of asparagine, from 20/1 to 2/1 v/v ratios of the two solutions (12/1 to 1.2/1 Au/A mole ratios) and also in time (Figure 6, panel A). By adding increasing volumes of doxorubicin solution (42 mg/L) to the GNP_C- asparagine 2/1 v/v mixture (named GNP_C/A), the colloidal GNP system is protected for a doxorubicin content up to 3.8 mg/L (volume ratio GNP_C/A-D = 10/1), but the aggregation begins right away for 5.25 mg/L D (volume ratio GNP_C/A-D = 7/1) and progresses rapidly in the first hour after mixing (Figure 6, panel B). It is to be noted that this instability appears in concentrated colloidal systems used in UV-Vis investigation. In the colloidal systems at low concentration of these biomolecules, as used in the cell culture, the stability of these diluted systems is highly increased for months, being deposited at 4 °C.

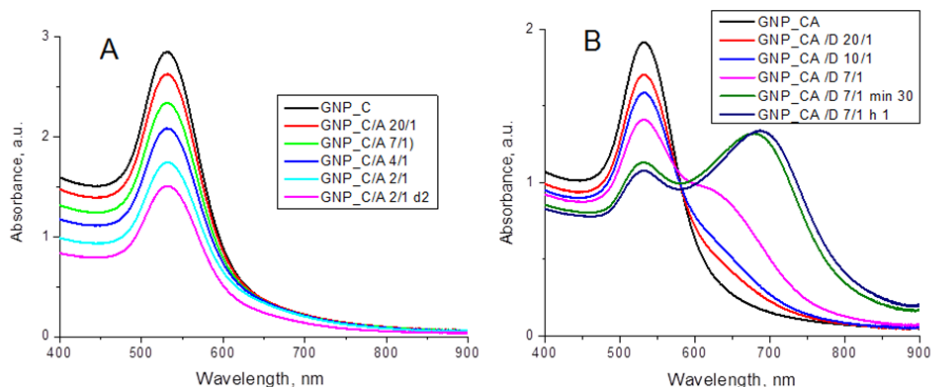


Figure 6. Panel A: UV-Vis spectra of 0.6 mM GNP_C solution at successive dilution with 10^{-3} M asparagine solution at the volume ratios given in figure, with an Au content (mg/L): 112.4 (20/1), 103.2 (7:1), 94.4 (4:1) and 78.7 (2:1), and after 2 days for the last solution. Panel B: Evolution of spectra of a solution containing GNP_C with asparagine (volume ratio 2:1 noted GNP_CA) at the addition of increasing volumes of doxorubicin (D) solution at the volume ratios GNP_CA/D given on figure: 20/1 (Au 75 mg/L, D 2 mg/L), 10/1 (Au 71.9 mg/L, D 3.82 mg/L,) and 7/1 (Au 68.9 mg/L; D 5.25 mg/L) and after 30 min and 1 h for the last mixture.

The functionalized GNP-C nanoparticles with piperine, as GNP_C 3.9 $\mu\text{g/mL}$, P 0.67 $\mu\text{g/mL}$, are shown in TEM image, Figure 2, panel C. The GNP-C nanoparticles stabilized with asparagine, A, and further functionalized with doxorubicin, as GNP_C/A 3.9 $\mu\text{g/mL}$, D 0.21 $\mu\text{g/mL}$, are presented in Figure 2, panel D. It is clear that the functionalized GNP_C nanoparticles are individually shown in TEM images, indicating in Figures 2C and 2D, an enhanced stability of these GNPs nanoparticles, in the experimental conditions without a clustering tendency. This is another good property of functionalized GNP_C nanoparticles, revealing that the agglomeration of these nanoparticles is not achieved under the experimental conditions. Moreover, the size of these functionalized GNP_C nanoparticles is close to the values of synthesized GNP_C nanoparticles (about 30 nm). AFM images of these functionalized GNP_C nanoparticles are revealing a similar nanostructure (not presented) as that shown in Figure 3.

Anticancer activity: cell viability and cytotoxic effects

In this study, we evaluated the cell viability and cytotoxic effect of GNP_C, also noted GNP-C (with 3.9 $\mu\text{g/mL}$, or with 19.83 μM , of tested AuNPs, sample 1, see Table 1), functionalized with resveratrol (0.5 $\mu\text{g/mL}$, sample 2), piperine (0.67 $\mu\text{g/mL}$, sample 3), as well as with very low doses of doxorubicin (0.21 $\mu\text{g/mL}$, sample 4) and icariin (1.67 $\mu\text{g/mL}$, sample 5) on the two breast carcinoma cell lines: MDA-MB-231 (in short MDA231) and MCF-7, as well as on tumor stem cells derived from glioblastoma (GM1) versus normal stem cells from the dental follicle (DF), treated with samples 1-4 (Table 2), by MTT assay. The MTT test shows cell viability depending on the cytotoxicity of an investigated compound. Cell viability was assessed after 24 hours of cells exposure to the chosen compounds. MTT solution (Sigma-Aldrich Chemicals GmbH, St. Louis, MO, USA) contains 3-(4,5-dimethylthiazolyl-2)-2,5-diphenyl tetrazolium bromide (which is a tetrazolium salt) that is reduced by mitochondrial enzymes active in viable cells. It results in a product, formazan, which is dark blue and is insoluble in aqueous solutions. The cells were incubated for another 1 h, and the formazan crystals were solubilized and the absorbance was measured by using a BioTek plate reader (see experimental part).

To perform the MTT viability test, MDA MB 231 cells and MCF-7 cells, as well DF stem cells and GM1 cells were seeded in 96-well plates and after 24 hours, when cells have adhered to the surface of the plate, the compounds to be studied were added in the concentrations indicated in Table1 and Table 2, respectively.

Table 1. Concentrations of tested compounds in $\mu\text{g/mL}$, and in $\mu\text{mol/L}$, for each sample (1 to 5) as well as mole ratios of Au/R, Au/P, Au/D and Au/Ic.

Samples (COMP)	Concentration		Mole ratios
	$\mu\text{g/mL}$	$\mu\text{mol/L}$	
1) GNP_C	Au 3.9	Au 19.83	-
2) GNP_C - R	Au 3.9; R 0.5	Au 19.83; R 2.2	Au/R 9.014
3) GNP_C - P	Au 3.9; P 0.67	Au 19.83; P 2.349	Au/P 8.442
4) GNP_C/A - D	Au 3.9; D 0.21	Au 19.83; D 0.36	Au/D 55.0
5) GNP_C - Ic	Au 3.9; Ic 1.67	Au 19.83; Ic 7.268	Au/Ic 2.728

The cells were treated with 19.83 μM of tested AuNPs and with chosen compounds given in Table 1, and after 24 h, the cell viability was determined by using MTT assay and the viable cells are given as % of Control, which is represented by untreated cells.

The graphic representation of the response of MDA MB 231 cells and MCF-7 cells to treatments with GNP-C, and GNP-C functionalized with resveratrol, piperine, and icariin, and GNP-C/A 3.9 $\mu\text{g/mL}$ / D 0.21 $\mu\text{g/mL}$, evaluated with the MTT viability test is given in Figure 7.

The two breast cancer lines, MDA MB 231 cells (in short MDA231) and MCF-7 cells were compared in terms of cell viability response to treatment with GNP_C (GNP-C) of 3.9 $\mu\text{g/mL}$ of tested AuNPs, and further functionalized as following: GNP-C 3.9 $\mu\text{g/mL}$ / R 0.5 $\mu\text{g/mL}$, GNP-C/R, GNP-C 3.9 $\mu\text{g/mL}$ / P 0.67 $\mu\text{g/mL}$, GNP-C/P, GNP-C stabilized with asparagine (A), namely GNP-C/A 3.9 $\mu\text{g/mL}$ / D 0.21 $\mu\text{g/mL}$ (GNP-C/A-D), GNP-C 3.9 $\mu\text{g/mL}$ / Ic 1.67 $\mu\text{g/mL}$, GNP-C/Ic. Non-functionalized GNP-C showed a statistically significant toxicity (about 14 %) on breast cancer cell lines compared with untreated controls, with a reduction in the percentage of viable cells to 86% for MDA MB 231 and 84.6% for MCF-7. Functionalization with resveratrol (0.5 $\mu\text{g/ml}$), GNP-C/R, induced an important similar decrease in cell viability with an increase in cytotoxicity to 25% for both tumor lines. ($p < 0.001$).

The functionalization of GNP-C with piperine, sample 3, GNP-C/P, and GNP-C/A/D complex, sample 4, induced a decrease in viability for MDA231 cells with 30% and with 25% for MCF-7 cells. The introduction of icariin into GNP-C, sample 5, GNP-C/Ic dispersion had more intense effects for the MDA MB 231 cell line, with a decrease in cell viability to 73.6% compared to untreated cells. MCF-7 cells showed similar viability to cells treated with non-functionalized GNP-C, sample 1, upon treatment with GNP-C/Ic, sample 5.

The *t*-test concluded that the differences between GNP-C vs. GNP-C/R, vs. GNP-C/A-D and vs. GNP-C/Ic are significant with a value of $p < 0.05^*$ for MDA MB 231 cells. MCF-7 cells showed a more pronounced decrease in the values obtained for GNP-C / R compared to GNP-C (*t* test $p < 0.05^*$), and for the values of GNP-C/A/D vs. GNP-C ($p < 0.01^{**}$), see Figure 7.

THE EFFECT OF GOLD NANOPARTICLES SYNTHESIZED BY SODIUM CITRATE AND FUNCTIONALIZED WITH ANTICANCER AND NATURAL COMPOUNDS ON CANCER CELL LINES

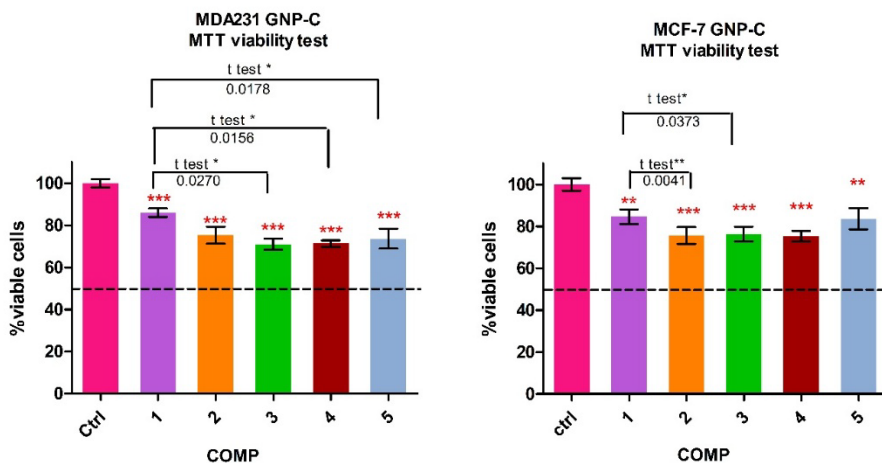


Figure 7. Cell viability (viable cells in % of Control (Ctrl), from MTT assay): Control (untreated cells); 1) GNP-C 3.9 $\mu\text{g}/\text{mL}$; 2) GNP-C 3.9 $\mu\text{g}/\text{mL}$, R 0.5 $\mu\text{g}/\text{mL}$; 3) GNP-C 3.9 $\mu\text{g}/\text{mL}$, P 0.67 $\mu\text{g}/\text{mL}$; 4) GNP-C/A 3.9 $\mu\text{g}/\text{mL}$, D 0.21 $\mu\text{g}/\text{mL}$; 5) GNP-C 3.9 $\mu\text{g}/\text{mL}$, Ic 1.67 $\mu\text{g}/\text{mL}$.

Two other cell types were also studied, the tumor stem cells isolated from a glioblastoma (GM1 cells) and the normal mesenchymal stem cells derived from the dental follicle (DF) to evaluate the possible antitumor effect of GNP-C functionalized or not, but also to ascertain the effects on normal cells. The stem cell lines were compared as response to treatment with GNP-C 3.9 $\mu\text{g}/\text{mL}$, sample 1, and functionalized with piperine (GNP-C 3.9 $\mu\text{g}/\text{mL}$ / P 0.67 $\mu\text{g}/\text{mL}$), sample 2, very low dose of doxorubicin (GNP-C/A 3.9 $\mu\text{g}/\text{mL}$ / D 0.21 $\mu\text{g}/\text{mL}$), sample 3, and icariin (GNP-C 3.9 $\mu\text{g}/\text{mL}$ / Ic 1.67 $\mu\text{g}/\text{mL}$), sample 4; the concentrations and mole ratios are noticed in Table 2.

Table 2. Type of composites, the concentration in $\mu\text{g}/\text{mL}$, and in $\mu\text{mol}/\text{L}$, for each sample (1-4) and mole ratios of Au/P, Au/D and Au/Ic.

Samples (COMP)	Concentrations		Mole ratios
	$\mu\text{g}/\text{mL}$	$\mu\text{mol}/\text{L}$	
1) GNP_C	Au 3.9	Au 19.83	-
2) GNP_C - P	Au 3.9; P 0.67	Au 19.83; P 2.349	Au/P 8.442
3) GNP_C/A - D	Au 3.9; D 0.21	Au 19.83; D 0.36	Au/D 55.0
4) GNP_C - Ic	Au 3.9; Ic 1.67	Au 19.83; Ic 7.268	Au/Ic 2.728

Graphic representation of the response of normal DF stem cells and GM1 glioblastoma tumor stem cells to treatments with GNP-C, sample 1, and with GNP-C functionalized with piperine, GNP-C/P, sample 2, and GNP-C/A 3.9 µg/mL/ D 0.21 µg/mL, sample 3, GNP-C/A/D, and with icariin, GNP-C/Ic, sample 4, evaluated with the MTT assay and viability test is given in Figure 8.

The obtained results showed a higher sensitivity of GM1 tumor stem cells to GNP-C, sample 1, treatments, with a 12.4% decrease in cell viability, in contrast to normal DF stem cells that were not affected by GNP-C administration. The functionalization of GNP-C with piperine (sample 2) and with icariin (sample 4) determined an increase in cytotoxicity by 6-8% compared to non-functionalized GNP-C (sample 1) in the case of GM1 cells, with a significant statistical difference at the t test ($p < 0.05^*$ for GNP-C vs. GNP-C/P; $p < 0.005^{**}$ for GNP-C vs. GNP-C/A/D. A similar response but of a lower intensity was also observed for normal DF stem cells. The effect of GNP-C functionalized with icariin, GNP-C/Ic, was gentler, with cell viability values of 88.2% for normal DF stem cells, than for GM1 tumor cells, showing a bigger decrease to 81% in cell viability (Figure 8).

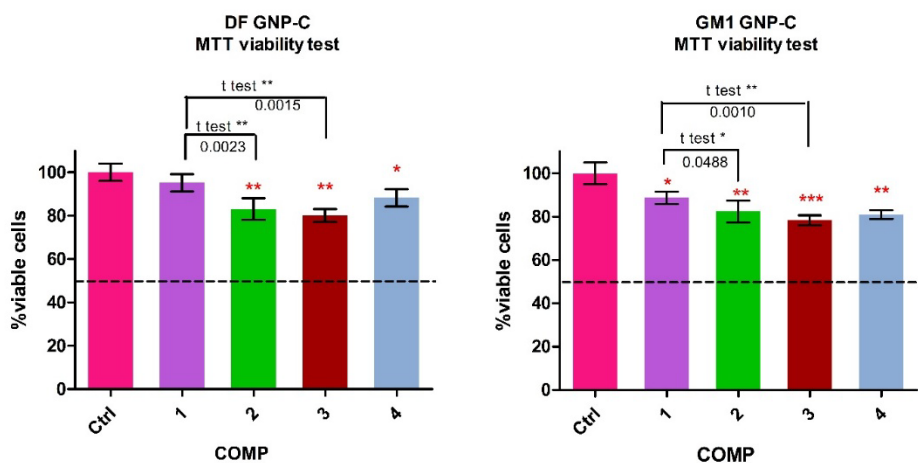


Figure 8: Cell viability (viable cells in % of Control, from MTT assay): Control (Ctrl); 1) GNP-C 3.9 µg/mL; 2) GNP-C 3.9 µg/mL / P 0.67 µg/mL; 3) GNP-C/A 3.9 µg/mL/ D 0.21 µg/mL; 4) GNP-C 3.9 µg/mL / Ic 1.67 µg/mL

The concentration of loaded bioactive molecules was very low in our study: for resveratrol 2.20 µmol/L, piperine 2.35 µmol/L, doxorubicin 0.36 µmol/L and for icariin 7.27 µmol/L, as shown in Table 1. GNP-C induced for all cells a reduced cytotoxicity, higher for breast cancer lines especially for hormone-dependent MCF-7 cells. Resveratrol loaded gold nanoparticles

have very similar effects on both breast cancer cell lines, in accordance with *Park et al. (2016)* study [46], which established that doses of 10 μM were non-toxic to MCF-7 breast cancer cells. The authors still reported that resveratrol-AuNPs showed better anti-invasive activity than resveratrol without cytotoxicity [43]. In a study conducted by *Wang et al. (2017)* [47], MDA-MB-231 cells treated with free resveratrol and resveratrol-loaded solid lipid nanoparticles found that both treatments inhibited cell viability in a dose-dependent manner.

In present study, GNP-C loaded with piperine and with doxorubicin induced a more intensive cytotoxic effect against MDA231 cells compared with MCF-7 cells. The molar ratios between Au and biocompounds and doxorubicin chosen in this study (Au/R-9.014; Au/P-8.442; Au/D-55.0; Au/ic-2.728) showed that the presence of gold in these formulations determined the efficient internalization of biocompounds and doxorubicin, which even in very low concentrations managed to exert their influence on the cellular response with the inhibition of proliferation and the triggering of cell death mechanisms. The clinical applications of these functionalized nanoparticles with biocompounds are materializing in lowering the doses of cytostatic agents by sensitizing tumor cells to chemotherapeutics [48].

The glioblastoma tumor stem cells showed a higher sensitivity to GNP-C, GNP-C functionalized with piperine, GNP-C/P, or with doxorubicin, GNP-C/A/D, and icariin, GNP-C/Ic, treatments with an increase in cytotoxicity in contrast to normal stem cells, DF, that were not affected by GNP-C administration. Cancer stem cells show characteristics close to normal DF stem cells, with a hyper-glycolytic metabolism (Warburg effect) and lowered mitochondrial respiration, compared to more differentiated cells.

The strategies to target cancer stem cells are different from conventional therapies, inhibiting their self-renewal and chemoresistance-related pathways, or inducing their differentiation. Promoting glioma cancer stem cells (GSCs) differentiation is a strategy to improve therapeutic efficacy, using bioactive phyto-compounds that reduce self-renewal and tumor forming capacity, eliciting differentiation of primary glioma-derived stem cells; also, glioma tumor stem cells might be targeted by impairing their metabolism [49]. Differentiated glioblastoma multiform (GBM) cells, compared to cancer stem cells are more sensitive to temozolomide (TMZ) treatment. *Jeong S. et al (2020)* [50] demonstrated that piperine alone at doses between 1- 200 μM inhibited temozolomide-resistant human glioma cell growth, similar to TMZ. Association of piperine with low concentration of TMZ induced apoptosis by activation of caspase-8/-9/-3, MMP loss, and inhibition of cell migration [50]. Piperine can also have a radio-sensitizing effect in micromolar concentrations in the human glioma cells [51]. In our experiments, GNP_C (GNP-C) functionalized

with piperine (GNP-C/P) or with doxorubicin (GNP-C/A/D) induced the more intensive cytotoxic response in glioblastoma (GM1) stem cells (Figure 8), thus adding the piperine or doxorubicin to gold nanoparticles enhances their effects sensitizing the cells to these treatments.

CONCLUSIONS

The optimization of the GNPs functionalization and their concentration for loading various biomolecules to their site of action is of paramount importance and specific for every type of human cancer cell line. Moreover, cytotoxicity effectiveness plays a critical role in determining their practical utility, for potential medical applications, having also a high biocompatibility with living normal cells, while in targeting cancer cells inducing apoptosis. Additionally, this study highlights the characterization techniques for GNPs, their functionalization using biomolecules, and their potential applications in cancer therapy, emphasizing their potential in advancing therapeutic strategies.

EXPERIMENTAL SECTION

Material and methods

Materials

We prepared gold nanoparticles, GNP_C (symbolized also as GNP-C), by the reduction of tetrachloroauric acid, ($\text{HAuCl}_4 \cdot 3\text{H}_2\text{O}$) 99.5% (Merck - Darmstadt, Germany), with trisodium citrate $\text{Na}_3\text{C}_6\text{H}_5\text{O}_7 \cdot 2\text{H}_2\text{O}$ (obtained from Sigma-Aldrich, Buchs, Switzerland). For the functionalization of GNP-C particles, anticancer biocompounds were used, namely: doxorubicin hydrochloride, D, (about 98%) from Sigma-Aldrich Chemie GmbH (Munich, Germany), trans-resveratrol, R, $\geq 99\%$ (HPLC assay), from Sigma-Aldrich, (Buchs, Switzerland), piperine, P, $\geq 98\%$ (HPLC assay), from AlfaAesar (Karlsruhe, Germany) and icariin, Ic, analytical standard ($\geq 94\%$) from Sigma-Aldrich (Steinheim, Germany). Aqueous solutions were prepared with bidistilled deionized water. For the solubilization of icariin, dimethyl sulfoxide (DMSO) from Sigma-Aldrich (Schnelldorf, Germany) was used. Dulbecco's phosphate buffered saline (PBS), without CaCl_2 and MgCl_2 , (pH 7.4), was necessary for the solutions used in cell cultures studies: it was purchased from AlfaAesar (Karlsruhe, Germany). We tried to stabilize the GNP_C solution against doxorubicin using the α -amino acid asparagine (Sigma-Aldrich, Steinheim, Germany).

Cell lines

Two breast cancer cell lines with different phenotypes / genotypes and different behaviors in terms of resistance to therapy were also tested: MDA-MB-231 (in short MDA231) and MCF-7, cell lines. Both human cell lines are derived from invasive ductal carcinoma. The MDA MB 231 cells are epithelial-type breast adenocarcinoma, negative for hormone receptors (triple negative) and with important mutations of anti-apoptotic protein p53. The lack of hormone receptors makes this cell line resistant to anti-hormonal therapies, but also to anticancer drugs [52, 53]. The MCF-7 line expresses estrogen receptors and are hormone-dependent [52]. Another particularly aggressive oncological localization was approached by performed tests on a line of tumor stem cells isolated from glioblastoma (GM1). The isolation method and the morphological and genetic characteristics, as well as the resistance to classical therapies were presented by *Tomuleasa et al (2010)* [39]. To evaluate the effect of gold nanoparticles on normal cells, stem cells derived from the dental follicle (DF) were used, which showed the phenotypic and functional characteristics of adult mesenchymal cells.

MDA MB 231 and MCF-7 (purchase from ATCC cell bank), glioblastoma GM1 cells and dental follicle (DF) stem cells were cultured in standard conditions. MCF-7 cells were cultured in Eagle's Minimum Essential Medium (MEM), supplemented with 10% fetal bovine serum (FCS), 2mM L-glutamine, 1% antibiotics, 1% non-essential amino acid solution (NEA). MDA MB 231 cells were cultured in RPMI-1640 medium supplemented with 10% fetal bovine serum (FCS), 2mM L-glutamine and 1% antibiotics. GM1 tumor stem cells derived from glioblastoma were cultured in DMEM medium with 4.5 g/L glucose, F12 HAM medium (DMEM / F12 1/1 ratio), with 10% fetal bovine serum (FCS), 1% antibiotics (penicillin and streptomycin), 2mM L-Glutamine, 1% NEA, and DF cells were maintained in Dulbecco's modified Eagle's medium (DMEM) high glucose/F-12HAM (Sigma) containing 15 % fetal calf serum (FCS, Sigma), 2 mM L-Glutamine, 1 % antibiotics, 1 % non-essential aminoacids (NEA), 55 μ M beta-mercaptoethanol, 1 mM natrium piruvate (all Sigma-Aldrich reagents).

Synthesis and functionalization of gold nanoparticles

In order to prepare the colloidal solution (dispersion) of GNP_C, 2 ml 1% (w/w) HAuCl₄·3H₂O aqueous solution (containing 0.05 mmol Au) was diluted with 80 ml ultrapure water, and 3 ml 1% aqueous trisodium citrate (Na₃C₆H₅O₇·2H₂O) solution, (containing 0.1 mmol citrate) was added; the mixture was boiled for 1 minute, then cooled to room temperature. This dispersion was stable for years.

For the functionalization of the GNP_C nanoparticles, in colloidal dispersions, and the evaluation of their stability against aggregation and precipitation, they were mixed at various ratios with solutions of anti-cancer compounds. The solutions used in this investigation and their concentrations are given in Table 3. Since icariin is not soluble in water, it was solubilized in dimethyl sulfoxide (DMSO, 11 mg/10 ml) and then 100 ml PBS were added to that solution.

Table 3. Solutions used in this study

Solution	Solvent	Chemical formula	Molar mass (g/mol)	Concentration	
				mg/L	mmol/L
GNP_C	water	Au	197	118	0.6
Doxorubicin. HCl, D	water	C ₂₇ H ₂₉ NO ₁₁ •HCl	580.0	42	0.072
Resveratrol, R	PBS	C ₁₄ H ₁₂ O ₃	228.2	30	0.131
Piperine, P	PBS	C ₁₇ H ₁₉ NO ₃	285.3	40	0.140
Icariin, Ic	DMSO, PBS	C ₃₃ H ₄₀ O ₁₅	676.7	100	0.148
Asparagine, A	Water	C ₄ H ₈ N ₂ O ₃	132.1	132	1

Characterization methods

UV-Vis spectra (190–900 nm wavelengths range) were measured with a Jasco UV-Vis V650 spectrophotometer (10 mm path length quartz cuvettes).

TEM images were recorded using JEOL standard software from a transmission electron microscope JEOL – JEM 1010. The GNPs colloidal dispersions were deposited on the carbon coated copper grids. After adsorption for 1 min the excess solution was removed with filter paper and the samples were air dried and ready for TEM examination.

AFM investigations were carried out on GNPs capped with citrate, GNP_C, as adsorbed layer (on glass plate) from the colloidal aqueous solutions for 10 s, washed with double distilled water and natural drying. Images were obtained using the AFM JEOL 4210 equipment, operated in tapping mode [5, 28], with standard cantilevers (resonant frequency 325 kHz, and spring constant 40 N/m) with silicon nitride tips. Scanned areas went from 10 μm × 10 μm to 0.5 μm × 0.5 μm on the same GNPs layer. The AFM images (2D- and 3D- topographies and phase images), were processed by the standard procedures with SPM2.0 processing software, JEOL, Japan.

Zeta- (ξ -) potential and dynamic light scattering (DLS) measurements were performed using the Malvern Zetasizer Nano-ZS90, on the colloidal gold solution.

X-Ray Diffraction (XRD) investigations were carried out using a Bruker D8 Advance diffractometer, in Bragg–Brentano geometry, equipped with a X-ray tube with copper target (K_{α} line, wavelength 1.541974 Å).

MTT viability assay

To perform the MTT viability test, MDA MB 231 cells, MCF-7 cells, DF stem cells and GM1 cells were seeded in 96-well plates at a cell density of 10^4 cells/well in 200 μ L complete medium/well. After 24 hours, after the cells have adhered to the surface of the plate, the compounds to be studied were added in the concentrations indicated in Tables 1 and 2.

The MTT viability test was performed after 24 hours of exposure to the compounds using the tetrazolium salt (3-(4, 5-dimethylthiazolyl-2)-2, 5-diphenyltetrazolium bromide) (Sigma-Aldrich Chemicals GmbH, St. Louis, MO, USA). After removing the medium from the cell cultures, 100 μ L of MTT solution (at concentration 1 mg/mL) was added to each well and after one hour of incubation at 37°C, in the dark, the MTT solution was discarded from the wells and added 150 μ L of DMSO/well to solubilize the formazan crystals. Optical density, OD, readings were performed at 570 nm with a BioTek Synergy 2 microplate reader (Winooski, VT, USA). Each MTT assay determination was performed in triplicate.

Obtained OD values were then calculated as reported percentages of the control value (untreated cells of 100% cell viability), see Figures 7 and 8.

For the statistical analysis, GraphPad Prism 5 software was used, with the application of two statistical analysis methods: *firstly, one-way ANOVA* followed by the "*Dunnett multiple comparison test*" in which the optical density values obtained from untreated (control) cells were compared with OD values of cells treated with the compounds; *secondly, t test* applied for comparing two selected samples. Significant values were set at a $p < 0.05$ (*).

ACKNOWLEDGMENTS

This work was supported by a grant from the Ministry of Research, Innovation and Digitization, CNCS/CCCDI-UEFISCDI, project PN-III-P4-ID-PCE-2020-1910, project no. 186, managed by the director Maria Tomoaia-Cotisel. The experimental facilities and the top equipment of the Scientific Research Center of Excellence in Physical Chemistry, part of STAR Institute, Babes-Bolyai University, were used in this research. The founder (2006) and director (2006–present) of this Research Center is Maria Tomoaia-Cotisel.

REFERENCES





1. R. L. Siegel; A. N. Giaquinto; A. Jemal; *CA Cancer J. Clin.*, **2024**, *74*, 12–49
2. K. Sztandera; M. Gorzkiewicz; B. Klajnert-Maculewicz; *Mol. Pharmaceutics*, **2019**, *16*, 1–23
3. H. Huang; R. Liu; J. Yang; J. Dai; S. Fan; J. Pi; Y. Wei; X. Guo; *Pharmaceutics*, **2023**, *15*, 1868
4. O. Horovitz, A. Mocanu, G. Tomoiaia, M. Crisan, L.-D. Bobos, Cs. Racz, M. Tomoiaia-Cotisel, *Studia Univ. Babeş-Bolyai, Chem.*, **2007**, *52* (3), 53-71
5. G. Tomoiaia; O. Horovitz; A. Mocanu; A. Nita; A. Avram; C. Pal Racz; O. Soritau; M. Cenariu; M. Tomoiaia-Cotisel; *Colloids Surf. B Biointerfaces*, **2015**, *135*, 726-734
6. A. Sobczak-Kupiec; D. Malina; M. Zimowska; Z. Wzorek; *Digest J. Nanomater. Biostruct.*, **2011**, *6*(2), 803-808
7. A. Jakhmola; V. Onesto; F. Gentile; F. M. Kashkooli; K. Sathiyamoorthy; E. Battista; R. Vecchione; K. Rod; M. C. Kolios; J. (Jahan) Tavakkoli; P. A. Netti; *Mater. Today Sustain.*, **2024**, *28*, 101012
8. M. M. Khalaf; F. F. El-Senduny; H. M. A. El-Lateef; H. Elsayy; A. H. Tantawy; S. Shaaban; *J. Mol. Liq.*, **2021**, *340*, 117202
9. J. Dong; P. L. Carpinone; G. Pyrgiotakis; P. Demokritou; B. M. Moudgil; *Kona Powder Part. J.*, **2020**, *37*, 224-232
10. J. Piella; N. G. Bastus; Victor Puentes; *Chem. Mater.*, **2016**, *28*, 1066–1075
11. N. Hanzic; T. Jurkina; A. Maksimovic; M. Gotic; *Radiat. Phys. Chem.*, **2015**, *106*, 77-82
12. J.-W. Park; J. S. Shumaker-Parry; *J. Am. Chem. Soc.*, **2014**, *136*, 1907–1921
13. A. G. Memon; I. A. Channa; A. A. Shaikh; J. Ahmad; A. F. Soomro; A. S. Giwa; Z. T. Baig; W. A. Mahdi; S. Alshehri; *Crystals*, **2022**, *12*, 1747
14. L. Shi; E. Buhler; F. Boue; F. Carn; *J. Colloid Interface Sci.*, **2017**, *492*, 191-198
15. A. Tirkey; P. J. Babu; *Sens. Int.*, **2024**, *5*, 100252
16. D. Luo; X. Wang; C. Burda; J. P. Basilion; *Cancers*, **2021**, *13*, 1825
17. R. Z. Cer; U. Mudunuri; R. Stephens; F. J. Lebeda; *Nucl. Acids Res.*, **2009**, *37*, W441–W445
18. M. M. Fathy; A. A. Elfiky; Y. S. Bashandy; M. M. Hamdy; A. M. Elgharib; I. M. Ibrahim; R. T. Kamal; A. S. Mohamed; A. M. Rashad; O. S. Ahmed; Y. Elkaramany; Y. S. Abdelaziz; F. G. Amin; J. I. Eid; *Sci. Rep.*, **2023**, *13*, 2749
19. C. Freese; C. Uboldi; M. I. Gibson; R. E. Unger; B. B. Weksler; I. A. Romero; P.-O. Couraud; C. J. Kirkpatrick; *Part. fibre toxicol.*, **2012**, *9*, 23
20. D. Kumar; I. Mutreja; K. Chitcholtan; P. Sykes; *Nanotechnology*, **2017**, *28*(47), 475101
21. V. Raji; J. Kumar; C. S. Rejiya; M. Vibin; V. N. Shenoi; A. Abraham; *Exp. Cell Res.*, **2011**, *317*, 2052-2058
22. J. C. Mohan; G. Praveen; K.P. Chennazhi; R. Jayakumar; S.V. Nair; *J. Exp. Nanosci.*, **2015**, *8*(1), 32-45

23. S. Y. Choi; S. Jeong; S. H. Jang; J. Park; J. H. Park; K. S. Ock; S. Y. Lee; S.-W. Joo; *Toxicol. In Vitro*, **2012**, *26*, 229-237
24. J. Lee; D. K. Chatterjee; M. H. Lee; S. Krishnan; *Cancer Lett.*, **2014**, *347*, 46-53
25. S. K. Surapaneni; S. Bashir; K. Tikoo; *Sci. Rep.*, **2018**, *8*, 12295
26. E. E. Connor; J. Mwamuka; A. Gole; C. J. Murphy; M. D. Wyatt; *Small*, **2005**, *3*, 325-327
27. N. Tlotleng; M. A. Vetten; F. K. Keter; A. Skepu; R. Tshikhudo; M. Gulumian; *Cell. Biol. Toxicol.*, **2016**, *32*(4), 305-321
28. O. Horovitz; G. Tomoaia; A. Mocanu; T. Yupsanis; M. Tomoaia-Cotisel; *Gold Bull.*, **2007**, *40*(4), 295-304
29. M. A. Ujica; C.-T. Dobrota; G. Tomoaia; A. Mocanu; C.-L. Rosoiu; I. Mang, V. Raischi, M. Tomoaia-Cotisel; *Acad. Rom. Sci. Ann. Ser. Biol. Sci.*, **2024**, *13*(2), 145-167.
30. D. Delmas; V. Aires; E. Limagne; P. Dutartre; Frederic Mazue; F. Ghiringhelli; N. Latruffe; *Ann. N. Y. Acad. Sci.*, **2011**, *1215*, 48-59
31. J. J. Johnson; M. Nihal; I. A. Siddiqui; C. O. Scarlett; H. H. Bailey; H. Mukhtar; N. Ahmad; *Mol. Nutr. Food Res.*, **2011**, *55*, 1169-1176
32. J. K. Tak; J. H. Lee; J.-W. Park; *BMB reports*, **2012**, *45*(4), 242-246
33. Z. Jiang; K. Chen; L. Cheng; B. Yan; W. Qian; J. Cao; J. Li; E. Wu; Q. Ma; W. Yang; *Ann. N. Y. Acad. Sci.*, **2017**, *1403*, 59-69
34. O. Vesely; S. Baldovska; A. Kolesarova; *Nutrients*, **2021**, *13*, 3095
35. S. Benayad; H. Wahnou; R. El Kebbjaj; B. Liagre; V. Sol; M. Oudghiri; E. M. Saad; R. E. Duval; Y. Limami; *Cancers*, **2023**, *15*, 5488
36. Z. Bi; W. Zhang; X. Yan; *Biomed. Pharmacother.*, **2022**, *151*, 113180
37. Z. Yu; J. Guo; M. Hu; Y. Gao; L. Huang; *ACS Nano*, **2020**, *14*, 4816-4828
38. Z. Wang; L. Yang; Y. Xia; C. Guo; L. Kong; *Biol. Pharm. Bull.*, **2015**, *38*(2), 277-284
39. C. Tomuleasa; O. Soritau; D. Rus-Ciucă; H. Ioani; S. Susman; M. Petrescu; T. Timis; D. Cernea; G. Kacso; A. Irimie; I. S. Florian; *J. Buon.*, **2010**, *15*(3), 583-591
40. R. Cailleau; R. Young; M. Olive; W. J. Reeves Jr.; *J. Natl. Cancer. Inst.*, **1974**, *53*(3), 661-674
41. R. Watkins; L. Wu; C. Zhang; R. M. Davis; B. Xu; *Int. J. Nanomedicine*, **2015**, *10*, 6055-6074
42. K. de Vries; M. Strydom; V. Steenkamp; *J. Herb. Med.*, **2018**, *11*, 71-77
43. V. Sanna; N. Pala; G. Dessi; P. Manconi; A. Mariani; S. Dedola; M. Rassu; C. Crosio; C. Iaccarino; M. Sechi; *Int. J. Nanomedicine*, **2014**, *9*, 4935-4951
44. M. A. Ujica; I. Mang; O. Horovitz; A. Mocanu; M. Tomoaia-Cotisel; *Studia Univ. Babeş-Bolyai, Chem.*, **2025**, *70* (1), 47-63
45. R. J. Hunter, *Zeta Potential in Colloid Science: Principles and Applications*, Academic Press, London, **1981**, pp. 363-369
46. S. Y. Park; S. Y. Chae; J. O. Park; K. J. Lee; G. Park; *Oncol. Rep.*, **2016**, *35*(6), 3248-3256
47. W. Wang; L. Zhang; T. Chen; W. Guo; X. Bao; D. Wang; B. Ren; H. Wang; Y. Li; Y. Wang; S. Chen; B. Tang; Q. Yang; C. Chen; *Molecules*, **2017**, *22*(11), 1814
48. Hakeem AN; El-Kersh DM; Hammam O; Elhosseiny A; Zaki A; Kamel K; Yasser L; Barsom M; Ahmed M; Gamal M; Attia YM; *Sci Rep.* **2024**, *14*, 18181

M. A. UJICA, I. MANG, O. HOROVITZ, O. SORITAU, GH. TOMOAI, A. MOCANU, H. R. C. BENE, V. RAISCHI, CS. VARHELYI, G. BORODI, M. TOMOAI-COTISEL

49. F. Pistollato; S. Bremer-Hoffmann; G. Basso; S. S. Cano; I. Elio; M. M. Vergara; F. Giampieri; M. Battino; *Targ. Oncol.*, **2016**, *11*(1),1-16
50. S. Jeong; S. Jung; G. S. Park; J. Shin; J. W. Oh; *Bioengineered*, **2020**, *11*(1), 791-800
51. S. Diehl; G. Hildebrandt; K. Manda; *Int. J. Mol. Sci.*, **2022**, *23*(15), 8548
52. T. A. Theodossiou; M. Ali; M. Grigalavicius; B. Grallert; P. Dillard; K. O. Schink; C. E. Olsen; S. Walchli; E. M. Inderberg; A. Kubin; Q. Peng; K. Berg; *NPJ Breast Cancer*, **2019**, *5*, 13
53. Y. Li; S. Upadhyay; M. Bhuiyan; F. H. Sarkar; *Oncogene*, **1999**, *18*(20),3166-3172

GREEN SYNTHESIS OF SILVER NANOPARTICLES USING *GALIUM VERUM* L. AQUEOUS EXTRACT AND EVALUATION OF ITS ANTIMICROBIAL ACTIVITY

Adriana-Maria ANDREICA^{a,*} , Mihaela Cecilia VLASSA^a ,
Rahela CARPA^b , Ioan PETEAN^c 

ABSTRACT. The development of cost-efficient and sustainable methods for the synthesis of nanomaterials still remains a scientific challenge. The aim of this study was to investigate the green synthesis of silver nanoparticles using aqueous extract of *Galium verum* L. (GV) as a potential source of biomolecules able to reduce the silver ions and stabilize them. Reaction parameters such as concentrations of AgNO₃, extract to AgNO₃ ratio, temperature, pH, and reaction time were optimized. The synthesis of silver nanoparticles (GV-AgNPs) using different parameters was monitored by ultraviolet-visible spectroscopy (UV-Vis). Fourier transform infrared spectroscopy (FTIR) results showed the presence of functional groups that act as reducing agents and stabilize the GV-AgNPs. Atomic force microscopy (AFM) confirmed that the particles were round-shaped with a diameter of about 25 nm. The GV-AgNPs show different antimicrobial activity depending on the type of sample and depending on the microbial strain tested.

Keywords: *green synthesis, nanoparticles, galium verum, antimicrobial activity*

INTRODUCTION

The production techniques of metallic nanoparticles and their applications made nanotechnology one of the most studied fields in the last decades [1, 2]. Metal nanoparticles have attracted considerable attention due to their diverse

^a Babeş-Bolyai University, "Raluca-Ripan" Institute for Research in Chemistry, 30 Fântânele str., RO-400294, Cluj-Napoca, Romania

^b Babeş-Bolyai University, Faculty of Biology and Geology, Molecular Biology and Biotechnology Department, 1 Mihail Kogălniceanu str., RO-400084, Cluj-Napoca, Romania

^c Babeş-Bolyai University, Faculty of Chemistry and Chemical Engineering, 11 Arany Janos str., RO-400084, Cluj-Napoca, Romania

* Corresponding author: adriana.andreica@ubbcluj.ro



applications in different fields such as biomedicine (fast diagnosis, imaging, tissue regeneration drug delivery, and development of new medical products) [3], catalysis [4], and electronics [5]. Generally, the synthesis of silver nanoparticles is carried out using physicochemical techniques such as autoclaving [6], gamma-ray radiation [7], and use of microemulsions [8], electrochemical techniques [9], chemical reduction [10], laser ablation [11], microwave irradiation [12], and photochemical reduction [13]. The synthesis has limitations such as the use of toxic chemicals and generation of hazardous waste, high functional cost, and energy requirement. Green nanotechnology has been developed as an alternative to the use of environmentally harmful processes and products [14]. Plant extracts can be used to obtain silver nanoparticles without the need for harmful reducing and capping chemicals, and high temperatures. The use of plant extracts for the synthesis of silver nanoparticles provides a low-cost, non-toxic, environmentally friendly method. There are several studies that report the synthesis of silver nanoparticles by exploiting the reducing capacity of flavonoids, phenolics, proteins, and carbohydrates from plants with pharmacological properties [15, 16].

Galium verum L., also known as Lady's Bedstraw, belonging to the Rubiaceae family, is a perennial herb widely used throughout history in traditional medicine as diuretic, choleric and treatment for gout and epilepsy [17]. *Galium verum* L. extracts are known to have antimicrobial and antioxidant properties [18, 19], improve *in vivo* cardiac function in rats, preserve the functional and morphological properties of the heart, and prevent coronary dysfunction after ischemia [20], and reveal a growth-inhibiting effect on chemo-sensitive and -resistant laryngeal carcinoma cell lines [21]. *Galium verum* L. extracts have been studied for their chemical composition, a variety of bioactive substances have been identified, such as iridoid glycosides [22], flavonoids [23, 24], and phenolic acids [25, 24].

Beyond the use of this plant for medicinal purposes and taking into account its chemical composition, *Galium verum* L. extract was chosen for the synthesis of silver nanoparticles.

The novelty of this study was the use for the first time of *Galium verum* L. extract as a source of biomolecules that can act as a reducing agent and stabilizer in the synthesis of silver nanoparticles in a highly sustainable manner and the testing of the antimicrobial activity of the obtained nanoparticles. The aim of the present study was to investigate the green synthesis of silver nanoparticles using the aqueous extract of *Galium verum* L. aerial parts, to optimize the reaction parameters, to characterize the obtained nanoparticles, and to evaluate their antimicrobial activity against Gram-positive, Gram-negative strains and fungal strain. To the best of our knowledge, the synthesis of GV-AgNPs and their antimicrobial activity have not been previously reported.

RESULTS AND DISCUSSION

To obtain GV-AgNPs, different parameters were evaluated, namely, silver salt concentration, temperature, volume ratio of plant extract to silver salt solution, pH value of the solution, and reaction time. The formation of silver nanoparticles was monitored by UV-Vis spectroscopy, which is the main tool used to study the synthesis. The formation of silver nanoparticles was first visually observed by the color change from yellow to dark brown due to the excitation of surface plasmon resonance (SPR) of the nanoparticles [26]. The reduction of silver ions using GV extract was confirmed by the UV-Vis spectrum, which showed a characteristic surface plasmon resonance peak at 411 nm, which was in agreement with the literature data [27]. This peak provides information on the morphology of the obtained silver nanoparticles.

The absorption peak of the GV-AgNPs was broad and less intense when the concentration of AgNO_3 was 1 mM, as shown in Figure 1 (A), which indicates that silver nanoparticles were agglomerated. By increasing the concentration of AgNO_3 , an increase in the intensity of the peak was observed. The absorption peak was 409 nm and became sharper. This suggests that obtained GV-AgNPs were relatively smaller as the AgNO_3 concentration increased to 10 mM. In Figure 1 (B) the effect of temperature variation on silver nanoparticle synthesis is presented. By increasing the temperature, the absorption peak was shifted from 421 nm at 30 °C and 424 nm at 50 °C to 409 nm at 70 °C. The disappearance of broadening and an increase in intensity of the absorption peak were also observed. The broad and shifted peak to longer wavelengths was attributed to agglomeration or an increase in size of the nanoparticles [28, 29].

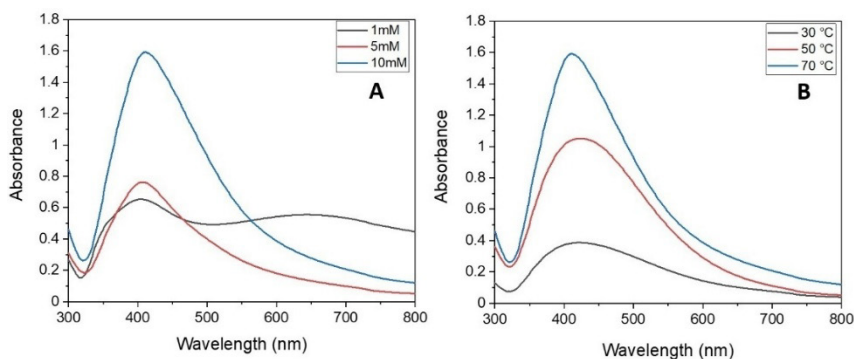


Figure 1. UV-Vis spectra: Effect of concentration and temperature on silver nanoparticles synthesis: (A) different concentrations of AgNO_3 , extract to AgNO_3 ratio = 1:20, $T = 70$ °C, $\text{pH} = 8$, reaction time = 4 h; (B) 10 mM AgNO_3 , extract to AgNO_3 ratio = 1:20, $\text{pH} = 8$ at different temperatures

The absorption peak of the GV-AgNPs was broad and less intense when extract to AgNO₃ volume ratios used in synthesis were 1:5 and 1:10, as shown in Figure 2 (C). The GV-AgNPs obtained with a 1:20 ratio between extract and AgNO₃ showed a strong and sharp absorption peak at 411 nm.

Based on other studies that confirm that an alkaline medium was favorable for the silver nanoparticles [30], pH = 8 was chosen to obtain GV-AgNPs, but the synthesis was also tested at pH 6 and pH 10, as illustrated in Figure 2 (D). By increasing the pH value of the reaction media, the absorption peak was shifted from 429 nm at pH = 6 to 411 nm at pH = 8 and 414 nm at pH = 10. The obtained silver nanoparticles at pH = 8 were smaller, and the absorption peak was sharp. The absorption peak shifts towards shorter wavelengths when the size of nanoparticles decreases [29], and an increase in the intensity peak means an increase in the concentration of nanoparticles [31].

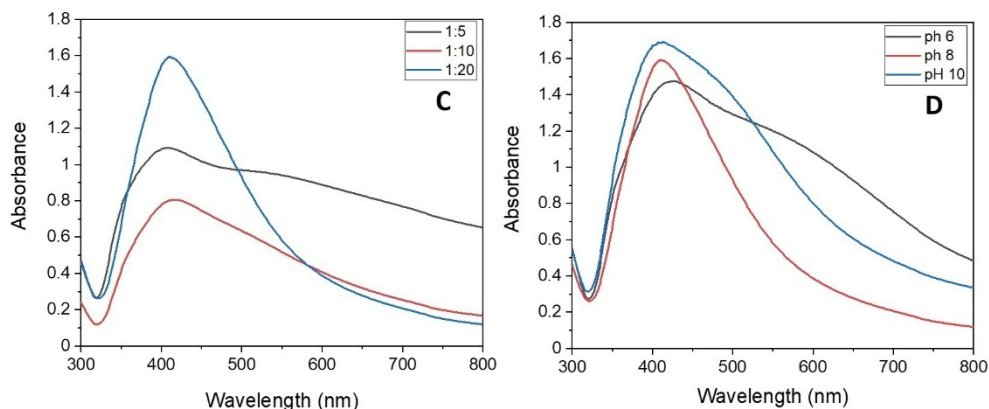


Figure 2. UV-Vis spectra: Effect of extract to AgNO₃ ratio and effect of pH on silver nanoparticles synthesis: (C) different extract to AgNO₃ ratio, 10 mM AgNO₃, pH = 8, T = 70 °C, reaction time = 4 h; (D) extract to AgNO₃ ratio = 1:20, 10 mM AgNO₃, T = 70 °C, reaction time = 4 h at different pH values

The effect of the reaction time on GV-AgNPs synthesis is presented in Figure 3.

The intensity of the absorption peak increased after 4 hours, indicating an increase in the concentration of silver nanoparticles with time [32], while at 6 hours the intensity of the absorption peak decreased.

The optimum parameters for the green synthesis of GV-AgNPs were AgNO₃ concentration 10 mM, 1:20 volume ratio of *Galium verum* L. extract to AgNO₃, pH 8, temperature 70 °C and reaction time 4 h.

GREEN SYNTHESIS OF SILVER NANOPARTICLES USING *GALIUM VERUM* L. AQUEOUS EXTRACT AND EVALUATION OF ITS ANTIMICROBIAL ACTIVITY

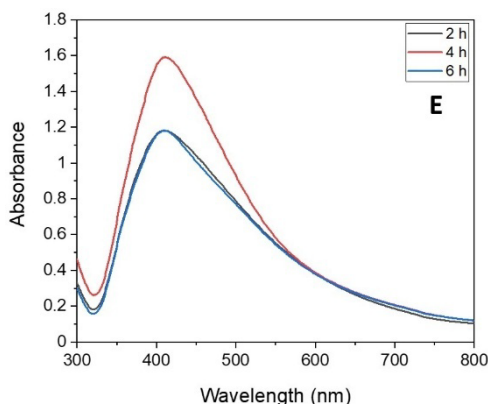


Figure 3. UV-Vis spectra: Effect of reaction time on silver nanoparticles synthesis: (E) 10 mM AgNO₃, extract to AgNO₃ ratio = 1:20, pH = 8, T = 70 °C

Fourier transformed infrared spectroscopy was used to identify the organic molecules from the aerial parts extract of the plant that act as reducing agents of the silver ions and stabilize the obtained silver nanoparticles. The FTIR spectra of *Galium verum* L. aqueous extract and silver nanoparticles obtained by the green synthesis are shown in Figure 4.

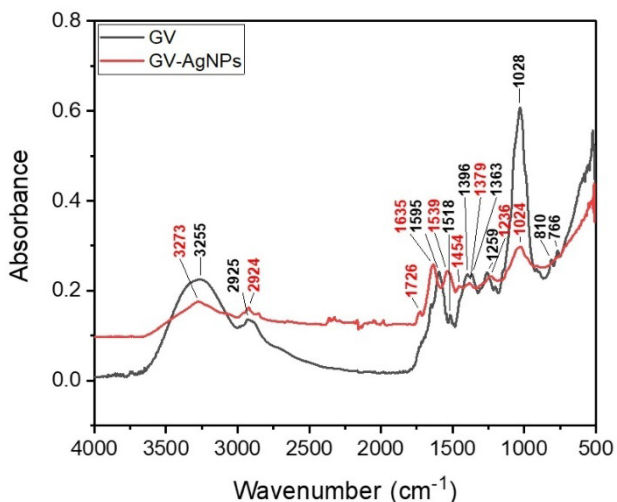


Figure 4. FTIR spectra for *Galium verum* L. extract and silver nanoparticles

The results of the FTIR analysis for both *Galium verum* L. extract and silver nanoparticles (GV-AgNPs) are presented in Table 1. The assignment of stretching and bending vibrations was carried out in accordance with the literature data.

Table 1. FTIR absorption bands assignment of *Galium verum* L. extract and obtained silver nanoparticles

Wavenumber (cm ⁻¹)		Assignment	Functional groups	References
GV	GV-AgNPs			
3255	3273	OH stretch	Alcohols/Phenols	[33]
2925	2924	CH stretching/ OH stretch	Alkanes/Alcohols (acid)	[34, 35]
	1726	C=O stretch	Carbonyl compounds	[35]
1595	1635	C=O and C=C stretching	Unsaturated Ketones	[35, 36, 37]
1518	1539	C=C stretch	Aromatic compounds	[38, 34]
	1454	CH bending/ C=C stretch	Alkanes/Aromatic compounds	[34, 35]
1396		CH bending	Alkanes	[35]
1363	1379	CH bending	Alkanes	[34]
1259	1236	C-O-C stretch	Ethers/Esters	[33, 35]
1028	1024	C-O stretch	Alcohols	[36]
810		C=C bending/C-Cl stretching	Alkanes/Halo compounds	[34]
766		C=C bending/C-Cl stretching	Alkanes/Halo compounds	[34]

In both the extract and GV-AgNPs FTIR spectra the presence of different functional groups that are involved in the synthesis and stabilization of silver nanoparticles was observed (Figure 4). In the *Galium verum* L. extract spectrum, the absorption band at 3255 cm⁻¹ was attributed to OH stretching vibrations of the phenols, and the band at 2925 cm⁻¹ was attributed to CH₂ asymmetric stretching vibrations or OH stretching in acid functional groups. The band at 1595 cm⁻¹ can be attributed to C=O and C=C stretching vibrations in α , β -unsaturated ketones. The absorption peaks between 1300 and 1600 cm⁻¹ show the presence of C=C stretch in a ring and CH bending from aromatic compounds and alkanes (CH₂ and CH₃ bending). The bands at 1259 cm⁻¹ were attributed to C-O-C stretch in ethers and esters, and the sharp one at 1028 cm⁻¹ to C-O stretch in alcohols. The bands at 810 cm⁻¹ and 766 cm⁻¹ were assigned to C=C bending vibrations in alkanes and C-Cl stretching in halo compounds. The FTIR spectrum of the extract was compared with the GV-AgNPs spectrum. Some shifts were observed as follows: OH, C=O and C=C, C=C, CH, C-O-C, C-O groups were shifted from 3255, 1595, 1518, 1363, 1259 and 1028 cm⁻¹ to 3273, 1635, 1539, 1379, 1236 and 1024 cm⁻¹. It was observed that nanoparticles showed a new band at 1726 cm⁻¹

GREEN SYNTHESIS OF SILVER NANOPARTICLES USING *GALIUM VERUM* L. AQUEOUS EXTRACT AND EVALUATION OF ITS ANTIMICROBIAL ACTIVITY

corresponding to carbonyl stretching vibrations in aldehydes or ketones. The stretching bands related to the carbonyl groups at 1635 cm^{-1} and 1726 cm^{-1} may be indicating the involvement of hydroxyl groups in the reduction of Ag^+ to Ag^0 resulting in oxidized polyphenols that act as capping agents and stabilize the formed silver nanoparticles [39, 40]. *Galium verum* L. extracts contain phenolic acids such as chlorogenic acid, caffeic acid, ferulic acid, coumaric acid, and flavonoids [41-43]. Many studies have mentioned the role of polyphenols from plant extracts in the green synthesis of silver nanoparticles that can reduce and stabilize them [44-47].

The atomic force microscopy (AFM) was used for the topographic characterization of the self assembled GV-AgNPs onto solid substrate. The general aspect of the formed thin film is uniform and smooth, indicating a uniform adsorption of the nanoparticles from the liquid dispersion, Figure 5a.

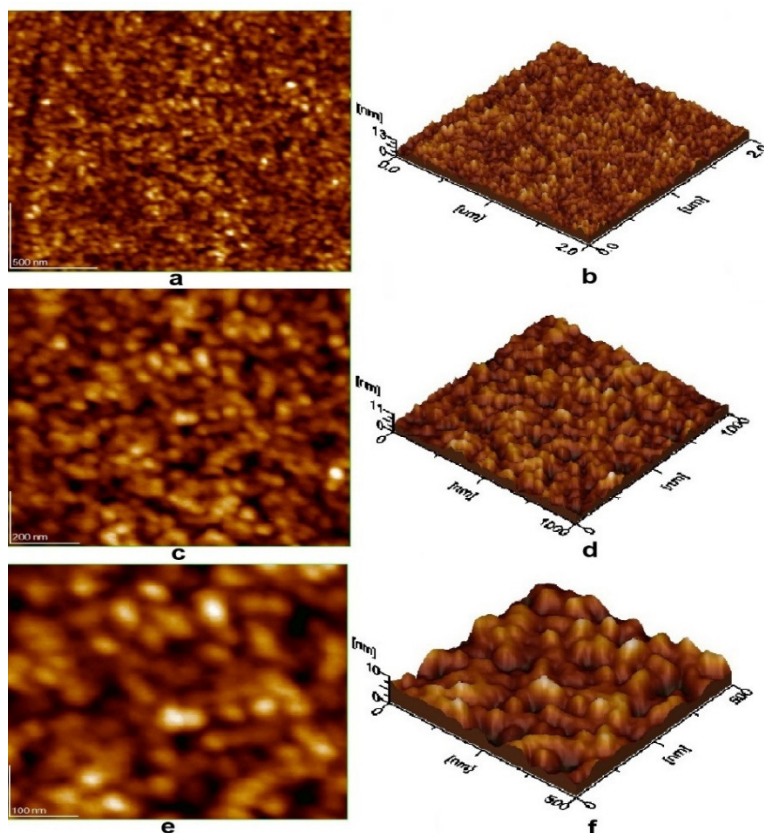


Figure 5. AFM images of synthesized GV-AgNPs; scanned area $2\ \mu\text{m} \times 2\ \mu\text{m}$; $1\ \mu\text{m} \times 1\ \mu\text{m}$; $0.5\ \mu\text{m} \times 0.5\ \mu\text{m}$: (a, c, e) 2D-topography; (b, d, f) three-dimensional profiles

It ensures a low surface roughness of 1.61 ± 0.28 nm, which is well correlated with the flat aspect of the three-dimensional profile presented in Figure 5b. A closer look to the self assembled structure can be observed at the scanned area of $1 \mu\text{m} \times 1 \mu\text{m}$ in Figure 5c. The nanoparticles appear well individualized without marginal coalescence, allowing observation of their rounded shape. The lack of submicron clusters, which would have been formed at a high coalescence gradient, indicates an increased efficiency of the nanoparticles to hit and penetrate the membranes of the pathogen agent causing their death.

The three-dimensional profile in Figure 5d reveals the nanoparticles deposition mode on specific areas of the targeted microorganism surface. The local roughness is situated around 1.62 ± 0.16 nm, it is significantly low as a thin film but its efficacy must to be proved by the antimicrobial testing results.

The nanostructural detail taken at the scanned area of $0.5 \mu\text{m} \times 0.5 \mu\text{m}$, Figure 5e, allows the proper measuring of the nanoparticles diameter, which is about 25 ± 3 nm.

The silver nanoparticles obtained by the use of *Majorana hortensis* extract were characterized by AFM, and the size of nanoparticles was in the range of 50 and 95 nm [48]. The literature data show that 25 nm is an ideal diameter for antibacterial purposes [15, 16]. The perfect individualization of the adsorbed nanoparticles is observed better in the three-dimensional profile in Figure 5e, revealing their adhesion mode on the pathogen cell membrane.

Evaluation of antimicrobial activity

After the end of the incubation period at 37°C , the zones of inhibition (mm) for the tested microbial strains were determined. It was observed that in all bacterial strains, the control sample CN10 (gentamicin) showed inhibition between 12 and 22 mm. For the *Candida albicans* strain, the control sample VOR1 (voriconazole) showed a stronger inhibition of 28 mm (Figure 6, Figure 7). The *Galium verum* extract showed a slight inhibition compared to the chosen control (CN10 for bacterial strains and VOR1 for fungal strain). However, *Galium verum* species can be used as a good source of polyphenols with antibacterial properties.

The diameter of the inhibition zone in microbial strains after the incubation period is presented in Figure 7.

For Gram positive bacterial strains, different diameters of inhibition were recorded. At *Staphylococcus aureus* ATCC 25923, inhibition was noticed only at the sample with GV-AgNPs (12 mm). At *Enterococcus faecalis* ATCC 29212, both samples showed inhibition, but the GV extract sample showed higher inhibition (15 mm) than the GV-AgNPs sample.

GREEN SYNTHESIS OF SILVER NANOPARTICLES USING *GALIUM VERUM* L. AQUEOUS EXTRACT AND EVALUATION OF ITS ANTIMICROBIAL ACTIVITY

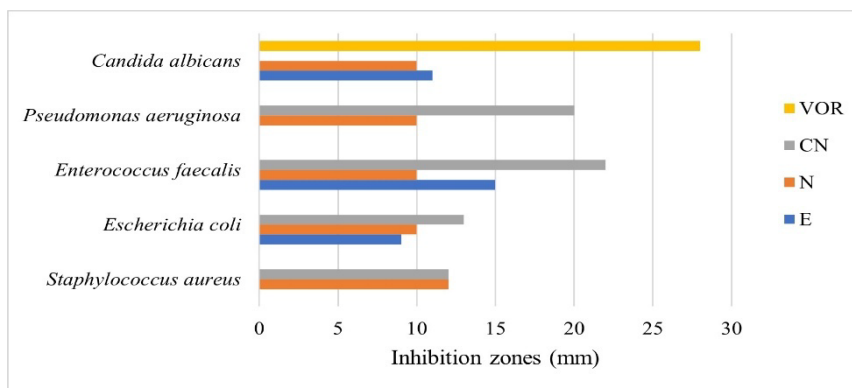


Figure 6. The diameter of the inhibition zones (mm) of the tested samples (E = GV extract, N = GV-AgNPs, CN = gentamicin, VOR = voriconazole)

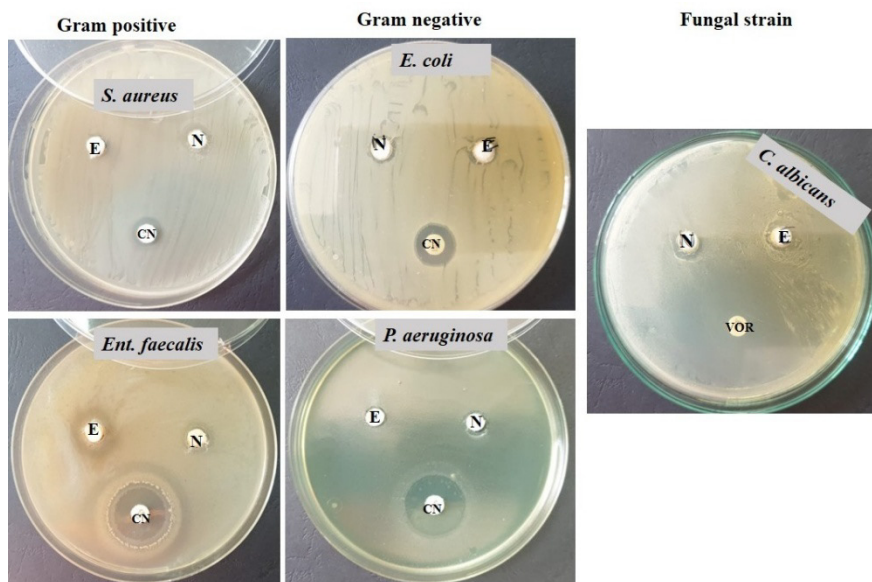


Figure 7. The diameter of the inhibition zone in microbial strains after the incubation period (E = GV extract, N = GV-AgNPs, CN = gentamicin, VOR = voriconazole)

For Gram negative bacterial strains, different inhibition diameters were recorded. At *Escherichia coli* ATCC 25922, both samples showed slight inhibition. In the *Pseudomonas aeruginosa* ATCC 27853 strain, only the sample with GV-AgNPs showed a slight inhibition (10 mm). It was observed that the Gram negative strains tested showed less inhibition than the Gram positive ones.

In the fungal strain *Candida albicans* ATCC 10231, the tested samples showed a slight inhibition (sample E = 10 mm and sample N = 11 mm) compared to the control sample (VOR), which recorded an inhibition of 28 mm.

CONCLUSIONS

The present study reports the green synthesis of silver nanoparticles using *Galium verum* L. extract as a source of biomolecules capable of the reduction and stabilization of the nanoparticles obtained. By optimizing the reaction parameters and using sustainable raw materials such as *Galium verum* L. extract, this process provides an easy way to obtain silver nanoparticles. UV-Vis spectroscopy was used to confirm the presence of the characteristic SPR peak at 411 nm, indicating the synthesis of GV-AgNPs. The presence of functional groups involved in the synthesis and stabilization of the GV-AgNPs was identified by FTIR spectroscopy. The topographic characterization of the GV-AgNPs by AFM indicated well individualized nanoparticles of rounded shape and with a diameter of about 25 nm.

The self assembly of the GV-AgNPs onto the solid surface indicates an efficient mode of targeting the membrane of the pathogen agent facilitating their antibacterial action.

The antimicrobial activity of GV-AgNPs was evaluated using an antimicrobial diffusion test on Gram positive, Gram negative bacterial strains, and fungal strain. Following these experiments on *Galium verum* L. extract and GV-AgNPs it can be stated that they show different antimicrobial activity depending on the type of sample and depending on the microbial strain tested.

The synthesis of GV-AgNPs by the green process is a promising tool for new research strategies due to its potential for various medical applications.

EXPERIMENTAL SECTION

Materials

The aerial parts of *Galium verum* L. were collected in June 2024 during the flowering period from Florești, Cluj County, România. The plant was identified at the “Alexandru Borza” Botanical Garden from Cluj-Napoca, and the voucher specimen (no. 674506) was deposited in the CL Herbarium Musei Universitatis Napocensis, Cluj-Napoca. Silver nitrate (AgNO_3) was purchased from Merck România and was of analytical grade. Ultrapure water (18.2 M Ω cm ionic purity at 25 °C) produced in the laboratory by means of a Simplicity system (Millipore; Bedford, MA, USA) was used in all experiments.

Preparation of aqueous extract

Aerial parts of the collected plant were washed with running tap water and dried in the shade at room temperature. The dried plant was ground to powder. 100 mL of ultrapure water was added to 10 g of plant powder and boiled for 20 minutes. The cooled extract was filtered with Whatman filter paper no. 1 and stored at 4 °C until further use.

Green synthesis of silver nanoparticles

For the synthesis of silver nanoparticles, 2.5 mL of plant extract was added to a 50 mL silver nitrate solution of different concentrations (1 mM, 5 mM, 10 mM). The reactions were effectuated at 30, 50, 70 °C. The volume ratios of extract to silver nitrate solution used in nanoparticle preparation were 1:5, 1:10, and 1:20. Different pH values (6, 8, 10) were investigated. The reaction was monitored by UV-Vis spectroscopy at 2 h, 4 h, and 6 h.

The best results were obtained as follows: extract (2.5 mL) was added to a 10 mM AgNO₃ solution (50 mL) using a 1:20 volume ratio of extract to AgNO₃ solution, and then pH of the reaction mixture was adjusted to 8 using a 0.1 M NaOH solution. After 4 hours of stirring at 70 °C, the obtained nanoparticles were purified by centrifugation for 20 minutes, washed three times with ultrapure water, and then lyophilized.

Characterization of the GV-AgNPs

The synthesis of AgNPs was monitored by UV-Vis spectroscopy using a Specord 205 Spectrophotometer (Analytik Jena, GmbH, Germany). The sample was diluted with ultrapure water, and then the UV-Vis spectra were recorded using ultrapure water as the blank. The identification of functional groups involved in both plant extract and silver nanoparticles was performed by Fourier transform infrared spectroscopy (FTIR) using FTIR 610 spectrometer (Jasco Corporation, Tokyo, Japan), equipped with an ATR attachment (attenuated total reflectance) with a horizontal ZnSe crystal (Jasco PRO400S) in the 4000-500 cm⁻¹ wave number range. The resolution of the spectra was 4 cm⁻¹ and scans were repeated of 100 times. All FTIR spectra were registered at room temperature.

The nanoparticles were transferred onto a solid substrate (e.g. a glass slide) by vertical adsorption for 20 seconds, followed by natural drying. Nanoparticles aspect and their self-assembly ability on solid substrate were investigated with Atomic Force Microscopy (AFM). It was effectuated with a JEOL JSPM 4210 Scanning Probe Microscope operated in tapping mode using NSC 15 Hard cantilever with a resonant frequency of 325 kHz and

a force constant of 40 N/m. The nanoparticles size and surface roughness were measured with specific software, WinSPM 2.0 produced by Jeol Company, Japan, according to the procedures previously described in literature [49, 50].

Antimicrobial activity evaluation of the GV-AgNPs

Antimicrobial diffusion test. *Staphylococcus aureus* ATCC 25923, *Escherichia coli* ATCC 25922, *Pseudomonas aeruginosa* ATCC 27853, *Enterococcus faecalis* ATCC 29212 and *Candida albicans* ATCC 10231 from Microbiology Lab (Faculty of Biology and Geology, UBB, Cluj-Napoca) were used in this research. Bacterial strains were cultivated on Nutrient Agar, while *Candida* was grown on Sabouraud Agar medium [51]. Then the bacterial culture was suspended in saline on 0.5 McFarland turbidity, and it was swabbed uniformly across an agar plate (Mueller Hinton-Oxoid).

The plates were dried for 15 minutes at 37 °C. For the samples to be tested, wells were made in the culture medium with sterile tips of 5 mm diameter. Then, in these wells, sterile cotton swabs were placed. Out of the tested samples (E = GV-extract, N = GV-AgNPs) 100 µL were placed in each well. CN10 = gentamicin (for bacterial strains) and VOR1 = voriconazole (for *Candida* strain) were used as control. The incubation time was 48 hours at 37 °C. The reading was made by measuring the diameter of the zone of inhibition that appeared around the well with the sample on the culture medium: the larger the diameter of the zone of inhibition, the greater the sensitivity of the bacteria to the respective antibacterial substances [52].

ACKNOWLEDGMENTS

The authors thank to dr. I. L. Szigyarto and dr. M. Puşcaş for *Galium verum* L. identification.

REFERENCES

1. K. K. Harish; N. Venkatesh; H. Bhowmik; A. Kuila; *Biomed. J. Sci. Tech. Res.*, **2018**, 4, 3765-3775
2. S. Padalkar; J. R. Capadona; S. J. Rowan; C. Weder; Y. H. Won; L. A. Stanciu; R. J. Moon; *Langmuir*, **2010**, 26, 8497-8502
3. K. S. B. Naidu; P. Govender; J. K. Adam; *J. Pure Appl. Microbiol.*, **2015**, 9, 103-112
4. X. Y. Dong; Z. W. Gao; K. F. Yang; W. Q. Zhang; L. W. Xu; *Catal. Sci. Technol.*, **2015**, 5, 2554–2574

5. R. Abbas; J. Luo; X. Qi; A. Naz; I. A. Khan; H. Liu; S. Yu; J. Wei; *Nanomaterials*, **2024**, *14*, 1425
6. A. Jamaludin; C. K. Faizal; *Indian J. Sci. Technol.*, **2017**, *10*, 1-5
7. P. Chen; L. Song; Y. Liu; Y. E. Fang; *Radiat. Phys. Chem.*, **2007**, *76*, 1165–1168
8. M. Andersson; J. S. Pedersen; A. E. C. Palmqvist; *Langmuir*, **2005**, *21*, 11387–11396
9. R. A. Khaydarov; R. R. Khaydarov; O. Gapurova; Y. Estrin; T. Scheper; *J. Nanopart. Res.*, **2009**, *11*, 1193–1200
10. H. Wang; X. Qiao; J. Chen; S. Ding; *Colloids Surf. A: Physicochem. Eng. Asp.*, **2005**, *256*, 111–115
11. A. Pyatenko; K. Shimokawa; M. Yamaguchi; O. Nishimura; M. Suzuki; *Appl. Phys. A.*, **2004**, *79*, 803–80
12. A. Pal; S. Shah; S. Devi; *Mater. Chem. Phys.*, **2009**, *114*, 530–532
13. R. F. Elsupikhe; M. B. Ahmad; K. Shameli; N. A. Ibrahi; N. Zainuddin; *IEEE Trans. Nanotechnol.*, **2016**, *15*, 209–213
14. P. Khandel, P; R. K. Yadav; D. K. Soni; L. Kanwar; S. K. Shahi; *J. Nanostruct. Chem.*, **2018**, *8*, 217-254
15. S. C. Jain; M. S. Mehata; *Sci. Rep.*, **2017**, *7*, 15867
16. L. Wang; Y. Wu; J. Xie; S. Wu; Z. Wu; *Mater. Sci. Eng. C.*, **2018**, *86*, 1-8
17. J. Bradic; A. Petkovic; M. Tomović; *Serb. J. Exp. Clin. Res.*, **2018**, *22*, 187-193
18. I. T. Vasilevna; G. O. Volodymyrivna; T. E. Leonidivna; K. I. Aleksandrovna; K. A. Mihaylovna; *Pharmacogn. Commn.*, **2016**, *6*, 42-47
19. P. -R. Laanet; P. Saar-Reismaa; P. Jõul; O. Bragina; M. Vaher; *Molecules*, **2023**, *28*, 2867
20. J. Bradic; V. Zivkovic; I. Srejavic; V. Jakovljevic; A. Petkovic; T. N. Turnic; J. Jeremic; N. Jeremic; S. Mitrovic; T. Sobot; N. Ponorac; M. Ravic; M. Tomovic; *Oxid. Med. Cell. Longev.*, **2019**, 4235405
21. M. Schmidt; C. J. Scholz; G. L. Gavril; C. Otto; C. Polednik; J. Roller; R. Hagen; *Int. J. Oncol.*, **2014**, *44*, 745-760
22. L. Ö. Demirezer; F. Gürbüz; Z. Güvenalp; K. Ströch; A. Zeeck; *Turk. J. Chem.*, **2006**, *30*, 525-534
23. C. C. Zhao; J. H. Shao; X. Li; X. D. Kang; Y. W. Zhang; D. L. Meng; N. Li; *J. Asian Nat. Prod. Res.*, **2008**, *10*, 611-615
24. A. D. Farcas; A. C. Mot; C. Zagrean-Tuza; V. Toma; C. Cimpoi; A. Hosu; M. Parvu; I. Roman; R. Silaghi-Dumitrescu; *PLoS One*, **2018**, *13*, e0200022
25. L. Vlase; A. Mocan; D. Hanganu; D. Benedec; A. Gheldiu; G. Crişan; *Digest J. Nanomater. Biostruct.*, **2014**, *9*, 1085-1094
26. P. Mulvaney; *Langmuir*, **1996**, *12*, 788–80
27. C. Ozdemir; M. Gencer; I. Coksu; T. Ozbek; S. Derman; *Arh. Hig. Rada Toksikol*, **2023**, *74*, 90-98
28. M. Ndikau; N. M. Noah; D. M. Andala; E. Masika; *Int. J. Anal. Chem.*, **2017**, 8108504
29. S. Ansar; H. Tabassum; N. S. M. Aladwan; M. N. Ali; B. Almaarik; S. AlMahrouqi; M. Abudawood; N. Banu; R. Alsubki; *Sci. Rep.*, **2020**, *10*, 18564
30. M. Vanaja; S. Rajeshkumar; K. Paulkumar; G. Gnanajobitha; C. Malarkodi; G. Annadurai; *Adv. Appl. Sci. Res.*, **2013**, *4*, 50-55

31. M. Sathishkumar; K. Sneha; Y. S. Yun; *Bioresour. Technol.*, **2010**, *101*, 7958-7965
32. S. Pugazhendhi; P. Sathya; P. K. Palanisamy; R. Gopalakrishnan; *J. Photochem. Photobiol. B*, **2016**, *159*, 155-160
33. S. Khan; S. Shujah; U. Nishan; S. Afridi; M. Asad; A. U. H. A. Shah; N. Khan; S. Ramzan; M. Khan; *Arab. J. Sci. Eng.*, **2023**, *48*, 7673–7684
34. A. D. Semenescu; E. A. Moacă; A. Iftode; C. A. Dehelean; D. S. Tchiakpe-Antal; L. Vlase; A. M. Vlase; D. Muntean; R. Chioibaş; *Molecules*, **2023**, *28*, 7804
35. J. B. Lambert; H. F. Shurvell; R. G. Cooks; *Organic Structural Spectroscopy*, Prentice-Hall Inc., New Jersey, **1998**
36. N. H. Reza zadeh; F. Buazar; S. Matroodi; *Sci. Rep.*, **2020**, *10*, 19615
37. S. Narath; S. S. Shankar; S. K. Sivan; B. George; T. D. Thomas; S. Sabarinath; S. K. Jayaprakash; S. Waclawek; V. V.T. Padil; *Ecol. Chem. Eng. S.*, **2023**, *30*, 7-21
38. A. Deep; M. Verma; R. K. Marwaha; A. K. Sharma; B. Kumari; *Curr. Cancer Ther. Rev.*, **2019**, *15*, 1-7
39. K. M. Kumar; B. K. Mandal; H. A. K. Kumar; S. B. Maddinedi; *Spectrochim. Acta A Mol. Biomol. Spectrosc.*, **2013**, *116*, 539-545
40. A. J. Kora; S. R. Beedu; A. Jayaraman; *Org. Med. Chem. Lett.*, **2012**, *2*, 17
41. A. O. Danila; F. Gatea; G. L. Radu; *Chem. Nat. Compd.*, **2011**, *47*, 22–26
42. A. O. Matei; F. Gatea; G. L. Radu; *J. Chromatogr. Sci.*, **2015**, *53*, 1147–1154
43. A. Mocan; G. Crişan; L. Vlase; B. Ivănescu; A. S. Bădărău; A. L. Arsene; *Farmacia*, **2016**, *64*, 95-99
44. N. Swilam; K. A. Nematallah; *Sci. Rep.*, **2020**, *10*, 14851
45. Q. Lin; H. Huang; L. Chen; G. Shi; *Biomed. Res.*, **2017**, *28*, 1276-1279
46. M. C. Lite; R. Constantinescu; E. C. Tănăsescu; A. Kuncser; C. Romaniţan; D. E. Mihaiescu; I. Lacatusu; N. Badea; *Materials*, **2023**, *16*, 3924
47. L. David; B. Moldovan; *Studia UBB Chemia, LXVII*, **2022**, *3*, 37-44
48. J. K. T. Al-Isawi; A. M. Mohammed; D. T. A. Al-Heetimi; *Studia UBB Chemia, LXVIII*, **2023**, *2*, 131-144
49. S. E. Avram; B. V. Birle; L. B. Tudoran; G. Borodi; I. Petean; *Water*, **2024**, *16*, 1027
50. S. E. Avram; L. B. Tudoran; S. Cuc; G. Borodi; B. V. Birle; I. Petean; *J. Compos. Sci.*, **2024**, *8*, 219
51. R. M. Atlas; *Handbook of Microbiological Media*, 4th ed., CRC Press, New York, **2010**
52. R. Carpa; M. Drăgan-Bularda; V. Muntean; *Microbiologie Generală Lucrări Practice (General Microbiology, Practical Works)*, Cluj University Press Publishing House, **2014**

DEDICATED TO THE MEMORY OF Professor RODICA MICU-SEMENIUC, whose contributions to science and education within the Faculty of Chemistry and Chemical Engineering of Babeş-Bolyai University were longstanding and far-reaching. She was, and still continues to be, an inspiration for all of us.

THE MOLECULAR AND SUPRAMOLECULAR STRUCTURE OF $\text{Mn}(4,4'\text{-DIAMINOBIPHENYL})_2(\text{NCS})_2(\text{EtOH})_2$

Radu F. SEMENIUC^{a,*} , Tiffany M. Smith PELLIZZERI^a 

ABSTRACT. The title compound was prepared from $\text{MnCl}_2 \cdot 4 \text{H}_2\text{O}$ in the presence of KSCN and 4,4'-diaminobiphenyl (DABPh), using ethanol as a solvent. The complex was thoroughly characterized by elemental analysis, IR spectroscopy, and single crystal X-ray diffraction. The coordination mode of the SCN^- anion (*i.e.* Mn – NCS vs. Mn – SCN) was investigated, and it was found that in the solid state the manganese(II) ion is coordinated by two SCN^- ligands N-bonded to the metallic center. The coordination sphere around the metal also contains two DABPh and two ethanol molecules. The supramolecular structure of the complex is held together by several O – H \cdots N and N – H \cdots S hydrogen bonds. These interactions build up a 3D grid with the Mn atoms positioned in the corners of an 8.548 Å x 13.809 Å x 14.622 Å parallelepiped.

Keywords: Manganese(II), 4,4'-diaminobiphenyl, isothiocyanate, single crystal X-ray diffraction structure, hydrogen bonds, supramolecular structure.

INTRODUCTION

Among ambidentate ligands like the cyanide, cyanate, nitrite, nitrosobenzene, 4,4'-bipyrimidine, and nicotinate species, the thiocyanate ion is one of the most studied [1]. Considering the coordination patterns of the $[\text{NCS}]^-$

^a Department of Chemistry and Biochemistry Eastern Illinois University, 600 Lincoln Ave, Charleston, IL 61920, USA

* Corresponding author: rsemeniuc@eiu.edu



anion, hard metals tend to form N-bonded complexes (isothiocyanates), while soft metal ions prefer the S-coordination mode (thiocyanates). Illustrating these different bonding modes, $K_2[Co(NCS)_4] \cdot H_2O \cdot 2 CH_3NO_2$ [2], $[Mn(py)_4(NCS)_2]$ [3], $Ba[Co(NCS)_4] \cdot 7 H_2O$ [4], and $Ni(NCS)_2(Py)_4$ [5] are typical examples for N-coordination, while the octahedral $(Ph_4P)_3[Rh(SCN)_6]$ [6] and $(Me_4N)_3[Ir(SCN)_6]$ [7], square planar $(n-Bu_4N)_2[M(SCN)_4]$ ($M = Pd, Pt$ [8]), and tetrahedral $K_2[Hg(SCN)_4]$ [9] illustrate the S-coordination of the NCS^- moiety to the metallic center. On another hand, the structures of $(n-Bu_4N)_2[Re(NCS)_6]$ [10] and $[Ph_2P(n-Pr)NMe_2]Pd[(NCS)(SCN)]$ [11] feature linkage isomerism, where both the SCN^- and NCS^- coordination modes were encountered.

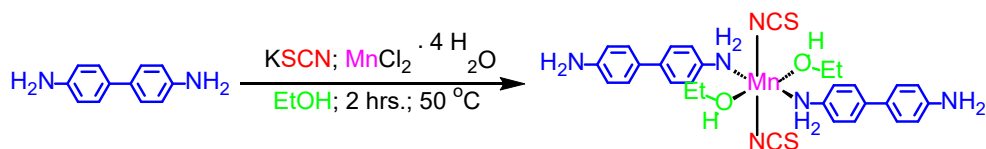
The IR spectra of these species can provide some insight into the coordination mode of the anion to the metallic center. This can be investigated by identifying the position of the C–N stretching vibration, where a band about 2060 cm^{-1} indicates an N-coordination (M–NCS), while a band around 2100 cm^{-1} and above suggests an S-coordination (M–SCN) of the ligand to the metal center [12–14]. However, it has been suggested that the coordination mode of the SCN^- ligand to the metal might be influenced by the anion concentration in solution [14].

In the early 1970's, Macarovici and Micu-Semeniuc studied metal complexes of the type $[MnL_2(NCX)_2]$, $[MnL_1(NCX)_2]$, $[Mn(L_2)_3(NCX)_2]$, and $[Mn(L_3)_3(NCX)_2]$ ($X = S, Se$; L, L_1 , and $L_2 = 2,2'$ -, $3,3'$ -, and $4,4$ -diaminobiphenyl, respectively, and $L_3 = \text{bis}(p\text{-aminophenyl})\text{methane}$) [15]. The complexes were characterized by IR, reflection spectra and magnetic susceptibility, and based on those studies, it was proposed that all complexes were six-coordinated. Regarding their structures, it was suggested that the compounds based on the $2,2'$ - and $4,4'$ -diaminobiphenyl ligands were discrete species, while those incorporating the $3,3'$ -derivative were polymeric. In this work, we revisit the synthesis and characterization of the manganese(II) complex bearing two $4,4'$ -diaminobiphenyl ($4,4'$ -DABPh), two SCN^- , and two EtOH ligands, in an attempt to definitely establish the coordination mode of the SCN^- group to the metal. In addition, given the bridging nature of the $4,4'$ -DABPh ligand, we also wanted to determine if the compound is a discrete species or a coordination polymer.

RESULTS AND DISCUSSION

The reaction of 4 $4'$ -diaminobiphenyl, manganese(II) chloride and potassium thiocyanate in ethanol yielded the corresponding metal complex $Mn(4,4'$ -DABPh) $_2(NCS)_2(EtOH)_2$ as a light, air, and moisture stable species, as pictured in Scheme 1.

THE MOLECULAR AND SUPRAMOLECULAR STRUCTURE OF $\text{Mn}(4,4'$ -
DIAMINOBIHENYL) $_2(\text{NCS})_2(\text{EtOH})_2$



Scheme 1. Synthesis of $\text{Mn}(4,4'$ -DABPh) $_2(\text{NCS})_2(\text{EtOH})_2$.

The complex is soluble in various organic solvents, but not in diethyl ether and hexanes. Its composition and structure have been established based on its analytical, spectral, and single-crystal X-ray diffraction data. Analytical data showed a metal to ligands ratio of 1 : 2 : 2 : 2. The IR spectrum of the complex recorded in a KBr matrix is typical for these types of compounds, with no unusual features. Of note however, are the characteristic CN and CS stretching and NCS bending vibrations of the SCN^- group, appearing at 2065, 821, and 478 cm^{-1} , respectively. This data implies that the Mn(II) ion is coordinated by the SCN^- group through its N atom.

Definite proof of the structure of the metal complex, and especially of the coordination mode of the SCN^- moiety, came from X-ray crystallographic studies. Relevant crystal data and structure refinement details are provided in the experimental section. Selected bond lengths and bond angles are given in Table 1 and the structure is pictured in Figure 1. The molecule consists of one manganese(II) cation coordinated by two 4,4'-DABPh and two EtOH ligands. The neutrality of the complex is ensured by the two N-bonded SCN^- anions. The bond lengths and bond angles fall within the normal range found for these types of compounds.

Table 1. Selected bond lengths [Å] and angles [°] for $\text{Mn}(4,4'$ -DABPh) $_2(\text{NCS})_2(\text{EtOH})_2$.

Mn1-O1	2.165(2)	N1-C1	1.154(4)
Mn1-N1	2.173(3)	S1-C1	1.646(4)
Mn1-N2	2.294(3)	O1-H1	0.844(19)
N2-H2A	0.964(19)	N2-H2B	0.967(18)
O1-Mn1-O1#1	180.00(13)	N1-Mn1-N1#1	180.0
N2-Mn1-N2#1	180.00(12)	N1-Mn1-N2	89.74(11)
N1#1-Mn1-N2	90.26(11)	N1#1-Mn1-N2#1	89.74(11)
O1-Mn1-N1	88.52(10)	O1-Mn1-N2	91.45(9)
O1-Mn1-N1#1	91.48(10)	O1#1-Mn1-N1#1	88.52(10)
O1#1-Mn1-N1	91.48(10)	O1#1-Mn1-N2	88.55(9)
O1-Mn1-N2#1	88.55(9)	O1#1-Mn1-N2#1	91.45(9)
N1-Mn1-N2#1	90.26(11)	N1-C1-S1	179.2(3)

Symmetry transformations used to generate equivalent atoms:

#1: -x+1, -y+1, -z+1

All ligands are positioned in a *trans* orientation around the Mn²⁺ ion, with an overall D_{4h} geometry of the MnN₄O₂ skeleton. The Mn1-O1, Mn1-N1, and Mn1-N2 bond lengths are 2.165(2) Å, 2.173(3) Å, and 2.294(3) Å, and the N1-Mn1-N2, O1#1-Mn1-N1, and O1-Mn1-N2#1 angles are 89.74(11)°, 91.48(10)°, and 88.55(9)°, respectively. Given these values, the geometry around the manganese(II) center can be described as a slightly distorted octahedron.

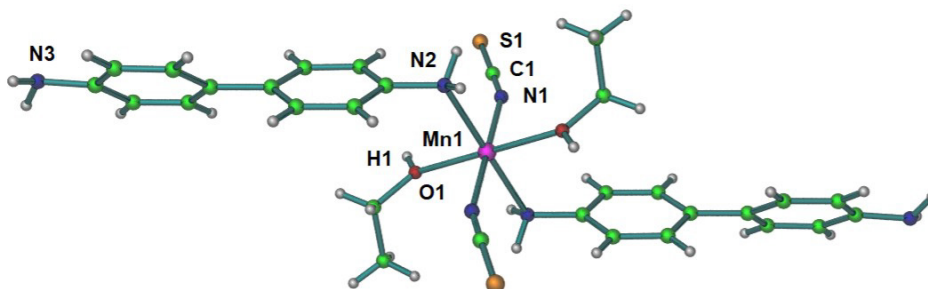


Figure 1. The molecular structure of the Mn(4,4'-DABPh)₂(NCS)₂(EtOH)₂ complex.

The (S)C-N-M angle is another geometrical parameter of interest. Coordination of the ligand through either the nitrogen or sulfur atoms occurs at various bonding angles [16]. In the case of isothiocyanates, the (S)C-N-M angle is closer to 180°, whereas for thiocyanates, the (N)C-S-M angle is usually found to be around 100°. These differences between the C-N-M and C-S-M bonding angles were observed for both terminal and bridging groups. In the case of Mn(4,4'-DABPh)₂(NCS)₂(EtOH)₂, the C-N-M angle was found to be 158.1(3)°, as observed with other compounds where the SCN⁻ species acted as a N-bonded ligand.

The supramolecular structure of the complex consists of chain-like architectures, held together by O – H ⋯ N and N – H ⋯ S hydrogen bonds [17], as shown in Figure 2. The ethanolic -OH functional group is involved in a close contact with the N3 atom positioned on a neighboring molecule, as seen in Figure 2a. On another hand, there are several N – H ⋯ S contacts involving the amine groups on the 4,4'-DABPh donor set and the S atom of the SCN⁻ anion, as depicted in Figure 2b-e. The geometrical parameters for these interactions are listed in Table 2. These distances are well below the sum of the van der Waals radii for hydrogen and nitrogen or hydrogen and sulfur, and the donor – hydrogen – acceptor angles are all above 140°, a clear indication of the formation of these hydrogen bonds [18].

THE MOLECULAR AND SUPRAMOLECULAR STRUCTURE OF $\text{Mn}(4,4'$ -
DIAMINOBIHENYL) $_2(\text{NCS})_2(\text{EtOH})_2$

Table 2. Geometrical parameters associated with the O – H \cdots N and N – H \cdots S hydrogen bonds.

Atoms	H \cdots A distance (Å)	D \cdots A distance (Å)	D – H – A angle (°)
O1 – H1 \cdots N3	1.970	2.805	169.94
N2 – H2A \cdots S1	2.521	3.392	150.35
N2 – H2B \cdots S1	2.581	3.522	165.49
N3 – H4A \cdots S1	2.512	3.403	169.41
N3 – H4B \cdots S1	2.794	3.572	147.58

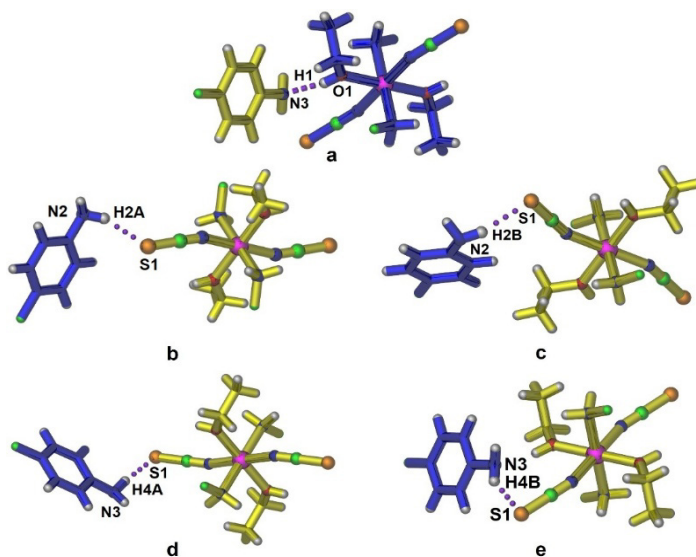


Figure 2. Details of the a) O – H \cdots N and b-e) N – H \cdots S hydrogen bonds in $\text{Mn}(4,4'$ -DABPh) $_2(\text{NCS})_2(\text{EtOH})_2$.

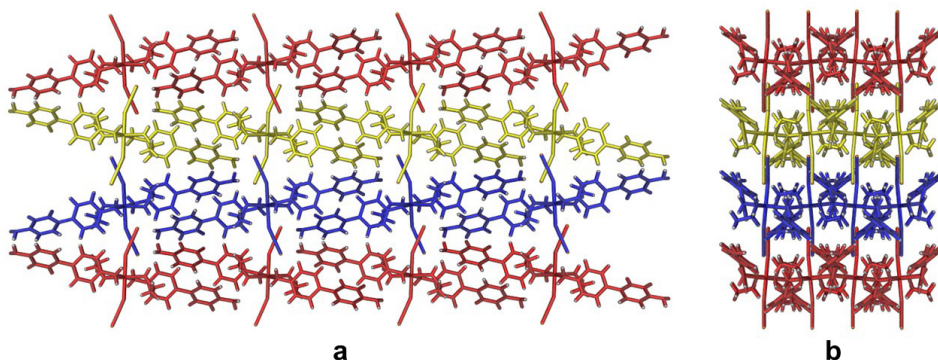


Figure 3. The crystal packing of the $\text{Mn}(4,4'$ -DABPh) $_2(\text{NCS})_2(\text{EtOH})_2$ complex: a) along the *b* axis of the unit cell; b) along the *c* axis of the unit cell.

The O – H \cdots N interactions build up 1D chains along the *c* axis of the unit cell, and the N – H \cdots S contacts extend the supramolecular structure into a 3D array along the *b* axis of the unit cell, as pictured in Figure 3. Within this framework, the manganese(II) ions are positioned at 13.81 Å, 8.12 Å, and 14.62 Å apart, thus generating a grid-like array of the metallic centers, as seen in Figure 4.

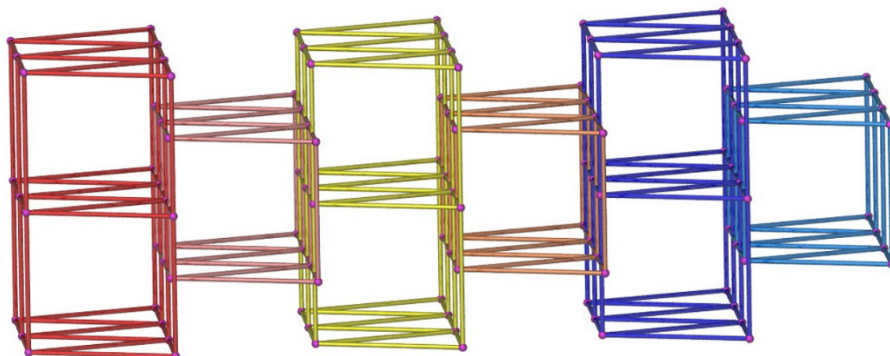


Figure 4. The grid-like arrangement of the manganese(II) cations in the $\text{Mn}(4,4'\text{-DABPh})_2(\text{NCS})_2(\text{EtOH})_2$ complex.

Comparing the structure described here with similar ones found in the literature, such as bis(4,4'-diaminodiphenylmethane)-diaqua-dichloro-Mn(II) [19] (see Figure 5) it can be seen that there are obvious structural differences between their molecular structures, with the latter complex having an overall D_{2h} geometry of the $\text{MnN}_2\text{O}_2\text{Cl}_2$ skeleton. However, there are some interesting similarities between their supramolecular structures, originating from the O – H \cdots Cl and N – H \cdots Cl hydrogen bonds, pictured in Figure 5 as dotted and dashed lines. In both compounds the building blocks are organized by these non-covalent interactions into three-dimensional architectures. The geometrical parameters associated with these interactions in bis(4,4'-diaminodiphenylmethane)-diaqua-dichloro-Mn(II) are listed in Table 3.

Table 3. Geometrical parameters associated with the O – H \cdots Cl and N – H \cdots Cl hydrogen bonds.

Atoms	H \cdots A distance (Å)	D \cdots A distance (Å)	D – H – A angle (°)
O1w – H1w2 \cdots Cl	2.164	3.116	165.22
N1 – H1B \cdots Cl	2.880	3.654	144.97

THE MOLECULAR AND SUPRAMOLECULAR STRUCTURE OF $\text{Mn}(4,4'$ -DIAMINOBIPHENYL) $_2(\text{NCS})_2(\text{EtOH})_2$

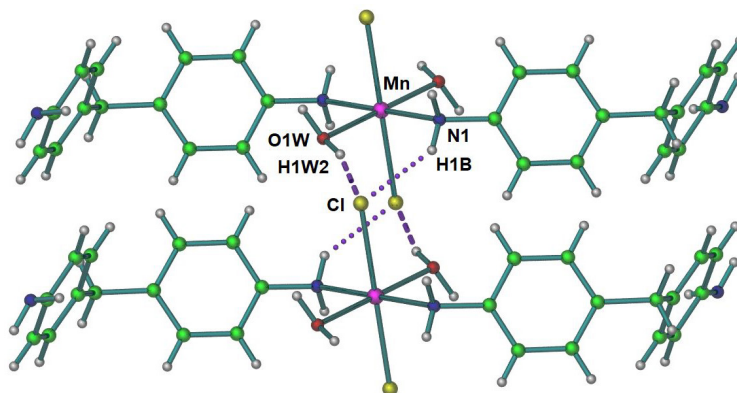


Figure 5. The structure of bis(4,4'-diaminodiphenylmethane)-diaqua-dichloro-Mn(II), and details of the O – H \cdots Cl and N – H \cdots Cl hydrogen bonds.

CONCLUSIONS

The reaction of 4 4'-DABPh, Mn(II) chloride and KSCN produced the $\text{Mn}(4,4'$ -DABPh) $_2(\text{NCS})_2(\text{EtOH})_2$ complex. The characteristic CN and CS stretching and NCS bending vibrations of the SCN^- group, were identified at 2065, 821, and 478 cm^{-1} , respectively. Structural studies showed that the molecule consists of one manganese(II) cation coordinated by two 4,4'-DABPh, two N-bonded SCN^- anions, and two EtOH ligands. All these ligands are positioned in a *trans* orientation around the Mn^{2+} ion, with an overall D_{4h} geometry of the MnN_4O_2 skeleton. The $\text{Mn}(4,4'$ -DABPh) $_2(\text{NCS})_2(\text{EtOH})_2$ molecules are associated into a three-dimensional grid-like supramolecular array by O – H \cdots N and N – H \cdots S hydrogen bonds.

EXPERIMENTAL SECTION

General information. All operations were performed in an ambient atmosphere. Infrared spectroscopy was performed on a Nicolet iS10 in a KBr matrix. All the reagents and solvents used in the synthesis described below are commercially available (Sigma-Aldrich and Oakwood) and used without further purification. Thiocyanate salts are harmful if swallowed or inhaled and can cause irritation to skin, eyes, and respiratory tract.

Synthesis of $\text{Mn}(4,4'$ -DABPh) $_2(\text{NCS})_2(\text{EtOH})_2$. A 100 mL flask was charged with a stirring bar, 4 4'-diaminobiphenyl (0.184 g, 1 mmol) and 50 mL ethanol. To this solution was added $\text{MnCl}_2 \cdot 4 \text{H}_2\text{O}$ (0.099 g, 0.5 mmol)

and KSCN (0.097 g, 1 mmol). The clear solution was stirred for two hours at 50° C. The solution was then filtered to remove any solid impurities, transferred into a 100 mL beaker and loosely covered with aluminum foil. Over three days, slow evaporation of this solution afforded the title compound as single crystals. Yield of the crystalline material 0.137 g (43.4 %). If desired, more material can be isolated by completely removing the solvent. The crystalline material obtained as described above was used in all subsequent experiments. Anal. Calcd. (%) for $C_{30}H_{36}MnN_6O_2S_2$: C, 57.04; H, 5.74; N, 13.30; found C, 57.34; H, 5.44; N, 13.68; selected IR (KBr matrix, cm^{-1}): CN stretch 2065 (s), CS stretch 821 (m), NCS bend 478 (w).

Crystallographic studies. A specimen of $Mn(4,4'-DABPh)_2(NCS)_2 \cdot (EtOH)_2$ ($C_{30}H_{36}MnN_6O_2S_2$, 0.240 mm x 0.350 mm x 0.420 mm) was used for the X-ray crystallographic analysis. The X-ray intensity data were measured using a Bruker Smart Apex 2 diffractometer with $CuK\alpha$ radiation ($\lambda = 1.54178 \text{ \AA}$) and a temperature of 100K. The Apex 3 software suite was used for data collection, data processing (SAINT), scaling, and absorption correction (SADABS, multi-scan) [20]. The space group of the structure was determined using XPREP, the structure solution was found by using the intrinsic phasing method (SHELXT), and the structure was refined by full-matrix least-squares methods on F^2 (SHELXL), which are all a part of the Bruker SHELXTL Software Package [21]. All non-hydrogen atoms were refined anisotropically, while hydrogen atoms were placed in calculated positions using appropriate riding models.

The integration of the data using an orthorhombic unit cell yielded a total of 20296 reflections to a maximum θ angle of 64.38° (0.85 Å resolution), of which 2726 were independent (average redundancy 7.445, completeness = 99.1%, $R_{int} = 3.45\%$, $R_{sig} = 2.06\%$) and 2575 (94.46%) were greater than $2\sigma(F^2)$. The final cell constants of $a = 13.8088(2) \text{ \AA}$, $b = 8.54780(10) \text{ \AA}$, $c = 27.9659(4) \text{ \AA}$, volume = $3300.95(8) \text{ \AA}^3$, are based upon the refinement of the XYZ-centroids of reflections above $20 \sigma(I)$. The calculated minimum and maximum transmission coefficients (based on crystal size) are 0.8240 and 1.0000.

The structure was refined using the space group $Pbca$, with $Z = 4$ for the formula unit, $C_{30}H_{36}MnN_6O_2S_2$. The final anisotropic full-matrix least-squares refinement on F^2 with 203 variables converged at $R1 = 4.79\%$ [22], for the observed data and $wR2 = 10.80\%$ [23] for all data. The goodness-of-fit was 1.307. The largest peak in the final difference electron density synthesis was $0.358 e^{-}/\text{\AA}^3$ and the largest hole was $-0.367 e^{-}/\text{\AA}^3$ with an RMS deviation of $0.066 e^{-}/\text{\AA}^3$. On the basis of the final model, the calculated density was 1.271 g/cm^3 and $F(000)$, 1324 e^{-} .

CCDC 2404484 contains the supplementary crystallographic data for Mn(4,4'-DABPh)₂(NCS)₂(EtOH)₂ described in this paper. The data can be obtained free of charge from the Cambridge Crystallographic Data Centre via www.ccdc.cam.ac.uk/data_request/cif.

ACKNOWLEDGMENTS

The authors thank Eastern Illinois University for financial support through a Council on Faculty Research grant.







REFERENCES

1. J. Burmeister, *Coord. Chem. Rev.* **1990**, *105*, 77-133.
2. J. S. Wood, R. K. McMullan, *Acta Cryst.*, **1984**, *C40*, 1803-1806.
3. C. Wellm, T. Neumann, G. Gallo, A. M. Dziubyna, M. Rams, R. E. Dinnebier, C. Näther, *Cryst. Growth Des.*, **2020**, *20*, 3374-3385.
4. K. Mereiter, A. Preisinger, *Acta Cryst.*, **1988**, *C44*, 1178-1181.
5. C.-F. Wang, Z.-Y. Zhu, X.-G. Zhou, L.-H. Weng, Q.-S. Shen, Y.-G. Yan, *Inorg. Chem. Commun.*, **2006**, *9*, 1326-1330.
6. J.-U. Vogt, O. Haeckel, W. Preetz, *Z. Anorg. Allg. Chem.*, **1995**, *621*, 1033-1036.
7. J.-U. Rohde, W. Preetz, *Z. Anorg. Allg. Chem.*, **1998**, *624*, 1319-1323.
8. J.-U. Rohde, B. von Malottki, W. Preetz, *Z. Anorg. Allg. Chem.*, **2000**, *626*, 905-910.
9. J. Bandemehr, M. Conrad, F. Kraus, *Acta Cryst. E.*, **2017**, *73*, 1073-1075.
10. R. González, N. Barboza, R. Chiozzzone, C. Kremer, D. Armentano, G. De Munno, J. Faus, *Inorg. Chim. Acta.*, **2008**, *361*, 2715-2720.
11. G. J. Palenik, G. R. Clark, *Inorg. Chem.*, **1970**, *9*, 2754-2760.
12. K. Nakamoto, *Infrared and Raman Spectra of Inorganic and Coordination Compounds: Part B: Applications in Coordination, Organometallic, and Bioinorganic Chemistry*, 6th ed., John Wiley & Sons, Inc.
13. A. Sabatini, I. Bertini, *Inorg. Chem.*, **1965**, *4*, 959-961.
14. Yu. V. Matveichuk, E. M. Rakhman'ko, and V. V. Yasinetskii, *Russ. J. Inorg. Chem.*, **2015**, *60*, 100-104.
15. C. Gh. Macarovici, R. Micu-Semeniuc, *Rev. Roum. Chim.*, **1971**, *16*, 1367-1376.
16. M. Kabesova, J. Gazo, *Chem. Papers*, **1980**, *34*, 800-841.
17. R. S. Rowland, Robin Taylor, *J. Phys. Chem.* **1996**, *100*, 7384-7391.
18. T. Steiner, *Angew. Chem. Int. Ed.* **2002**, *41*, 48-76.
19. L. Carlucci, G. Ciani, D. M. Proserpio, F. Porta, *CrystEngComm* **2006**, *8*, 696-706.
20. *APEX 3*, v2017.3; Bruker-AXS Inc.: Madison, WI, **2017**.
21. Sheldrick, G. M. *Acta Crystallogr., Sect. C: Struct. Chem.*, **2015**, *71*, 3-8.

22. $R_1 = \frac{\sum |F_o| - [F_c]}{\sum |F_o|}$

23. $wR_2 = \{\sum [w(F_o^2 - F_c^2)^2] / \sum [wF_o^2]\}^{1/2}$

EVALUATION OF FERROCENYLMETHYLNUCLEOBASES DERIVATIVES INTERACTING WITH DNA: INSIGHTS FROM ELECTROCHEMICAL, SPECTROSCOPIC, DFT CALCULATION, MOLECULAR DOCKING AND MOLECULAR DYNAMIC SIMULATIONS

Mohammed Larbi Ben AMOR^{a,b}, Elhafnaoui LANEZ^{a,c,*} ,
Yahia BEKKAR^a , Aicha ADAIKA^a , Touhami LANEZ^a ,
Kaouther NESBA^d , Lazhar BECHKI^{e,f} 

ABSTRACT. This study investigates the binding of ferrocenylmethyl nucleobase derivatives to DNA through electrostatic interactions, employing a combination of experimental and theoretical approaches to elucidate binding mechanisms and explore their potential for DNA targeting. UV–Vis spectroscopy and cyclic voltammetry (CV) were used to evaluate binding affinities and structural alterations in DNA. The derivatives exhibited DNA interactions, evidenced by negative formal potential shifts in CV data. Binding constants and free binding energies derived from docking simulations aligned well with UV–Vis and CV analyses. Additionally, voltammetric data provided insights into the binding site size. Molecular docking simulations confirmed the critical role of electrostatic interactions in the binding of FcMeCy, FcMeTh,

-
- ^a *University of El Oued, Faculty of exact Sciences, Department of Chemistry, VTRS Laboratory, B.P.789, 39000, El Oued, Algeria*
^b *University of El Oued, Faculty of Technology, Department of Process Engineering and Petrochemical, P.O. Box 789, El Oued 39000, Algeria*
^c *University of El Oued, Faculty of Biology, Department of Cellular and Molecular Biology, 39000, El Oued, Algeria*
^d *University of El Oued, Faculty of Arts and Languages, Department of English Language, 39000, El Oued, Algeria*
^e *Kasdi Merbah University, Faculty of Mathematics and Material Sciences, Department of Chemistry, 30000, Ouargla, Algeria*
^f *Kasdi Merbah University, VPRS Laboratory, Department of Chemistry, Faculty of Mathematics and Material Sciences, 30000 Ouargla, Algeria*
* *Correspondent author e-mail: yahia-bekkar@univ-eloued.dz*



and (FcMe)₂Ad to DNA. Molecular dynamics simulations further revealed the stability of DNA-ligand complexes, with RMSD and radius of gyration (Rg) analyses indicating compact and stable DNA structures, emphasizing the robustness of these interactions for therapeutic applications. Theoretical investigations, including geometry optimization, Mulliken charge distribution, molecular electrostatic potential (MEP) analysis, and HOMO-LUMO surface analysis using density functional theory (B3LYP/aug-cc-pVTZ/6-311++G(d,p)), offered deeper insights into structural properties, reactive sites, and chemical reactivity. These results provide a comprehensive understanding of the interaction mechanisms and potential applications of these derivatives.

Keywords: *Ferrocene Nucleobase, Molecular dynamic simulation, Molecular docking, DFT*

INTRODUCTION

DNA functions as a template for protein synthesis, and its interactions with pharmacological agents can modulate protein replication, offering potential therapeutic strategies for cancer treatment [1,2]. Small molecules, including organometallic compounds, interact with cellular DNA, inducing damage either through direct interaction or by inhibiting enzymes responsible for maintaining DNA integrity [3–5]. Organometallic compounds that target DNA non-specifically, like cisplatin, are widely recognized as potent and successful anticancer drugs [6]. Since the late 1970s, ferrocene derivatives have been developed and investigated for their anticancer properties [7–11]. These derivatives are considered promising candidates due to their unique electrochemical characteristics and their capacity for robust interactions with DNA. Their effectiveness as anticancer agents have been demonstrated in various cancer cell lines, including those associated with breast cancer [12,13]. Over the past decade, significant research has focused on the chemistry of metal compounds and their interactions with DNA, aiming to enhance our understanding of their biological properties [14,15]. A number of these compounds have shown considerable biological activity when compared to standard pharmaceuticals [16–18].

Grasping the intricacies of the binding mechanisms and the variables that impact the affinity of these compounds for DNA is vital for creating and advancing effective agents that target DNA. This research aims to investigate the electrostatic binding interactions of N1-ferrocenylmethylcytosine (FcMeCy), N1-ferrocenylmethylthymine (FcMeTh), and N6,9-bis(ferrocenylmethyl)adenine ((FcMe)₂Ad) with chicken blood DNA (CB-DNA) through an integrated approach involving both theoretical and experimental methods. Techniques such as

UV–Vis spectroscopy and cyclic voltammetry (CV), alongside theoretical approaches including molecular docking, molecular dynamics simulations (MDS), and density functional theory (DFT), were employed to clarify the binding mechanisms and assess the capacity of these derivatives as DNA-targeting agents.

The findings demonstrate that all three compounds display a binding affinity for double-helical DNA via electrostatic interactions. Detailed insights into the free binding energies, binding constants, and binding site sizes were obtained from both theoretical and experimental data. This study enhances our knowledge of the electrostatic interactions between DNA and ferrocenylmethyl nucleobase derivatives, providing a foundation for their potential applications in DNA sensing and drug design.

RESULTS AND DISCUSSIONS

1. Cyclic Voltametric Studies

Figure S1 presents the cyclic voltametric response of 1 mM FcNB derivatives, both in the absence of and with progressively higher concentrations of CB-DNA at a bare glassy carbon electrode. The introduction of CB-DNA into the FcNB derivative solutions induced a negative shift in the anodic peak potential, along with a notable reduction in the anodic peak current density. This reduction is attributed to the formation of slowly diffusing adducts [19], which reduce the concentration of free compounds available for charge transfer reactions [20]. The observed negative shift is ascribed to the physical interaction between the FcNB derivatives and CB-DNA [21,22].

Binding constants (K_b) for the studied compounds were determined using **Equation 1**, which correlates the reduction in the anodic peak current density of the formed adducts to the free FcNB derivatives. In this equation, [DNA] is the DNA concentration, i_0 denotes the anodic peak current density in the absence of DNA and i indicates the anodic peak current density in the presence of DNA.

$$\log \frac{1}{[BSA]} = \log \frac{i}{i_0 - i} + \log K_b \quad (\text{Eq.1})$$

The binding number was determined to be 1, signifying the establishment of a 1:1 association complex between CB-DNA and the inclusion complexes [23]. K_b values for FcMeCy, FcMeTh, and (FcMe)₂Ad with CB-DNA were derived from the y-intercept of the linear plot of $\log(i/(i_0-i))$ versus $\log(1/[DNA])$ (**Figure S2**) and were calculated to be 3.25×10^4 , 4.75×10^4 , and $4.43 \times 10^4 \text{ M}^{-1}$, respectively.

The binding energies (ΔG in $\text{kJ}\cdot\text{mol}^{-1}$), as listed in **Table 1**, were calculated using **Equation 2** [11]:

$$\Delta G = -RT \ln K_b \quad (\text{Eq.2})$$

where T represents the absolute temperature equal to 301 K; R is the gas constant, $8.32 \text{ J}\cdot\text{mol}^{-1}\cdot\text{K}^{-1}$.

Table 1. The linear equations of $\log(i/(i_0-i))$ versus $\log(1/[\text{DNA}])$, binding free energy and binding constant values of FcMeCy-DNA, FcMeTh-DNA, and $(\text{FcMe})_2\text{Ad}$ -DNA obtained from CV data at pH = 7.2 and T = 301 K

Adduct	Equation	R ²	K _b (M ⁻¹)	-ΔG (kJ.mol ⁻¹)
FcMeCy-DNA	y = 0.839x + 4.511	0.992	3.25 × 10 ⁴	25.755
FcMeTh-DNA	y = 0.749x + 4.677	0.967	4.75 × 10 ⁴	26.701
(FcMe) ₂ Ad-DNA	y = 0.773x + 4.646	0.947	4.43 × 10 ⁴	26.528

1.1. Ratio of binding constants

The cyclic voltammograms shown in **Figure S3** illustrate the behavior of 1 mM solutions of FcMeCy, FcMeTh, and $(\text{FcMe})_2\text{Ad}$ in the absence and presence of 30 μM CB-DNA. These voltammograms facilitate the calculation of the binding constant ratios between the reduced form of the FcNB derivatives and CB-DNA, as well as the oxidized form $[\text{FcNB}]^+$ and CB-DNA. By examining the shifts in cathodic and anodic peak potentials caused by the introduction of CB-DNA, the binding constant ratios can be deduced [24].

When the presence of DNA induces shifts in both cathodic and anodic peak potentials, the equilibria depicted in **Figure S4** can be employed [25]. **Equation 3** is derived using the Nernst equation applied to these equilibria, describing the redox interactions of the studied compounds with DNA as shown in **Figure S3**.

$$\Delta E^0 = E_f^0 - E_b^0 = E^0(\text{FcNB}) - E^0(\text{FcNB} - \text{DNA}) = 0.06 \log \frac{K_{ox}}{K_{red}} \quad (\text{Eq.3})$$

In **Equation 3**, E_0^f and E_0^b represent the formal potentials of the $\text{FcNB}^+/\text{FcNB}$ redox pair for the free and DNA-bound states, respectively. The formal potential shifts, derived from the voltammograms in **Figure S3**, are summarized in **Table 2**. The binding constant ratios were determined using **Equation 3**, incorporating ΔE^0 values from **Table 2**. These binding constant ratios, also displayed in **Table 2**, indicate that the oxidized forms of the derivatives exhibit a slightly stronger binding affinity to DNA compared to their reduced forms.

Table 2. Electrochemical data of the free and DNA-bound FcMeCy, FcMeTh, and (FcMe)₂Ad used to calculate the ratio of the binding constants

Sample code	E _{pa}	E _{pc}	E ⁰ (V)	ΔE ⁰ (V)	K _{ox} /K _{red}
FcMeCy	0.2783	0.1991	0.2387	0.0219	2.351
FcMeCy-DNA	0.2567	0.1769	0.2168		
FcMeTh	0.4708	0.3569	0.41385	0.0624	11.397
FcMeTh-DNA	0.4026	0.3004	0.3515		
(FcMe) ₂ Ad	0.5436	0.4377	0.49065	0.0626	11.508
(FcMe) ₂ Ad-DNA	0.4815	0.3746	0.42805		

1.2. Diffusion coefficients

Figure S5 illustrates the electrochemical behavior of FcMeCy, FcMeTh, and (FcMe)₂Ad at varying scan rates, revealing distinct and stable anodic peaks. The diffusion coefficients of the free and DNA-bound forms of these compounds were calculated using the Randles–Sevcik **Equation 4** [26]:

$$i = 2.69 \times 10^5 n^3/2 S C D^{1/2} \nu^{1/2} \quad (\text{Eq.4})$$

where *i* represents the peak current (A), *n* is the number of electrons transferred during oxidation, *ν* is the scan rate (V.s⁻¹), *D* is the diffusion coefficient (cm².s⁻¹), *C* is the bulk concentration (mol cm⁻³) of the electroactive species, and *S* is the electrode surface area (cm²).

The linear relationship between the square root of the scan rates and the anodic peak current density (**Figure S6**) indicates a diffusion-controlled redox process [27]. Diffusion coefficients for both the free and DNA-bound ligands were derived from the slopes of the linear regressions based on **Equation 6**. The lower diffusion coefficients observed for the DNA-bound ligands compared to the free ligands further support the formation of adducts [28] (**Table 3**).

Table 3. Diffusion constants values of the free and DNA-bound forms of FcMeCy, FcMeTh, and (FcMe)₂Ad

Adduct	Equation	R ²	D (cm ² .s ⁻¹)
FcMeCy	y = 1.369x + 1.083	0.999	3.837 × 10 ⁻⁸
FcMeCy-DNA	y = 1.083x + 2.239	0.999	2.396 × 10 ⁻⁸
FcMeTh	y = 1.312x + 0.979	0.994	3.519 × 10 ⁻⁸
FcMeTh-DNA	y = 0.591x + 0.069	0.977	7.135 × 10 ⁻⁹
(FcMe) ₂ Ad	y = 1.801x + 1.174	0.996	6.631 × 10 ⁻⁸
(FcMe) ₂ Ad-DNA	y = 1.205x + 1.359	0.987	2.966 × 10 ⁻⁸

1.3. Binding site size

The binding site size (*s*) was determined using **Equation 5** [29]:

$$\frac{c_b}{c_f} = K \left[\frac{\text{free base pairs}}{s} \right] \quad (\text{Eq.5})$$

where C_b represents the concentration of ligand-DNA bound species, C_f is the concentration of free species, K is the binding constant, and s represents the binding site size in terms of base pairs.

Taking into account the concentration of DNA in terms of nucleotide phosphate [NP], the concentration of DNA base pairs can be expressed as $([DNA]/2)$. Consequently, **Equation 5** can be reformulated as:

$$\frac{C_b}{C_f} = K \frac{[DNA]}{2s} \quad (\text{Eq.6})$$

The ratio C_b/C_f can be expressed as $(i_0 - i)/i$ [30], where i_0 and i denote the experimental peak current densities in the absence and presence of DNA, respectively. The plots of C_b/C_f versus [DNA] are depicted in **Figure S7**.

The equations derived from the linear regression analysis for FcMeCy, FcMeTh, and $(FcMe)_2Ad$ within the investigated concentration range are shown in **Table 4**, where y represents the C_b/C_f ratio and x denotes the sample concentration, expressed in μM . The small values of the binding site size further imply an electrostatic interaction between FcMeCy, FcMeTh, and $(FcMe)_2Ad$ with DNA.

Table 4. Site size values of FcMeCy, FcMeTh, and $(FcMe)_2Ad$ obtained using the Plot of C_b/C_f versus [DNA]

Adduct	Equation	R ²	s
FcMeCy-DNA	$y = 0.031x - 0.034$	0.984	0.54092
FcMeTh-DNA	$y = 0.048x - 0.089$	0.895	0.49878
$(FcMe)_2Ad$ -DNA	$y = 0.043x - 0.071$	0.950	0.51428

2. Absorption spectral study

To corroborate the findings from the voltammetry experiments, the interaction between FcNB derivatives with CB-DNA was further investigated using electronic spectroscopy (ES) titration. This method enabled the evaluation of the interaction parameters of the FcNB-DNA complexes. As depicted in **Figure S8**, the absorption spectra for a constant concentration of each FcNB derivative were recorded, both without and with increasing amounts of CB-DNA.

The absorption bands at 435.4, 436.8, and 388.6 nm for all compounds displayed a reduction in intensity (hypochromicity) as the concentration of CB-DNA increased, without any significant hypsochromic shift. This clearly indicates the formation of the FcNB-DNA adducts [31,32]. The observed hypochromicity further supports the hypothesis that the primary interaction between FcNB derivatives and double-stranded CB-DNA is predominantly electrostatic [32,33].

The binding constants of the FcNB-DNA adducts were determined using the Benesi-Hildebrand **Equation 7**, which is founded on the reduction in

absorbance noted when FcNB compounds are added to a CB-DNA solution [33,34]:

$$\frac{A_0}{A-A_0} = \frac{\varepsilon_0}{\varepsilon-\varepsilon_0} \left(1 + \frac{1}{K_b[\text{DNA}]}\right) \quad (\text{Eq.7})$$

where A_0 and A denote the absorbance of the FcNB without and with CB-DNA, respectively, ε_0 and ε are their corresponding extinction coefficients. $[\text{DNA}]$ refers to the concentration of CB-DNA, and K_b denotes the binding constant. The plots of $1/[\text{DNA}]$ vs. $A_0/(A - A_0)$ are shown in **Figure S9**.

The linear correlation coefficients in the range of 0.993–0.998 suggest a binding stoichiometry of 1:1, indicating the formation of a 1:1 association adduct between the compounds and CB-DNA [35].

The binding constants of FcNB derivatives with CB-DNA were determined by calculating the ratio of the slope to the y-intercept of the linear equation, which allowed for the derivation of binding free energies. The values obtained for FcMeCy, FcMeTh, and (FcMe)₂Ad were -24.73, -24.78, and -25.20 kJ·mol⁻¹, respectively, as presented in **Table 5**. Both spectroscopic and electrochemical analyses indicate that all FcNB derivatives can form relatively stable inclusion complexes with CB-DNA.

Table 5. The linear equations of $1/[\text{DNA}]$ versus $A_0/(A-A_0)$, binding free energy and binding constant values of FcMeCy-DNA, FcMeTh-DNA, and (FcMe)₂Ad-DNA obtained from ES data at pH = 7.2 and T = 301 K

Adduct	Equation	R ²	K _b (M ⁻¹)	-ΔG (kJ·mol ⁻¹)
FcMeCy-DNA	y = -168.768x + 3.629	0.998	2.15 × 10 ⁴	24.73
FcMeTh-DNA	y = -465.596x + 10.213	0.993	2.19 × 10 ⁴	24.78
(FcMe) ₂ Ad-DNA	y = -689.716x + 17.905	0.997	2.59 × 10 ⁴	25.20

3. Viscosity measurement

Viscosity studies complement spectroscopic methods by providing precise insights into the interaction mechanisms of small molecules with DNA [36,37]. This straightforward and highly sensitive technique can detect changes in DNA length induced by such interactions [38]. In this research, viscosity measurements were conducted to elucidate the binding modes of FcMeCy, FcMeTh, and (FcMe)₂Ad with CB-DNA. Classical intercalators like ethidium bromide (EB) typically cause a substantial increase in DNA viscosity. This effect is due to the extension of the DNA molecule as base pairs are separated at the intercalation sites, leading to an overall increase in DNA length. In contrast, interactions through electrostatic or groove binding do not alter the DNA length significantly, thus exhibiting minimal or no effect on DNA viscosity [39].

Figure 1 shows the influence of increasing concentrations of FcMeCy, FcMeTh, (FcMe)₂Ad, and EB on the viscosity of CB-DNA. The results

indicate that higher concentrations of FcMeCy, FcMeTh, and (FcMe)₂Ad do not significantly alter CB-DNA viscosity, corroborating the conclusion that these compounds bind to CB-DNA primarily through electrostatic or groove binding modes. These conclusions are further supported by the UV-Vis spectroscopy data.

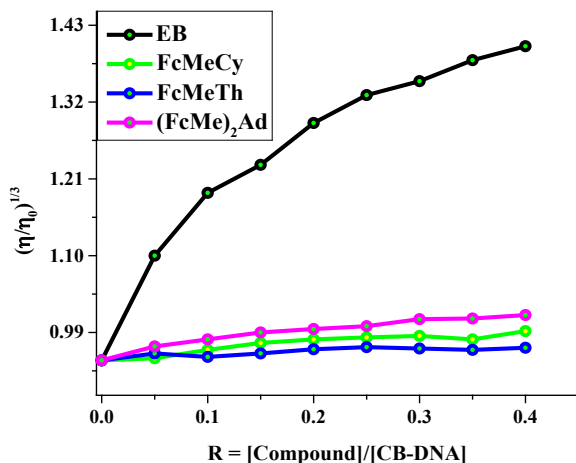


Figure 1. The effect of various concentrations of FcMeCy, FcMeTh, (FcMe)₂Ad, and EB on the viscosity of CB-DNA.

4. Theoretical approach

4.1. Structure optimization

Optimizing the structure of small molecules is essential for accurately determining their binding behavior. To elucidate this, the structures of FcMeCy, FcMeTh, and (FcMe)₂Ad were fully optimized using the DFT/B3LYP method, as detailed in the Materials and Methods Section. The optimized geometries of these compounds are depicted in **Figure S10**. This figure shows that the ferrocene portion of these molecules features a sandwich-like structure, consisting of two cyclopentadienyl rings with an Fe²⁺ ion positioned between them. As illustrated in **Figure S10**, the optimized geometry of FcMeCy and FcMeTh align well with their X-ray crystallographic structure.

4.2. MEP surface and atomic charge

The molecular electrostatic potential (MEP) surface visualizes charge distribution, identifying electron-rich (red, electrophilic sites) and electron-deficient (blue, nucleophilic sites) regions [40,41]. **Figure S11** presents the MEP maps for FcMeCy, FcMeTh, and (FcMe)₂Ad. In all cases, oxygen and

nitrogen atoms of the nucleobases exhibit negative electrostatic potential, highlighting their susceptibility to electrophilic interactions, while the ferrocene moiety remains electrostatically neutral. The MEP values range from $-2.375 \cdot 10^{-2}$ to $+2.375 \cdot 10^{-2}$ for FcMeCy, $-1.747 \cdot 10^{-2}$ to $+1.747 \cdot 10^{-2}$ for FcMeTh, and $-0.90 \cdot 10^{-2}$ to $+0.90 \cdot 10^{-2}$ for (FcMe)₂Ad.

Mulliken charge analysis further supports these findings, indicating that oxygen atoms carry negative charges, reinforcing their role in potential electrophilic interactions. The dipole moments calculated for FcMeCy, FcMeTh, and (FcMe)₂Ad were 5.773, 5.091, and 2.652 Debye, respectively.

4.3. HOMO-LUMO analysis

The HOMO-LUMO energy gap (ΔE_{L-H}) provides insights into molecular stability and reactivity [42,43]. **Figure S12** presents the HOMO-LUMO surfaces for FcMeCy, FcMeTh, and (FcMe)₂Ad, showing HOMO localization on the ferrocene moiety and LUMO association with the nucleobase group. The calculated energy gaps are 4.338 eV (FcMeCy), 4.397 eV (FcMeTh), and 4.496 eV ((FcMe)₂Ad), indicating an increasing stability trend: (FcMe)₂Ad > FcMeTh > FcMeCy. Correspondingly, chemical reactivity follows the reverse order: FcMeCy > FcMeTh > (FcMe)₂Ad.

Additional quantum descriptors (**Table 6**) reveal that FcMeTh exhibits the highest electrophilicity index ($\omega = 3.02$), indicating a greater tendency to interact with biomolecules such as DNA. The absolute electronegativity (χ) suggests that FcMeTh is the strongest Lewis acid among the three compounds. Lower chemical hardness (η) and higher softness (σ) for FcMeCy and FcMeTh indicate greater reactivity compared to (FcMe)₂Ad. These results suggest FcMeTh's strong potential for biomolecular interactions due to its higher electrophilicity and lower chemical hardness.

Table 6. The calculated quantum chemical parameter for FcMeCy, FcMeTh, and (FcMe)₂Ad using DFT

Compound	FcMeCy	FcMeTh	(FcMe) ₂ Ad
E_{HOMO}	-5.577	-5.840	-5.431
E_{LUMO}	-1.189	-1.443	-0.935
ΔE_{L-H}	4.338	4.397	4.496
χ	3.38	3.64	3.18
Π	-3.38	-3.64	-3.18
η	2.19	2.20	2.25
σ	0.46	0.45	0.44
ω	2.61	3.02	2.25
ΔN_{max}	1.54	1.66	1.42

5. Molecular docking evaluation

Molecular docking simulations are an essential tool for elucidating the interactions between small molecules and DNA at an atomic level, playing a critical role in the process of drug discovery. These simulations provide insights into the DNA-drug interaction mechanisms, thereby aiding rational drug design [44]. In this investigation, the binding sites of DNA with the compounds FcMeCy, FcMeTh, and (FcMe)₂Ad were examined to validate our experimental results and predict the interaction types within the DNA-compound system [45]. The simulations identify the most stable binding poses ($\Delta G < 0$) of these compounds when bound to a macromolecule.

Multiple docking runs were executed, revealing that the most favorable binding energies for FcMeCy, FcMeTh, and (FcMe)₂Ad with DNA were -6.77, -6.59, and -7.60 Kcal/mol, respectively. This indicates a robust interaction between DNA and (FcMe)₂Ad, following the binding strength order: (FcMe)₂Ad > FcMeCy > FcMeTh. These findings are consistent with those obtained from electronic absorption spectroscopy. As shown in **Figure S13**, FcMeCy, FcMeTh, and (FcMe)₂Ad engage with DNA through a groove binding mode, primarily facilitated by electrostatic interactions.

For FcMeCy, the interaction with DNA is characterized by: (i) a strong electrostatic attraction between the aniline group and DC9 (Electrostatic Attraction Distance, EAD = 1.911 Å), and (ii) two hydrogen bonds between DG10 and the carbonyl group (=O) (Hydrogen Bond Distances, HBD = 2.075 Å and 2.1 Å). The interaction of FcMeTh with DNA involves two hydrogen bonds between DG10 and the carbonyl group (HBD = 2.018 Å and 1.859 Å). For (FcMe)₂Ad, the interactions include: (i) a strong electrostatic attraction between DC21 and the aniline group (EAD = 1.874 Å), and (ii) a hydrogen bond between DA5 and a nitrogen atom (HBD = 2.024 Å). These interactions suggest that FcMeCy forms more extensive interactions with DNA compared to FcMeTh and (FcMe)₂Ad, which is in agreement with the global electrophilicity (ω) values. Consequently, electrostatic interactions are crucial for the binding of FcMeCy, FcMeTh, and (FcMe)₂Ad to DNA. The docking simulation results align well with those from UV-Vis and viscosity experiments, though minor discrepancies in ΔG values are attributed to the computational studies being conducted in the vacuum, while experimental measurements were performed in the solid phase [46].

6. Molecular dynamic simulation

6.1. Root mean square deviation (RMSD)

Molecular dynamics (MD) simulations were performed to evaluate the stability of the DNA-ligand complexes [47]. The optimal binding poses obtained from the docking studies served as the initial configurations for these

simulations. To examine systematic deviations over time, the root mean square deviation (RMSD) values for all complexes were calculated and plotted, as depicted in **Figure 2**.

The analysis of RMSD profiles reveals interesting stability patterns for the DNA-ligand complexes under study. FcMeCy and FcMeTh consistently maintain their binding to DNA, as indicated by their RMSD values, which remain below 2.5 Å throughout the simulation duration. This minimal deviation from the initial structure signifies a stable interaction, with the convergence of RMSD values further underscoring the robustness of these complexes (**Figure 2**). In stark contrast, the (FcMe)₂Ad complex demonstrates significant instability, with RMSD values showing significant fluctuations, reaching up to 9.78 Å over the 100 ns simulation period. This pronounced deviation highlights a lack of structural stability, suggesting that the (FcMe)₂Ad complex does not maintain a consistent binding configuration with DNA.

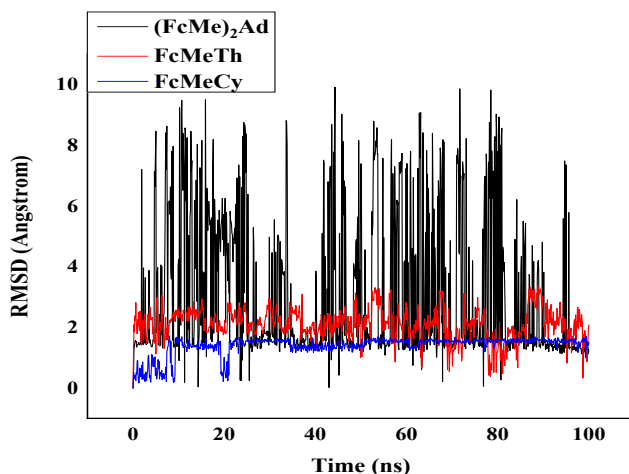


Figure 2. RMSD graphs for: FcMeCy, FcMeTh, and (FcMe)₂Ad ligands complexed with DNA during 100 ns.

6.2. Radius of gyration (Rg)

To assess the structural compactness of DNA when bound to FcMeCy, FcMeTh, and (FcMe)₂Ad, we analyzed the radius of gyration (Rg). This metric provides insights into DNA compactness, where lower Rg values indicate tighter packing, while higher values suggest potential unfolding during the simulations [48]. Throughout the simulation period, the Rg values for FcMeCy and FcMeTh complexes remained stable, ranging from 2.17 to 3.75 Å, as shown in **Figure 3**.

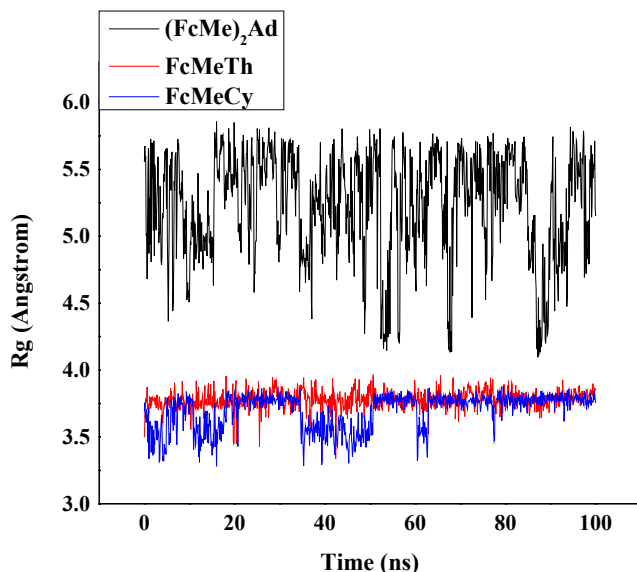


Figure 3. The Rg plots of FcMeCy, FcMeTh, and (FcMe)₂Ad complexes as a function of simulation time

This stability indicates that DNA maintains a compact conformation when interacting with these compounds. The consistent Rg values align with the RMSD results, further confirming the structural robustness of these complexes. However, the (FcMe)₂Ad complex displayed significantly higher Rg values, between 4.39 and 5.69 Å, throughout the simulation. This indicates a less compact structure and suggests that (FcMe)₂Ad induces structural changes, leading to potential unfolding or destabilization of the DNA. The elevated Rg values correspond with the higher RMSD values observed for (FcMe)₂Ad, highlighting its relative instability compared to the other two compounds.

MATERIALS AND MEASUREMENTS

1. Chemical and Reagents

Reagents and solvents used in this study were of analytical grade and sourced from various commercial suppliers, with no additional purification performed. Chicken blood samples were collected from a butcher in Eloued city using sterilized 20 ml bottles containing 2 ml of EDTA [49]. These samples were stored at 0°C and were processed for extraction within 24

hours [50]. All stock solutions were freshly prepared and utilized within five days, stored at 4 °C until needed. The phosphate buffer solution (PBS), maintaining a physiological pH of 7.2, was prepared with disodium hydrogen phosphate and sodium dihydrogen phosphate from Sigma-Aldrich, along with double-distilled water. Tetrabutylammonium tetrafluoroborate (Bu_4NBF_4) (electrochemical grade 99%; Sigma-Aldrich) served as the supporting electrolyte. Nitrogen gas, used in the experiments, was supplied from a research-grade cylinder (99.99%; Linde Gaz Algeria). All results presented in this study reflect the average of three independent experimental measurements.

2. Synthesis

N1-ferrocenylmethylcytosine (FcMeCy), N1-ferrocenylmethylthymine (FcMeTh) and N6,9-bis(ferrocenylmethyl)adenine ((FcMe) $_2$ Ad) synthesized through the reaction of the quaternary salt N,N,N-trimethylammonium-methylferrocene iodide with cytosine, thymine and adenine, respectively, following the procedure previously reported by our group [51,52]. The analytical and spectroscopic data obtained for all compounds were consistent with the proposed structures (Figure 4).

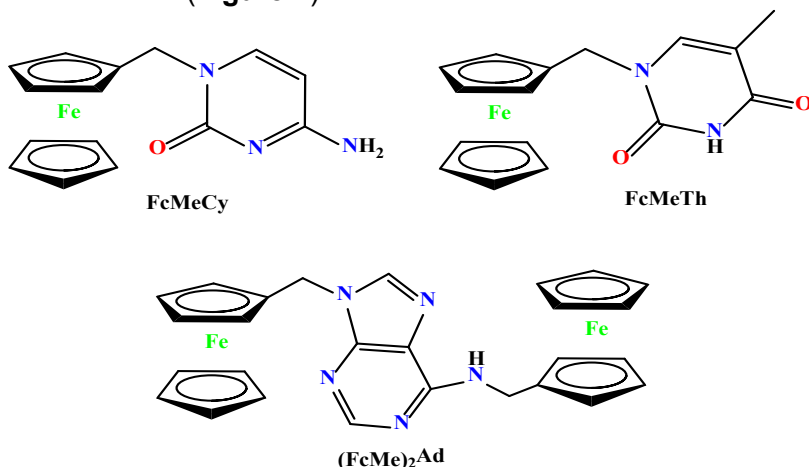


Figure 4. Structures of FcMeCy, FcMeTh, FcMeAd and (FcMe) $_2$ Ad

3. DNA Extraction

DNA was extracted from chicken blood (CB-DNA) using established protocols [53,54]. After extraction, the DNA was dissolved in a PBS at pH 7.2, diluted with 90% aqueous ethanol, and subsequently stored at 4 °C. The concentration of the DNA stock solution was determined by measuring UV absorbance at 260 nm, using a molar absorption coefficient of $6600 \text{ M}^{-1} \text{ cm}^{-1}$ [55].

The purity of the extracted DNA was verified by the absorbance ratio at 260 nm and 280 nm, which was ranged from 1.69 to 1.90, indicating minimal protein contamination [56].

To prepare 10 mM stock solutions of the compounds, each compound was accurately weighed and dissolved in 5 mL of distilled water. The solutions were buffered with a PBS (0.1 M $\text{KH}_2\text{PO}_4/\text{K}_2\text{HPO}_4$) to maintain a pH of 7.2. This buffering condition was chosen to avoid the degradation of the ferrocenium state in basic environments and to prevent the protonation of the ferrocenyl group in highly acidic conditions [57].

4. Cyclic Voltammetry Measurements

Cyclic voltammetry experiments were performed using a VoltaLab 40 (Radiometer Analytical SAS, France) linked to an electrochemical cell. This cell featured a glassy carbon electrode (area: 0.077 cm^2) as the working electrode, and a 0.5 mm thick platinum wire as the counter electrode a saturated calomel electrode as the reference electrode. Voltammograms were recorded for each compound solution, both in the absence and presence of various concentrations of CB-DNA. Prior to measurements, the solutions were purged with nitrogen gas for 15 minutes to eliminate dissolved oxygen. Between each electrochemical assay, the working electrode was meticulously cleaned and polished.

5. UV-Vis Spectroscopic Measurements

Absorption spectra were recorded using a Shimadzu 1800 UV-Vis spectrometer (Japan). Initially, the electronic spectra of 1 mM FcMeCy, FcMeTh and $(\text{FcMe})_2\text{Ad}$ were measured in a 0.1 M PBS at pH 7.2 and a temperature of 298 K. Subsequently, the spectral responses were assessed by adding gradually increasing concentrations of CB-DNA solution to the solution samples. Each sample was allowed to stabilize for at least 5 minutes before each measurement.

6. Viscosity Measurement

To corroborate the findings from absorption spectroscopy, interactions with DNA were further investigated through detailed hydrodynamic studies, specifically viscosity measurements. These investigations involved altering the concentration of the compounds while keeping the DNA concentration constant, utilizing an Ostwald viscometer. The experiments were conducted in triplicate, and the average flow time was determined using a digital stopwatch. Ethidium bromide (EB), a standard intercalator, was used as a control. The concentrations of ferrocenylmethyl nucleobase (FcNB) derivatives and EB

were varied from 0 to 24 μM , while the concentration of CB-DNA was kept constant at 0.1 mM to achieve binding ratios (R) ranging from 0.00 to 0.40 ($R = [\text{compounds}]/[\text{CB-DNA}]$). Viscosity measurements were calculated using **Equation 8**. [58,59].

$$\eta = \frac{(t-t^0)}{t^0} \quad (\text{Eq.8})$$

While t^0 represents the flow time of the pure compound and t denotes the flow time of the compound-DNA solution, where η is the viscosity of the solution. The results were plotted as $(\frac{\eta}{\eta_0})^{1/3}$ against the binding ratio R [60].

7. DFT calculation

Utilizing the density functional theory (DFT) methodology, the geometry optimization of FcNB derivatives was performed with Gauss View 6.0 for visualization and the Gaussian 09 W package [61,62]. The compounds were fully optimized using the B3LYP correlation functional, employing the aug-cc-pVTZ basis set for the iron (Fe) atom and the 6-311++G(d,p) basis set for lighter atoms such as carbon (C), hydrogen (H), nitrogen (N), and oxygen (O) [63]. All calculations were conducted in the gas phase at the ground state to determine the intrinsic electronic properties of the compounds. While DFT calculations in vacuum do not fully capture biological environments, they provide a reliable foundation for understanding fundamental electronic properties, charge distributions, and molecular reactivity. These insights serve as a basis for further computational and experimental investigations in solution-phase or biological contexts. Additionally, the study encompassed an examination of molecular electrostatic potential (MEP) surfaces, Mulliken charge distribution, and frontier molecular orbitals (FMOs) including HOMO (highest occupied molecular orbital) and LUMO (lowest unoccupied molecular orbital) surfaces. These analyses were aimed at identifying electrophilic and nucleophilic regions as well as assessing the reactivity of the compounds, all conducted under the same theoretical framework.

8. Molecular docking

8.1. Receptor preparation

A DNA segment (PDB ID: 453D) was selected for docking experiments, with its X-ray crystal structure (resolution: 1.80 Å; R-value: 0.251) obtained from the RCSB Protein Data Bank [64]. This DNA structure, which comprises the sequence 5'-D(*CP*GP*CP*GP*AP*AP*TP*TP*CP*G-P*CP*G)-3', was

originally complexed with benzimidazole. To prepare the DNA segment for docking studies, benzimidazole and all water molecules were eliminated from the protein using AutoDock Tools 1.5.6 (ADT) software [65]. Although DNA in solution exhibits dynamic flexibility, the selected structure provides a reasonable approximation for studying molecular interactions, as supported by previous studies [66–69].

8.2. Structural optimization

The 3-dimensional structures of the ligands were constructed initially, and the most stable conformer of each was identified using Spartan software [70] with the semiempirical PM6 method [71]. Subsequently, the optimal conformer for each ligand was refined using density functional theory (DFT) with the B3LYP/6-311++G(d,p) method, which includes dispersion interactions [72], implemented in Gaussian software. This approach was selected based on prior benchmark studies of ferrocene derivatives conducted by our research group [49,50]. The optimized structures of all ligands were saved in pdb format. All iron atoms coordinated within the ferrocene moiety in this study were maintained in the +1-oxidation state.

8.3. Docking simulations

The ADT software [65] was utilized to prepare docking input files for each ferrocene derivatives structure and the DNA segment. Hydrogen atoms were added to the crystal structure. A grid box measuring 80, 80, and 100 points along the x, y, and z axes, respectively, was centered on the DNA to encompass the entire structure. Each docking process was set to generate 10 poses, following default parameters. Docking simulations were performed using AutoDock Vina, which provided binding affinities represented as Gibbs free binding energies. Previous studies have successfully employed similar methodologies to investigate ferrocene interactions with biomolecules, yielding meaningful insights [66–69]. The structure with the most favorable binding free energy was selected and further analyzed using Discovery Studio 4.5 [73]. In the scoring process, metals are treated as hydrogen bond donors, potentially affecting the differentiation of substrates with different metal compositions [74,75].

The binding free energies (ΔG in kcal/mol) obtained from AutoDock Vina were subsequently used to calculate binding constants (K_b) using **Equation 9**:

$$K_b = e^{[(\Delta G \times 1000)/RT]} \quad (\text{Eq.9})$$

where R represents the universal gas constant (1.987 cal/mol.K), and T is the temperature (298 K).

9. Molecular dynamics simulation

Molecular dynamics (MD) simulations were conducted using the Desmond simulation software from Schrödinger LLC [76]. All simulations utilized the NPT ensemble at a temperature of 300 K and a pressure of 1 bar. Each simulation was conducted for duration of 100 ns, with a relaxation time of 1 ps for all ligands. The OPLS force field parameters were consistently applied throughout the simulations. [77]. Long-range electrostatic interactions were computed using the particle mesh Ewald method [78], employing a Coulomb interaction cutoff radius of 9.0 Å. Water molecules were modelled using the simple point charge model [79]. Implicit solvent effects were considered to partially account for ionic interactions. Pressure control employed the Martyna-Tuckerman-Klein chain coupling scheme [80] with a coupling constant of 2.0 ps, while temperature control utilized the Nose-Hoover chain coupling scheme [80]. Nonbonded forces were computed using an r-RESPA integrator, updating short-range forces every step and long-range forces every three steps. Trajectories were saved every 4.8 ps for subsequent analysis.

The Desmond MD package's Simulation Interaction Diagram tool was utilized to investigate the interactions between ligands and DNA. The stability of MD simulations was assessed by monitoring the Root Mean Square Deviation (RMSD) of ligand atoms over time. This analysis focused on the DNA-ligand complexes involving FcMeCy, FcMeTh and ((FcMe)₂Ad, with detailed findings presented in the Results and Discussion section.

CONCLUSION

In this study, we explored how ferrocenylmethyl nucleobase derivatives (FcMeCy, FcMeTh, and (FcMe)₂Ad) interact with DNA through both experimental and theoretical methods. Our findings showed strong electrostatic interactions and binding affinity, highlighted by a noticeable negative shift in the anodic peak potential during cyclic voltammetry. The DFT analyses confirmed that bond lengths and angles were consistent, while the MEP analysis pointed out that the nucleobase groups are particularly susceptible to nucleophilic attack. From the HOMO-LUMO analysis, we found that the energy gap follows this order: (FcMe)₂Ad > FcMeTh > FcMeCy. Docking studies underlined the importance of electrostatic interactions in the binding process, with the binding constants aligning well with our experimental data. In molecular dynamics simulations, FcMeCy and FcMeTh showed stable binding to DNA, as evidenced by RMSD values remaining below 1.5 Å

throughout the simulations, which indicates the formation of stable complexes. Additionally, the R_g measurements remained steady, suggesting that DNA's compactness was preserved even in the presence of these ligands. These results underscore the interactions between DNA and the ferrocenylmethyl derivatives and point to their potential for further exploration in therapeutic applications.

SUPPLEMENTARY INFORMATION

The supplementary data for this study, including additional computational details and supporting figures, have been deposited in Mendeley Data and are publicly accessible at:

BEN AMOR, Mohammed Larbi; LANEZ, Elhafnaoui; Bekkar, Yahia; ADAIKA, Aicha; LANEZ, Touhami; NESBA, Kaouther; BECHKI, Lazhar (2025), "Evaluation of Ferrocenylmethylnucleobases Derivatives Interacting with DNA: Insights from Electrochemical, Spectroscopic, DFT Calculation, Molecular Docking and Molecular Dynamic Simulations", Mendeley Data, V1, DOI: 10.17632/kht6hnrw4s.1.

CREDIT AUTHORSHIP CONTRIBUTION STATEMENT

M. L. BEN AMOR: Software, formal analysis, investigation, methodology, writing reviewing and editing. E. LANEZ: Supervision, validation, writing—reviewing and editing. Y. Bekkar: validation, writing, reviewing and editing. A. ADAIKA: Software, writing and editing. T. LANEZ: Supervision, validation. K. NESBA: writing and editing. L. BECHKI: Supervision, validation.

DECLARATION OF COMPETING INTEREST

The authors declare that they have no known competing financial interests or personal relationships that could have appeared to influence the work reported in this paper.

ACKNOWLEDGMENTS

This work was supported by the directorate-general of scientific research and technological development (DGRSDT) and the laboratory of valorization and technology of Saharan resources (VTRS) (project code: B00L01UN390120150001).

FUNDING DECLARATION

This research did not receive any specific grant from funding agencies in the public, commercial, or not-for-profit sectors.

REFERENCES

1. Y. Sun, Y. Liu, X. Ma, H. Hu, *Int J Mol Sci*, **2021**, 22, 6923.
2. J.F. Alhmoud, J.F. Woolley, A.-E. Al Moustafa, M.I. Mallei, **2021**, 309–339.
3. R. Mehandi, R. Arif, M. Rana, S. Ahmedi, R. Sultana, M.S. Khan, M. Maseet, M. Khanuja, N. Manzoor, N. Nishat, *J Mol Struct*, **2021**, 1245, 131248.
4. M. Rana, M.I. Faizan, S.H. Dar, T. Ahmad, Rahisuddin, *ACS Omega*, **2022**, 7, 22639–22656.
5. E.J. Anthony, E.M. Bolitho, H.E. Bridgewater, O.W.L. Carter, J.M. Donnelly, C. Imberti, E.C. Lant, F. Lermyte, R.J. Needham, M. Palau, *Chem Sci*, **2020**, 11, 12888–12917.
6. J. Zegers, M. Peters, B. Albada, **2023**, 28, 117–138.
7. Q. Cheng, T. Zhou, Q. Xia, X. Lu, H. Xu, M. Hu, S. Jing, *RSC Adv*, **2021**, 11, 25477–25483.
8. L. Tabrizi, T.L.A. Nguyen, H.D.T. Tran, M.Q. Pham, D.Q. Dao, *J Chem Inf Model*, **2020**, 60, 6185–6203.
9. C. Ornelas, **2011**, 35, 1973–1985.
10. N. Zegheb, C. Boubekri, T. Lanez, E. Lanez, T.T. Küçükılınç, E. Öz, A. Khenoufa, S. Khamouli, S. Belaidi, *Anticancer Agents Med Chem*, **2021**, 22, 1426–1437.
11. A. Khenoufa, L. Bechki, T. Lanez, E. Lanez, N. Zegheb, *J Mol Struct*, **2021**, 1224, 129052.
12. G. Gasser, I. Ott, N. Metzler-Nolte, *J Med Chem*, **2011**, 54, 3–25.
13. R. Wang, H. Chen, W. Yan, M. Zheng, T. Zhang, Y. Zhang, *Eur J Med Chem*, **2020**, 190, 112109.
14. A.M. Abu-Dief, M.A. Said, O. Elhady, N. Alahmadi, S. Alzahrani, T.N.A. Eskander, M.A.E.A.A. Ali, *Inorg Chem Commun*, **2023**, 155, 110955.
15. S. Masood, M. Jamshaid, M.N. Zafar, E.U. Mughal, M. Ashfaq, M.N. Tahir, *J Mol Struct*, **2024**, 1295, 136571.
16. M. Sumi, N.T. Nevaditha, B.S. Kumari, *J Mol Struct*, **2023**, 1272, 134091.
17. A.M. Abu-Dief, R.M. El-Khatib, T. El-Dabea, A. Abdou, F.S. Aljohani, E.S. Al-Farraj, I.O. Barnawi, M.A.E.A.A. Ali, *J Mol Liq*, **2023**, 386, 122353.
18. A.M. Abu-Dief, M.A. Said, O. Elhady, H.A. Al-Abdulkarim, S. Alzahrani, T.N.A. Eskander, M.A.E.A.A.A. El-Remaily, *Appl Organomet Chem*, **2023**, 37, e7162.
19. M. Hanane, T. Lanez, I. Zafar, M.S. Afghan, N. Zegheb, *J Coord Chem*, **2023**, 76, 1984–1998.
20. H. Mouada, T. Lanez, I. Zafar, *J Organomet Chem*, **2024**, 1007, 123026.
21. N. Li, Y. Ma, C. Yang, L. Guo, X. Yang, *Biophys Chem*, **2005**, 116, 199–205.

22. M.T. Carter, M. Rodriguez, A.J. Bard, *J Am Chem Soc*, **1989**, 111, 8901–8911.
23. P. Şenel, S. Agar, M. Yurtsever, A. Gölcü, *J Pharm Biomed Anal*, **2023**, 115746.
24. A. Shah, M. Zaheer, R. Qureshi, Z. Akhter, M.F. Nazar, *Spectrochim Acta A Mol Biomol Spectrosc*, **2010**, 75, 1082–1087.
25. X. Chu, G.-L. Shen, J.-H. Jiang, T.-F. Kang, B. Xiong, R.-Q. Yu, *Anal Chim Acta*, **1998**, 373, 29–38.
26. C.M.A. Brett, O. Brett, **1993**, 67, 444.
27. E. Lanez, M. Saidi, T. Lanez, **2023**, 44, 542–558.
28. M.A. Neelakantan, F. Rusalraj, J. Dharmaraja, S. Johnsonraja, T. Jeyakumar, M. Sankaranarayana Pillai, *Spectrochim Acta A Mol Biomol Spectrosc*, **2008**, 71, 1599–1609.
29. G.-C. Zhao, J.-J. Zhu, J.-J. Zhang, H.-Y. Chen, *Anal Chim Acta*, **1999**, 394, 337–344.
30. M. Aslanoglu, G. Ayne, *Anal Bioanal Chem*, **2004**, 380, 658–663.
31. T. Sarwar, S.U. Rehman, M.A. Husain, H.M. Ishqi, M. Tabish, *Int J Biol Macromol*, **2015**, 73, 9–16.
32. D.K. Jangir, S. Charak, R. Mehrotra, S. Kundu, *J Photochem Photobiol B*, **2011**, 105, 143–148.
33. K. Roy, S. Kar, P. Ambure, **2015**, 145, 22–29.
34. N. Shahabadi, M. Falsafi, *Spectrochim Acta A Mol Biomol Spectrosc*, **2014**, 125, 154–159.
35. A.M. Abu-Dief, T. El-Dabea, R.M. El-Khatib, M. Feizi-Dehnayebi, F.S. Aljohani, K. Al-Ghamdi, I.O. Barnawi, M.A.E.A.A. Ali, *J Mol Liq*, **2024**, 399, 124422.
36. D. Suh, J.B. Chaires, *Bioorg Med Chem*, **1995**, 3, 723–728.
37. S.Z. Moradi, A. Nowroozi, K. Sadrjavadi, S. Moradi, K. Mansouri, L. Hosseinzadeh, M. Shahlaei, *Int J Biol Macromol*, **2018**, 114, 40–53.
38. F.A. Qais, K.M. Abdullah, M.M. Alam, I. Naseem, I. Ahmad, *Int J Biol Macromol*, **2017**, 97, 392–402.
39. Z. Seferoğlu, M.M.A. Mahmoud, H. Ihmels, **2016**, 125, 241–248.
40. M. Milusheva, M. Todorova, V. Gledacheva, I. Stefanova, M. Feizi-Dehnayebi, M. Pencheva, P. Nedialkov, Y. Tumbarski, V. Yanakieva, S. Tsoneva, **2023**, 16, 1660.
41. A.S. Dorafshan Tabatabai, E. Dehghanian, H. Mansouri-Torshizi, M. Feizi-Dehnayebi, *J Biomol Struct Dyn*, **2024**, 42, 5447–5469.
42. I.M. Khan, M. Islam, S. Shakya, N. Alam, S. Imtiaz, M.R. Islam, *J Biomol Struct Dyn*, **2022**, 40, 12194–12208.
43. S. Shakya, I.M. Khan, B. Shakya, Y.H. Siddique, H. Varshney, S. Jyoti, *J Mater Chem B*, **2023**, 11, 1262–1278.
44. I.M. Khan, S. Shakya, R. Akhtar, K. Alam, M. Islam, N. Alam, *Bioorg Chem*, **2020**, 100, 103872.
45. I.M. Khan, S. Shakya, M. Islam, S. Khan, H. Najnin, *Phys Chem Liquids*, **2021**, 59, 753–769.
46. M. Feizi-Dehnayebi, E. Dehghanian, H. Mansouri-Torshizi, *J Mol Struct*, **2021**, 1240, 130535.

47. H. Laraoui, E. Lanez, N. Zegheb, A. Adaika, T. Lanez, M. Benkhaled, *ChemistrySelect*, **2023**, 8, e202204512.
48. M.T. Rehman, M.F. AlAjmi, A. Hussain, *Curr Pharm Des*, **2021**, 27, 3577–3589.
49. T. Lanez, M. Feizi-Dehnayebi, E. Lanez, *J Mol Struct*, **2024**, 138386.
50. A. Yahiaoui, N. Benyza, A. Messai, T. Lanez, E. Lanez, **2023**,.
51. E. Lanez, L. Bechki, T. Lanez, **2019**, 20,.
52. E. Lanez, L. Bechki, T. Lanez, *Chemistry (Easton)*, **2020**, 14, 146–153.
53. E. Lanez, L. Bechki, T. Lanez, **2019**, 13, 11–17.
54. T. Lanez, H. Benaicha, E. Lanez, M. Saidi, **2018**, 39, 76–88.
55. R. Vijayalakshmi, M. Kanthimathi, V. Subramanian, B.U. Nair, *Biochem Biophys Res Commun*, **2000**, 271, 731–734.
56. J.A. Glasel, *Biotechniques*, **1995**, 18, 62–63.
57. C.-S. Lu, X.-M. Ren, C.-J. Hu, H.-Z. ZHU, Q.-J. MENG, *Chem Pharm Bull (Tokyo)*, **2001**, 49, 818–821.
58. R. Bera, B.K. Sahoo, K.S. Ghosh, S. Dasgupta, *Int J Biol Macromol*, **2008**, 42, 14–21.
59. S. Qamar, F. Perveen, Z. Akhter, S. Yousuf, M. Sultan, S.E. Ela, N. Ullah, M. Fatima, K. Fatima, U. Nazir, *J Mol Struct*, **2022**, 1253, 132250.
60. S. Satyanarayana, J.C. Dabrowiak, J.B. Chaires, *Biochemistry*, **1992**, 31, 9319–9324.
61. M. Frisch, F. Clemente, **2009**, 20–44.
62. R. Dennington, T.A. Keith, J.M. Millam, **2016**,.
63. N.B. Balabanov, K.A. Peterson, *J Chem Phys*, **2005**, 123,.
64. H.M. Berman, *Nucleic Acids Res*, **2000**, 28, 235–242.
65. G.M. Morris, R. Huey, W. Lindstrom, M.F. Sanner, R.K. Belew, D.S. Goodsell, A.J. Olson, *J Comput Chem*, **2009**, 30, 2785–2791.
66. E. Lanez, A. Kedadra, T. Lanez, A. Adaika, N. Zegheb, *J Organomet Chem*, **2024**, 1017, 123284.
67. A. Adaika, Y. Bekkar, S. Youmbai, L. Bourougaa, E. Lanez, M.L. Ben Amor, K. Nesba, T. Lanez, L. Bechki, *Appl Organomet Chem*, **2025**, 39,.
68. A. Yahiaoui, N. Benyza, A. Messai, T. Lanez, L. Elhafnaoui, **2024**, 8, 93–102.
69. M.L. BEN AMOR, E. LANEZ, Y. Bekkar, A. ADAIKA, T. LANEZ, K. NESBA, L. BECHKI, *ChemistrySelect*, **2025**, 10, 1–16.
70. L. Ozalp, S.S. Erdem, B. Yüce-Dursun, Ö. Mutlu, M. Özbil, *Comput Biol Chem*, **2018**, 77, 87–96.
71. J.J.P. Stewart, *J Mol Model*, **2009**, 15, 765–805.
72. S. Grimme, *Wiley Interdiscip Rev Comput Mol Sci*, **2011**, 1, 211–228.
73. D.S. Biovia, **2017**, 936, 240–249.
74. G. V Dhoke, C. Loderer, M.D. Davari, M. Ansorge-Schumacher, U. Schwaneberg, M. Bocola, *J Comput Aided Mol Des*, **2015**, 29, 1057–1069.
75. O. Trott, A.J. Olson, *J Comput Chem*, **2010**, 31, 455–461.
76. K.J. Bowers, E. Chow, H. Xu, R.O. Dror, M.P. Eastwood, B.A. Gregersen, J.L. Klepeis, I. Kolossvary, M.A. Moraes, F.D. Sacerdoti, in: Proceedings of the 2006 ACM/IEEE Conference on Supercomputing, 2006, pp. 84-es.

MOHAMMED LARBI BEN AMOR, ELHAFNAOUI LANEZ, YAHIA BEKKAR, AICHA ADAIKA,
TOUHAMI LANEZ, KAOUTHER NESBA, LAZHAR BECHKI

77. J.L. Banks, H.S. Beard, Y. Cao, A.E. Cho, W. Damm, R. Farid, A.K. Felts, T.A. Halgren, D.T. Mainz, J.R. Maple, *J Comput Chem*, **2005**, 26, 1752–1780.
78. A.Y. Toukmaji, J.A. Board Jr, *Comput Phys Commun*, **1996**, 95, 73–92.
79. J. Zielkiewicz, *J Chem Phys*, **2005**, 123,.
80. G.J. Martyna, M.L. Klein, M. Tuckerman, *J Chem Phys*, **1992**, 97, 2635–2643.

ASSESSMENT OF GREENHOUSE GAS (GHG) EMISSIONS ASSOCIATED WITH RAPESEED FARMING IN ROMANIA

Lucian DORDAI^{a,*}, Marius ROMAN^a, Levente LEVEI^a

ABSTRACT. Agriculture plays a role in greenhouse gas (GHG) emissions, especially by cultivating biofuel crops like rapeseed (*Brassica napus*). This study assesses the GHG emissions associated with rapeseed farming in Romania, focusing on 2022–2024. Data were collected from rapeseed cultivation at Mihai Viteazu, Cluj, under various fertilization and irrigation conditions. The study reveals that GHG emissions range from 89 to 231 kg CO₂ eq/l biodiesel, with irrigation reducing emissions by approximately 1.3 times compared to non-irrigated conditions. Notably, nitrogen fertilization significantly increases nitrous oxide (NO_x) emissions, which account for 80% of total GHG emissions, particularly under higher nitrogen application rates. The results highlight the need for optimized nitrogen management to balance yield increases with environmental impacts, as excessive nitrogen use intensifies NO_x emissions due to enhanced nitrification and denitrification processes. The study also finds that irrigation mitigates GHG and NO_x emissions, emphasizing its role in sustainable rapeseed farming. This research underscores the importance of precision nitrogen management and irrigation in reducing the carbon footprint of rapeseed biodiesel production while enhancing crop productivity in Romania.

Keywords: *greenhouse gas emissions, GHG, rapeseed farming, nitrogen fertilization, biofuels, sustainable agriculture*

INTRODUCTION

Rapeseed (*Brassica napus*) is one of the most widely grown oilseed crops in the world, playing a crucial role in both the agricultural and biofuel sectors. Its cultivation and use in biofuel production significantly affect greenhouse

^a INCDO-INOE 2000, Research Institute for Analytical Instrumentation, 67 Donath str., RO-400293, Cluj-Napoca, Romania

* Corresponding author: lucian.dordai@icia.ro



gas (GHG) emissions and global climate change mitigation efforts. Agricultural practices, particularly nitrogen fertilization and irrigation, have been identified as key factors influencing GHG emissions from rapeseed farming, especially in the context of nitrous oxide (N_2O) emissions, potent contributors to global warming [1, 2].

The environmental impacts of rapeseed cultivation have been widely researched, revealing that nitrogen management practices and irrigation methods significantly affect GHG emission levels in rapeseed fields [3, 4]. In regions such as Eastern Europe, and specifically Romania, the importance of sustainable rapeseed cultivation is paramount, given its role in biofuel production and the region's agricultural economy [5]. Studies have demonstrated that adopting more sustainable farming practices can lead to significant reductions in GHG emissions from rapeseed cultivation, particularly through improved nitrogen use efficiency and better irrigation management [6, 7].

Recent assessments of biofuel production systems have emphasized the need for a life cycle approach to evaluate the full environmental impact of rapeseed biodiesel, from cultivation to fuel combustion. Such evaluations are critical for understanding the potential GHG savings associated with rapeseed biofuels and their role in meeting international climate targets, including those set by the European Union's Directive 2009/28/EC, which promotes the use of renewable energy sources [8, 9, 17, 23]. In this context, life cycle assessments (LCAs) have been used to quantify GHG emissions across the biofuel production chain, highlighting the importance of both agricultural practices and energy inputs in determining the overall carbon footprint of rapeseed biodiesel [10, 11, 19]. To contextualize the findings, comparisons with studies from other European countries indicate that the GHG emissions from Romanian rapeseed biodiesel are comparable to those reported for Germany (63-68 g CO_2 eq/MJ) and Sweden (66-70 g CO_2 eq/MJ), with Romanian figures ranging between 62-75 g CO_2 eq/MJ. These values suggest that Romania aligns closely with sustainable benchmarks while highlighting areas for potential improvement [24, 25].

Furthermore, irrigation practices and their impact on GHG emissions have gained attention in recent studies. The use of irrigation in rapeseed farming can lead to higher biomass production, but it also increases the risk of N_2O emissions due to enhanced nitrogen availability in the soil [12]. Comparative studies between irrigated and non-irrigated systems suggest that while irrigation may boost yields, it can also exacerbate GHG emissions if not managed carefully [13, 14, 15]. Similar findings were reported in France, where irrigated rapeseed cultivation increased yields by 20-30% but contributed to a 15-18% rise in N_2O emissions, illustrating the delicate trade-offs involved [26].

As such, optimizing both irrigation and fertilization practices is essential for reducing the environmental footprint of rapeseed cultivation [15].

Given these challenges, this study aims to provide a comprehensive assessment of the GHG emissions associated with rapeseed cultivation in Romania. The research focuses on critical aspects such as nitrogen fertilization strategies, soil management practices, and carbon sequestration potential. It is widely understood that nitrogen fertilization plays a crucial role in rapeseed production, but improper management can lead to significant emissions of nitrous oxide (N₂O), a potent GHG. Similarly, soil management practices, particularly tillage methods, can influence soil organic carbon levels, which are important for carbon sequestration [16, 18, 20, 21].

By optimizing these variables—such as selecting nitrogen fertilizers with lower emission profiles, fine-tuning nitrogen application rates, and adopting reduced or no-tillage farming methods—it may be possible to significantly reduce the GHG emissions associated with rapeseed biodiesel production. This study not only evaluates the direct effects of these practices on emission levels but also explores their potential to enhance soil carbon sequestration, thereby contributing to long-term climate mitigation strategies. The findings offer valuable insights into the pathways for producing more sustainable biofuels in Romania, and they align with broader efforts to lower the agricultural sector's GHG emissions, while supporting the transition to cleaner energy sources [22].

RESULTS AND DISCUSSION

For GHG calculations, data from rapeseed cultivation under Mihai Viteazu, Cluj conditions (2022–2024) were used. Specific treatments included:

- **Disease, Pest, and Weed Management:**
 - **Seed treatment:** ROVRAL 50 WP was applied at 1 kg/tonne.
 - **Vegetation treatment:** FOLICUR SOLO (Bayer CropScience) was applied at 0.5 l/ha. Diseases such as rust, powdery mildew, downy mildew, and alternariosis were managed using the same treatments: ROVRAL 50 WP at 1 kg/tonne for seeds and FOLICUR SOLO at 0.5 l/ha for vegetation.
 - **Pest control:** Ground fleas, rape beetle, cruciferous weevils, and green aphids were treated with MELIPAX 60 EC at 3 l/ha during flowering. Glossy beetles and rape wasps were controlled with VICTENON at 0.75 kg/ha.

- **Weed control:** DUAL was applied as a pre-sowing treatment at 3–4 l/ha, while post-sowing treatment utilized LONTREL at 0.3–0.5 l/ha.
- **Fertilization Regimes:**
 - **Fertilization was carried out in three gradations:**
 - **B₂:** 100 kg/ha nitrogen, 75 kg/ha phosphorus, and 20 kg/ha sulfur.
 - **B₃:** 150 kg/ha nitrogen, 75 kg/ha phosphorus, and 20 kg/ha sulfur.
 - **B₄:** 270 kg/ha nitrogen, 75 kg/ha phosphorus, and 20 kg/ha sulfur.

Additionally, **NUTRIENT EXPRESS® (Miller)** was applied at 2.5 kg/ha. This fertilizer contains a high concentration of microelements, seaweed extract, carbohydrates, and essential amino acids, with the following composition:

- 18% total nitrogen (4.9% ammonia, 5.5% nitrate, and 7.6% urea nitrogen)
- 18% mobile phosphorus (P₂O₅)
- 18% soluble potassium (K₂O)
- Chelated microelements: 0.05% copper (Cu), 0.10% iron (Fe), 0.50% magnesium (Mg), 0.05% manganese (Mn), 0.001% molybdenum (Mo), and 0.05% zinc (Zn).

- **Foliar Fertilization:**

FOLICARE 17-9-33 (Yara Suomi) was applied at 5 kg/ha. This high-efficiency fertilizer contains 2000 mg/kg boron (B) and has the following composition:

- 8% nitrogen (N)
- 9% phosphorus (P₂O₅)
- 33% potassium (K₂O)
- 2% magnesium oxide (MgO)
- 5% sulfur trioxide (SO₃)
- Trace elements: 0.02% copper (Cu), 0.05% iron (Fe), 0.05% manganese (Mn), 0.002% molybdenum (Mo), and 0.05% zinc (Zn).

Table 1 shows the GHG emissions recorded for all the cultivation variants tested at Mihai Viteazu - Cluj during 2022-2024. Since the rapeseed is cultivated for biofuel production, the GHG emissions per liter of biodiesel produced were calculated. GHG emissions are expressed in carbon dioxide equivalent CO₂ eq/l biodiesel (CO₂ eq) is the universal unit of measure used to indicate the global warming potential of GHG). Carbon dioxide is the reference gas by which all greenhouse gases are calculated and reported.

ASSESSMENT OF GREENHOUSE GAS (GHG) EMISSIONS ASSOCIATED
WITH RAPESEED FARMING IN ROMANIA

Table 1. GHG emissions, calculated for the rapeseeds crop variants realized at Mihai Viteazu - Cluj, 2022- 2024

Crop variants	Average yield (t/ha)	GHG emissions (kg CO ₂ eq/l)	NO _x emissions from soils (kg CO ₂ eq/l)
^a a1 x ^c b1 nonirrigated x nonfertilized	16,882	0,013	0,001
^a a1 x ^d b2 nonirrigated x fertilized 100N	19,415	0,089	0,076
^a a1 x ^e b3 nonirrigated x fertilized 150N	23,127	0,107	0,096
^a a1 x ^f b4 nonirrigated x fertilized 270N	24,480	0,175	0,162
^b a2 x ^c b1 irrigated x nonfertilized	21,104	0,010	0,001
^b a2 x ^d b2 irrigated x fertilized 100N	27,856	0,062	0,053
^b a2 x ^e b3 irrigated x fertilized 150N	31,232	0,079	0,071
^b a2 x ^f b4 irrigated x fertilized 270N	32,581	0,131	0,122

^aa₁- non-irrigated; ^ba₂-irrigated; ^cb₁-fertilized; ^db₂- fertilized 100kg/ha azote(N)+75 kg/ha phosphorus(P)+20 kg/ha sulphur (S) ; ^eb₃-fertilized 150kg/ha azote(N)+75 kg/ha phosphorus(P)+20 kg/ha sulphur (S); ^fb₄-fertilized 270kg/ha azote(N)+75 kg/ha phosphorus(P)+20 kg/ha sulphur (S);

Figures 1-3 show the average productions of the rapeseed crop recorded in 2008, the GHG emissions associated with them due to the fertilizers and pesticides used, as well as the NO_x emissions due to the nitrogen fertilization of the rapeseed crop.

The influence of the experimental factor B, fertilization, on rapeseed culture: average production, GHG emissions and NO_x emissions from associated soils

The analysis of the results presented in **Table 1** highlights the following situations for the rape culture variants tested.

Control sample: non-irrigated x non-fertilized. NO_x emissions from soil represent 7.6% of total GHG emissions.

The experimental factor B, fertilization, graduation b₂ (nitrogen dose of 100 kg/ha) had a significant influence and determined an increase in production of 2533 kg/ha (15%), an increase in GHG emissions by 6.8 times and a 76-fold increase in NO_x emissions compared to the experimental control. In the experimented culture variant (graduation a₁ x b₂) NO_x emissions represent 85% of total GHG emissions.

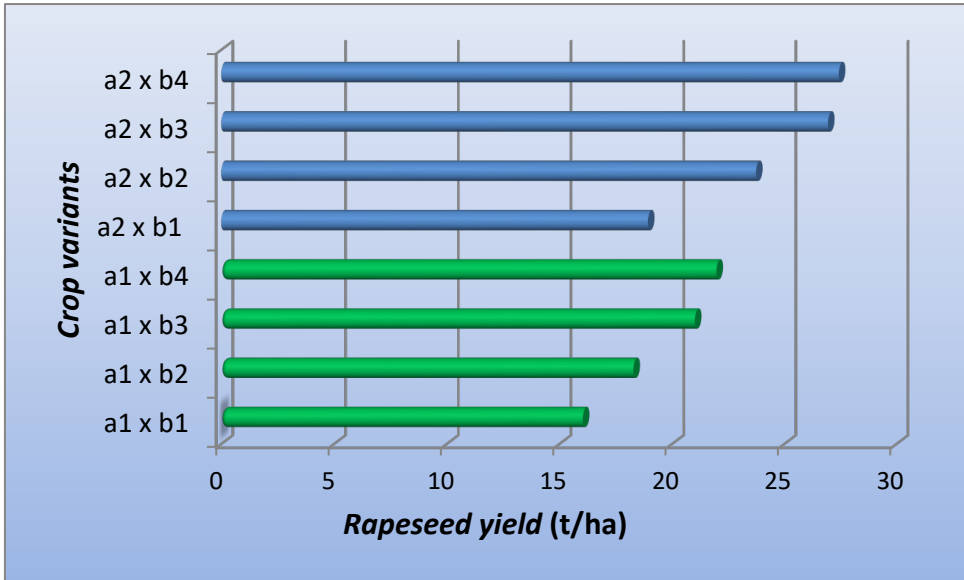


Figure 1. Yield of rapeseed crop obtained for the experimented crop variants, 2022-2024

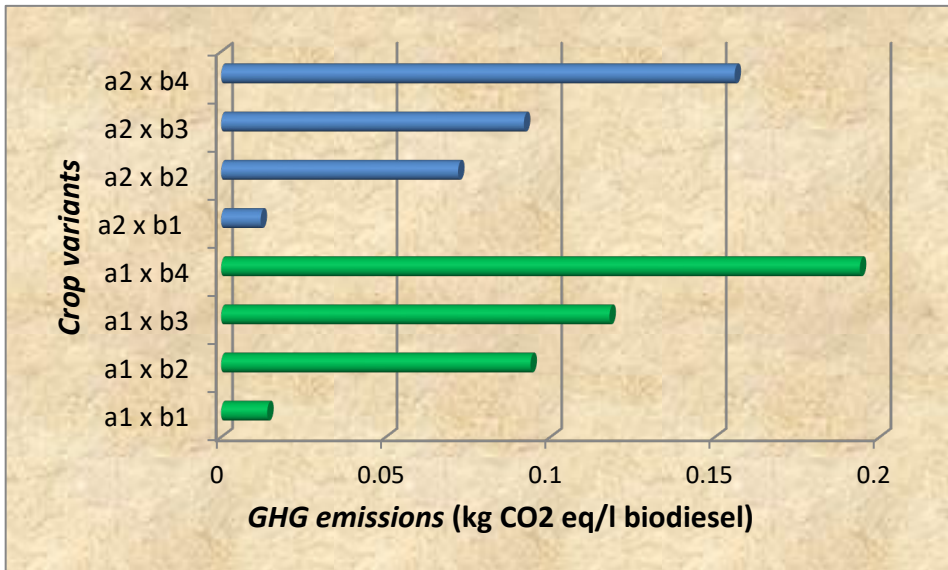


Figure 2. GHG emissions calculated for the rapeseed crop variants, Mihai Viteazu - Cluj, 2022-2024

ASSESSMENT OF GREENHOUSE GAS (GHG) EMISSIONS ASSOCIATED
WITH RAPESEED FARMING IN ROMANIA

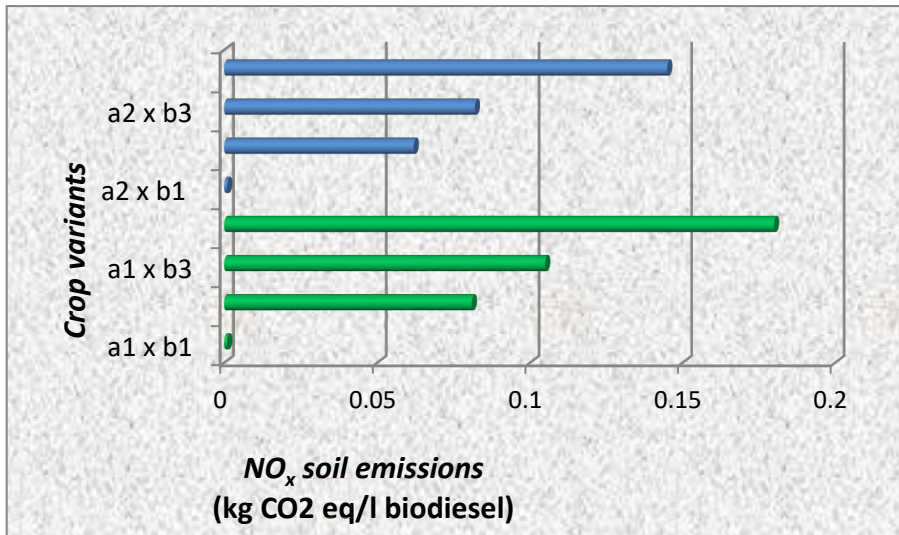


Figure 3. NO_x emissions from soils calculated for the rapeseed crop variants, Mihai Viteazu - Cluj, 2022-2024

By fertilizing during the growing season of the crop, type b3 (nitrogen dose of 150 kg/ha), an increase in production of 6245 kg/ha (36.9%), an increase in GHG emissions by 8.2 times was obtained and NO_x emissions 96 times, compared to the control variant chosen. In this crop variant (graduation a1 x b3) the NO_x emissions from the soil represent 89% of the total GHG emissions.

It is found that if, during the growing season of the crop, fertilization is applied with grading b4 - the nitrogen dose of 270 kg/ha, a production increase of 5296 kg/ha (45.0%), an increase in GHG emissions of 13.4 times and 162 times of NO_x emissions, compared to the chosen witness. NO_x emissions from the soil represent 92% of total GHG emissions in the experimented crop variant (a1 x b4 grading).

Control sample: irrigated x unfertilized. NO_x emissions from soil represent 10% of total GHG emissions.

When applying fertilization, grading b2 - the nitrogen dose of 100 kg/ha has a great influence on rapeseed culture and led to an increase in production of 4896 kg/ha (30.5%), an increase in GHG emissions of 5.8 times and of NO_x emissions from the soil 71 times, compared to the control version of the experiment NO_x emissions from the soil have a weight of 85.4% of total GHG emissions in the experimented version (a2 x b2 grading).

Experimental factor B, fertilization, graduation b3 - nitrogen dose of 150 kg/ha, influenced rape production and determined an increase of 10128 kg/ha (47.9%), an increase of GHG emissions by 7.9 times and of NOx emissions from the soil 71 times compared to the control variant chosen. In this case, (grading a2 x b3) NOx emissions from the soil represent a percentage of 89% of total GHG emissions.

It was observed that even with the application of fertilization grade b4 (nitrogen dose of 270 kg/ha), there was a 54.3% increase in yield to 11,477 kg/ha, along with a 13.1-fold rise in GHG emissions and a 122-fold increase in NOx emissions from the soil compared to the control. NOx emissions accounted for 91.7% of the total GHG emissions (a2 x b4 level). Analyzing the results, it is evident that fertilization (factor B) greatly influenced the crop, leading to higher GHG and NOx emissions from the soil across all tested variants. As nitrogen doses increased, both GHG and NOx emissions from the soil also rose.

Comparisons with other European data reveal a similar trend, where increasing nitrogen application consistently increases GHG emissions. For instance, research in Denmark observed a 12- to 15-fold rise in N₂O emissions when nitrogen application increased from 90 kg/ha to 270 kg/ha [26]. This aligns closely with the findings from this study, where NOx emissions increased by 13.4 times under similar nitrogen fertilization rates.

The influence of the experimental factor A, irrigation regime, on rapeseed culture: average production, GHG emissions and NOx emissions from associated soils

Compared to the non-irrigated x non-fertilized control variant, the application, during the vegetation period of the crop, of irrigation (graduation a2 x b1) leads to production in the rapeseed crop with an increase of 4222 kg/ha (25%), a decrease in GHG emissions of 1.3 times, and equal emissions of NOx from the soil for both variants.

The application of irrigation during the vegetation period of the crop (graduation a2 x b2) determined an increase in production of 8441 kg/ha (43.4%), a decrease in GHG emissions by 1.4 times and NOx emissions from the soil by 1,3 times, compared to the non-irrigated x fertilized control version - grading b2.

Compared to the non-irrigated x fertilized control variant - grading b3, the application of irrigation (grading a2 x b3) determined an increase in production of 8105 kg/ha (35.0%), a decrease in GHG emissions by 1.35 times and emissions NOx from soil 1.35 times.

ASSESSMENT OF GREENHOUSE GAS (GHG) EMISSIONS ASSOCIATED WITH RAPESEED FARMING IN ROMANIA

It is found that by applying irrigation during the growing season of the crop, there was an increase in production of 8101 kg/ha (33.0%), a decrease in GHG emissions by 1.3 times and NOx emissions from the soil by 1.3 times compared to the non-irrigated x fertilized control variant - grading b4.

Upon analyzing the results, it is evident that experimental factor A, the irrigation regime, specifically at the a2-irrigated level, significantly impacts the crop by reducing both GHG and NOx emissions from the soil across all tested variants.

At a first analysis of the obtained results, the best crop variant seems to be irrigated x fertilized - grading b4 in which the production recorded an increase of 54.3%, compared to 47.9% - the variant irrigated x fertilized - grading b3 but, analyzing from the point of view of the impact on the environment, we recommend the irrigated x fertilized crop variant - grading b3 because the increase in GHG emissions is only 7.9 times compared to 13.1, and the NOx emissions from the soil are only 71 times compared to 122.

Method of Calculating GHG and NOx Emissions (Carbon Dioxide Equivalent)

The method for calculating GHG emissions, particularly NOx emissions in carbon dioxide equivalent, follows standard guidelines from the Intergovernmental Panel on Climate Change (IPCC) and the European Commission's Joint Research Centre (JRC) for life cycle assessments (LCAs). The CO₂ equivalent is calculated by multiplying the amount of each gas emitted by its respective Global Warming Potential (GWP) factor [27].

For example, nitrous oxide (N₂O) has a GWP of 298, meaning that one kilogram of N₂O is equivalent to 298 kilograms of CO₂. The emissions from fertilizers are calculated based on the amount of nitrogen applied and the emission factors provided by the IPCC guidelines for agricultural practices. The NOx emissions are primarily calculated from soil nitrogen dynamics (nitrification and denitrification processes), which are influenced by fertilizer types and application methods.

CONCLUSIONS

The study conducted at Mihai Viteazu between 2022 and 2024 provides valuable insights into the greenhouse gas (GHG) emissions associated with rapeseed cultivation under various conditions. The findings indicate that GHG emissions vary significantly depending on whether the crops are irrigated or not. Specifically, in 2022, GHG emissions ranged from 89 to 175 kg CO₂ eq/l under non-irrigation conditions and from 62 to 131 kg

CO₂ eq/l under irrigation conditions. In 2023, these values increased to 117 to 231 kg CO₂ eq/l for non-irrigated crops and 82 to 180 kg CO₂ eq/l for irrigated crops. Similarly, in 2024, GHG emissions were recorded at 94 to 194 kg CO₂ eq/l under non-irrigation and 72 to 156 kg CO₂ eq/l under irrigation.

The study also highlights the significant contribution of NO_x emissions from soils, particularly in fertilized crop variants. In 2022, NO_x emissions ranged from 76 to 162 kg CO₂ eq/l under non-irrigation and 53 to 122 kg CO₂ eq/l under irrigation. The following year, these emissions increased to 101 to 214 kg CO₂ eq/l for non-irrigated crops and 71 to 167 kg CO₂ eq/l for irrigated crops. In 2024, NO_x emissions were recorded at 81 to 180 kg CO₂ eq/l under non-irrigation and 62 to 145 kg CO₂ eq/l under irrigation.

The results show that NO_x emissions from soils contributed to an average of 80% of the total GHG emissions across all variants. This underscores the significant role of nitrogen fertilizers in increasing soil NO_x emissions, largely due to intensified nitrification and denitrification processes. The increase in NO_x output highlights the challenge of balancing the need for nitrogen fertilization to boost yields with its environmental impact. Excessive nitrogen application can exacerbate these processes, resulting in higher GHG emissions.

The study emphasizes that nitrogen fertilization is necessary to achieve higher crop yields, but this comes at the cost of increased GHG emissions. Fertilizer application, while essential for boosting agricultural productivity, must be optimized to prevent excessive nitrogen use. To mitigate emissions, it is crucial to match nitrogen input precisely to the crop's requirements and adopt more efficient nitrogen management techniques. This may involve enhancing nitrogen use efficiency (NUE) to ensure crops absorb nutrients more efficiently, thereby reducing nitrogen losses to the environment.

The data also show a consistent decrease in both GHG and NO_x emissions with the application of irrigation. This suggests that irrigation not only promotes improved crop growth but also reduces emission intensity per unit of production. By maintaining optimal soil moisture levels, irrigation helps minimize nitrogen losses through volatilization and leaching, ultimately reducing total emissions.

The findings from 2022 to 2024 for rapeseed cultivation at Mihai Viteazu, Cluj, reinforce the importance of balanced nitrogen fertilization for improving yields while minimizing environmental impact. The application of irrigation proves beneficial in reducing GHG and NO_x emissions, suggesting that integrating these practices can help achieve more sustainable rapeseed farming. When benchmarked against other European studies, Romanian rapeseed cultivation demonstrates a comparable environmental profile, with opportunities for further optimization. For example, adopting advanced precision farming techniques,

ASSESSMENT OF GREENHOUSE GAS (GHG) EMISSIONS ASSOCIATED
WITH RAPESEED FARMING IN ROMANIA

as successfully implemented in Sweden, could reduce nitrogen-related emissions by up to 25% while maintaining yield efficiency [25]. Future strategies should focus on precision nitrogen management and controlled irrigation to optimize production efficiency and reduce the carbon footprint associated with rapeseed biodiesel production.

In conclusion, although nitrogen fertilization is crucial for optimizing rapeseed yields, its effect on GHG and NO_x emissions requires careful management. Implementing more efficient nitrogen use practices and irrigation can greatly lessen the environmental impact of rapeseed cultivation, making it a more sustainable choice for biofuel production in Romania.

EXPERIMENTAL SECTION

Rapeseed culture was carried out on an experimental lot in Mihai Viteazu, Cluj County. The studied perimeter is located in the Transylvanian Plain, its southwestern limit, in the lower region of the Aries hydrographic basin. The town of Mihai Viteazu is located on DN 75, approx. 45 km from the city of Cluj-Napoca (**Figure 4** source: <http://www.hartionline.ro>). The geographical position corresponds to the coordinates 46° 34' north latitude and 23° 46' east longitude Greenwich and an altitude of 345 - 493 m compared to the level of the Adriatic Sea.



Figure 4. The location of the experimental field in Cluj County
(source: www.hartionline.ro)

The comparative crops were developed in a polifactorial system, completely randomized, with subdivided parcels, as factor A is the water regime (two graduations), factor B is fertilization (four graduations) and factor C – rapeseed variety (three graduations), the biological material chosen. Three repetitions were provided for each comparative crop. Irrigation was performed by furrows. The experiments contained several 3 repetitions (n = 3), the number of varieties analyzed through the experiment was 24 (v = 2 x 4 x 3), the total number of experimental parcels was 72 (p = 24 x 3) (Figure 5). The experimental factors studied and their graduations are briefly presented in Table 2.

Table 2. Summary of the experimental factors, Mihai Viteazu - Cluj, 2022-2024

Analyzed factors	Graduations
Factor A	a ₁ –non-irrigated
Irrigation regime	a ₂ – irrigated at 50% from IUA
Factor B	b ₁ –non-fertilized
Fertilization	b ₂ – fertilized 100 N kg/ha + 75 kg /ha phosphorus + 20 kg/ha sulphur
	b ₃ – fertilized 150 N kg/ha + 75 kg /ha phosphorus + 20 kg/ha sulphur
	b ₄ – fertilized 270 N kg/ha + 75 kg /ha phosphorus + 20 kg/ha sulphur
Factor C	c ₁ – Dexter
Rapeseed variety	c ₂ - NK Caravel
	c ₃ – NK Tehnic

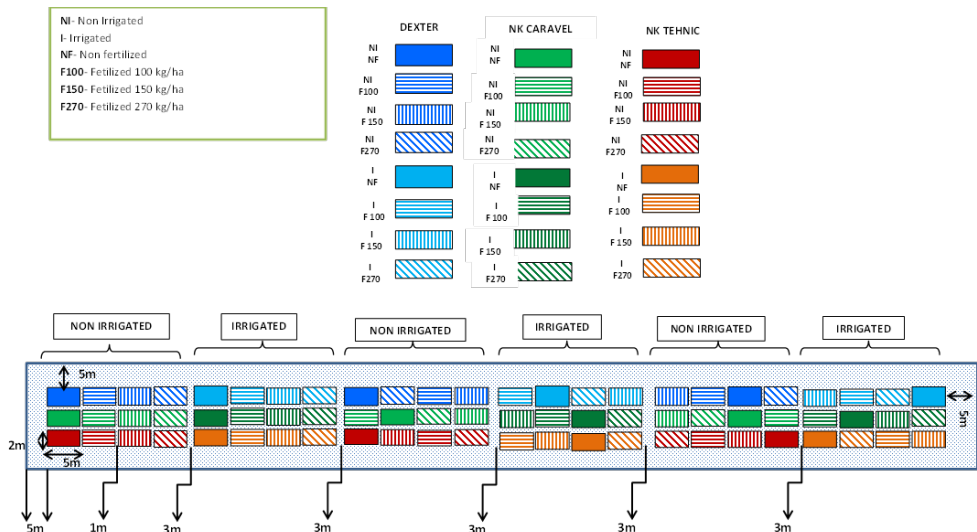


Figure 5. The research organization in the experimental filed

For the statistical analysis of the results, the POLIFACT statistical program was used - analysis of variance for completely randomized multifactorial experiments.

ACKNOWLEDGMENTS

This work was carried out through the Core Program within the National Research Development and Innovation Plan 2022-2027, carried out with the support of MCID, project no. PN 23 05.

REFERENCES

1. J. Smith, A. Brown, *Agriculture and Environmental Sustainability*, **2020**, 1-8.
2. R. Johnson, P. Silva, *Renewable Energy Systems*, **2019**, 10-15.
3. R. C. Buturca, C. Gasol, D. Scarpete, X. Gabarrell, *International Journal of Environmental and Ecological Engineering*, **2013**, 7(9), 644-648.
4. M. Popescu, L. Mihai, *Journal of Agricultural Sciences*, **2021**, 22-29.
5. C. Dragomir, E. Stoica, *Sustainable Agriculture Practices*, **2022**, 33-40.
6. T. Carter, A. Evans, *Climate Change Mitigation in Agriculture*, **2018**, 44-51.
7. V. C. Tudor, T. A. Dinu, M. Vladu, D. Smedescu, I. M. Vlad, E. A. Dumitru, C. L. Costuleanu, *Labour implications on agricultural production in Romania. Sustainability*, **2022** 14(14), 8549.
8. S. Marin, O. Toma, *Journal of Climate Smart Agriculture*, **2023**, 55-63.
9. D. Ionescu, M. Radulescu, *Biofuels and Sustainable Energy*, **2020**, 64-70.
10. P. George, H. Lee, *Environmental Impact Assessment in Agriculture*, **2019**, 71-78.
11. K. Thompson, J. Green, *Renewable and Sustainable Energy Reviews*, **2021**, 79-87.
12. L. Zhang, M. Wang, *Precision Agriculture Innovations*, **2017**, 88-95.
13. R. Fischer, T. Weber, *European Agricultural Sustainability*, **2016**, 96-102.
14. B. Petrescu, I. Cazacu, *Irrigation and Agricultural Emissions*, **2022**, 103-110.
15. F. Dumitrescu, A. Lupescu, *Soil and Crop Science*, **2018**, 111-119.
16. V. Popa, E. Stefan, *Agricultural Economics and Environment*, **2020**, 120-126.
17. J. McDonald, K. Roberts, *European Environmental Policy*, **2015**, 127-134.
18. C. Stan, R. Iliescu, *Sustainability in Agriculture*, **2023**, 135-142.
19. D. Carter, P. Singh, *Bioenergy Research*, **2020**, 143-151.
20. F. Rossi, G. Marchetti, *Journal of Environmental Protection*, **2019**, 152-159.
21. A. Kovacs, M. Horvath, *Journal of Climate Change and Agriculture*, **2021**, 160-167.
22. T. Ivanov, S. Georgiev, *Agricultural Science and Technology*, **2019**, 168-175.
23. *** *DIRECTIVE 2009/28/EC OF THE EUROPEAN PARLIAMENT AND OF THE COUNCIL of 23 April 2009 on the promotion of the use of energy from renewable sources and amending and subsequently repealing Directives 2001/77/EC and 2003/30/EC*

24. N. Lange, D. Moosmann, S. Majer, K. Meisel, K. Oehmichen, S. Rauh, D. Thrän, In *Progress in Life Cycle Assessment*, **2023**, 85-101.
25. H. Thers, M.T. Knudsen, P.E. Lærke, *Heliyon*, **2023**, 9.6.
26. X. Botton, L. Nitschelm, M. Juillard, H.M. Van der Werf, *The International Journal of Life Cycle Assessment*, **2024**, 1-16.
27. H.S. Eggleston, et al. "*IPCC guidelines for national greenhouse gas inventories. Volume 4: Agriculture, Forestry and Other Land Use.*" Institute for Global Environmental Strategies: Hayama, Japan 4, **2006**.

XANTHAN GUM AND GUAR GUM – POTENTIAL GREEN INHIBITORS FOR SCALE FORMATION

Andra TĂMAȘ^a, Laura COCHECI^{a*} , Lavinia LUPA^a 

ABSTRACT. Unwanted scale deposits cause numerous technical and economic problems and, for this reason, it is desired to inhibit their formation. The paper studied the possibility of using guar gum and xanthan gum as scale inhibitors mainly in the food industry, due to the fact that they are biodegradable and non-toxic. The two gums, with concentrations between 50 and 100 mg/L, have proven their effectiveness in the case of waters with initial total hardness below 10 mval/L. The scaling inhibition capacity was also correlated with the variation in electrical conductivity of the water samples. X-ray diffraction analysis of CaCO₃ scale formed in waters with initial total hardness over 10 mval/L, stationed for 24 hours in a thermostatic oven at 80°C, demonstrates the presence, mainly, of two polymorphic forms, calcite and aragonite.

Keywords: *calcium carbonate, guar gum, hardness, inhibitor, water scales, xanthan gum*

INTRODUCTION

Hard water is a water that contains a high percentage of calcium and magnesium ions coming from its passage through calcareous layers, mostly made up of calcium and magnesium carbonates, bicarbonates and sulphates.

When hard water is subject to changes in temperature, pressure or velocity, the dissolved minerals precipitate out of the solution and migrate to the area where the fluid has the lowest velocity (usually the inner surfaces of the pipes and equipment), making difficult the fluid flow. Thus, a scale is formed that acts as an insulator.

^a Politehnica University Timișoara, Faculty of Chemical Engineering, Biotechnologies and Environmental Protection, 6 Vasile Pârvan Bd., RO-300223, Timișoara, Romania

* Corresponding author: laura.cocheci@upt.ro



Undesirable scale deposits cause many technical and economical problems: partial or total obstruction of pipes leading to a decrease in flow rate, valves blockage and filters fouling, as well as the decreasing of heat transfer [1]. This last aspect is related to the increase of the thermal resistance to conduction, both in terms of increasing the thickness of the scale layer, as well as due to its low thermal conductivity which gives it insulating properties. The increase of the thermal resistance to conduction has as a consequence the decrease of the overall heat transfer coefficient and, subsequently, the need to increase the surface of heat transfer. Thus, at 2 mm thick deposit, depending on the chemical composition of water scale, the thermal flow is reduced for 10% to 40% [2].

The formation of scales can be done either by deposition (adhesion) of salts on surfaces in contact with aqueous solutions (especially at high temperatures) or by precipitation [3], and results from the succession of two distinct phases: germination and growth [1]. The most important factor that determines the intensity of scale formation is the level of supersaturation of the species that form deposits. Most of the scale-forming salts (CaCO_3 , CaSO_4 , $\text{Mg}(\text{OH})_2$) have inverse solubility characteristics, meaning that their solubility decreases with temperature increasing [3,4]. Scale deposits are mainly composed from calcium carbonate which precipitates in three different forms: calcite, aragonite and vaterite [2].

Scale deposition can be controlled by chemical or physical methods that affect the salts solubility, can prevent the growth of crystals or change the potential of solid surfaces [5]. Scale inhibitors are chemical substances that are added to the solution to stop nucleation, growth and deposition of crystals on a solid surface. Their effectiveness depends on pH, temperature, type of divalent ions and other chemicals compounds in the solution [6].

Traditional scale inhibitors include phosphorus-based compounds, both organic (phosphates, aminophosphates, phosphinocarboxylic acids, phosphonates) and inorganic (polyphosphates). Other classes of compounds that have prove their effectiveness as scale inhibitors are of a polymeric nature – polymers containing phosphate groups, sulfonate groups (polysulfonic acid, polyethylene sulfonic acid), carboxylic acids (polyacrylic, polymethacrylic, polymaleic, polyamino polyether acid methylene phosphonic) [7,8], maleic acid-acrylic acid copolymers, respectively maleic acid – acrylamide with close molecular weights [9]. A particular efficiency in preventing the formation of CaCO_3 scales in seawater desalination processes presents polyacrylic acid with low molecular weight and hydrophobic end groups of medium length (hexyl/cyclohexyl isobutyrate) or long end groups (hexadecyl isobutyrate), such as polyacrylic acid with high molecular weight and hydrophobic end groups with medium length (hexyl isobutyrate) [7].

Phosphorus-based inhibitors are particularly effective in that they can disperse water-insoluble inorganic salts, prevent or interfere with the precipitation and scaling of insoluble inorganic salts on the metal surface and maintain a better heat transfer effect in metal equipment [10]. On the other hand, a large part of them are pollutants for the environment, so it is necessary to replace them with “green” inhibitors, with a high degree of biodegradability. Thus, the following have been successfully used: polyaspartic acid or polyaspartic acids with narrow dispersity and controllable chain length, inulin, carboxymethyl inulin, folic acid polyepoxysuccinic acid [6, 11-14] or its sodium salt [15], polyethyleneimine, polyethyloxazoline, polyaminoamide-type dendrimers [4], depolymerized carboxyalkyl polysaccharide-type biodegradable inhibitors having a degree of substitution of up to 3 carboxylic groups per sugar unit [16], carboxymethylcellulose and its combination with hydroxyethylcellulose [17], fluorescent-tagged scale inhibitor containing fluorescent monomer, acrylic acid and chitosan [18], inhibitor based on Aloe Vera gel [19], extracts from leaves, flowers, fruits, seeds and rhizomes [20-32], pomegranate peel extracts [33], the mixture formed by vitamins B1 and B6 [34].

Recent research also focuses on the use of phosphonates with low phosphorus content, respectively on the implementation of biodegradable fragments in polyacrylate matrices to improve biodegradability [35].

The food industry plays an important role in everyday life, and it is a branch in which the appearance of scales in various technological processes must be avoided all the more. Based on our literature review, we did not find specific studies addressing the use of scale inhibitors for mineral waters utilized in the food industry. Thus, the purpose of this work is to evaluate the efficiency of some non-phosphoric “green” scale inhibitors that can be used successfully in the food industry. Therefore, the effectiveness of guar gum and xanthan gum as scale inhibitors was studied, taking into account that the two gums are used in this industry as stabilizing and thickening agents.

RESULTS AND DISCUSSION

The variation of total hardness for the samples without scale inhibitor, after standing in the oven at 80°C for 24 hours, is shown in Figure 1a (sparkling water) and Figure 1b (still drinking water).

For the same blank samples, the variation in temporary hardness after standing in the oven at 80°C for 24 hours is shown in Figure 2a (sparkling water) and Figure 2b (still drinking water).

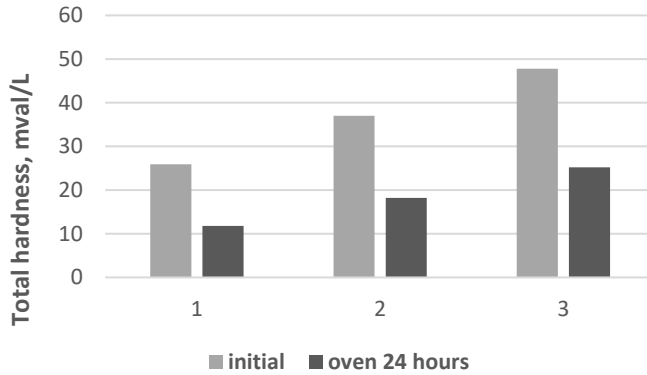


Figure 1a. Variation of total hardness in sparkling water blank samples
1 – $H_t = 25.9$ mval/L; 2 – $H_t = 37$ mval/L; 3- $H_t = 47.8$ mval/L

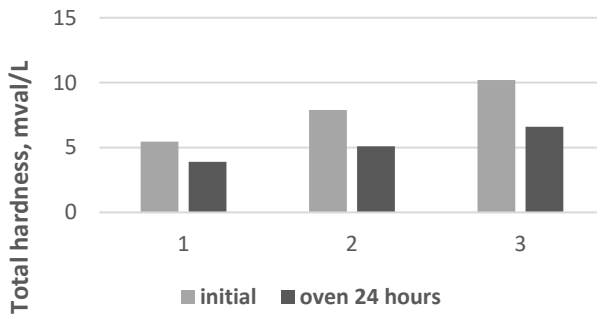


Figure 1b. Variation of total hardness in still drinking water blank samples
1 – $H_t = 5.45$ mval/L; 2 – $H_t = 7.9$ mval/L; 3- $H_t = 10.2$ mval/L

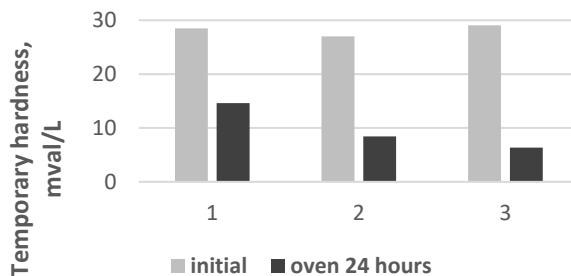


Figure 2a. Variation of temporary hardness in sparkling water blank samples
1 – $H_t = 25.9$ mval/L; 2 – $H_t = 37$ mval/L; 3- $H_t = 47.8$ mval/L

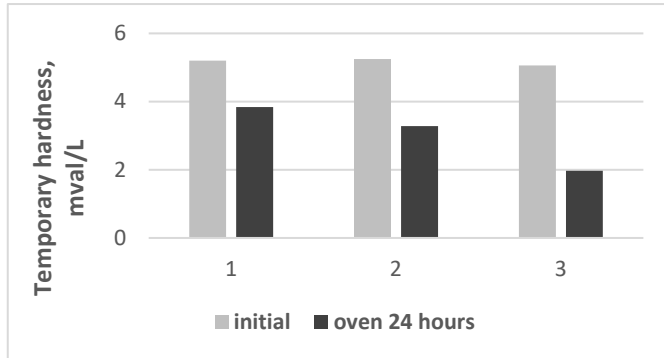


Figure 2b. Variation of temporary hardness in still water blank samples
1 – $H_t = 5.45$ mval/L; **2** – $H_t = 7.9$ mval/L; **3**– $H_t = 10.2$ mval/L

It is found that both the total and the temporary hardness of the sparkling water are clearly higher to those of still drinking water, both before and after standing in the oven. Also, the initial temporary hardnesses for each type of water are approximately equal, regardless of the initial value of total hardness. The percentages of decrease in total and temporary hardness, after keeping the samples in the oven, are shown in Figure 3.

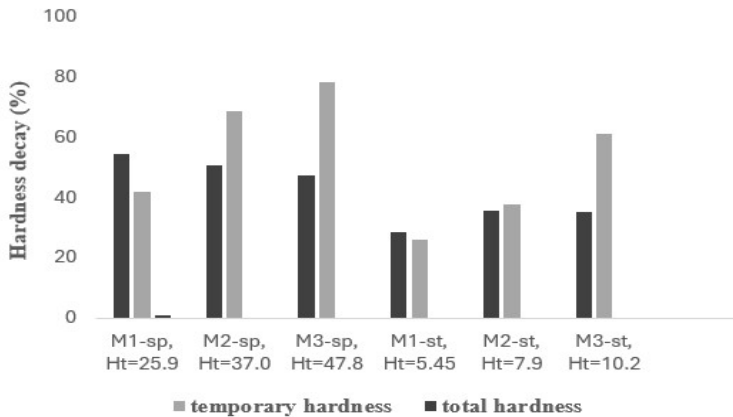


Figure 3. Decrease in temporary/total hardness of the blank samples after standing in the oven

It is observed that the hardness decay slow down with the increasing of total hardness within sparkling water. On the other hand, the increasing of temporary hardness facilitates the hardness decay for both type of studied waters.

For sparkling and still water samples treated with xanthan gum (XG) or guar gum (GG) (concentration 50mg/L or, respectively, 100mg/L) and kept in the oven under identical conditions to the blank samples, the efficiency of the scale inhibitor, calculated with rel. (1), is shown in Figures 4a and 4b.

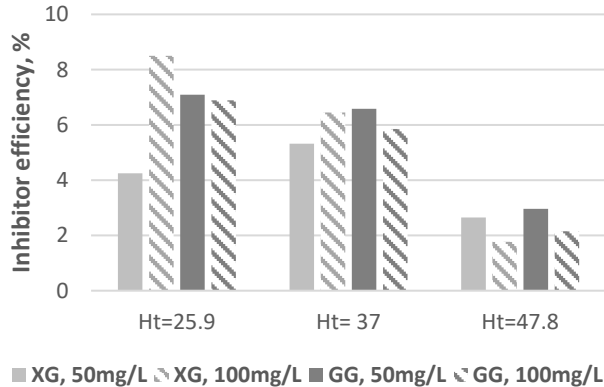


Figure 4a. The efficacy of xanthan/guar gums as scale inhibitor for sparkling water

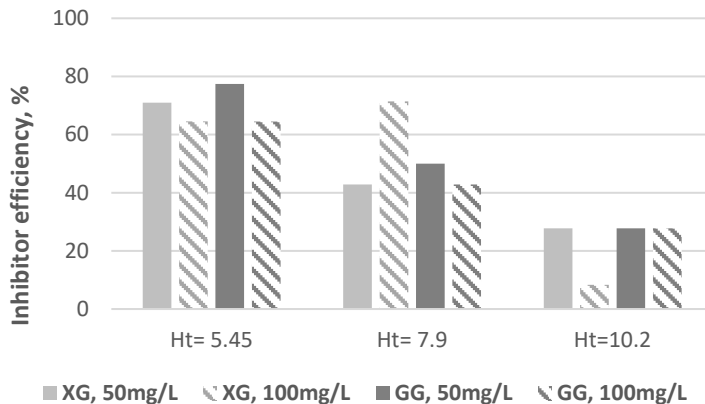


Figure 4b. The efficacy of xanthan/guar gums as scale inhibitor for still water

The two gums are found to be most effective in waters with lower initial hardness. Also, doubling the xanthan/guar gum concentration does not significantly influence the scale inhibition efficiency.

The effectiveness of xanthan/guar gum as scale inhibitor in waters with different total hardnesses was also verified by measuring electrical conductivity (σ), before and after standing in the oven, Table 1.

Table 1. Variation of electrical conductivity of water samples in the presence of scale inhibitors

Initial values	<i>Inhibition efficiency (%) / Electrical conductivity, $\mu\text{S/cm}$</i>				
	blank	XG 50mg/L	XG 100mg/L	GG 50mg/L	GG 100mg/L
$H_{\text{tot},i} = 5.45$ mval/L $\sigma_i = 490$ $\mu\text{S/cm}$	0 / 390	70 / 470	65 / 460	78 / 480	63 / 380
$H_{\text{tot},i} = 7.9$ mval/L $\sigma_i = 810$ $\mu\text{S/cm}$	0 / 541	42.9 / 676	71.4 / 794	50 / 755	42.9 / 686
$H_{\text{tot},i} = 25.9$ mval/L $\sigma_i = 1900$ $\mu\text{S/cm}$	0 / 1326	4.25 / 1361	8.5 / 1398	7.1 / 1389	-

The lower values of the efficiency of inhibiting the formation of scales in the case of the two gums are correlated with a more pronounced decrease in electrical conductivity, as a consequence of the reduction of ions number in the solution, therefore of the formation of scales.

The mechanism of crystal growth inhibition by the two gums can be explained by the electrostatic interaction between the partially negative charge of the functional groups of the inhibitor (OH groups or ether oxygen atoms) and the positive charges of the ions in the solution, according to [36]. The monosaccharide residues in the two gums contain multiple polar, hydroxylic groups which, through the density of electrons (non-participating p) constitute centers that electrostatically attract cations. Also, in the case of xanthan gum, a chemical adsorption between the carboxyl groups of glucuronic acid (C1:C6) and the cations in the solution is also possible.

In the case of water samples in which the efficiency of xanthan/guar gums had low values, the X-ray diffraction analysis of the precipitates formed after standing in the oven was carried out. Thus, for the blank sample of sparkling water having the initial total hardness of 25.9 mval/L, the X-ray diffractogram is presented in Figure 5a. For the water samples with the same initial hardness but with the addition of xanthan/guar gum (concentration 50mg/L), the corresponding diffractograms are shown in Figures 5b and 5c.

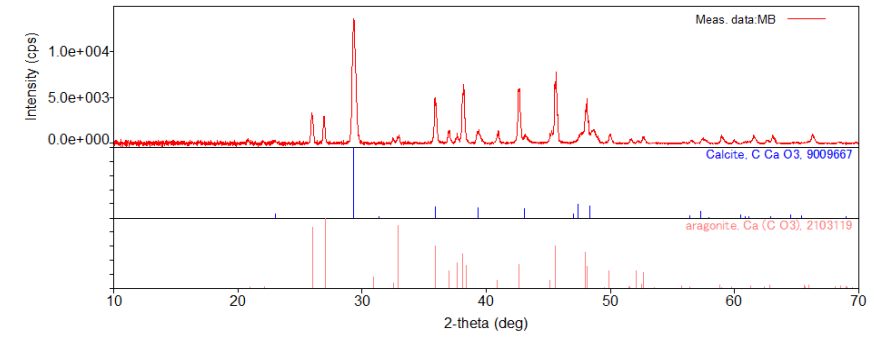


Figure 5a. X-ray diffractogram of CaCO_3 formed from the water sample with initial total hardness 25.9 mval/L

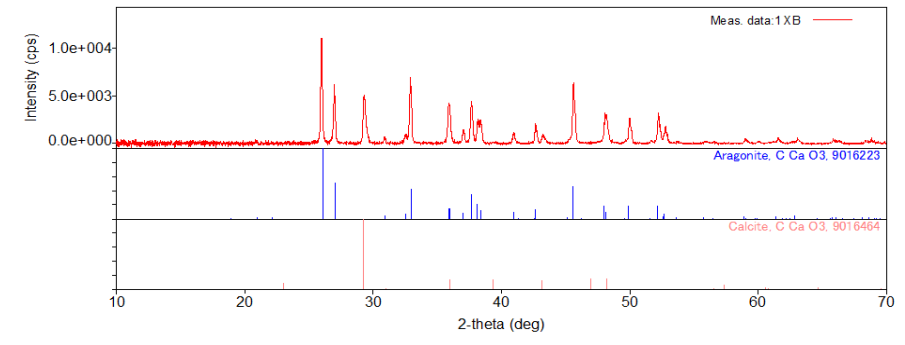


Figure 5b. X-ray diffractogram of CaCO_3 formed from the water sample with initial total hardness 25.9 mval/L and addition of XG 50mg/L

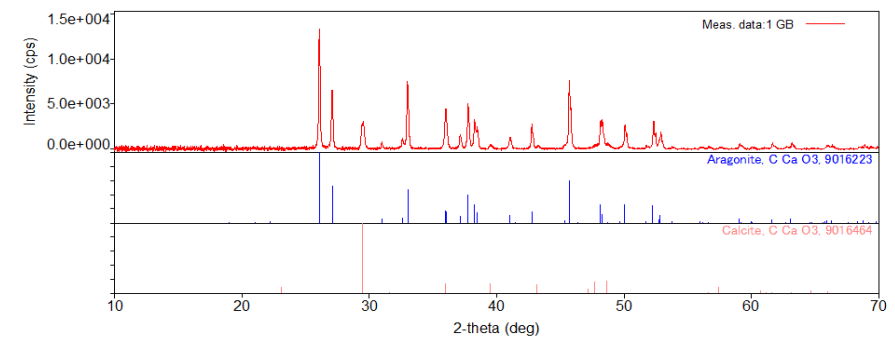


Figure 5c. X-ray diffractogram of CaCO_3 formed from the water sample with initial total hardness 25.9 mval/L and addition of GG 50mg/L

From the analysis of the three diffractograms it can be seen that the precipitate, formed after standing in the oven of the water sample without gums (sample MB in Figure 5a), has calcite (COD file 9009667) as its main phase and aragonite (COD file 2103119) as secondary phases. This fact is in accordance with a study regarding the characterization of powders obtained by drying natural sparkling mineral waters from public springs in Borsec which reveals that the dominant mineral (over 50% wt) is calcite [37]. Also, the precipitates formed after standing in the oven of the water samples with 50mg/L xanthan gum (sample 1XB in Figure 5b) and with 50mg/L guar gum (sample 1GB in Figure 5c) have aragonite (COD file 9016223) as the main phase, and as secondary phase calcite (COD file 9016464). It is observed that the intensity of the main peak in the diffractogram of the MB material, located at $2\theta = 29.3^\circ$ and corresponding to the calcite, is lower in the diffractograms of the 1XB and 1GB materials. At the same time, the first two peaks, located at 2θ of 26.0° and 27.0° and attributed to aragonite, have the most pronounced intensities in the 1XB and 1GB diffractograms compared to the MB diffractogram.

X-ray diffraction analysis of the precipitates demonstrates that, generally, the gums favor the crystallization of calcium carbonate in the form of aragonite as the main phase. The statement is also supported by data from the literature [38] which concludes that the main crystalline phase of CaCO_3 changes from calcite to aragonite after the addition of scale inhibitors.

CONCLUSIONS

Water samples with different values of the initial total hardness (natural or obtained by adding CaCl_2), to which aqueous solutions of guar gum or xanthan gum were added so that their concentration in the final solution was between 50mg/L and 100mg/L, were subjected to analysis. Xanthan gum and guar gum are part of the carbohydrate class, being natural, non-toxic and accessible polysaccharides that can be modified into more advantageous forms.

Both types of gums have proven their effectiveness in the inhibiting the formation of scales in waters with initial total hardness lower than 10mval/L.

Taking into account that low hardness waters are used in the processes of the food industry, the use of these types of gums as scale inhibitors has many benefits compared to the toxic inorganic inhibitors used regularly: (1) compatibility with the environment due to the fact that they are natural, biodegradable compounds; (2) high inhibition efficiency; (3) low costs

due to the fact that these gums are found in food industrial processes as stabilizing and thickening agents, thus minimizing the addition of additional reagents.

EXPERIMENTAL SECTION

Samples preparation and the working method

The analyzes were performed on still drinking water or sparkling water (products of the same company) without or with the additional addition of calcium salt (CaCl_2) to obtain a predetermined value of total hardness. The composition of the samples used in this study is presented in Table 2. From each type of water, 250 mL were measured to which were added the corresponding amounts of guar gum or xanthan gum aqueous solutions (initial concentrations of 1g/L and, respectively 2g/L), so that their final concentrations were either 50mg/L or 100mg/L. The flasks with water, covered, were placed in the thermostatic oven at 80°C for 24 hours. At the end of the stationary time in the oven, the water samples were cooled, filtered and were determined by titration their total and temporary hardness. These types of hardness were also measured before placing the samples in the oven. Both guar gum and xanthan gum were purchased from Sigma-Aldrich.

The electrical conductivity of the water samples, before and after the stationary time in the oven, was measured with a Multi 3320 WTW conductometer.

The phase composition of some of the precipitates collected on the filter paper was made using a Rigaku Ultima IV diffractometer (40 kV, 40 mA), equipped with a D/teX Ultra detector, using $\text{Cu}_{K\alpha}$ ($\lambda = 0,15406$ nm) radiation, in range $2\theta = 10\text{-}70^\circ$, with speed of $5^\circ/\text{min}$ and step of 0.01° . The assignment of the peaks corresponding to the crystalline phases present in the samples was performed by the Rigaku diffractometer software using the COD database [39].

Determination of the total and temporary hardness and calculation of scale inhibition effectiveness

The temporary hardness was determined by titrating a known volume of hard water with a 0.1N hydrochloric acid solution with a known factor, in the presence of methyl orange as indicator according to [40]. The total hardness was determined by the complexometric method, which involves titrating the sample with a solution of complexon III 0.01M (disodium salt of ethylenediaminetetraacetic acid – EDTA disodium salt) in the presence of Eriochrome Black T as indicator, at a pH value between 9 and 10, according to [40].

The scale inhibition efficiency (E) was calculated with rel. (1):

$$E = \frac{d_2 - d_1}{d_0 - d_1} \cdot 100 \quad (1)$$

where: d_0 - initial total hardness, d_1 – the total hardness of the blank sample after the oven, d_2 – the total hardness of the sample with inhibitor after the oven.

Table 2. Water samples composition

Sample	CaCl ₂ added (g/L)	Total hardness (mval/L)	Temporary hardness (mval/L)
M1-st	-	5.45	5.20
M2-st	0.1360	7.90	5.60
M3-st	0.2829	10.2	5.06
M1-sp	-	25.9	28.5
M2-sp	0.6160	37.0	28.8
M3-sp	1.3407	47.8	29.1

REFERENCES

1. D. Liu; *Research on performance evaluation and anti-scaling mechanism of green scale inhibitors by static and dynamic methods*, PhD Thesis, L'Ecole Nationale Supérieure d'Arts et Métiers Paris Tech, France, **2011**, pp.12-14
2. D. Dobersek; D. Goricanec; *Int. J. Math. Models Methods Appl. Sci.*, **2007**, 1(2), 55-61
3. Z. Amjad; P.G. Koutsoukos; *Desalination*, **2014**, 335, 55-63
4. D. Hasson; H. Shemer; A. Sher; *Ind. & Eng. Chem. Res.*, **2011**, 50, 7601-7607
5. J. MacAdam; S.A. Parsons; *Rev. Environ. Sci. Biotechnol.*, **2004**, 3, 159-169
6. R. Erany; *A study of scale and scaling potential during high salinity and low salinity waterflooding*, Master's Thesis, University of Stavanger, Norway, **2016**, pp. 23-32
7. A.A. Al-Hamzah; C.M. Fellows; *Desalination*, **2015**, 359, 22-25
8. C.B. Chew; R. Mat; *Chem. Eng. Trans.*, **2015**, 45, 1471-1476
9. B. Senthilmurugan; B. Ghosh; S.S. Kundu; M. Haroun; B. Kameswari; *J. Pet. Sci. Eng.*, **2010**, 75 (1-2), 189-195
10. W. Wand; Y-G. Yi; Z-F. Sun; S-B. Dong; W-C. Du; *Key Eng. Mater.*, **2019**, 814, 511-516
11. D. Liu; W. Dong; F. Li; F. Hui; J. Ledion; *Desalination*, **2012**, 304, 1-10
12. D. Peronno; H. Cheap-Charpentier; O. Horner; H. Perrot; *J. Water Process Eng.*, **2015**, 7, 11-20
13. M-L. Zhang; Z. Ruan; Y. Han; Z-W. Cao; L. Zhao; Y-Q. Xu; Z-Y. Cao; W-Y. Shi; Y. Xu; *Desalination*, **2024**, 570, 117080
14. A. Mohseni; L. Mahmoodi; M.R. Malayeri; *Adv. Powder Technol.*, **2023**, 34, 103954
15. X. Zhou; Y. Sun; Y. Wang; *J. Environ. Sci.*, **2011**, 23, S159-S161
16. F. De Campo; S. Kesavan; G. Woodward; *Polysaccharide based scale inhibitor*, European Patent EP 2 148 908 B1, **2010**

17. R.S. Fernandes; W.D.L. Santos; D.F. de Lima; M.A.F. de Souza; B.B. Castro; R.C. Balaban; *Desalination*, **2021**, 515, 115201
18. S. Zhang; J. Ding; D. Tian; M. Chang; X. Zhao; M. Lu; *J. Mol. Struct.*, **2023**, 1272, 134157
19. L. Castillo; E. Torin; J.A. Garcia; M. Carrasquero; M. Novas; A. Vilorio; *New product for inhibition of calcium carbonate scale in natural gas and oil facilities based on Aloe Vera: Application in venezuelan oilfields*, Latin American and Caribbean Petroleum Engineering Conference, Cartagena, **2009**, SPE-1230077-PP
20. M.A.J. Mazumder; *Coatings*, **2020**, 10, 928-956
21. Z. Belarbi; J. Gamby; L. Makhloufi; B. Sotta; B. Tribollet; *J. Cryst. Growth*, **2014**, 386, 208-214
22. Z. Belarbi; B. Sotta; L. Makhloufi; B. Tribollet; J. Gamby; *Electrochim. Acta*, **2016**, 189, 118-127
23. O. Horner; H. Cheap-Charpentier; X. Cachet; H. Perrot; J. Ledion; D. Gelus; N. Pecoul; M. Litaudon; F. Roussi; *Desalination*, **2017**, 409, 157-162
24. A.M. Abdel-Gaber; B.A. Abd-El-Nabey; E. Khamis; D.E. Abd-El-Khalek; *Desalination*, **2008**, 230 (1-3), 314-328
25. A.M. Abdel-Gaber; B.A. Abd-El-Nabey; E. Khamis; D.E. Abd-El-Khalek; *Desalination*, **2011**, 278 (1-3), 337-342
26. Z. Mohammadi; M. Rahsepar; *Res. Chem. Intermed.*, **2018**, 44(3), 2139-2155
27. M. El Housse, A. Hadfi, N. Iberache, I. Karmal, F. El-Ghazouani, S. Ben-Aazza, M. Belattar, I. Ammayen, M. Nassiri, S. Darbal, Y. Riadi, M. Ikiss, A. Driouiche; *Ind. Crops Prod.*, **2024**, 222, 120030
28. Karmal, M. El Housse, A. Hadfi, J. El Gaayda, A. Oulmekki, J.E. Hazm, S. Ben_Aazza, M. Belattar, S. Mohareb, N. Hafid, R.A. Akbour, M. Hamdani, A. Driouiche; *Desalin. Water Treat.*, **2021**, 240, 115-123
29. M. Nassiri, I. Karmal, S. Darbal, M. El Housse, S. Ben-Aazza, M. Belattar, A. Driouiche; *J. Water Process Eng.*, **2024**, 65, 105846
30. E.S. Suharso, A.K. Agung, H.S. Buhani, *Desalin. Water Treat.*, **2019**, 169, 29-37
31. G. Vasyliiev, V. Vorobyova, T. Zhuk, O. Kalinchuk; *Mater. Today Proc.*, **2022**, 50, 477-482
32. Z. Mohammadi; M. Rahsepar; *J. Alloys Compd.*, **2019**, 770, 669-678
33. A.M. Abdel-Gaber; B.A. Abd-El-Nabey; E. Khamis; H. Abd-El-Rhmann; H. Aglan; A. Ludwick; *Int. J. Electrochem. Sci.*, **2012**, 7, 11930-11940
34. R. Menzri; S. Ghizellaoui; M. Tlili; *Desalination*, **2017**, 404, 147-154
35. K.I. Popov; N.E. Kovaleva; G.Y. Rudakova; S.P. Kombarova; V.E. Larchenko; *Therm. Eng.*, **2016**, 63, 122-129
36. A.E. Elkholy; H.F. El-Taib; A.M. Rashad; K.Zakaria; *J.Pet.Sci.Eng.*, **2018**, 166, 263-273
37. S.A. Avram; D.V. Platon; L.B.Tudoran; G.Borodi; I.Petean; *Appl.Sci.-Basel*, **2024**, 14(23), 10806
38. X. Li; B. Gao; Q. Yue; D. Ma et al.; *J. Environ. Sci.*, **2015**, 29, 124-130
39. Crystallography Open Database, <http://www.crystallography.net/cod/>
40. L. Andronic; A. Duță; *Analize fizico-chimice și metode avansate de epurare a apelor uzate*, Ed. Universității Transilvania, Brașov, **2013**.

GREEN SPECTROPHOTOMETRIC METHOD FOR CONCURRENT ESTIMATION OF PIROXICAM AND MEFENAMIC ACID MIXTURE

Fatma A. A. AL ANI^a, Azhar S. HAMODY^a , Ruaa M. MAHMOOD^a,
Nahla A. ALASSAF^a , Dhafir T.A. AL-HEETIMI^{a,*} 

ABSTRACT. The purpose of this work is to concurrently estimate the UV-visible spectra of binary combinations of piroxicam and mefenamic acid using the chemometric approach. To create the model, spectral data from 73 samples (with wavelengths between 200 and 400 nm) were employed. A two-layer artificial neural network model was created, with two neurons in the output layer and fourteen neurons in the hidden layer. The model was trained to simulate the concentrations and spectra of piroxicam and mefenamic acid. For piroxicam and mefenamic acid, respectively, the Levenberg-Marquardt algorithm with feed-forward back-propagation learning produced root mean square errors of prediction of 0.1679 µg/mL and 0.1154 µg/mL, with coefficients of determination of 0.99730 and 0.99942, respectively. The suggested approach's ease of use, affordability, and environmental friendliness make it a suitable replacement for the use of hazardous chemicals in the routine investigation of the selected drugs.

Keywords: *piroxicam, mefenamic acid, concurrent estimation, artificial neural networks model*

INTRODUCTION

Nonsteroidal anti-inflammatory drugs, or NSAIDs, are among the most prescribed therapeutic agents. They can be used alone or in conjunction with other medications to treat a variety of clinical signs and symptoms, including both acute and chronic pain, as well as a variety of musculoskeletal disorders [1].

^a Department of Chemistry, College of Education for Pure Science/ Ibn Al-Haitham, University of Baghdad, Baghdad-Iraq.

* Corresponding author: dhafir.t.a@ihcoedu.uobaghdad.edu.iq, dhafir1973@gmail.com



In 1982, piroxicam was first made available as Feldene in the United States, where it was quickly accepted [2]. It is used to treat acute gout and to relieve the symptoms of rheumatoid arthritis, osteoarthritis, and both in short- and long-term therapy [3]. One derivative of anthranilic acid is mefenamic acid [4]. Although it has some mild anti-inflammatory activity, its principal use since its introduction to the United States in 1967 has been pain relief [2]. Mefenamic acid inhibits both the generation of prostaglandins and the tissue's reaction to them. It is mostly eliminated in the urine and is strongly attached to plasma proteins [5]. Figure 1 displays the mefenamic acid and piroxicam structural formulas [6].

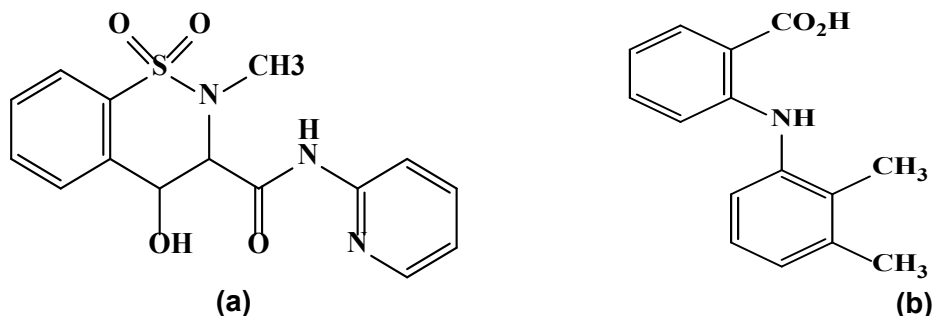


Figure 1. Structures formula of (a) piroxicam and (b) mefenamic acid

A review of the literature reveals several standard analytical methods for the simultaneous or individual quantification of pharmaceutical formulations, bodily fluids, and the pharmaceuticals under study in bulk. Spectrophotometry [7–9], potentiometry [10–11], GC-Mass [12–13], flow injection analysis [14,15], and HPLC [16–18] are a few of these techniques.

For quantitative pharmaceutical analysis, spectrophotometry in conjunction with chemometric methods like artificial neural networks (ANNs) is the most practical, cost-effective, and adaptable analytical approach [19]. As far as we are aware, no report has utilised this technique (ANNs) to determine piroxicam and mefenamic acid together.

The primary objective of this study is to broaden the application of chemometric techniques, such as artificial neural networks (ANNs), for the simultaneous prediction of mefenamic acid and piroxicam in their binary synthetic mixes. ANNs are well-suited to model the nonlinear relationships between variables. This making them effective for analyzing complex chemical

data where traditional linear methods might fall short. ANNs learn from data, meaning they can be trained on a dataset of known spectra and concentrations to develop a model that can predict the concentrations of piroxicam and mefenamic acid in unknown samples. This data-driven approach allows for high accuracy and adaptability. Once trained, ANNs can quickly and accurately analyze new samples without the need for extensive manual intervention. This makes the method highly efficient for routine analysis in laboratories. Finally, ANNs can handle noisy and incomplete data better than many traditional methods. This robustness is particularly valuable in chemical analysis, where experimental data can often be imperfect.

The primary distinction between the current green investigation and the earlier published work is the simultaneous determination of both forms without the need for laborious stages like species masking or separation, minimizes waste generation by using UV spectra, and in addition, the ANN method performed at ambient temperature and pressure, reducing energy consumption.

RESULTS AND DISCUSSION

Having overlapped spectral features makes it difficult to distinguish between different species when conducting spectrophotometric studies of them in combination. An ANN model made it feasible to conduct these kinds of investigations, where there is a great deal of overlap in the responses of the components under study [19].

Figure 2 represents the absorption spectra of piroxicam and mefenamic acid as well as their mixture which show a strong spectral overlap. To overcome this problem, the ANN method was proposed, which was associated with spectrophotometry.

To build up the ANN model, spectral data of 73 synthetic binary mixture at various piroxicam concentrations (1.0–13.0 $\mu\text{g/mL}$) and mefenamic acid (1.0–18.0 $\mu\text{g/mL}$) were used (Figure 3). This range of concentration is adopted to ensure that the absorption value of the mixture is kept within the limits preferred in Pierre Lambert's law, namely (1.5-2.0). These spectra were recorded in wavelength range of (200–400) nm to improve, standardize, and validate the recommended model. In this method, there is no optimal wavelength to measure, but the entire absorption spectrum is taken to describe the concentration in question.

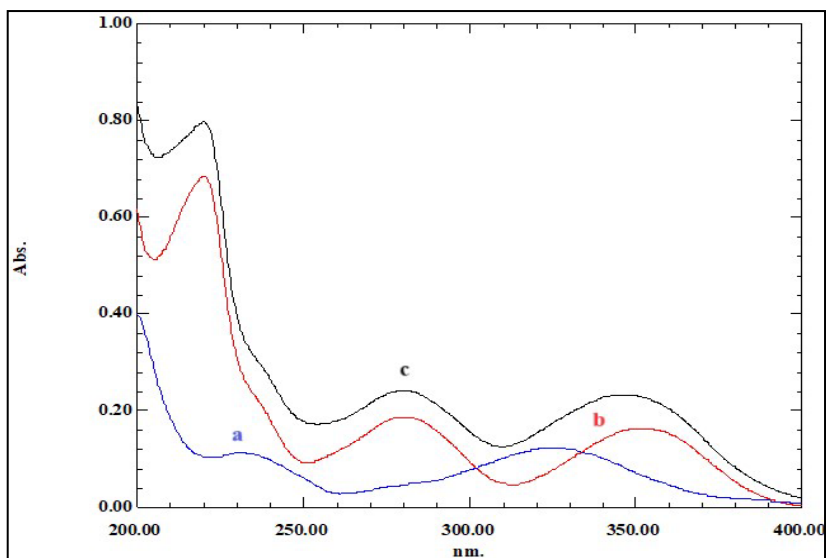


Figure 2. Absorption spectra of (a) 2µg/mL piroxicam (b) 6µg/mL mefenamic acid and (c) mixture of 2µg/mL piroxicam and 6µg/mL mefenamic acid, all of it against methanol as a blank solution

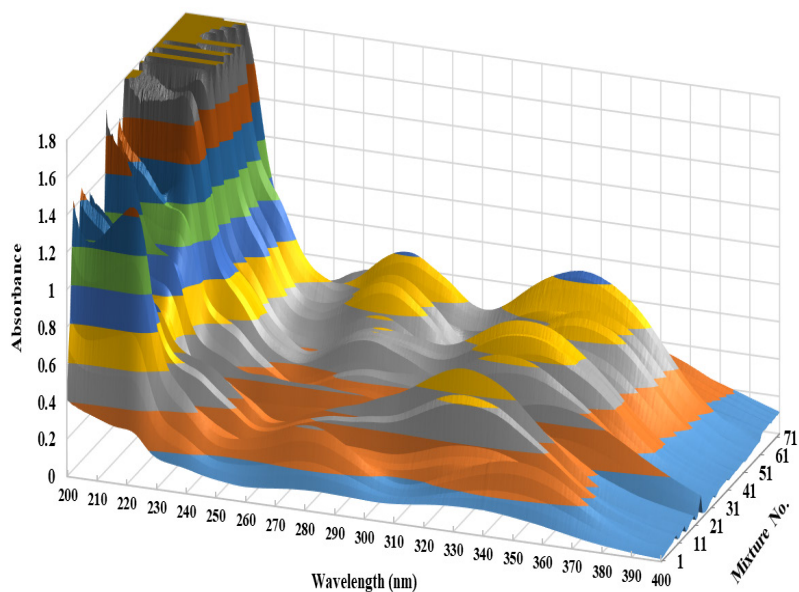


Figure 3. Three-dimensional absorbance spectra of 73 mixtures of piroxicam (1.0-13.0 µg/mL) and mefenamic acid (1.0-18.0µg/mL) against methanol as a blank solution

GREEN SPECTROPHOTOMETRIC METHOD FOR CONCURRENT ESTIMATION
OF PIROXICAM AND MEFENAMIC ACID MIXTURE

In order to model the concentrations of piroxicam and mefenamic acid, the spectral data matrix of their mixtures, which included the absorbance of 73 mixture, was added as an input data, and the experimental concentrations of both drugs were added to the network toolbox separately as target matrices. This is because the ANN construction is a crucial parameter to determine the performance of the model. The total number of inputs was 2002, with 1001 inputs for absorption and 1001 inputs for wavelengths. The wavelength increased in increments of 0.2 nm, ranging from 200 nm to 400 nm.

A multi-layered neural network with Levenberg–Marquardt training algorithm for its quick merging was established. A MATLAB program for a two-layered artificial neural network was created. This model has two input vectors (wavelengths and absorbances), two output vectors (concentration of piroxicam and mefenamic acid), and fourteen neurones in the hidden layer. Figure 4 shows the created neural network and its training techniques as well as its performance over time.

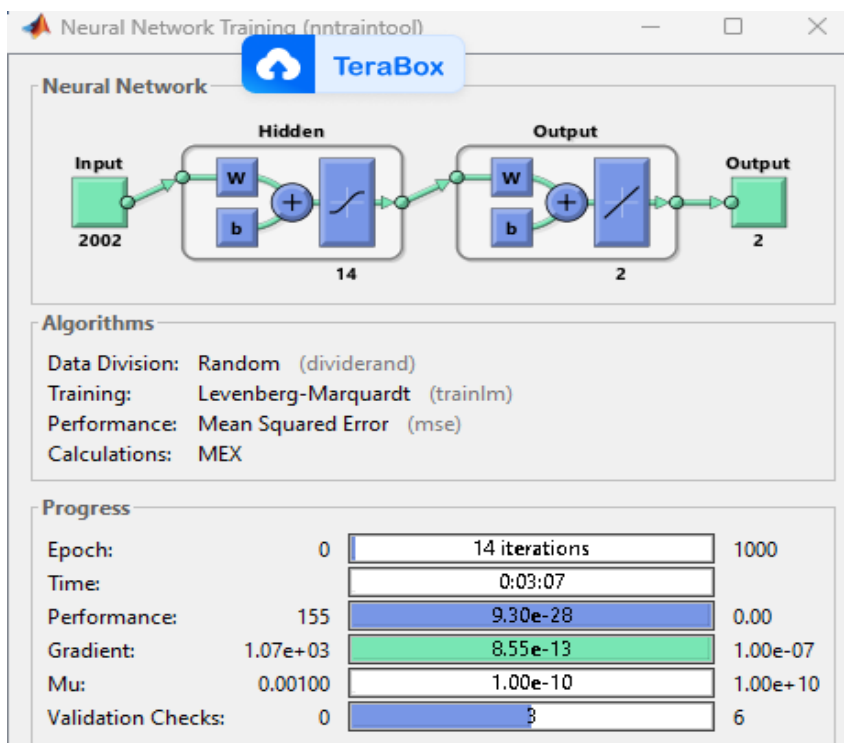


Figure 4. Architecture of the proposed ANN used for training the experimental spectral data

In accordance with standard protocol for ANN model training, seventy percent of the data were allocated to network training (51 mixture), fifteen percent were used for network validation (11 mixture), and the remaining fifteen percent were fed into the network (11 mixture) as test data to gauge the model's predictive capacity. Figure 5 shows the performance of the model over multiple epochs. An epoch refers to one complete pass through the entire training dataset. During an epoch, the model processes each example in the training set once, and the model's parameters (weights and biases) are updated based on the errors made during this pass. Highlighting the point at which the model achieved its best validation performance is crucial for understanding the model's learning process and determining the optimal number of epochs for training. "Best Validation Performance is 0.49767 at epoch 11," indicating that the lowest validation error was achieved at epoch 11 with a value of 0.49767.

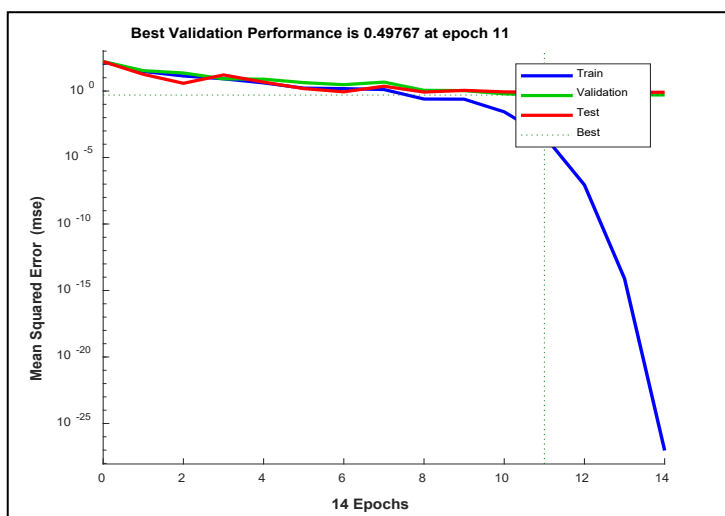


Figure 5. The training 14 epoch versus mean square error (mse)

As seen in Figure 6, the predicted and actual concentrations of mefenamic acid and piroxicam are plotted. Better predictions from both components are supported by higher values of the coefficient of determination (R) for training, validation, and testing. Rejecting and retraining any findings that are not satisfactory is a crucial step in the computation mode.

GREEN SPECTROPHOTOMETRIC METHOD FOR CONCURRENT ESTIMATION OF PIROXICAM AND MEFENAMIC ACID MIXTURE

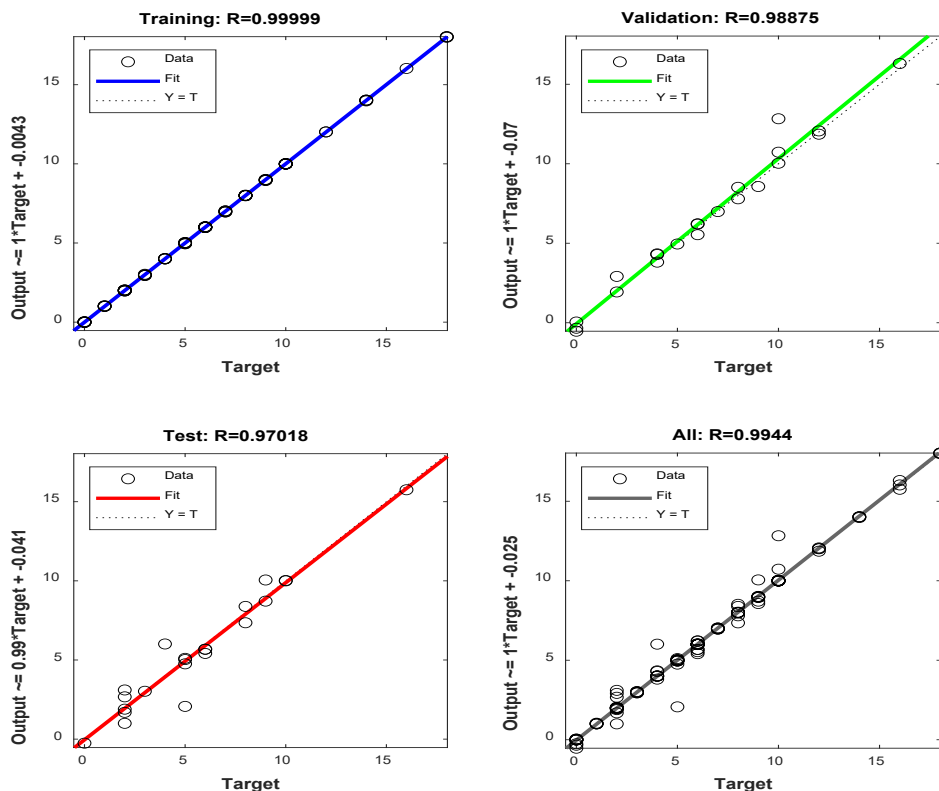


Figure 6. Actual concentrations versus the predicted concentrations and R values for training, validation, and testing series of the proposed ANN model

Following model fine-tuning, the ANN's training phase was carried out independently for each component using Levenberg-Marquardt techniques for error minimisation. Table 1 shows the RMSE and R² for each component at each step.

Table 1. The performance parameters of the proposed ANN model

Data	No. of Samples	Mefenamic acid		Piroxicam	
		RMSE (µg/mL)	R ²	RMSE (µg/mL)	R ²
Training	51	0.09903585	0.999324	0.17661867	0.997241
Validation	11	0.10195360	0.999602	0.08162060	0.999648
Testing	11	0.09854842	0.999512	0.21328921	0.993747

The following formulas are used to compute the coefficient of determination (R^2) and root mean square error (RMSE) [20]:

$$RMSE = \sqrt{\frac{\sum_{i=1}^N (\hat{y}_i - y_i)^2}{N}}$$

$$R^2 = 1 - \frac{\sum_{i=1}^N (\hat{y}_i - y_i)^2}{\sum_{i=1}^N (\bar{y}_i - y_i)^2} \quad , \text{ where:}$$

\hat{y}_i predicted concentration in the i th sample,
 y_i actual value for the sample concentration,
 \bar{y}_i mean of the actual values,
 N number of samples in validation group.

After retraining, the data evaluated in the model indicated about 100% fitting, which is indicative of the conformation of the ANN model. Figures 7 and 8 show the plotted architecture of the ANN model. The blue line represents the taken concentration ($\mu\text{g/mL}$) that was supposed to be present in each sample while the red line represents the predicted (found) concentration ($\mu\text{g/mL}$) detected in each sample through analysis. The closer the red line is to the blue line, the more accurate the detection method is. By examining the trends in the graph, we can identify patterns or anomalies in the detection process.

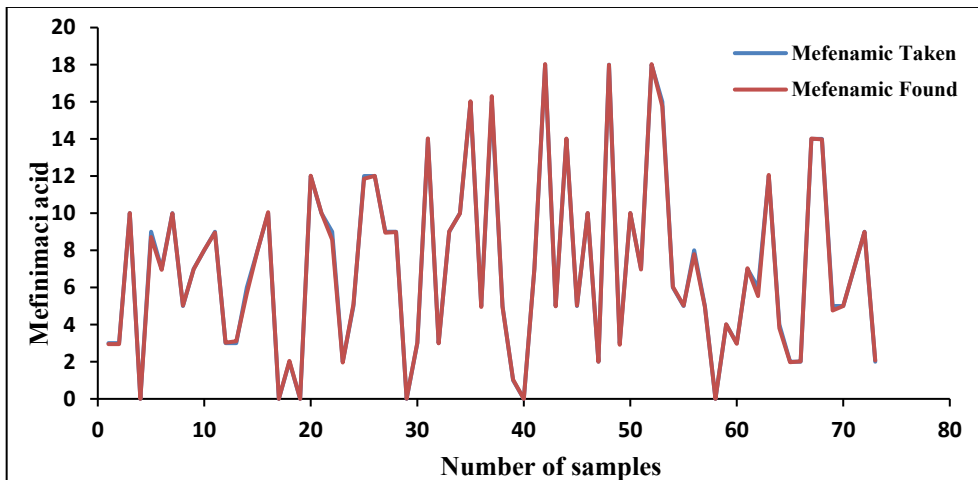


Figure 7. ANN model for Mefenamic acid

GREEN SPECTROPHOTOMETRIC METHOD FOR CONCURRENT ESTIMATION
OF PIROXICAM AND MEFENAMIC ACID MIXTURE

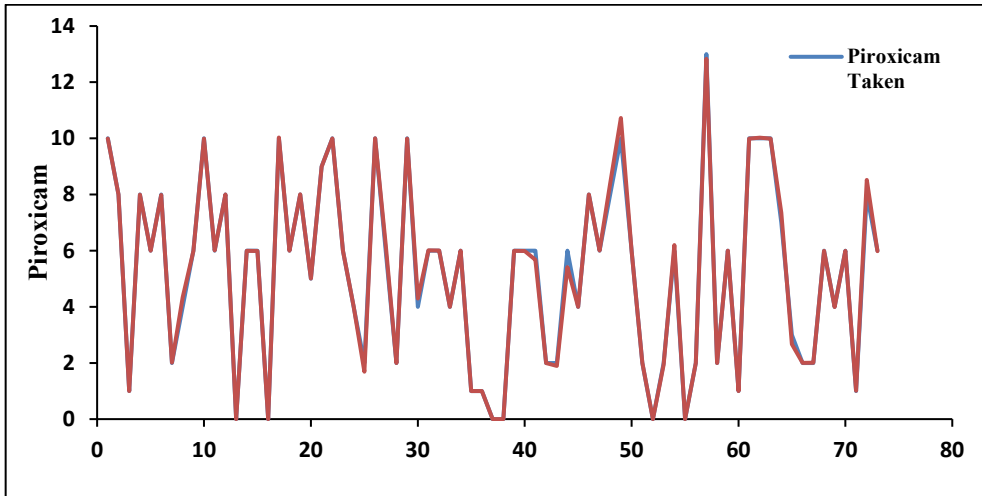


Figure 8. ANN model for Piroxicam

Figure 9 represent the error distribution where the majority of errors are centred around zero, indicating that the model's predictions are generally close to the actual target values. The blue bars represent the errors for the training dataset. Most of these errors are clustered around zero, with a few instances showing larger errors. This indicates that the model has learned well from the training data. The green bars represent the errors for the validation dataset. These errors are also mostly centred around zero, but there are some instances with larger errors. This suggests that the model is generalizing well to new data, but there is still room for improvement. The red bars represent the errors for the test dataset. Similar to the validation dataset, the errors are mostly centred around zero, with a few larger errors. This indicates that the model's performance on unseen data is consistent with its performance on the validation data. The orange line represents zero error, serving as a reference point. The closer the bars are to this line, the better the model's predictions. The ANN model's display of the error histogram indicates random variation in the absence of systematic error.

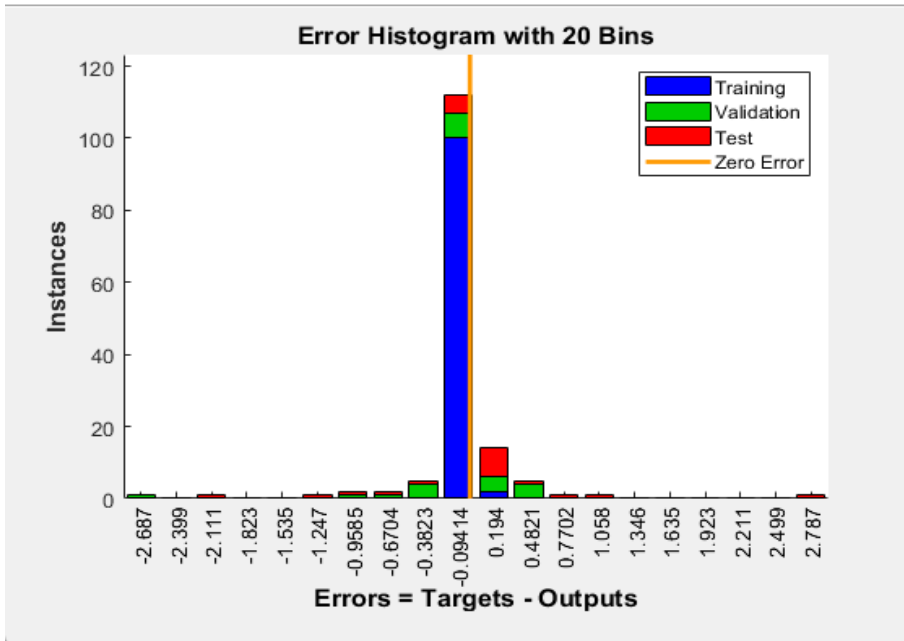


Figure 9. Error histogram for ANN model

The performance of the proposed method is also evaluated using the percentage recovery values (Rec%) of the concentrations of both mefenamic acid and piroxicam. Results of Rec% in Table 2 show the successful applicability of ANN model for concurrent estimation of both components in their mixture.

Table 2. Recoveries of mefenamic acid and piroxicam in 11 test samples by the ANN model

Mixture No.	Mefenamic acid			Piroxicam		
	Taken (µg/mL)	Found (µg/mL)	Rec%	Taken (µg/mL)	Found (µg/mL)	Rec%
1	18	18.033	100.18	10	9.991	99.91
2	10	10.013	100.13	6	5.984	99.73
3	12	12.020	100.17	13	12.831	98.70
4	14	14.025	100.18	2	2.003	100.15
5	16	16.027	100.17	2	2.010	100.50
6	18	18.033	100.18	6	5.995	99.92
7	10	9.984	99.84	4	3.994	99.85
8	12	11.859	98.83	6	5.993	99.88
9	14	13.975	99.82	1	1.011	101.10
10	18	17.994	99.97	10	10.023	100.23
11	16	15.754	98.46	6	5.984	99.73

GREEN SPECTROPHOTOMETRIC METHOD FOR CONCURRENT ESTIMATION
OF PIROXICAM AND MEFENAMIC ACID MIXTURE

Using Anova: Single Factor, the findings of the suggested ANN model for each drug were statistically compared with those of the created RP-HPLC method [16] in term of recoveries of the found concentration from calibration graphs (Figure 6) and PLS calibration model [9] in term of recoveries of the predicted concentration of validation set (Figure 6, A and D). The results of Table 3 show that there is a statistically significant difference between the means of the three groups, as indicated by a higher F statistic value (7.67608, 7.66838 for mefenamic acid and piroxicam, respectively) and a p-value less than $\alpha = .05$. Therefore, the null hypothesis of the ANOVA is rejected. Based on the summary statistics and ANOVA results, the ANN method appears to be the best for estimating mefenamic acid and piroxicam, as it has the highest average and the lowest variance, indicating more accurate and consistent results.

Table 3. An summary of the one-way ANOVA comparison between the reported methods (HPLC method and PLS model) and the proposed ANN model

<i>Summary Statistics of Mefenamic acid estimation</i>						
<i>Method</i>	<i>Count</i>	<i>Sum</i>	<i>Average</i>	<i>Variance</i>		
PLS	10	992.9867	99.2987	2.86314		
HPLC	10	978.9289	97.8929	1.66270		
ANN	10	1000.5516	100.0552	0.17965		
ANOVA						
<i>Source of Variation</i>	<i>SS</i>	<i>df</i>	<i>MS</i>	<i>F</i>	<i>P-value</i>	<i>F crit</i>
Between Groups	24.0797	2	12.03987	7.67608	0.00229	3.35413
Within Groups	42.3493	27	1.56849			
<i>Summary Statistics of Piroxicam estimation</i>						
<i>Method</i>	<i>Count</i>	<i>Sum</i>	<i>Average</i>	<i>Variance</i>		
PLS	10	995.2936	99.5294	1.00113		
HPLC	10	981.7495	98.1746	2.15856		
ANN	10	1000.0700	100.0070	0.37511		
ANOVA						
<i>Source of Variation</i>	<i>SS</i>	<i>df</i>	<i>MS</i>	<i>F</i>	<i>P-value</i>	<i>F crit</i>
Between Groups	18.07078	2	9.03539	7.66838	0.00231	3.35413
Within Groups	31.81320	27	1.17827			

- Null hypothesis: The means of all selected datasets are equal.
- Alternative hypothesis: The means of one or more selected datasets are different.
- At the 0.05 level, the population means are not significantly different.

CONCLUSION

Because of spectrum overlap, it might be difficult to accurately determine the concentration of two species at the same time using traditional spectroscopy. In many domains, chemometric and machine learning algorithms are increasingly widely used, but they are particularly well-liked in multivariate spectroscopic investigation of complicated mixtures. The relationship between UV spectra and the simultaneous levels of piroxicam and mefenamic acid was modelled using an artificial neural network.

In addition to having low mean square error values for prediction, the constructed ANN model also has a high determination coefficient from the model's external validation and adequate recovery values, which make it capable of resilient concurrent analysis.

EXPERIMENTAL

Apparatus

Shimadzu 1800 UV-vis spectrophotometer, equipped with 1 cm quartz cells with UV Prob 2.34 software included, was used to accomplish all of the absorption spectra. The 200–400 nm wavelength range, 0.2 nm data interval, medium scan rate, single scan mode, and 1.0 mm slit width were all used for the scans. Every sample was scanned three times, and its representation was derived from the average of three spectra. No pre-processing was done on the spectral data.

Software

A Simplex Lattice Mixture Design, developed by JMP® 11.0.0 SAS Institute Inc., was utilised to generate a series of calibration mixtures for the simultaneous measurement of piroxicam and mefenamic.

Chemicals and reagents

The State Company for Drug Industries and Medical Appliances Samara-Iraq (SDI) provided the piroxicam and mefenamic acid raw powders utilised in this investigation, which had a purity of 99.99%. The methanol used in this study was an analytical grade reagent.

Standard and working solutions

Mefenamic acid and piroxicam standard stock solutions (1000 µg/mL) were made individually by dissolving 0.050 g of each medication in 50 mL methanol. Working solutions were prepared as needed by the process of serial dilution.

Data analysis

MATLAB (version 9.1.0 R2021a, Math Work, Inc) was used for obtaining the analysed data.

ACKNOWLEDGEMENT





I express my sincere gratitude to Ass. Prof. Saad Ali Ahmed for his efforts in creating the artificial neural network model that served as the basis for this investigation. His help was invaluable in expediting the decision-making process and enabling the analysis performed for this study.

REFERENCES

1. R. Brennan; M. Wazaify; H. Shawabkeh; I. Boardley; J. McVeigh; M.C.Van Hout; *Drug Saf.*, **2021**, *44*,917-928.
2. V. F. Roche; S. W. Zito; T. L. Lemke; D. A. Williams; *Foye's principles of medicinal chemistry*, 8th ed.; Lippincott Williams & Wilkins, **2019**, p.1018.
3. V. Alagarsamy; *Textbook of medicinal chemistry*, Elsevier Health Sciences, **2010**, p.92.
4. J. K. Aronson; *Meyler's side effects of analgesics and anti-inflammatory drugs*; Elsevier, **2009**, p.310.
5. H. Benzon; S. N. Raja; S. M. Fishman; S. Liu; S. P. Cohen; *Essentials of pain medicine*, 3rd ed.; Elsevier Health Sciences, **2011**, p.135.
6. *British Pharmacopoeia*, London, UK, **2022**, volume II, 217, 648.
7. S. Singh; J. R. Patel; S. Kare; *Asian J. Res. Chem.*, **2016**, *9*(2), 82-84.
8. H. Wasit; D. Purnamasar; M. S. Fareza; *Malaysian J. Anal. Sci.*, **2021**, *25*(1),71-80.
9. R. M. Mahmood; S. A. Darweesh; N. A. Alassaf; R. S. Al-Khalisy; *Methods Objects Chem. Anal.*, **2024**,*19*(2), 101-110.
10. N. Rajendraprasad; K. Basavaiah; *Curr. Chem. Lett.*, **2016**, *5*(1), 33-46.
11. Z. A. Kormosh; O. Y. Matviichuk; I. P. Antal; Y. R. Bazel; *J. Anal. Chem.*, **2020**, *75*(6), 820-828.

12. A. Krokos; E. Tsakelidou; E. Michopoulou; N. Raikos; G. Theodoridis; H. Gika; *Separations*, **2018**, 5, 37.
13. B.M. El Haj; A.M. Al Ainri; M.H. Hassan; R.K. Bin Khadem; M.S. Marzouq; *Forensic Sci. Int.*, **1999**, 105, 141–153.
14. R. I. Abed; H. Hadi; *Bull. Chem. Soc. Ethiop.*, **2020**, 34(1), 13-23.
15. L. Al-Ameer; K. K. Hashim; D. N. Taha; *Water Pract. Technol.*, **2022**, 17(9), 1881-1892.
16. S. B. Dikran; R. M. Mahmood; *J. Univ. Babylon Pure Appl. Sci.*, **2018**, 26(5), 387-399.
17. M. Celebier; M. Nenni; O. Kaplan; E. Akgeyik; M. S. Kaynak; S. Şahin; *Turkish J. Pharm. Sci.*, **2020**, 17(5), 535-541.
18. V.N.K. Kopparapu; P. Kasula; A.K.R. Ankinapalli; M. Venkateswarlu; *International Journal of Pharmaceutical Quality Assurance*, **2019**, 10(4), 583-587.
19. A.S. Hamody; F.H. Zankanah; S.A. Ali; N. Alassaf; S.B. Dikran; *Methods Objects Chem. Anal.*, **2022**, 17(3), 118-124.
20. Y. Nausheen; S. M. Naqvi; S. M. Akhter; *Heliyon*, **2024**, 10(4), 2024, e26373,

DEVELOPMENT AND VALIDATION OF AN LC-MS/MS METHOD FOR THE QUANTIFICATION OF SIX CANNABINOIDS IN COMMERCIAL PRODUCTS

Ruxandra ȘTEFĂNESCU^a, Robert-Alexandru VLAD^{a*},
Silvia IMRE^{a,d}, Amelia TERO-VESCAN^b, Bianca-Eugenia ÓSZ^a,
Dan-Dragoș SITA^c, Lénárd FARCZÁDI^d

ABSTRACT. Cannabidiol (CBD) oils and products have become extremely popular in the last decade. These products are marketed as having different effects and are recommended for many chronic diseases. Various food supplements with CBD are now available on the market, but due to legislative lacks the declared concentration of CBD and other cannabinoids in the products is often significantly different compared with the real concentration. Products that don't meet quality criteria result from a lack of control and standardization. The aim of this study was to develop and validate an LC-MS/MS method for the routine quantification of cannabinoids in herbal drugs and food supplements. An LC-MS/MS method was developed using an UHPLC system coupled with a QTOF mass spectrometer, and the chromatographic separations were performed on a C18 column with isocratic elution, electrospray ionization in negative mode with a run-time of 10

^a George Emil Palade University of Medicine, Pharmacy, Science and Technology of Targu Mures, Faculty of Pharmacy, Gheorghe Marinescu Street, no. 38, 540142, Târgu Mureș, Romania

^b George Emil Palade University of Medicine, Pharmacy, Science and Technology of Targu Mures, Faculty of Medicine in English, Gheorghe Marinescu Street, no. 38, 540142, Târgu Mureș, Romania

^c George Emil Palade University of Medicine, Pharmacy, Science and Technology of Targu Mures, Faculty of Medicinal Dentistry, Gheorghe Marinescu Street, no. 38, 540142, Târgu Mureș, Romania

^d George Emil Palade University of Medicine, Pharmacy, Science and Technology of Targu Mures, Chromatography and mass spectrometry laboratory, Center for Advanced Medical and Pharmaceutical Research, Gheorghe Marinescu Street, no. 38, 540142, Târgu Mureș, Romania

* Corresponding author: robert.vlad@umfst.ro



minutes. According to the international guidelines, the method was validated concerning linearity, selectivity, stability, precision, and accuracy. Out of the ten tested products, in three of the supplements, significant differences were noticed in CBD concentration compared to the declared content. Other cannabinoids were also identified in some of the samples.

This study raises awareness regarding insufficient controlled food supplements.

Keywords: *cannabinoids, cannabidiol, LC-MS/MS, food supplements*

INTRODUCTION

Cannabinoids are lipophilic phenolic substances, benzopyran derivatives, whose concentration and distribution in commercial products are highly variable, depending on the *Cannabis* chemotype from which the extraction was made, as well as the technological process by which it was obtained [1].

In plants, cannabinoids are synthesized in the glandular trichomes. The biosynthetic pathway starts from hexanoyl-CoA, and the first cannabinoid precursor is cannabigerolic acid which is formed through the prenylation of olivetolic acid. THC and CBD are formed through the non-enzymatic decarboxylation of their acidic precursors, namely Δ^9 -tetrahydrocannabinolic acid (Δ^9 -THCA) and cannabidiolic acid (CBDA). THCA is formed from cannabigerolic acid (CBGA) under the action of THCA synthase, CBDA is formed from CBGA under the action of CBDA synthase, and cannabichromenic acid is formed under the action of cannabichromenic acid synthase [2]. Until now, over 100 cannabinoids have been isolated in *Cannabis* species, but the most abundant ones are: Δ^9 -tetrahydrocannabinol (Δ^9 -THC), cannabidiol (CBD), cannabichromene (CBC), Δ^9 -THCA, CBDA, cannabigerol (CBG), cannabigerolic acid, cannabinol (CBN) [2,3]. CBDA and CBN are formed through the oxidation of Δ^9 -THCA and Δ^9 -THC, under different conditions (light, oxygen, long storage) [2,4,5].

Until now, there are only two approved (by the Food and Drug Administration and/or by European Medicines Agency) *Cannabis-based* drugs. Sativex[®] (nabiximols) is an oromucosal spray standardized in THC and CBD. Epidyolex[®] is an oral solution that contains CBD in a concentration of 100 mg/mL. It is approved by the European Medicines Agency for the treatment of epilepsy crisis associated with Lennox-Gastaut syndrome or with Dravet syndrome [6,7]. However, a plethora of food supplements with CBD, especially 'CBD oils', have appeared in pharmacies in the last years.

CBD products have rapidly gained popularity due to their marketed health benefits, ranging from anxiety relief to pain management. Due to the lack of definitions, it is unclear what type of oils are sold on the food supplements market (reconstituted from fatty oils with synthetic CBD or extracted from the plant product). However, the regulatory framework governing these products is unclear. The law in Romania regarding food supplements has numerous loopholes, which increases the risk of significant side effects. At the same time, the legislation in Romania is quite ambiguous regarding the products obtained from *Cannabis sp.* and/or products containing cannabidiol. *Cannabis*, *cannabis* resin, *cannabis* extracts, and tinctures belong to the category of narcotic substances of medical interest and are subjected to strict control [8]. Cannabidiol and other cannabinoids, except THC and THCA, are not included in this list, but there are also no clear regulations regarding their presence in different products (food supplements, cosmetics, oils, etc.). Regarding the effects of cannabidiol, numerous studies have highlighted multiple effects induced by a complex pharmacodynamic mechanism [9–11]. Also, other cannabinoids may act synergistically with CBD, enhancing its activity [12]. As noticed by Hayduc et al, these interactions are hard to predict, and are dose-dependent [13]. If extracted from the herbal drug, CBD oils contain other active lipophilic phytochemicals, different cannabinoids and non-cannabinoids such as volatile terpenes [14–17].

The toxicological studies have revealed that CBD is a compound with a good safety profile, with few and mild side effects even at high doses up to 1500 mg/day [18,19]. The most common side effects noticed in clinical trials were: decreased appetite, diarrhoea and dizziness [20,21].

The CBD market has quickly expanded, and the consumer has a very large portfolio of products from which he can choose. However, as how was previously noticed, there are many inconsistencies between the declared composition and the actual composition. Given the diverse nature of the routes of administration by which CBD has been studied, its pharmacokinetic profile is influenced by an important number of variables. All these variations are making the efficiency of CBD products to differ consistently between the products.

It is important to emphasize that more pharmacokinetic studies and more clinical trials are needed to validate the long-term efficacy and safety of using CBD as a food supplement.

CBD oils are standardized in CBD, but not in the other cannabinoids that can be extracted from hemp. A routine use of an LC-MS/MS analysis should be implemented for the evaluation of food supplements and other cannabinoid-based products. The analysis of cannabinoids using HPLC and LC-MS has evolved significantly over the past decade, offering a range of methods for precise and sensitive detection of these compounds. The

European Pharmacopoeia (11.5) method for determining cannabinoids in cannabis flower uses liquid chromatography with a polar-embedded octadecylsilyl silica gel column and a mobile phase of trifluoroacetic acid and acetonitrile, and a total run time of approximately 35 minutes. The process involves ethanol extraction, dilution, and filtration of the sample, with UV detection at 228 nm to identify and quantify cannabinoids like cannabidiol, THC, and their acidic forms based on retention times and reference standards [22].

The most practical detection method for analysing naturally occurring cannabinoids is mass spectrometric detection, which offers important structural details for differentiating different cannabinoids [23]. Table 1 summarizes relevant data from methods published between 2020 and 2025, detailing the types of methods, chromatographic conditions, the cannabinoids that were quantified, and the type of samples. The data highlight that the reversed-phase C18 columns commonly used for cannabinoid detection range in length from 50 mm to 150 mm, depending on the specific application and desired resolution. Particle sizes of columns used during this period predominantly fall below 3 μm , reflecting a trend toward improved separation efficiency and resolution. While advanced techniques such as nano-LC offer high sensitivity, they remain cost-prohibitive for many laboratories [24]. Therefore, while numerous validated methods exist, it is essential to revalidate protocols when instrumentation or columns are changed to ensure reliability.

Table 1. Analytical methods published between 2020 and 2025 regarding the analysis of cannabinoids in herbal products, food products and cosmetics

Method	Chromatographic conditions	Cannabinoids	Samples	Reference
LC-PDA Column: 2.1 × 50 mm, 1.8 μm (C18)	Mobile phase: 0.1% formic acid (A) and ACN containing 0.1% formic acid (B) Total run time: 7.5 min Detection: 210, 221 nm	CBD, CBDA, THC, THCA	CBD tea products	Mouton et al, 2024 [25]
LC-MS/MS Column: 4.6 × 50 mm, 2.7 μm (C18)	Mobile phase: water with 0.1% (v/v) formic acid (A) and MeOH (B) (gradient elution) Total run time: 10 min Detection: ESI in positive mode	CBN, 11-THC-OH, 11-THC-COOH, THC, CBD, CBC, CBG	Cannabis-based edibles	Christodoulou et al, 2023 [26]

DEVELOPMENT AND VALIDATION OF AN LC-MS/MS METHOD FOR THE QUANTIFICATION OF SIX CANNABINOIDS IN COMMERCIAL PRODUCTS

Method	Chromatographic conditions	Cannabinoids	Samples	Reference
LC-MS/MS Column: 2.1 × 100 mm, 1.6 μm (C18)	Mobile phase: 0.1% formic acid in water (A) and acetonitrile (B) (isocratic elution) Total run time: 13 min Detection: HRMS/MS	CBDV, CBE, CBDVA, THCV, THCVA, CBD, CBDA, CBG, CBN, CBGA, Δ9-THC, Δ8-THC, CBL, CBC, CBT, CBNA, THCA	e-cigarette liquids	Barhdadi et al, 2023 [27]
LC-MS/MS Column: 3 × 100 mm, 2.6 μm (C18)	Mobile phase: water (A) and methanol (B); both contained 0.1% formic acid and 2 mM ammonium formate (gradient elution) Total run time: 13 min Detection: ESI/MS-MS in positive mode	THC, THCA-A, CBD, CBDA, CBG, CBGA, CBC, CBV, CBDVA, CBGVA, CBN, THCVA, THCV, + 117 synthetic cannabinoids	Food products and food supplements	Galant et al, 2022 [28]
LC-MS/MS Column: 3.0 mm × 100 mm, 25 μm (C18)	Mobile phase: 10 mM ammonia formate buffer (A) and 10 mM ammonia formate buffer in methanol (B) Total run time: 13 min Detection: ESI/MS-MS in positive mode	THC, CD, CBN	Hemp oil based cosmetic products	Hsu et al, 2021 [29]
LC-MS/MS Column: not specified	0.1% formic acid in water (mobile phase A) and 0.1% formic acid in acetonitrile (mobile phase B) (gradient elution) Total run time: 22 min	Δ9-THC	Food products and beverages	Pisciottano et al, 2021 [30]
LC-MS/MS Column: 2.1 × 100 × mm, 1.7 μm (C18)	Mobile phase: 0.1% formic acid in water (A) and acetonitrile (B) Total run time: 13 min Detection: ESI-MS/MS in positive and negative mode	CBD, CBDA Δ9-THC, THCA, CBN, CBC, CBCA, CBDV, CBDVA, CBG, CBGA, THCV, THCVA, Δ8-THC	Food samples	Christinat et al, 2020 [31]

Method	Chromatographic conditions	Cannabinoids	Samples	Reference
LC-MS/MS Column: 2.0 x 100 mm, 3 μm	Mobile phase: 0.1% formic acid in water (A) and acetonitrile (B) (gradient elution) Total run time: 18 min Detection: ESI-MS/MS in positive mode	CBD, THC	Food and dietary supplements	Lee et al, 2020 [32]
HPLC/UV Column: 4.6 x 150 mm, 2.7 μm	Mobile phase: water (A) and acetonitrile (B) both containing 0.085 % phosphoric acid (gradient elution) Total run time: 10 min Detection: 220 nm	CBDV, CBDA, CBGA, CBG, CBD, THCV, CBN, Δ9-THC, Δ8-THC, CBC, THCA	Cannabis light preparations (THC/CBD ratio <<1)	Dei Cas et al, 2020 [33]

Therefore, this study aimed to develop and validate a fast and reliable LC-MS/MS method for the routine quantification of cannabinoids in food supplements.

RESULTS AND DISCUSSION

Cannabinoid analysis is a popular topic with many challenges, and the interest in this domain has constantly increased in the last 20 years, worldwide. There are different proposed methods for the quantification of cannabinoids in different matrices, most of them based on HPLC-DAD [5,34–36]. Most HPLC-validated methods have long run times, making them not quite suitable for routine analysis. Tandem mass spectrometry has the advantage of offering high sensitivity and specificity, and it has been widely used in the last 5 years [28,30,32,33,36].

In the present study, an accurate, fast, and robust method was developed and validated for the quantification of 6 cannabinoids in food supplements. All standards showed a good linearity in the tested concentration range, with $R \geq 0.99$. The lower limit of quantification (LLOQ) was 5 ng/mL. Compared with the LC-MS/MS method proposed by Christodoulou et al, our method had a lower LOQ for CBD [26]. As anticipated, the sensitivity of our proposed LC-MS/MS method significantly surpasses that of the LC-PDA method developed by Mouton et al. [25].

DEVELOPMENT AND VALIDATION OF AN LC-MS/MS METHOD FOR THE QUANTIFICATION OF SIX CANNABINOIDS IN COMMERCIAL PRODUCTS

The retention time of CBDA was 1.25 min, of CBGA was 1.41 min, of CBVA was 0.84 min, of CBD was 4.79 min, of CBG was 4.69 min, and of CBN was 8.34 min, with a total run time of 10 minutes. For the validation procedure the guidelines described by the USFDA and the EMA for bioanalytical method validation were used. Following those general guidelines and steps we validated the applicable and relevant parameters for our application [37,38]. In figure 1 and 2 MS spectrum and chromatograms of the six cannabinoids are presented.

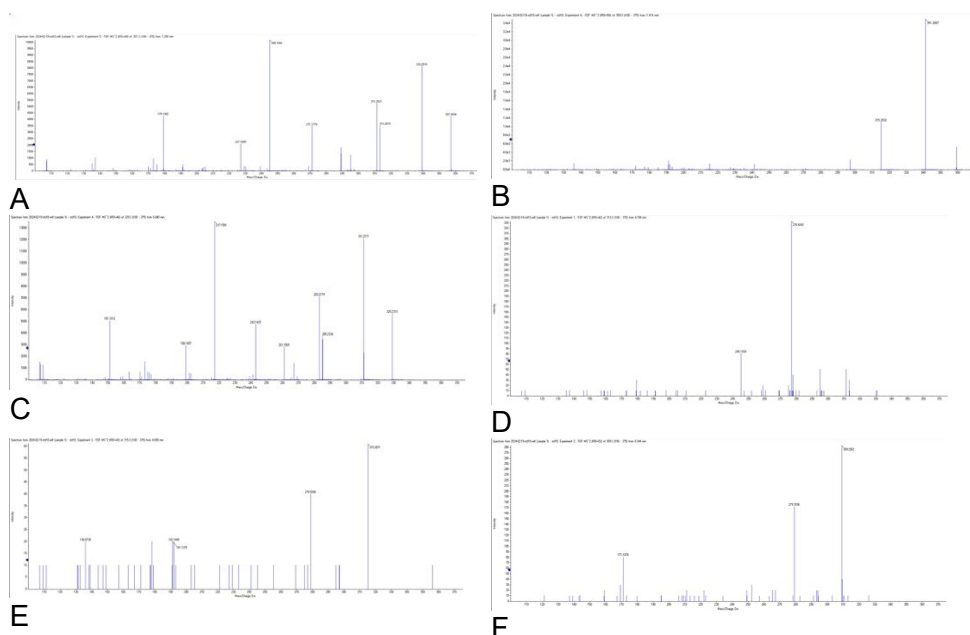


Figure 1. MS spectrum of compounds: A - CBDA, B - CBGA, C - CBVA, D - CBD, E - CBG, F – CBN

No carry-over effect was detected, with no peaks detected in the blank solution for any of the analytes.

No interfering peaks were observed at the retention times of the analytes in the blank solution. To provide the necessary sensitivity and selectivity, the areas of the analytes at the limit of quantification must be at least five times larger than the area of any peaks present in the blank samples.

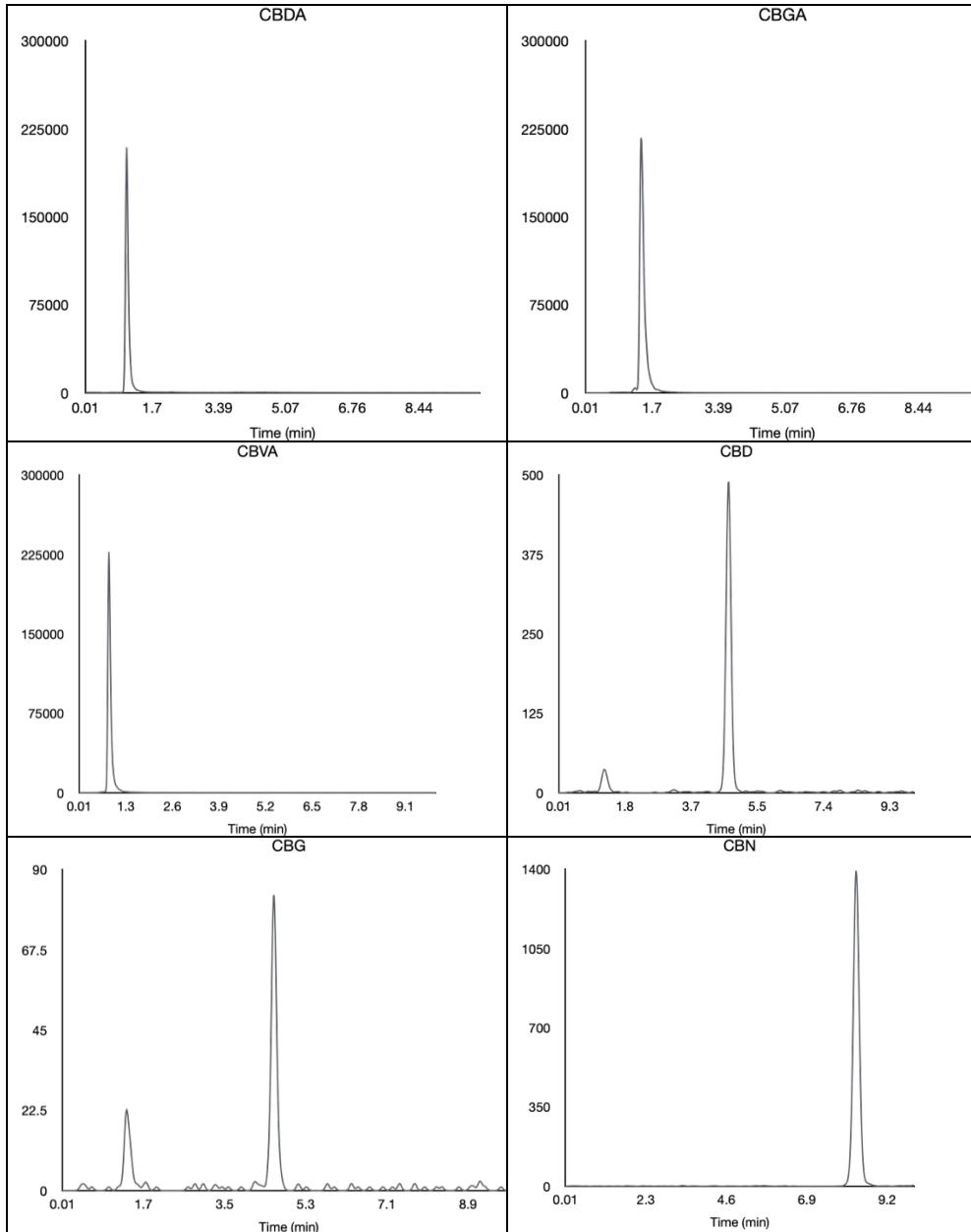


Figure 2. Representative chromatograms of the analyzed cannabinoids

DEVELOPMENT AND VALIDATION OF AN LC-MS/MS METHOD FOR THE QUANTIFICATION OF SIX CANNABINOIDS IN COMMERCIAL PRODUCTS

Five samples of each control sample were analyzed in a single run to determine within-run accuracy and precision (table 2). The mean concentration, mean deviation from the nominal value (accuracy) and relative standard deviation (RSD% - precision) of the analyzed control standards were calculated. Average accuracy and precision were within $\pm 15\%$ and $\pm 20\%$ respectively in the case of LLOQ.

Table 2. Within-run accuracy and precision (n = 3)

Analyte	Nominal concentration (ng/ mL)	Measured concentration (ng/ mL)	Accuracy (%)	Precision (%)
CBDA	5	4.89 \pm 0.15	97.8	3.07
	25	23.4 \pm 2.31	93.4	9.90
	250	251 \pm 8.68	100	3.46
	500	555 \pm 38.6	111	6.97
	750	735 \pm 68.1	98.0	9.27
CBGA	5	4.88 \pm 0.23	97.6	4.83
	25	24.3 \pm 2.55	97.1	10.5
	250	241 \pm 5.59	96.5	2.32
	500	549 \pm 31.7	110	5.77
	750	742 \pm 43.1	98.9	5.81
CBVA	5	4.72 \pm 0.18	94.4	3.84
	25	24.7 \pm 1.85	98.8	7.50
	250	267 \pm 14.7	107	5.51
	500	554 \pm 26.4	111	4.76
	750	730 \pm 31.3	97.4	4.29
CBD	5	5.33 \pm 0.36	107	6.83
	25	27.1 \pm 2.06	108	7.62
	250	233 \pm 16.6	93.5	7.09
	500	551 \pm 12.9	110	2.34
	750	702 \pm 41.0	93.6	5.85
CBG	5	5.58 \pm 0.48	112	8.63
	25	25.2 \pm 2.15	101	8.52
	250	237 \pm 21.4	94.9	9.03
	500	503 \pm 35.1	101	6.98
	750	757 \pm 45.7	101	6.04
CBN	5	5.43 \pm 0.33	109	6.15
	25	25.3 \pm 2.10	101	8.32
	250	272 \pm 15.6	109	5.74
	500	538 \pm 30.3	108	5.62
	750	746 \pm 16.7	99.5	2.24

Five samples from each control sample, one from each sample in each sequence, were analyzed to determine between-run accuracy and precision (table 3). The mean concentration, mean deviation from the nominal value (accuracy), and relative standard deviation (RSD% - precision) of the analyzed control standards were calculated. Average accuracy and precision were within $\pm 15\%$ and $\pm 20\%$ respectively in the case of LLOQ.

Table 3. Between-run accuracy and precision (n = 3)

Analyte	Nominal concentration (ng/mL)	Measured concentration (ng/ mL)	Accuracy (%)	Precision (%)
CBDA	5	5.33 \pm 0.32	107	5.95
	25	23.5 \pm 1.86	94.1	7.90
	250	227 \pm 19.6	90.8	8.63
	500	515 \pm 41.5	103	8.07
	750	740 \pm 51.8	98.7	7.00
CBGA	5	5.31 \pm 0.53	106	9.93
	25	24.4 \pm 1.99	97.8	8.16
	250	226 \pm 18.9	90.3	8.39
	500	513 \pm 17.7	102.6	3.44
	750	708 \pm 66.5	94.4	9.39
CBVA	5	5.21 \pm 0.64	104	12.2
	25	25.2 \pm 1.94	101	7.68
	250	231. \pm 29.8	92.5	12.9
	500	515 \pm 26.7	103	5.18
	750	720 \pm 61.7	96.0	8.56
CBD	5	5.23 \pm 0.55	105	10.5
	25	26.6 \pm 1.71	106	6.44
	250	224 \pm 11.6	89.49	5.17
	500	540 \pm 32.3	108	5.99
	750	741 \pm 68.6	98.8	9.27
CBG	5	5.28 \pm 0.59	106	11.1
	25	25.3 \pm 2.81	101	11.1
	250	244 \pm 17.1	97.4	7.01
	500	521 \pm 61.5	104	11.8
	750	745 \pm 75.3	99.3	10.1
CBN	5	5.25 \pm 0.59	105	11.4
	25	24.2 \pm 1.89	96.7	7.80
	250	252 \pm 19.4	101	7.69
	500	522 \pm 27.4	104	5.25
	750	726 \pm 30.4	96.8	4.18

Table 4. CBD concentration found in samples versus the declared concentration

Sample	Concentration (%)	Declared concentration (%)
1	11.5 ± 0.38	10
2	2.38 ± 0.20	2.5
3	0.15 ± 0.03	n.d.
4	6.44 ± 0.04	10
5	2.01 ± 0.03	2.5 (CBD + terpenes)
6	2.10 ± 0.04	5
7	14.2 ± 0.08	10
8	0.02 ± 0.001	n.d.
9	0.53 ± 0.06	n.d.
10	0.21 ± 0.02	n.d.

The most abundant cannabinoids found in the tested samples were CBD, CBN, and CBG, as it can be seen in table 4 and 5. Within the tested products, in three products the CBD content was significantly different compared with the declared concentration. Samples 4 and 6 had lower concentrations of CBD compared to the declared concentration, while in sample 7 the CBD concentration was higher. Our results are in accordance with Johnson et al, who have concluded that only 8% of the tested products had CBD concentrations within 10% of the advertised values [39].

Table 5. Cannabinoid concentration found in samples (mg/100 g)

Sample	CBG	CBN	CBDA	CBGA	CBVA
1	447 ± 6.70	1386 ± 45.6	4.65 ± 0.21	0.07 ± 0.003	0.12 ± 0.01
2	42.2 ± 4.16	8.31 ± 1.28	110 ± 4.20	5.58 ± 0.22	13.0 ± 1.18
3	0.98 ± 0.24	1.86 ± 0.19	3.77 ± 0.11	4.20 ± 0.21	0.03 ± 0.002
4	904 ± 42.1	403 ± 9.55	79.2 ± 3.38	71.7 ± 1.51	11.46 ± 0.45
5	8.24 ± 0.09	3.99 ± 0.12	1.85 ± 0.19	0.58 ± 0.13	0.03 ± 0.003
6	9.26 ± 1.21	0.94 ± 0.09	6.43 ± 0.30	5.28 ± 0.42	0.08 ± 0.01
7	268 ± 11.9	21.1 ± 3.64	0.61 ± 0.03	0.51 ± 0.03	0.01 ± 0.0002
8	N.D.	0.31 ± 0.04	13.0 ± 1.04	0.59 ± 0.04	0.87 ± 0.05
9	35.4 ± 7.81	1.82 ± 0.10	55.9 ± 1.87	10.8 ± 1.26	6.04 ± 0.49
10	6.16 ± 0.39	2.40 ± 0.29	37.4 ± 0.70	5.24 ± 0.36	6.46 ± 0.22

N.D. – not detected

LC-MS/MS offers superior sensitivity, selectivity, and speed, which are essential for quantifying cannabinoids, particularly in complex food supplement matrices where multiple cannabinoids might co-exist at varying concentrations. Unlike GC, LC-MS/MS eliminates the need for derivatization and provides precise quantification of both neutral and acidic cannabinoids.

Additionally, the capability to operate in electrospray ionization mode further enhances detection specificity.

Most regulations regarding the cannabinoid levels in food supplements are only focused on THC because of its psychoactive effects. However, other non-psychoactive cannabinoids can have different actions and may act in synergy with CBD. Cannabigerol has been shown to have anti-inflammatory and neuromodulatory effects. These are primarily explained by the affinity of CBG to different receptors like α -2, 5-HT_{1A}, and PPAR γ [40,41].

The present study showed the great diversity of commercial products that are found on the market. Our results are similar to those obtained by other researchers regarding the irregularities in the advertised concentration of CBD, with the mention that in our study, the problematic products were fewer compared with other studies [23].

Due to the wide variety of cannabinoid types and the products in which they can be found, there is no universal analytical method that allows for the accurate and precise quantification of these compounds with appropriate detection limits. Therefore, the analytical methodology must be adapted according to the sample treatment required by their matrix and the types and concentrations of substances expected or suspected to be present in products intended for consumption or medical treatment. Additionally, adapting a method published in the specialized literature often proves to be difficult or even impossible, either due to the inadequate technical performance of the equipment on which the method is intended to be implemented, the more laborious and costly sample preparation process proposed, or the discovery of limitations in methodologies that are not always clearly highlighted in the articles [42,43].

In this regard, the present study proposes an LC-MS/MS method that considers six cannabinoids as target analytes and two categories of products: oils and plant-based products. Based on the advanced type of mass spectrometry detection used, Q-TOF, the method ensures specificity/selectivity and an appropriate quantification level for the intended purpose.

Through relatively simple sample preparation methods, such as dilution, solvent extraction from plants, and filtration, the developed and validated LC-MS/MS method allows for the identification and quantification of the selected analytes with accuracy and precision within a short analysis time of 10 minutes. It also enables the detection of some investigated substances in commercial products, even in cases where their presence is not declared.

Lastly, this study proposes an LC-MS/MS fingerprinting method for commercial dietary supplements and provides an overview of the situation in Romania. Based on a review of specialized literature, there are some recent data regarding the analysis of dietary supplement trends in Romania, but significantly fewer analytical studies on their quality control [44].

CONCLUSIONS

The validated method allows the simultaneous quantification of CBDA, CBGA, CBVA, CBD, CBG, and CBN in commercial products. The method showed good linearity across a wide concentration range for each cannabinoid. Regarding the quality control of the food supplements, significant differences in concentrations were observed for three tested products, between the advertised concentration versus the actual CBD concentration. Because of this unregulated industry it is difficult to assess the quality of these types of food supplements and to ensure the safety of cannabinoid-containing food supplements for consumers. Overall, our work contributes to the field by offering a robust alternative that can be readily adopted for routine and regulatory cannabinoid analysis.

EXPERIMENTAL SECTION

Chemicals and reagents

Cannabidiol (CBD), cannabinal (CBN), cannabigerol (CBG), cannabidiolic acid (CBDA), cannabigerolic acid (CBGA), and cannabidivarinic acid (CBVA) were purchased from Cayman Chemical Company (Michigan, USA). LC-MS grade acetonitrile was purchased from Riedel-de Haen (Seelze, Germany), methanol was purchased from VWR International (Fontenays, France) and ammonium formate was purchased from Fluka (Buchs, Switzerland). Ultrapure water was obtained from a Millipore Direct-Q water purification system (Millipore, Bedford, MA, USA).

Calibration curve

Stock solutions of 2.5 mg/ mL in methanol were prepared for CBDA, CBGA, CBVA, and CBG, while stock solutions of 5 mg/mL in methanol were prepared for CBD and CBN.

A solution of 1 $\mu\text{g}/\text{mL}$ of each CBD, CBN, CBG, CBDA, CBGA, and CBVA in a mixture of water:methanol (3:7, v/v) was obtained using these stock solutions and was further diluted with the same solvent to obtain calibration curve standards within the range of 5–1000 ng/mL. The calibration curve was composed of 10 levels with nominal concentrations between 5 – 1000 ng/mL for each analyte. The average calibration curve was plotted using a linear fit and $1/y^2$ weighting and the accuracy of each calibration standard was calculated for each calibration curve.

Sample preparation

Ten food supplements with CBD, from different manufacturers, were purchased from local pharmacies.

Table 6. The type of food supplements included in the present study

No. of sample	Type of product	Label mentions
1	10% CBD oil	
2	2.5 % CBD oil	
3	Mouthwash	
4	Hemp seed oil 1000 mg CBD	5% CBDA, 5% CBGA
5	2.5% CBD oil	
6	CBD	
7	CBD	
8	CBD tea	tea mixture with 10% aerial parts from <i>Cannabis sativa</i>
9	<i>Cannabis sativa</i> leaves tea	
10	<i>Cannabis sativa</i> CBD tea	

The CBD oils were diluted with a 1:1 (v/v) mixture acetonitrile: methanol, sonicated for 10 minutes at room temperature and centrifuged at 11000 rpm for 5 minutes with a digital angle centrifuge (Nahita 2615/1, Spain). From the herbal products, 1 g was extracted with 50 mL acetonitrile–methanol (1:1, v/v) mixture in an ultrasonic water bath (Nahita 626, Spain) for 30 minutes, at 40 °C [45,46]. All samples were filtered through a 0.45 μm Rotilabo mini-tip syringe filter, before the analysis.

LC-MS/MS instrumentation and conditions

The LC-MS/MS system consisted of an UHPLC Flexar FX-10 (Perkin Elmer, USA) system coupled with a triple quadrupole tandem mass spectrometer (QTOF 4600, AB Sciex). The chromatographic separations were carried out using a Kinetex XB-C18 column (3.0 x 100 mm, 2.5 μm), using a mixture with a ratio of 35% ammonium formate 20 mM (solvent A) and acetonitrile (solvent B) as a mobile phase, with isocratic elution and a flow rate set to 0.8 mL/min. The injection volume was 5 μL, the column temperature was set at 15 °C, the temperature of the samples was 20 °C, and the analysis time was 10 minutes. An electrospray ionization source with negative ion mode was used. Ionization parameters were as follows: Spray voltage: -4500V, vaporizer temperature: 450 °C, Ion Gas Source 1: 50 bar, Ion Gas Source 2: 35 bar, Curtain Gas: 10 bar, Declustering Potential: -100V, Ion Release Delay: 42 ms, Ion Release Width: 18. Data files were processed by AB Sciex Analyst Mass Spectrometry Software.

The detections of analytes were performed by monitoring the sum of ion fragments generated from molecular ions at specific collision energy as follows:

- Cannabidiolic acid (CBDA) ions m/z 179.16, m/z 245.22, m/z 311.30 and m/z 339.29 from m/z 357.3 at a collision energy of -34V;
- Cannabigerolic acid (CBGA) ions m/z 191.16, m/z 241.23, m/z 297.30, m/z 315.32 and m/z 341.30 from m/z 359.32 at a collision energy of -20V;
- Cannabidivarinic acid (CBVA) ions m/z 217.18, m/z 243.17, m/z 283.25, m/z 311.25 and m/z 199.17 from m/z 329.2 at a collision energy of -32V;
- Cannabidiol (CBD) ions m/z 179.10, m/z 245.20 and m/z 311.25 made from m/z 313.3 at a collision energy of -25V;
- Cannabigerol (CBG) ions m/z 136.09 and m/z 191.15 made from m/z 315.3 at a collision energy of -31V;
- Cannabinol (CBN) ions m/z 171.13 and m/z 279.21 made of m/z 309.3 at a collision energy of -35V.

Method validation

Carry over

To check the carry-over effect, a blank solution (mobile phase) was injected immediately after the injection of the standard solution with the highest concentration.

Sensitivity and selectivity

To check the sensitivity and selectivity of the method, a blank solution was injected at the beginning of each sequence and the peaks (if any) at the retention times of the analytes were compared with those of the standard solution with the lowest concentration (LLOQ).

Linearity

Linearity was checked for each of the five validation sequences and for each sequence used for sample analysis. The fitted calibration curves were checked for correlation coefficient ($r > 0.99$) and accuracy of recalculated calibration standard concentrations compared to theoretical concentrations - a bias (%) not greater than $\pm 15\%$, except LLOQ for which a higher inaccuracy of $\pm 20\%$ was accepted.

Accuracy and precision

Accuracy and precision of the method were determined at 5 concentration levels (5, 25, 250, 500, and 750 ng/mL for each analyte) using quality control (QC samples). For accuracy a bias (%) not greater than $\pm 15\%$ was considered acceptable, except LLOQ for which an inaccuracy of $\pm 20\%$ was accepted. For precision, a coefficient of variation not greater than 15% was considered acceptable, except for LLOQ for which the acceptable value was 20%.

ACKNOWLEDGMENTS

This work was supported by the George Emil Palade University of Medicine, Pharmacy, Science and Technology of Targu Mures, Research Grant number 163 /7/ 10.01.2023.

REFERENCES

1. R. Mechoulam and L. Hanuš, *Chem. . Phys. . Lipids*, **2000**, 108, 1–13.
2. X. Luo, M. A. Reiter, L. d’Espaux, J. Wong, C. M. Denby, A. Lechner, Y. Zhang, A. T. Grzybowski, S. Harth, W. Lin, H. Lee, C. Yu, J. Shin, K. Deng, V. T. Benites, G. Wang, E. E. K. Baidoo, Y. Chen, I. Dev, C. J. Petzold and J. D. Keasling, *Nature*, **2019**, 567, 123–126.
3. M. N. Tahir, F. Shahbazi, S. Rondeau-Gagné and J. F. Trant, *J. Cannabis. Res.*, **2021**, 3, 7.
4. K. A. Aliferis and D. Bernard-Perron, *Front. Plant Sci.*, **2020**, 11, 554.
5. O. Aizpurua-Olaizola, J. Omar, P. Navarro, M. Olivares, N. Etxebarria and A. Usobiaga, *Anal. Bioanal. Chem.*, **2014**, 406, 7549–7560.
6. S. Inglet, B. Winter, S. E. Yost, S. Entringer, A. Lian, M. Biksacky, R. D. Pitt and W. Mortensen, *Ann. Pharmacother.*, **2020**, 54, 1109–1143.
7. M. P. Barnes, *Expert Opin. . Pharmacother.*, **2006**, 7, 607–615.
8. *LEGE 339 29/11/2005 - privind regimul juridic al plantelor, substanțelor și preparatelor stupefiante și psihotrope*, Parlamentul României, MONITORUL OFICIAL nr. 1095 din 5 decembrie **2005**.
9. Z. Gáll, K. Kelemen, A. Tolokán, I. Zolcseak, I. Sável, R. Bod, E. Ferencz, S. Vancea, M. Urkon and M. Kolcsár, *Biomedicines*, **2022**, 10, 1811.
10. G. Jițcă, B. E. Ósz, C. M. Ruzs, A. Pușcaș, A. Tero-Vescan, M. G. Bătrînu and R. E. Ștefănescu, *AMM*, **2022**, 68, 150–153.
11. U. S. Kosgodage, P. Matewele, B. Awamaria, I. Kraev, P. Warde, G. Mastroianni, A. V. Nunn, G. W. Guy, J. D. Bell, J. M. Inal and S. Lange, *Front. Cell. Infect. Microbiol.*, **2019**, 9.
12. A. L. Dawidowicz, M. Olszowy-Tomczyk and R. Typek, *Fitoterapia*, **2021**, 153, 104992.
13. S. A. Hayduk, A. C. Hughes, R. L. Winter, M. D. Milton and S. J. Ward, *Biomedicines*, **2024**, 12, 1145.
14. S. Hourfane, H. Mechqoq, A. Y. Bekkali, J. M. Rocha and N. El Aouad, *Plants*, **2023**, 12, 1245.
15. F. Borrelli, I. Fasolino, B. Romano, R. Capasso, F. Maiello, D. Coppola, P. Orlando, G. Battista, E. Pagano, V. Di Marzo and A. A. Izzo, *Biochem. Pharmacol.*, **2013**, 85, 1306–1316.
16. M. M. Radwan, S. Chandra, S. Gul and M. A. ElSohly, *Molecules*, **2021**, 26, 2774.
17. C. Citti, D. Braghiroli, M. A. Vandelli and G. Cannazza, *J. Pharm. Biomed. Anal.*, **2018**, 147, 565–579.

DEVELOPMENT AND VALIDATION OF AN LC-MS/MS METHOD FOR THE QUANTIFICATION OF SIX CANNABINOIDS IN COMMERCIAL PRODUCTS

18. L. A. Walker, I. Koturbash, R. Kingston, M. A. ElSohly, C. R. Yates, B. J. Gurley and I. Khan, *J. Diet. Suppl.*, **2020**, 17, 493–502.
19. K. Iffland and F. Grotenhermen, *Cannabis and Cannabinoid Res.*, **2017**, 2, 139–154.
20. C. Larsen and J. Shahinas, *J. Clin. Med. Res.*, **2020**, 12, 129–141.
21. K. A. Jadoon, S. H. Ratcliffe, D. A. Barrett, E. L. Thomas, C. Stott, J. D. Bell, S. E. O’Sullivan and G. D. Tan, *Diabet. Care*, **2016**, 39, 1777–1786.
22. Council of Europe. European Pharmacopoeia. 11.5th ed. Strasbourg, France: European Directorate for the Quality of Medicines & HealthCare (EDQM), **2024**.
23. L. Nahar, A. Onder and S. D. Sarker, *Phytochem. Anal.*, **2020**, 31, 413–457.
24. L. Žampachová, Z. Aturki, F. Mariani and P. Bednář, *Molecules*, **2021**, 26, 1825.
25. M. Mouton, M. Gerber and F. Van der Kooy, *Rev. Bras. Farmacogn.*, **2024**, 34, 197–201.
- 26 M. C. Christodoulou, A. Christou, I. J. Stavrou and C. P. Kapnissi-Christodoulou, *J. Food Compos. Anal.*, **2023**, 115, 104915.
27. S. Barhdadi, P. Courselle, E. Deconinck and C. Vanhee, *J. Pharm. Biomed. Anal.*, **2023**, 230, 115394.
28. N. Galant, J. Czarny, J. Powierska-Czarny and A. Piotrowska-Cyplik, *Molecules*, **2022**, 27, 8601.
29. Y.-H. Hsu, M.-C. Fang, S.-C. Huang, Y.-M. Kao, S.-H. Tseng and D.-Y. Wang, *J. Food Drug. Anal.*, **2021**, 29, 502–509.
30. I. Di Marco Pisciotto, G. Guadagnuolo, V. Soprano, M. Esposito and P. Gallo, *Food Chem.*, **2021**, 346, 128898.
31. N. Christinat, M.-C. Savoy and P. Mottier, *Food Chem.*, **2020**, 318, 126469.
32. J. H. Lee, A. Y. Min, J. H. Han, Y. J. Yang, H. Kim and D. Shin, *Food Addit. Contam. Part A*, **2020**, 37, 1413–1424.
33. M. Dei Cas, E. Casagni, A. Saccardo, S. Arnoldi, C. Young, S. Scotti, E. Vieira de Manicor, V. Gambaro and G. Roda, *Forensic Sci. Int.*, **2020**, 307, 110113.
34. W. Gul, S. W. Gul, M. M. Radwan, A. S. Wanas, Z. Mehmedic, I. I. Khan, M. H. M. Sharaf and M. A. ElSohly, *J. AOAC Int.*, **2015**, 98, 1523–1528.
35. W. Peschel, *Sci. Pharm.*, **2016**, 84, 567–584.
36. A. K. Hewavitharana, F. Gloerfelt-Tarp, M. Nolan, B. J. Barkla, S. Purdy and T. Kretzschmar, *Separations*, **2022**, 9, 85.
37. U.S. Department of Health and Human Services. Food and Drug Administration. Center for Drug Evaluation and Research (CDER). Center for Veterinary Medicine(CVM). Guidance for Industry. Bioanalytical Method Validation. 2013 Sep; available at: <http://www.fda.gov/downloads/drugs/guidancecomplianceregulatoryinformation/guidances/ucm368107.pdf>.
38. European Medicines Agency. Committee for Medicinal Products for Human Use (CHMP). Guideline on bioanalytical method validation. 2011, Jul; available at http://www.ema.europa.eu/docs/en_GB/document_library/Scientific_guideline/2011/08/WC500109686.pdf
39. D. A. Johnson, M. Hogan, R. Marriot, L. M. Heaney, S. J. Bailey, T. Clifford and L. J. James, *J. Cannabis Res.*, **2023**, 5, 28.

40. A. Jastrzab, I. Jarocka-Karpowicz and E. Skrzydlewska, *Int.J. Molec. Sci.*, **2022**, 23, 7929.
41. R. Nachnani, W. M. Raup-Konsavage and K. E. Vrana, *J. Pharmacol. Exp. Ther.*, **2021**, 376, 204–212.
42. J.N. Kleis, C. Hess, T. Germerott, J. Roehrich, *Drug Test Anal.*, **2021**, 13(8): 1535 - 1551.
43. G. Meyer, M. Adisa, Z. Dodson, E. Adejumo, E. Jovanovich, L. Song, *J Pharm Biomed Anal.*, **2024**, 238:115847.
44. C. Andrei, G.M. Nitulescu, G. Nitulescu, A. Zanfirescu, *Pharmacy*, **2024**, 12(6): 176.
45. I. G. C. Oliveira, C. F. Grecco, I. D. de Souza and M. E. C. Queiroz, *Green Anal. Chem.*, **2024**, 11, 100161.
46. C. Monton, W. Chanduaykit, T. Mongkhonvanich, S. Srikaenchan, J. Suksaeree, L. Charoenchai and T. Songsak, *Arab. Chem.*, **2024**, 17, 105847.

METHOD VALIDATION FOR COPPER DETERMINATION IN HUMAN HAIR SAMPLES THROUGH GRAPHITE FURNACE ATOMIC ABSORPTION SPECTROMETRY

Nicoleta MATEI^a, Semaghiul BIRGHILA^{a*},
Simona DOBRINAS^a, Alina SOCEANU^a, Ana-Maria ILIE^a,
Viorica POPESCU^a

ABSTRACT. A simple, cheap, and sensitive analytical method was validated for the determination of copper in human hair after microwave digestion. Method validation parameters such as linearity, precision, accuracy, limit of detection (LOD) and limit of quantification (LOQ) were determined. A graphite furnace atomic absorption spectrophotometer has been used. The developed method was linear in the concentration range of 2 - 20 µg/L with a 0.9979 coefficient of determination. The recoveries obtained for the copper ranged from 90.46-94.96%, with a precision not exceeding 3.95% relative standard deviation (RDS%) and system suitability test with RSD% lower than 1.58%. LOD was found to be 0.05632 µg/g and LOQ 0.18745 µg/g. The analyzed samples were from healthy humans and the study shown similar concentration of copper in hairs collected from adult, teenager men and female. The proposed method was considered adequate for the determination of copper in hair samples.

Keywords: GFAAS, hair, copper, validation

INTRODUCTION

Copper is an indispensable element of life and a dynamic, anti-infectious, antiviral, anti-inflammatory mineral. The adult human body contains about 75 mg of copper. The body mobilizes it in cases of microbial

^a Ovidius University of Constanta, Faculty of Applied Sciences and Engineering, Department of Chemistry and Chemical Engineering, 124 Mamaia Blvd., RO-900527, Constanta, Romania, nmatei@univ-ovidius.ro, sbirghila@univ-ovidius.ro, sdorbinas@univ-ovidius.ro, asoceanu@univ-ovidius.ro, anamarianiculescu@yahoo.com, vpopescu@univ-ovidius.ro

* Corresponding author: sbirghila@univ-ovidius.ro



aggression in infections. Copper helps our bodies to produce energy, to form important neurotransmitters and our connective tissue, supports the production of melanin in our skin and helps the transport of iron in the body. Consumption of foods that contain copper can prevent certain diseases or deficiencies (AIDS, leukemia, osteoporosis, stomach ulcer, allergies) [1].

Copper is widespread in foods, fruits and meat: in the liver, shells, nuts, vegetables, in most cereals, cocoa powder and in grapes [2]. The amount of copper in water varies depending on the natural mineral content of the water and the pH or the presence of copper pipes in the systems.

For children, adequate intakes between 400 μ g Cu/day (7—11 months aged) to 1100 μ g Cu/day (< 18 aged girls), and 1300 μ g Cu/day (< 18 aged boys) respectively, are proposed by EFSA (European Food Safety Authority) [3]. It has been found that the presence of zinc and vitamin C inhibits the retention of copper, and alcohol consumption can amplify the deficit. The deficiency of copper is mainly caused by genetic disorders and is manifested by anemia [1, 4-7], the discoloration of the hair and skin, bone demineralization, spontaneous fractures, increased blood cholesterol, brain degeneration, damage of the nervous system.

The copper toxicity determined by food intake is considered impossible, but it occurs because of water consumption with increased copper concentrations or those with professional exposure. The symptoms of acute copper poisoning are nausea, vomiting, diarrhea and abdominal pain, liver and kidney lesions, coma [1]. Wilson disease is a disorder of copper metabolism, based on a low serum ceruloplasmin level and a high urinary excretion of copper.

Hair is a bioindicator that offers important indices about nutritional imbalances in the body. It is used to detect chronic intoxication before symptoms appear, because concentrations of toxic metals are ten times higher in hair than in other biological materials [7]. The correct functioning of enzymes in the body is conditioned by vitamins and minerals. If minerals are missing, proteins cannot work correctly. Copper is an essential element of some enzymatic systems involved in hemoglobin production, carbohydrate metabolism and the formation of cross-linking between collagen, elastin and keratin fibers in the hair [8].

In medical analysis laboratories, the copper content of clinical samples is determined by ICP-MS [8-12], ICP-OES [13], ICP-AES [14,15] or AAS [8, 9, 16]. For the analysis of the copper of the hair, the AAS technique is recommended, preceded by an acidic digestion of the samples because thus the organic matter is effectively removed [7, 17]. GFAAS has wide application for trace elements, low operational and instrumental costs, is an accessible technique in most routine laboratories and it's easy to operate [9, 18].

The aim of this study is the validation (linearity and range, limit of detection, limit of quantification, precision, and accuracy) of a simple, cheap, and sensitive analytical method for the determination of copper content in hair samples through graphite furnace atomic absorption spectrophotometry (GFAAS). Determining the copper content in different human hairs can be used as an index of exposure to this potentially toxic element or as information on a person's health status.

RESULTS AND DISCUSSION

The graphite furnace atomic absorption spectrophotometry applied in this study was tested for system suitability by aspirating five replicates of copper samples. The best conditions are adequately selected. The system suitability was performed to provide that the testing system (instrument, reagents, and analyst) is appropriate for the copper analysis in hair samples. The primary parameters can include repeatability (%RSD) for five absorbance readings. The RSD% values are presented in Table 1.

Table 1. System suitability testing of copper determination in hair by GFAAS

Copper standard (µg/L)	Absorbances reading					RSD%
2	0.093	0.087	0.087	0.085	0.088	1.58
5	0.171	0.171	0.168	0.170	0.172	0.74
9	0.293	0.290	0.293	0.293	0.262	1.45
13	0.416	0.420	0.416	0.420	0.420	0.45
17	0.539	0.538	0.536	0.538	0.541	0.27
20	0.659	0.661	0.665	0.665	0.674	0.76

The proposed and validated analytical method was used to determine the copper in 12 hair samples. The hair samples, including 9 normal and 3 dye, were collected from both sexes aged from 12 to 75. The results are presented in tables 2-5.

The RSD% for copper absorbance readings should not be more than 2.0% [19]. Results presented in Table 1 demonstrated the suitability of the complete system for the copper analysis in hair samples.

Table 2. Intra-day repeatability of the proposed method

Sample	Theoretical copper concentration ($\mu\text{g/g}$)	Measured copper concentration ($\mu\text{g/g}$)* \pm sd	Relative standard deviation (%)
Standard 1	13	12.8 \pm 0.352	2.75
Standard 2	20	20.5 \pm 0.170	0.83
Hair sample	-	11.4 \pm 0.362	3.18

* mean of six measurements

The homogeneity variance test (applied for the lowest and the highest concentration values of proposed concentration range, each of them measured by ten times) established a value of 3.24. F test was applied with the following acceptance criterion: F value is 5.35 higher than 3.24 value. This means that no significant differences were found between the variances of the concentration range limits.

The calibration curve for copper was constructed by plotting the absorbances versus concentrations. Linearity is observed in a concentration range from 2 $\mu\text{g/L}$ to 20 $\mu\text{g/L}$ of copper. The least squares method showed the linearity of the proposed method obtaining a linear regression equation $y = 0.0324x$ and the determination coefficient (R^2) equal to 0.9979. The value of R^2 showed excellent linearity of the calibration curve for the method with LOD = 0.0563 $\mu\text{g/g}$ and LOQ = 0.1874 $\mu\text{g/g}$.

Table 3. Inter-day reproducibility for copper standard solutions for proposed method

Sample	Day	Theoretical copper concentration ($\mu\text{g/L}$)	Measured copper concentration ($\mu\text{g/L}$)* \pm sd	Relative standard deviation (%)
Standard 1	1 st	13	12.90 \pm 0.101	0.79
	2 nd	13	12.93 \pm 0.249	1.93
	3 rd	13	12.85 \pm 0.204	1.59
Standard 2	1 st	20	20.40 \pm 0.191	0.94
	2 nd	20	20.30 \pm 0.416	2.05
	3 rd	20	20.90 \pm 0.211	1.01

* mean of six measurements

METHOD VALIDATION FOR COPPER DETERMINATION IN HUMAN HAIR SAMPLES THROUGH GRAPHITE FURNACE ATOMIC ABSORPTION SPECTROMETRY

Table 4. Inter-day reproductibility for different hair samples

Sample	Day	Measured copper concentration ($\mu\text{g/g}$)* \pm sd	Relative standard deviation (%)
adult male hair sample	1 st	11.4 \pm 0.362	3.18
	2 nd	11.2 \pm 0.356	3.18
	3 rd	11.3 \pm 0.205	1.82
adult female hair sample	1 st	199.09 \pm 4.200	2.11
	2 nd	191.80 \pm 4.089	2.14
	3 rd	196.30 \pm 3.788	1.93
teenager male hair sample	1 st	130.0 \pm 5.018	3.86
	2 nd	133.2 \pm 5.261	3.95
	3 rd	127.2 \pm 1.869	1.47
teenager female hair sample	1 st	11.31 \pm 0.321	2.84
	2 nd	11.41 \pm 0.416	3.65
	3 rd	11.27 \pm 0.373	3.31

* mean of six measurements

Table 5. Levels of copper in hair samples

Hair sample	Treatment	Concentration ($\mu\text{g/g}$) \pm confidence interval
adult male - 46 years old	normal	11.24 \pm 2.230
adult male - 50 years old	normal	45.42 \pm 2.206
adult male - 75 years old	normal	50.50 \pm 0.891
teenager male - 15 years old	normal	130.17 \pm 0.638
teenager male - 18 years old	normal	64.27 \pm 2.196
adult female - 44 years old	dyed	197.21 \pm 0.064
adult female - 58 years old	dyed	145.06 \pm 0.283
adult female - 61 years old	dyed	142.18 \pm 0.393
adult female - 21 years old	normal	74.17 \pm 1.038
adult female - 29 years old	normal	98.59 \pm 1.321
teenager female - 13 years old	normal	11.33 \pm 0.826
teenager female - 12 years old	normal	56.06 \pm 2.583

Precision was determined by analyzing results from the intra-day repeatability and inter-day reproductibility for the known concentrations of copper standard solutions (n= 6). Simultaneous replicates at different times, on different hair samples, were performed during the study period, in the same way as for standard solution to obtain more representative values [20]. The relative standard deviations are based on Horwitz equation which suggest that $RSD < 2^{(1-0.5\lg c)}$, where c is the concentration of the analyte. The obtained %RSD values for the standard solution of copper and for hair samples, were lower than those obtained using the Horwitz equation (table 2 - 4). Also, according to the acceptance criteria established by the Commission of the European Communities all the calculated RSD values were lower than 15%, demonstrating an adequate precision [21].

By combining the data obtained, it can be found that with the increase in the number of samples analyzed, the confidence in the precision of the measurements made increases; with the increase of analytical variability, no deterioration of RSD% is observed.

The accuracy values obtained for the different additions of standard solutions containing 7.20 µg/g, 18.08 µg/g and 36 µg/g of copper are 92.91%, 94.96% and 90.46%, respectively. These results (table 6) highlight the fact that the recovery obtained is between 90.46-94.96%, falling within the acceptance criterion for fortification tests which requires recovery values within the range of 80 to 110 % [20]. It is evident that the method is accurate within the desired range.

Table 6. The results for accuracy at the copper determination from hair using the GF AAS technique.

Sample	A multielement stock solution concentration added (calculated) µg/g	Concentration recovered µg/g	Recovery (%)
adult male hair sample	-	11.03	
	+7.20	17.72	92.91
	+18.08	28.2	94.96
	+36.00	43.6	90.46

Method Applicability

Copper concentrations detected in studied hair samples (Table 5) are comparable and some are higher as those reported in other studies [6, 9-16, 18, 22-24]. The data obtained indicate that higher amounts of copper are found in adult female hair samples; the amount are higher probably due to the dyed hair. These differences in the composition of colored or untreated hair are because coloring process leads to the opening of the hair cuticle and the partial exchange of element between the hair and the dye [25, 26].

Copper concentrations in studied hair samples were higher in the female subjects than male subjects. This probably can be assigned to the different hormonal balance between sexes. The copper level increased from teenager female to adult female (normal treatment of hair), but it decreased from teenager man to adult male. This can be explained by the high intake required during adolescence period for teenager man and in case of teenager female was observed a different behavior due to the beginning of menstruation [4].

Grzegorz Izydorczyk and co. publish a study about hair mineral analysis in the population of Poland. They found that the copper levels are higher on female than male as in our study (Table 5) and smoking, occupation, dietary habits, local crops consumption are the factors that influences the copper level in hair [27].

The copper content in hair samples is influenced by a series of factors such as: metabolism, lifestyle, health status, geographical and economical living conditions as well the type of hair, and hair treatment [2, 28 - 30].

CONCLUSION

The data obtained from the validation procedure shows that the proposed GFAAS method is accurate and corresponds to the criteria of linearity, repeatability, intermediate precision, LOD and LOQ, implemented by Council Directive 96/23/EC. Validation was performed by studying analytical curve linearity ($R^2=0.9979$) and range (2 - 20 $\mu\text{g/L}$), estimated limit of detection (LOD) - 0.05632 $\mu\text{g/g}$ and limit of quantification (LOQ) - 0,18745 $\mu\text{g/g}$. The method accuracy ranged from 90.46-94.96% and the precision measured as intra-day repeatability and inter-day reproductibility did not exceed 3.95% RDS%. The system suitability test was performed with RSD% lower than 1.58%. This study confirms that the proposed method is suited to copper analysis from human hair samples. It was concluded that the copper concentration in the dyed hair samples is higher than the normal hair samples. Also, the data obtained indicated that higher amounts of copper may be required for growing of teenagers.

EXPERIMENTAL SECTION

Sample Preparation

The human hair samples were collected from healthy adults and teenagers in the age range of 12 -75. Each sample was cut in 5 mm length with sterilized stainless-steel scissors and packaged in polyethylene bags. In the laboratory, one gram of each sample was washed with detergent, then rinsed with ultrapure water, acetone and dry for 6 h at 80°C. The ground dry hair sample (50 mg) was accurately weighed into a PTFE vessel and 2.5 ml of HNO_3 65 % was added (suprapur HNO_3 65 %, Merck KGaA, Darmstadt, Germany). The vessel was closed, shaken, and placed inside the microwave digestion system for 15 min at 170°C, table 7. At the end of digestion, the samples were removed from the digestion oven, cooled at room temperature, and diluted to 50 ml final

volume with deionised water. Finally, the solutions were filtered using a 0.45 μm pore size filter. Mineralisation was carried out in a Microwave Digestion System (Berghof Speedwave®, ENTRY, Germany), in high-pressure PTFE vessel, using a standard acid digestion protocol for hair [31]. The blanks were submitted to the same digestion procedure mentioned above.

Table 7. Temperature program

Step	Temperature (°C)	Ramp (min)	Time (min)
1	130	3	8
2	155	2	5
3	170	2	15
4	75	1	10

Instrumentation

The copper content was determined by graphite furnace atomic absorption spectrometry (GFAAS, model: ContraAA 800D, Analytik Jena Instruments, Germany) using standard calibration technique. Blank samples were prepared by adding same the reagents into a PTFE vessel without the sample and subsequently diluted in the same manner as described above. To reduce the risk of contamination, the whole glass was carefully cleaned and rinsed with ultrapure water.

To provide results directly proportional to the analyte concentration in the sample within a set range, calibration curve was prepared through 1000 ppm standard solution dilution (ICP multi-element standard solution IV, Merck, Germany). Deionized water (Direct Q UV, Millipore, approximately 18.0M Ω) was used in the preparation of all solutions. The solutions were kept in polyethylene vials. The graphite furnace parameters of analytical method are: 324.754 nm (wavelength – primary line), with 900°C for pyrolysis and 2000°C for atomization (without modifier), table 8. The atomic absorption spectrometer has a Xenon short arc lamp as a single light source.

Table 8. Graphite furnace parameters (platform)

Step	Name	Temperature (°C)
1	Drying	80
2	Drying	90
3	Drying	110
4	Pyrolysis	350
5	Pyrolysis	900
6	Gas adaption	900
7	Atomize	2000
8	Clean	2450

Method Validation

In this study validation parameters such as linearity and range, limit of detection (LOD), limit of quantification (LOQ), precision, and accuracy were evaluated.

Linearity

The linearity of this method was evaluated by constructing a calibration curve in the range 2 µg/L - 20 µg/L.

A set of copper standard solutions were freshly prepared by appropriate dilution of the stock intermediate standard solution (20 µg/L) to get calibration curve. The appropriate volumes were measured from the intermediate stock solution automatically inserted with the autosampler in the GF-AAS. For each sample five readings were noted and the % relative standard deviation for absorbance for each copper standard solution were calculated. System suitability parameters were evaluated.

The homogeneity variance test was used to test the linearity range. To the obtained variances, the F test was applied to evaluate the significant differences of concentration range limits and to evaluate the regression and lack of fit significances [32].

Limit of Detection (LOD) and Limit of Quantification (LOQ)

LOD and LOQ were calculated using the calibration data and regression statistic, using the formulas: $LOD = a + 3 s(r)$; $LOQ = a + 10 s(r)$; where $s(r)$ is the residual standard deviation or residual standard error and a is the y-intercept [33]. Residual standard error is a statistical measure of the deviation of the data from the fitted regression line. It is possible to calculate a confidence interval for the predicted values using the calibration function, an interval that appears in the literature under the name "standard error of prediction". The prediction interval provides an estimate of the uncertainty associated with the predicted values of x . The 13µg/L standard solution was used to evaluate the detection limit of the method and the absorbance of three measurements was used in the calculations.

Precision

Intra-day repeatability. The repeatability of the analytical method was determined by relative standard deviation (%RSD) for six determination of the copper standard solution (medium level concentration - 13µg/L and high-level concentration - 20µg/L) and an adult male hair sample, performed on the same day with an interval of an hour under the same experimental and laboratory conditions.

Inter-day reproducibility. Inter-day reproducibility is the estimation of variations in analysis when a method is used in the same laboratory, on the different day and different analyst or when a method is used within laboratories. The inter-day reproducibility is assessed by analyzing simultaneous replicates at different times, on different hair samples (adult male, adult female, teenager male and teenager female hair samples), were performed during the study period, in the same way as for standard solutions.

Accuracy

In this study, accuracy was demonstrated by performing additions of different concentrations of copper standard solution (7.20 µg/g, 18.08 µg/g and 36.00 µg/g) to a known pre-analyzed sample.

The % recovery of the added copper standard solution calculated as, %Recovery = $[(Ct - Cs) / Ca] \times 100$, where Ct is the total analyte concentration measured after standard addition; Cs, analyte concentration in the sample; Ca, analyte concentration added to sample.

REFERENCES

1. C. Croitoru; *Tratat de stiinta alimentatiei si cunoasterea alimentelor. Bazele alimentatiei si sanatatea*, Editura AGIR, Bucuresti, Romania, **2014**, pp. 473.
2. M. Herman; A. Przybylowicz; E. Florek; W. Piekoszewski; *J. of Anal. Chem.*, **2013**, 68, 360-367.
3. EFSA NDA Panel (EFSA Panel on Dietetic Products, Nutrition and Allergies), 2015 Scientific Opinion on Dietary Reference Values for copper. *EFSA Journal* **2015**; 13(10):4253, pp. 51.
4. T. Sakai; M. Wariishi; K. Nishiyama; *Biol. Trace Elem. Res*, **2000**, 77(1), 43-50.
5. M. Nasiri-Majd; M.A. Taher; H. Fazelirad; *Ionics*, **2016**, 22, 289-296.
6. F. Shah; T.G. Kazi; H.I. Afridi; N. Kazi; J.A. Baig; A.Q. Shah; S. Khan; N.F. Kolachi; S.K. Wadhwa; *Biol. Trace Elem. Res.* **2011**, 141(1-3), 131-48.
7. T.G. Kazi; H.I. Afridi; G.H. Kazi; M.K. Jamali; M.B. Arain; N. Jalbani; *Clin. Chim. Acta*, **2006**, 369(1), 52-60.
8. O.A. Denisenko; P.S. Novikov; N.A. Cherevko; A.N. Kucher; E.S. Ikhalaïnen; V.I. Otmahov; A.V. Obukhova; *Mosc. Univ. Chem. Bull.*, **2019**, 74, 149-152.
9. M. Herman, A. Przybylowicz, E. Florek, W. Piekoszewski. *J Anal Chem* **2013**, 68, 360–367.
10. J. Guo, W. Deng, L. Zhang, Ch.Li, P. Wu, M. Peiling, *Biol. Trace Elem. Res.*, **2007**, 116, 3, 257- 271.
11. H.S. Park, K.O. Shin, J.S. Kim, *Biol. Trace Elem. Res.*, **2007**, 116, 2, 119-130.
12. M.Slotnick, J. Nriagu, M. Johnso, A. Linder, K. Savoie, H. Jamil, A. Hammad, *Biol. Trace Elem. Res.*, **2005**, 107, 2, 113-126.

METHOD VALIDATION FOR COPPER DETERMINATION IN HUMAN HAIR SAMPLES THROUGH GRAPHITE FURNACE ATOMIC ABSORPTION SPECTROMETRY

13. A. Unkiewicz Winiarczyk, A. Bagniuik, K. Gromysz Kalkowska, E. Szubartowska, *Biol. Trace Elem. Res.*, **2009**, 128, 2, 152-160.
14. K. Sreenivasa Rao, T. Balaji, T. Prasada Rao, Y. Babu, G.R.K. Naidu, *Spectrochim. Acta*, Part B, **2002**, 57, 1333-1338.
15. W. Ashraf, A. Jaffar, K. Anwer, U. Ehsan, *Environ. Poll.*, **1995**, 87, 61-64.
16. A. Sukumar, R. Subramanian, R., *Biol. Trace Elem. Res.*, **2005**, 107, 113-126.
17. I. Bancuta; A. Chilian; O.R. Bancuta; F. Stan; S. Mihai; V. Miron_Alexe; *J. Sci.Arts*, **2022**, 22(4), 965-976.
18. N. Dalali M. Ashouri, S. Nakisa, *J Iran Chem Soc.*, **2012**, 9, 181–188
19. S. Ata; F.H. Wattoo; M. Ahmed; M.H. Sarwar Wattoo; A.S. Tirmizi; A. Wadood; *Alex. J. Med.*, **2015**, 51(1), 19-23.
20. *AOAC Guidelines for Single Laboratory Validation of Chemical Methods for Dietary Supplements and Botanicals*. AOAC International, Gaithersburg, MD, USA, **2002**.
21. The Commission of the European Communities. Commission decision 2002/657/EC of 12 August 2002 implementing Council Directive 96/23/EC concerning the performance of analytical methods and the interpretation of results. *Official Journal of European Communities*, **2002**, 1, p. 29.
22. N. Dalali; M. Ashouri; S. Nakisa; *J. Iran. Chem. Soc.*, **2012**, 9, 181-188.
23. F.U. Tian; Y.H. Chen; Y.A.N. Zhang; *J. Anal. Chem.*, **2015**, 70, 436-439.
24. B. Czerny; K. Krupka; M. Ożarowski A. Seremak-Mrozikiewicz, *Sci. World J.*, Article ID 953181, **2014**, 1-15
25. K.H. Kim; E. Kabir; S.A. Jahan; *Environ. Int.*, **2016**, 222, 89-90.
26. E.H.N. Pehlic; H. Husein; A. Aldžić-Baltić; *New Technologies, Development and Application*, I. Karabegović (Ed.): NT 2018, LNNS, **2019**, 42, p. 561.
27. G. Izydorczyk; M. Mironiuk; S. Baśladyńska; M. Mikulewicz; K. Chojnacka; *Environ. Res.*, **2021**, 196, 110441
28. J.R. Forero-Mendieta; J.D. Varón-Calderón; D.A. Varela-Martínez; D.A. Riaño-Herrera; R.D. Acosta-Velásquez; J.A. Benavides-Piracón; *Separations*. **2022**, 9, 158, 1-14.
29. X. Dong; Y. Nakaguchi; K. Hiraki; *Anal. Sci.* **1998**, 14, 785-789.
30. N.F. Kolachi; T.G. Kazi; H.I. Afridi; N. Kazi; G.A. Kandhro; A.Q. Shah; J.A. Baig S.K. Wadhwa; S. Khan; F. Shah; M.K. Jamali; M.B Arain; *Biol. Trace Elem. Res.*, **2011**, 143(1), 116-130.
31. <https://www.berghof-instruments.com/en/products/speedwave-entry/> Application Report; SPEEDwave Entry V 9.0; S.19/1, www.berghof.com, 53-0202-87-00-01-003; V 9.0; S.35/1www.berghof.com, 53-0202-87-00-01-001
32. A.G. Gonzalez; A. Herrador; *Trends in Analytical Chemistry*, **2007**, 26, 227-238.
33. O. Magnusson; *Eurachem Guide: The Fitness for Purpose of Analytical Methods - A Laboratory Guide to Method Validation and Related Topics*, <http://www.eurachem.org> 2nd ed. June 14, 2015.

CHEMOMETRIC SMART APPROACHES USING ARTIFICIAL NEURAL NETWORKS AND CONTINUOUS WAVELET TRANSFORM FOR SIMULTANEOUS QUANTITATIVE ANALYSIS OF CIPROFLOXACIN-ORNIDAZOLE TABLETS

Erdal DİNÇ^{a*}, Burak ARI^a, Eda BÜKER^b, Dorina CASONI^c

ABSTRACT. New chemometric smart approaches, Artificial Neural Network (ANN) and Continuous Wavelet Transform (CWT), based on UV spectrophotometric data, were proposed for the simultaneous quantitative analysis of ciprofloxacin and ornidazole in tablets. Both methods enabled the study of the two-component mixtures containing these drugs without requiring a pre-separation process. The ANN calibration model was developed by establishing a relationship between the absorbance measurement matrix and the calibration set, which was constructed using a full factorial design methodology. To quantify ciprofloxacin and ornidazole, Symlets8 continuous wavelet transform (sym8-CWT) exhibited to be a suitable tool for transforming the UV spectra during the calibration and prediction stages. Both chemometric methods were applied within the linear working range of 3–24 µg/mL for ciprofloxacin (CIP) and 6–32 µg/mL for ornidazole (ORN). The validity of the proposed ANN and sym8-CWT approaches was confirmed through the analysis of independent test samples, as well as intra-day, inter-day, and standard addition experiments. The ANN method provided impressive recovery rates of 99.9% for CIP and 100.1% for ORN. Similarly, the sym8-CWT method achieved recovery rates of 98.5% for CIP and 101.5% for ORN. Both ANN and sym8-CWT approaches were successfully applied to the real sample analysis of CIP-ORN tablets, demonstrating precise and accurate results at a low cost and with minimal sample preparation.

Keywords: UV-Spectrophotometry, Artificial Neural Network, Continuous Wavelet Transform, Ciprofloxacin, Ornidazole

^a Ankara University, Faculty of Pharmacy, Emniyet mah. Döğol Cad., 06560, Yenimahalle-Ankara, Turkey

^b Gazi University, Faculty of Pharmacy, Taç sok., 06330, Yenimahalle-Ankara, Turkey

^c Babeş-Bolyai University, Faculty of Chemistry and Chemical Engineering, 11 Arany Janos str., RO-400028, Cluj-Napoca, Romania

* Corresponding author: dinc@ankara.edu.tr



INTRODUCTION

Ciprofloxacin, chemically known as 1-cyclopropyl-6-fluoro-4-oxo-7-piperazin-1-ylquinoline-3-carboxylic acid (Figure 1), is an antibiotic effective against a wide range of bacterial infections. It exhibits activity against both Gram-positive (Gram +) bacteria, such as *Streptococcus pneumoniae*, and Gram-negative (Gram -) bacteria, such as *Helicobacter pylori*. Ciprofloxacin is commonly prescribed for urinary tract infections, certain gastrointestinal infections, gynecological infections, sexually transmitted diseases, skin infections, and upper and lower respiratory tract infections, including sinusitis, pneumonia, and bronchitis [1].

Ornidazole, chemically named 1-Chloro-3-(2-methyl-5-nitro-1H-imidazol-1-yl)propan-2-ol, is an antibiotic primarily used to treat protozoan infections. Its antimicrobial spectrum is similar to that of metronidazole, but it is better tolerated. Initially, ornidazole was introduced to treat trichomoniasis, a condition caused by protozoan and anaerobic bacterial infections [2]. It has also been found effective in managing Crohn's disease [3]. Additionally, ornidazole demonstrates activity against coliform bacteria in vivo, despite in vitro resistance [4]. It is suggested that the drug remains active against aerobic Gram-negative microorganisms in the presence of anaerobic bacteria [5].

In previous studies, various analytical methods, including high-performance liquid chromatography (HPLC) [1–4, 6–9] and spectroscopy [5–8, 10–13], have been documented for analyzing the combination of ciprofloxacin and ornidazole in tablets. Additionally, the estimation of these substances in spiked serum has been conducted using thin-layer chromatography (TLC) [14] and HPLC [15].

While widely used, Chromatographic methods come with notable drawbacks, including the need for sophisticated instrumentation, time-consuming procedures, high costs, and a considerable environmental impact [16–18]. In contrast, spectrophotometry offers a straightforward, cost-effective alternative that does not require complex steps or processes. However, one of the key challenges in spectrophotometric analysis is the spectral overlap of analytes, where the absorption spectra of different components in a mixture may interfere with one another, complicating accurate analysis.

This issue of spectral data overlap can be effectively addressed by integrating chemometric methods with spectrophotometric data. Unlike chromatographic techniques, this approach eliminates the need for tedious sample pretreatment [19, 20]. Spectrophotometry, as an analytical technique, measures the absorption or transmission of light by a sample as a function of wavelength, providing a simple and economical method for analysis. When

combined with advanced chemometric tools, it becomes a powerful solution for resolving spectral overlaps, offering reliable and practical results without extensive sample preparation [19-20].

Additionally, the combined use of spectrophotometric data with chemometric methods aligns with the principles of green analytical chemistry, enhancing the “greenness” of the analytical process. This synergy reduces resource consumption through miniaturization, minimizes using bio-accumulative or non-green reagents, and decreases waste production. Tools like the Analytical Eco-Scale and the National Environmental Methods Index (NEMI) are commonly employed to evaluate the environmental sustainability of such methods, grounded in the twelve principles of green chemistry [21].

Although liquid chromatographic techniques are often applied to quantify overlapping spectra of drugs with similar chemical structures, they are less favored in green analytical practices due to their higher environmental impact. The combination of spectrophotometric techniques and chemometric methods offers an efficient, eco-friendly alternative for accurate and sustainable pharmaceutical analysis.

In recent years, using two or more active substances rather than a single active ingredient in pharmaceutical formulations has become increasingly common. This approach aims to achieve enhanced therapeutic effects or prevent the progression of diseases by targeting multiple pathways or mechanisms. However, the inclusion of multiple active compounds in a formulation introduces significant challenges in terms of quality control and routine analytical procedures. As previously mentioned, a significant challenge is the complexity caused by overlapping spectral bands of analytes within the same spectral region, making it impossible to analyze multicomponent mixtures using direct absorbance measurement techniques.

To overcome this challenge, advanced chemometric techniques such as Artificial Neural Networks (ANN) and Continuous Wavelet Transform (CWT) have proven to be highly effective tools. By utilizing ANN models and CWT signal processing on UV absorbance measurement data, accurate and reliable quantitative resolution of complex mixtures containing two or more analytes can be achieved. These methods provide a robust and innovative solution to the limitations of conventional analytical techniques, enabling more efficient, precise, and reliable analysis in pharmaceutical research and quality control applications.

Artificial Neural Network (ANN) and Continuous Wavelet Transform (CWT) methods are among the most significant numerical and graphical tools employed in academic and pharmaceutical sectors to address complex analytical problems, respectively, without the need for a preliminary separation procedure. Continuous Wavelet Transform (CWT) is a well-known method in

the field of chemometrics [22-24]. It employs wavelet functions to analyze spectral reflections at various scales, breaking down the spectral signal into a series of wavelet coefficients. CWT's most significant advantage is its ability to simultaneously detect the phase and instantaneous frequency of a nonstationary signal, which is achieved through time-frequency analysis.

Although liquid chromatographic techniques effectively resolve overlapping spectra of similar drugs, their high resource demands, and environmental impact make them less favorable. Chemometric methods, including Continuous Wavelet Transform (CWT) and Artificial Neural Networks (ANN), overcome these limitations by improving signal-to-noise ratios and minimizing spectral interference. Despite challenges in determining zero points and selecting optimal wavelet families, recent studies highlight the successful application of CWT, ANN, and UV-Vis spectrophotometry for the simultaneous quantification of ciprofloxacin (CIP) and ornidazole (ORN) in synthetic mixtures and commercial formulations.

This study aimed to improve advanced methods, Continuous Wavelet Transforms (CWTs), and Artificial Neural Networks (ANN) using the UV absorbance measurements for the simultaneous quantitative estimation of ciprofloxacin (CIP) and ornidazole (ORN) in a tablet dosage form. Among the various wavelet functions tested, the symlets8 family was identified as the most suitable for the determination of these drugs. Calibration graphs for CIP and ORN were established within their respective working ranges of 3–24 µg/mL and 6–32 µg/mL, yielding accurate and reliable results. In the architect of the ANN model, 273 input neurons, five hidden neurons, and two output neurons were used for the ANN chemometric calibration using full absorbance measurement and a concentration set of 17 mixtures containing CIP and ORN drugs. After validation of the proposed chemometric approaches, the methods were applied to quantify the relevant substances (CIP and ORN) in commercial tablets.

RESULTS AND DISCUSSION

In analytical practice, one of the key challenges when applying Continuous Wavelet Transform (CWT) for resolving overlapping UV spectral bands is identifying the most suitable wavelet family that provides optimal quantification of the relevant drugs in their mixture. In the present study, various wavelet families with distinct scaling factors were systematically tested for their ability to resolve the overlapping spectral bands of ciprofloxacin (CIP) and ornidazole (ORN). Among the tested families, the sym8-CWT wavelet family emerged as the most effective tool, delivering precise, accurate, and reliable results for the simultaneous quantitative estimation of CIP and ORN

in tablet formulations. The enhanced application of the sym8-CWT approach, in conjunction with the Artificial Neural Network (ANN) model, is discussed in detail below.

As previously outlined, calibration solutions of CIP and ORN were prepared within their respective working ranges of 3.0–24.0 $\mu\text{g/mL}$ for CIP and 6.0–32.0 $\mu\text{g/mL}$ for ORN. The UV spectra of the calibration standards, test samples (binary mixtures), and commercial tablet formulations were recorded across a wavelength range of 220–400 nm. The spectral overlap of CIP and ORN was clearly illustrated in Figure 1. As observed, traditional spectrophotometric methods are insufficient for the simultaneous quantitative analysis of CIP and ORN due to the pronounced overlap of their UV absorption spectra within the same spectral region. This spectral interference poses a significant challenge in distinguishing between the two analytes in complex tablet matrices.

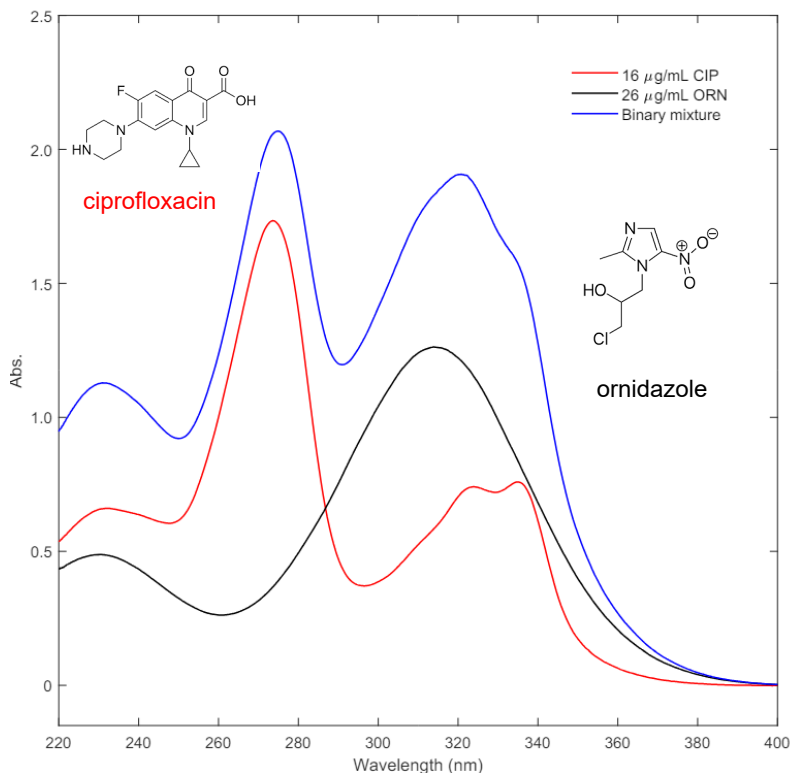


Figure 1. Chemical structure of CIP and ORN, UV spectrum of CIP, ORN and mixture of CIP and ORN

To overcome this limitation, we explored novel signal processing techniques based on wavelets, which have been proven effective for resolving mixtures of compounds without the need for complex sample separation steps. The preliminary results of these tests revealed that the sym8-CWT wavelet family was the most suitable for transforming the UV spectral data vectors of both the calibration and validation samples. This transformation enabled accurate and reliable quantitative analysis of the CIP-ORN tablets, highlighting the robustness of the sym8-CWT approach in complex pharmaceutical formulations.

Application of ANN and CWT Methods

As explained above, the calibration samples containing CIP and ORN in the concentration range of 3.0-24.0 µg/mL for CIP and 6.0-32.0 µg/mL for ORN in base media and methanol were individually prepared by using standard stock solutions of the analyzed compounds. The absorption spectra of the analyzed samples were recorded between 220.0-400.0 nm. The recorded absorbance data vectors were transferred into Microsoft Excel. This Excel file for the wavelet analysis of the data was saved on the computer. Figure 1 indicates the chemical structures of CIP and ORN, the UV spectrum of CIP (16 µg/mL), ORN (28 µg/mL), and a mixture of CIP (16 µg/mL) and ORN (28 µg/mL). Figure 2a shows the UV absorption spectra of the calibration samples of CIP and ORN in their working concentration range. Some continuous wavelet families at different scale parameters (a) were applied to process the UV absorbance data vectors. From the wavelet analyses, sym8-CWT was identified to get the optimal signal transformation of the original UV spectra for more precise and accurate assay results. The CWT spectra of CIP and ORN, obtained by applying the CWT signal processing methods to the absorbance data vectors, are indicated in Figure 2b. From these CWT spectra in Figure 2, it was observed that three different CWT approaches became very suitable for resolving overlapping UV spectra for the analysis of CIP-ORN tablets.

For the quantitative estimation of the related substances, the calibration curves were obtained by regression of the concentration on the sym8-CWT amplitude at 320 nm and 341 nm for CIP and ORN, respectively (Figure 2b). The statistical results related to the linear regression analyses for the analyzed active compounds are listed in Table 1. CIP and ORN were determined by means of the computed calibration curves.

In the application of the ANN model, input 273 neurons, hidden 5 neurons, and output 2 neurons were used as a methodological architect. A concentration set containing 17 mixtures of CIP and ORN was prepared using the full factorial design with two factors and four levels (Table 2.).

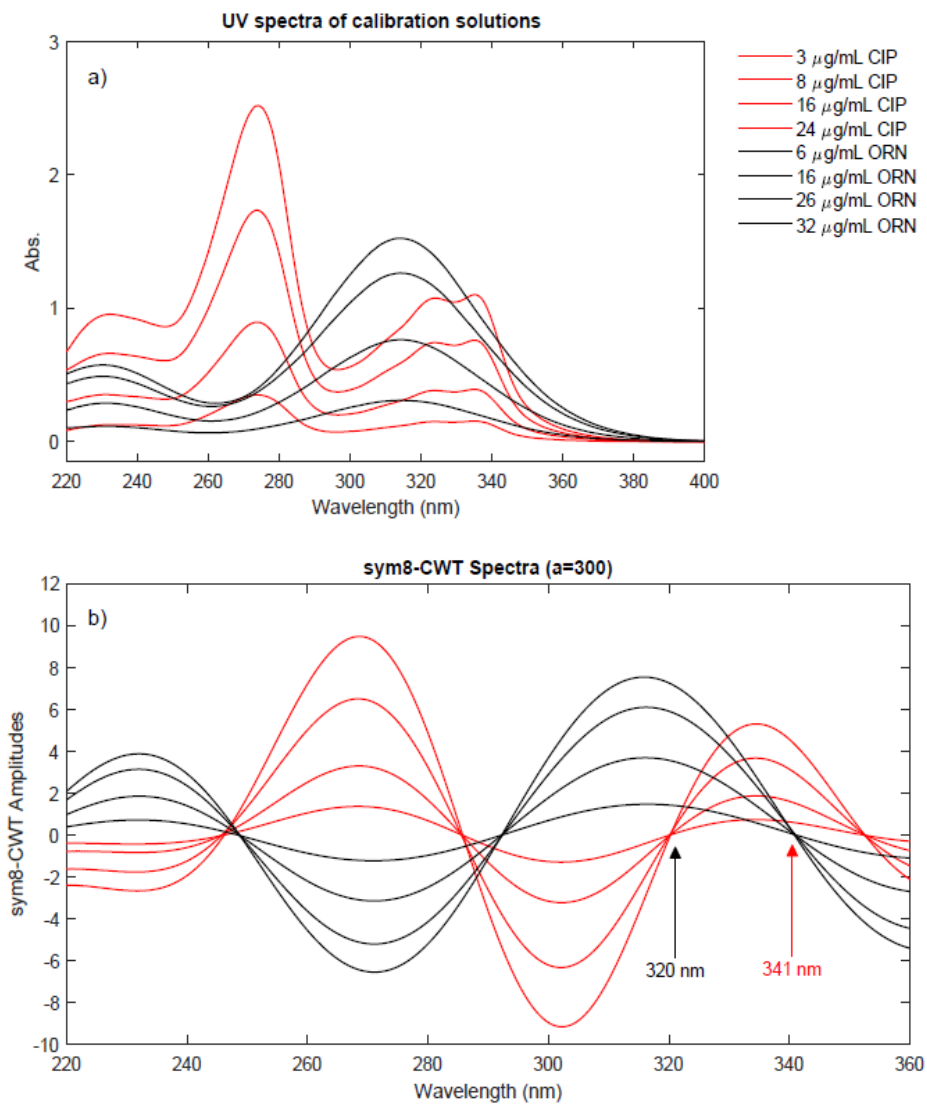


Figure 2. Zero order absorption spectra (a), sym8-CWT method (b), of 3-24 $\mu\text{g/mL}$ CIP (—) and 6-32 $\mu\text{g/mL}$ ORN (—) mixtures using methanol as blank.

Table 1. Calibration results obtained by the proposed sym8-CWT method for the analysis of CIP and ORN in mixture samples

	CIP	ORN
m	0.1615	0.2195
n	0.0760	0.0424
r	0.9998	0.9998
SD(m)	2.35×10^{-3}	3.12×10^{-3}
SD(n)	3.53×10^{-2}	6.97×10^{-2}
SD(r)	1.03×10^{-2}	1.01×10^{-2}
LOD	0.66	0.95
LOQ	2.19	3.17

m=slope; n=intercept; r=correlation coefficient; SD (m)=standard deviation of slope; SD (n)=standard deviation of intercept; SD (r)=Standard deviation of correlation coefficient; LOD=detection limit ($\mu\text{g/mL}$); LOQ=quantitation limit ($\mu\text{g/mL}$)

In building the ANN calibration procedure, the performance of the method is illustrated in Figure 3. The build ANN model was applied to the quantification of the related drugs in analyzed samples.

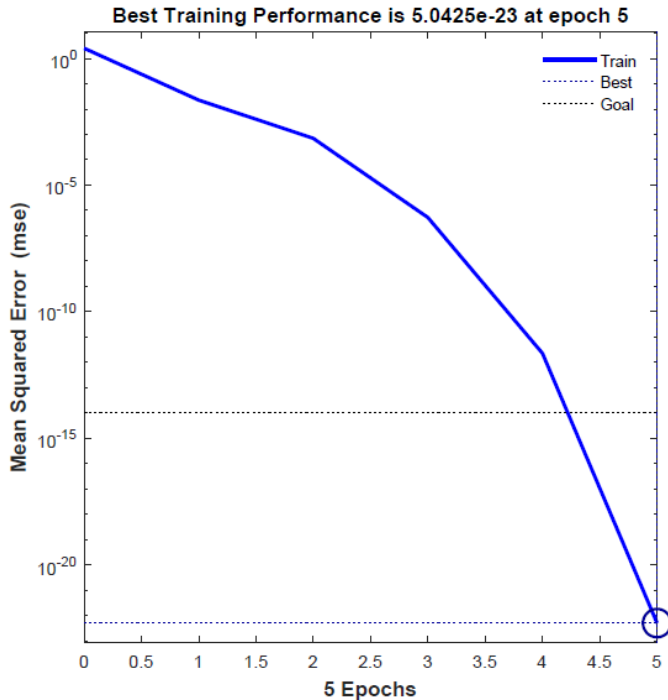


Figure 3. Performance of ANN method

Analytical validity of the applied methods

In this research, the analytical validity of the applied methods, ANN and sym8-CWT, was assessed based on several factors, including range, linearity, accuracy, precision, selectivity, limit of detection (LOD), and limit of quantitation (LOQ) for the analysis of CIP and ORN in tablets. The results showed that the concentration range for both compounds was linear, with a range of 3.0–24.0 µg/mL for CIP and 6.0–32.0 µg/mL for ORN. Higher correlation coefficients were obtained for the calibration curves of CIP and ORN using sym8-CWT, as shown in Table 1. In the validation process, LOD and LOQ were determined using the standard deviation and slope values from the calibration curves, with the corresponding results presented in Table 1.

Table 2. Full factorial design of the analysis

Sample Number	CIP µg/mL	ORN µg/mL
K2	8	6
K3	16	6
K4	24	6
K5	3	16
K6	8	16
K7	16	16
K8	24	16
K9	3	26
K10	8	26
K11	16	26
K12	24	26
K13	3	32
K14	8	32
K15	16	32
K16	24	32
K17	18	18

Several binary mixtures with different concentration levels of the active compounds were analyzed to evaluate the accuracy and precision of the proposed methods, as described in the recovery and intra-day and inter-day studies. Percent mean recoveries and relative standard deviations were calculated. The assay results, obtained using the signal processing methods, are presented in Tables 3 and 4. The experiments showed that the proposed wavelet and derivative methods provided satisfactory accuracy and precision without requiring a preliminary separation step.

Table 3. Recovery results of CIP and ORN in laboratory prepared mixtures by the ANN and CWT methods

Sample Code	Added ($\mu\text{g/mL}$) CIP ORN		ANN				sym8-CWT			
			Found ($\mu\text{g/mL}$) CIP ORN		Recovery (%) CIP ORN		Found ($\mu\text{g/mL}$) CIP ORN		Recovery (%) CIP ORN	
M1	3	18	2.97	17.62	99	97.9	3	18.29	100.1	101.6
M2	12	18	12.26	18.28	102.2	101.6	12.03	18.81	100.2	104.5
M3	24	18	23.31	17.95	97.1	99.7	23.29	18.37	97	102
M4	18	6	18.25	5.94	101.4	98.9	17.46	6.11	97	101.8
M5	18	20	17.73	20.23	98.5	101.2	17.7	19.72	98.3	98.6
M6	18	32	18.15	32.39	100.8	101.2	17.66	32.1	98.1	100.3
				Mean	99.9	100.1		Mean	98.5	101.5
				SD	1.94	1.48		SD	1.86	1.89
				RSD	1.94	1.47		RSD	1.85	1.9

 \bar{X} : Mean

SD: Standard deviation

RSD: Relative standard deviation

To assess the method's precision and accuracy, calculations for percent mean recovery and relative standard deviation (%) for the test samples, prepared as described in the "Preparation of Validation Samples" section, are shown in Table 3. The optimized ANN and CWT methods performed well in analyzing independent test samples containing CIP and ORN at various concentration levels, as indicated in the table.

To evaluate the precision and accuracy of the intra-day and inter-day analysis using the optimized ANN and sym8-CWT methods, samples were prepared at three different concentration levels: 6.0, 12.0, and 18.0 $\mu\text{g/mL}$ for CIP and 8.0, 16.0, and 24.0 $\mu\text{g/mL}$ for ORN. These samples were analyzed three times within the same day (intra-day) and over three consecutive days (inter-day). This process was repeated three times for each concentration level. The results of the intra-day and inter-day assays, obtained using the optimized ANN and CWT methods, are shown in Table 4. As indicated in the table, the recovery results were satisfactory, demonstrating high precision and accuracy. The table also presents the relative standard deviations and relative standard errors for both drugs.

To assess the specificity and selectivity of the method and determine whether tablet excipients influence the analysis of the target drugs, a recovery study was performed using standard addition (spiked) samples. As outlined in the "Preparation of Validation Samples" section, these samples were prepared by adding known quantities of the investigated compounds into a portion of the tablet solution. The total amounts of the analytes in the spiked samples were determined by comparing the measured peak areas

Table 4. Intra-day and inter-day results of CIP and ORN in mixture samples by the proposed ANN and CWT method

	ANN				Sym8-CWT			
	Added ($\mu\text{g/mL}$)		Found ($\mu\text{g/mL}$)		Added ($\mu\text{g/mL}$)		Found ($\mu\text{g/mL}$)	
	CIP	ORN	CIP	ORN	CIP	ORN	CIP	ORN
Inter-day	6	8	6.23	8.09	6	8	5.99	8.13
	12	16	12.7	16.15	12	16	12.14	16.46
	18	24	18.11	24.71	18	24	18.18	24.22
Intra-day	6	8	6.1	8.19	6	8	5.86	7.95
	12	16	12.13	16.27	12	16	12.04	16.53
	18	24	17.76	24.23	18	24	17.66	23.78
	Recovery (%)				Recovery (%)			
Inter-day			103.8	101.1			99.9	101.6
			105.8	100.9			101.2	102.9
			100.6	102.9			101.0	100.9
Intra-day			101.7	102.3			97.7	99.4
			101.1	101.7			100.3	103.3
			98.6	100.9			98.10	99.10
	RSD (%)				RSD (%)			
Inter-day			0.15	1.37			1.29	1.10
			0.86	0.61			1.45	0.82
			1.32	0.66			0.84	0.58
Intra-day			0.49	2.1			1.17	0.54
			0.51	0.32			1.30	1.59
			0.4	0.59			1.05	0.52
	RSE (%)				RSE (%)			
Inter-day			3.80	1.12			-0.10	1.61
			5.81	0.92			1.15	2.86
			0.63	2.94			1.00	0.92
Intra-day			1.70	2.35			-2.34	-0.59
			1.12	1.69			0.33	3.32
			-1.35	0.94			-1.91	-0.91

RSD: Relative standard deviation

RSE: Relative standard error

against the calibration curves. Subsequently, the amounts of the individual drugs were calculated by subtracting the drug content in the tablet solution from the total amount found in the spiked sample. Recovery and relative standard deviation (RSD) were then calculated using the formulas: Recovery (%) = (found amount/added amount) \times 100 and RSD (%) = (SD/mean) \times 100. The results for added recovery and standard deviations are provided in Table 5. The analysis of the spiked samples demonstrated no interference from excipients, confirming that the spectrophotometric data were suitable for the analysis and that each spectrum contained only the target drug.

Table 5. Standard addition results of CIP and ORN in mixture samples by the proposed CWT methods

ANN				
	Added ($\mu\text{g/mL}$)		Found ($\mu\text{g/mL}$)	
	CIP	ORN	CIP	ORN
Formulation	5	6	4.95	5.98
Formulation	10	12	10.68	11.96
Formulation	15	18	15.11	17.76
			Recovery (%)	
			99	99.6
			106.8	99.7
			100.8	98.7
			RSD (%)	
			1.21	0.09
			0.1	0.05
			0.06	0.16
Sym8-CWT				
	Added ($\mu\text{g/mL}$)		Found ($\mu\text{g/mL}$)	
	CIP	ORN	CIP	ORN
Formulation	5	6	4.96	6.12
Formulation	10	12	9.96	12.18
Formulation	15	18	14.73	18.3
			Recovery (%)	
			99.3	102
			99.6	101.5
			98.2	101.7
			RSD (%)	
			0.03	0.02
			0.18	0.11
			0.11	0.1

RSD: Relative standard deviation

Analysis of Commercial Tablets

In this study, the quantification of CIP and ORN in commercial tablets was accurately carried out using the innovative ANN and sym8-CWT methodologies. The results of these analyses, obtained through the proposed analytical approaches, are presented in Table 6. The UV spectra of the commercial tablets were recorded within the wavelength range of 220-400 nm. Subsequently, these spectra were processed through advanced signal processing techniques, facilitating the precise and reliable determination of CIP and ORN concentrations in the tablets, as shown in Figure 1. A strong correlation

between the observed results underscores the robustness and applicability of the proposed methods, demonstrating their efficacy in the simultaneous quantification of CIP and ORN in pharmaceutical tablets.

Table 6. Determination of CIP and ORN in ORCIPOL ® tablets by the proposed ANN and CWT methods

ANN			sym8-CWT		
Experiment No.	mg/tablet		Experiment No.	mg/tablet	
	CIP	ORN		CIP	ORN
1	16.1	15.5	1	16.2	15.7
2	15.5	16.1	2	16	16
3	15.8	16	3	15.9	15.9
4	15.7	16	4	15.9	15.8
5	15.9	16.2	5	16.3	15.9
6	16.3	16.3	6	16.2	16.6
7	15.9	16.2	7	16.2	16.1
8	15.7	15.9	8	15.7	16.1
9	15.8	16.2	9	15.9	16.4
10	15.8	15.8	10	16.2	16.1
Mean	15.9	16	Mean	16	16.1
SD	0.24	0.24	SD	0.2	0.25
RSD	1.5	1.53	RSD	1.24	1.53

Label claim is 16 mg CIP and ORN in a tablet.

SD: standard deviation; RSD: Relative standard deviation.

CONCLUSIONS

In this study, we developed and validated the effectiveness of two distinct methods, Artificial Neural Networks (ANN) and Continuous Wavelet Transform (CWT), for the simultaneous quantitative analysis of binary mixtures of CIP and ORN. Both approaches were applied independently, and the results demonstrated that they provided comparable and reliable outcomes for the analysis of CIP and ORN in tablet formulations without requiring chemical pre-treatment or preliminary separation steps.

The ANN model and the sym8-CWT signal processing approach both proved to be highly effective in overcoming the challenge of spectral overlap, a common issue in spectrophotometric analysis. These methods showed excellent precision and accuracy, supporting their potential for routine analysis and quality control in pharmaceutical settings.

By using both ANN and CWT methods, we were able to achieve simultaneous and quantitative resolution of CIP and ORN in a commercial pharmaceutical formulation, further validating the applicability of these methods. The findings suggest that both approaches offer versatile solutions for spectrophotometric analysis in the presence of overlapping spectra, making them suitable alternatives to traditional separation techniques in pharmaceutical quality control.

EXPERIMENTAL SECTION

Apparat and software

In this study, a Shimadzu UV-2550 series double-beam UV-Vis spectrophotometer was employed to acquire UV absorption spectra of the analyzed samples. The system was interfaced with a computer running Shimadzu UV Probe 2.32 software, which facilitated data collection and spectral analysis.

The development and implementation of the Artificial Neural Network (ANN) and Continuous Wavelet Transform (CWT) approaches were carried out using the Wavelet Toolbox in MATLAB software. For statistical evaluation and data processing, Microsoft Excel software was used, ensuring a robust and reliable analysis workflow.

Chemicals and Material

In this study, the CIP and ORN standards were obtained from the reputable World Medicine Pharmaceuticals Company in Turkey, and the commercial product ORCIPOL tablet was utilized. Methanol, used as the solvent for standard and validation sample solutions, was procured from Fisher Scientific (UK), along with high-purity distilled water.

All sample solutions were freshly prepared daily at room temperature, ensuring consistency and reliability in the analysis. Methanol (Fisher Scientific (UK)), HCl (Merck, Darmstadt-Germany) were used as the solvent for all solutions throughout the study. Laboratory-prepared mixtures of CIP and ORN were employed for pharmaceutical validation, serving as essential components in the analytical preparations.

In the analysis of the commercial real sample, the commercial ORCIPOL® tablet, manufactured by World Medicine Pharmaceuticals in Istanbul, Turkey, was selected as the real sample for analysis. Each tablet contains 554.92 mg (equivalent to 500 mg ciprofloxacin, CIP) of ciprofloxacin hydrochloride and 500 mg of ornidazole (ORN), and the label of excipient

content is sodium starch glycolate 141.44 mg, croscarmellose sodium 50 mg, sunset yellow FCF for film coating, and tartrazine for film coating. To analyze this formulation, two advanced methods, Artificial Neural Network (ANN) and Symlet 8 Continuous Wavelet Transform (sym8-CWT) were employed.

Preparation of Standard Stock Solutions and Calibration Samples

To prepare stock solutions of ciprofloxacin (CIP) and ornidazole (ORN) at concentrations of 10 mg/50 mL, each compound was accurately weighed and separately dissolved in methanol within a 50 mL volumetric flask. The final volume was adjusted to the mark with methanol, and sonication was applied for a few minutes to facilitate dissolution.

Calibration solutions were prepared by diluting the stock solutions to achieve concentrations ranging from 3.0 to 24.0 $\mu\text{g/mL}$ for CIP and 6.0 to 32.0 $\mu\text{g/mL}$ for ORN. Each calibration solution was prepared in a 10 mL volumetric flask. To create an acidic medium, 2 mL of 0.1 M HCl was added to each flask, and the final volume was adjusted to the mark with methanol. All UV spectra of these prepared samples in an acidic methanolic medium were recorded.

Preparation of Validation Samples

To validate the method, three sets of laboratory-prepared solutions were used. The first set consisted of 11 binary synthetic mixtures of the target drugs, prepared daily to ensure the accuracy and precision of the spectrophotometric method. The second set included intra-day and inter-day samples of ciprofloxacin (CIP) at concentrations of 6.0, 12.0, and 18.0 $\mu\text{g/mL}$, and ornidazole (ORN) at concentrations of 8.0, 16.0, and 24.0 $\mu\text{g/mL}$, across three different concentration levels. This set was designed to assess the accuracy and precision of the assay results obtained by the method. The third set consisted of standard addition samples, where drug standards were added to the solution of the commercial sample (ORCIPOL®) at a constant concentration. For CIP, the standard concentrations were 5, 10, and 15 $\mu\text{g/mL}$, and for ORN, the concentrations were 6, 12, and 18 $\mu\text{g/mL}$. This set was used to evaluate the selectivity of the method. To determine the recovery of the added standards in the standard addition samples, a solution of the commercial tablet sample, which did not contain drug standards, was prepared. Each sample solution was prepared in a 10 mL volumetric flask in the validation procedures. In preparing the solutions, 2 mL of 0.1 M HCl was added to each flask to create an acidic environment, and the final volume was adjusted to the mark with methanol.

Preparation of Tablet Sample

Ten ORCIPOL® tablets were finely powdered and homogenized. A quantity equivalent to one tablet (500 mg of each drug) was weighed and transferred to a 100 mL volumetric flask. After placing the flask in an ultrasound bath for 30 minutes, methanol was added to bring the solution to the mark. The resulting solutions were then carefully filtered through a 0.20 µm membrane filter (Sartorius Minisart, Hannover, Germany). The filtered solution was diluted to the CIP and ORN working ranges using the same solvent. In this dilution step, each sample solution was prepared in a 10 mL volumetric flask. In preparing the solutions, 2 mL of 0.1 M HCl was added to each flask to create an acidic environment and the final volume was adjusted to the mark with methanol. This sample preparation process was repeated ten times to ensure consistency. The UV spectra of the prepared samples were recorded.

ACKNOWLEDGMENTS

This study was conducted in the Chemometric Laboratory of the Faculty of Pharmacy, with support from the Ankara University Scientific Research Fund (Project No. 10A3336001).

REFERENCES

1. R. Davis; A. Markham; J. A. Balfour; *Drugs*, **1996**, 51(6),1019-74
2. I. Furtat; M. Lupatsii; T. Murlanova; P. Vakuliuk; A. Gaidai; O. Biliayeva; H. Sobczuk; A. Golub; *Appl. Nanosci.*, **2020**, 10, 3193–3203.
3. P. Rutgeerts; G. V. Assche; S. Vermeire; G. D'haens; F. Baert; M. Noman; I. Aerden; G. De Hertogh; K. Geboes; M. Hiele; A. D'hoore; F. Penninckx; *Gastroenterology*, **2005**, 128, 856–861.
4. H. Giamarellou; M. Gelhoff-Volanaki; A. Avlami; K. Kanellakopoulou; G. K. Daikos; *J. Antimicrob. Chemother.*, **1981**, 7, 5, 569–574.
5. J. C. Alados; A. Martínez-Brocal; C. Miranda; M. D. Rojo; V. García; M. C. Domínguez; *Enferm. Infecc. Microbio. Clin.*, **1991**, 9, 4, 219-22.
6. J. R. Krishna; *J. Adv. Pharm. Edu. Res.*, **2014**, 4, 4, 440–3.
7. I. Carolin Nimila; P. Balan; R. Sathiya Sundar; J. Ashok Kumar; S. Rajasekar; *Asian J. Res. Chem.*, **2011**, 4, 2, 227–30.
8. A. K. Tunca; D. Karakaya; S. Bulbul; *Pak. J. Pharm. Sci.*, **2020**, 33, 3, 1105–14.
9. K. S. Damerakonda; M. Hima Bindu; K. Swamy Damerakonda; M. Hima Bindu; *Int. J. Pharm. Bio. Sci.*, **2015**, 5, 3, 94–101.

10. A. S. Grewal; S. K. Patro; S. K. Kanungo; S. K. Bhardwaj; *Int. J. Pharm. Sci. Res.*, **2012**, 3, 8, 2716–20.
11. J. R. Krishna; B. Naga; S. H. Sandhya; V. V. Prasad; *J. Adv. Pharm. Edu. Res.*, **2014**, 4, 4, 405–8.
12. A. A. Sakur; D. A. L. Zakri; *Heliyon*, **2023**, 23, 9, 12.
13. S. V. Gandhi, A. D. Waghmare; Y. S. Nandwani; A. S. Muthaet; *ARC J. Pharm. Sci.*, **2017**, 3, 1, 19–25.
14. A. R. Rote; R. B. Saudagar; *Pharm. Methods.*, **2016**, 7, 2, 89– 93.
15. A. R. Rote; R. B. Saudagar; *Pharm. Anal. Chem. Open.*, **2015**, 1, 1, 1-4.
16. V. Arabzadeh; M.R. Sohrabi; N. Goudarzi; M. Davallo; *Spectrochim. Acta A Mol. Biomol. Spectrosc.*, **2019**, 215, 266–275.
17. N. Goudarzi; S. Farsimadan; M. Arab Chamjangali; Gh. A. Bagherian; *J. Sep. Sci.*, **2015**, 38, 3254–3261.
18. S. Farsimadan; N. Goudarzi; M. Arab Chamjangali; Gh.A. Bagherian; *Microchem. J.*, **2016**, 128, 47–54.
19. Z. Shahrokhi; M.R. Sohrabi; S. Mortazavi Nik; *Optik - Int. J. Light Electron. Optics.*, **2020**, 203, 164010.
20. Sh. Shokouhi; M.R. Sohrabi; Sh. Mofavvaz; *Optik - Int. J. Light Electron. Optics.*, **2020**, 206, 164304
21. M. L. Cervera; M. de la Guardia; S. Dutta; A. K. Das; *Spectrosc. Lett.*, **2009**, 42, 6, 7, 284–295.
22. I. Suslu; E. Dinc; S. Altinoz; *Math. Methods Eng.*, **2007**, 9, 303–313.
23. E. Dinc; N. Ozdemir; Ö. Ustundag; E. Buker; G. Tilkan; V. D. Hang; *J. Mex. Chem. Soc.*, **2022**, 66, 4, 488-499.
24. S. Dermis; E. Buker; Z. C. Ertekin; E. Korkmaz; *Asian J. Chem.*, **2018**, 30, 11, 2567-2570.

RHEOLOGICAL CHARACTERIZATION OF ALGERIAN CRUDE OILS

Farid SOUAS^{a,b*} , Abdelhamid SAFRI^a,
Ahmed Salah Eddine MEDDOUR^a 

ABSTRACT. This study examines the rheological behavior of three Algerian crude oils, focusing on steady flow, yield stress, and thixotropic behavior across temperatures. The oils exhibit non-Newtonian pseudoplastic behavior with a yield stress at the onset of flow. Results show that viscosity and shear stress decrease with temperature, reducing yield stress and improving flow. The Herschel-Bulkley model best fits crude oil 1, while the Casson model is more suitable for oils 2 and 3 at 30°C, and the power law and Herschel-Bulkley models apply at 20°C. Over the 20–50°C range, apparent viscosity and shear stress decrease by 71%, 77%, and 79% for oils 1, 2, and 3, respectively, while yield stress drops by 24.4%, 48.5%, and 54%. Thixotropic behavior is also observed, with reduced hysteresis area at higher temperatures, indicating reduced internal friction. These findings highlight the role of temperature in enhancing crude oil flow properties, suggesting heat treatment improves transportability.

Keywords: *Crude oil, rheology, temperature, thixotropy, viscosity, yield stress.*

INTRODUCTION

Energy acquisition remains a critical objective for nations worldwide, with crude oil representing 37% of the global energy supply, positioning it as the primary energy source. Historically, hydrocarbons have served as the

^a LEGHYD Laboratory, Faculty of Civil Engineering, University of Science and Technology Houari Boumediene (USTHB), Bab Ezzouar, Alger, Algeria

^b Research Unit Materials, Processes and Environment (UR-MPE), Faculty of Engineering Science, University M'Hamed Bougara, Boumerdes, Algeria

* Corresponding author: fa.souas@gmail.com, farid.souas@usthb.edu.dz



dominant commercial energy source, continuing through the late 20th century. Crude oil is a complex mixture of various hydrocarbons, which gives rise to a diverse set of physical and chemical properties depending on its composition. These characteristics vary based on the oil's specific content, including asphaltenes, saturated hydrocarbons, aromatics, and resins. Crude oils can be classified into four categories—light, medium, heavy, and extra heavy—based on their properties, including sulfur content, specific gravity (API), and density [1,2]. Specifically, crude oil from Algeria is classified as light based on average values of these parameters [3].

Pipeline transportation is the most practical and cost-effective method for moving crude oil and its derivatives. However, crude oil transport via pipelines is complicated by the inherent variability in its physical and chemical properties, which can change in response to climatic conditions. These variations affect the flow characteristics and transport behavior of crude oil. The non-Newtonian nature of crude oil, attributed to its complex chemical composition and the presence of suspended particles, further complicates long-distance pumping operations. These particles tend to deposit as fouling layers in various facilities, including heat exchangers, fired heaters, oil reservoir rocks, and transfer lines, leading to reduced energy recovery and increased operational costs [4]. The rheological properties of petroleum oils are crucial in several processes involving fluid movement, including migration within reservoirs and transportation through pipelines. Understanding the viscosity and flow behavior of crude oil is essential for designing and optimizing the infrastructure necessary for production and refining operations [5]. Therefore, accurate measurement of the rheological properties of crude oil is vital for the development of pumping stations and pipeline systems, as these properties can vary significantly depending on the crude oil's origin.

The rheological behavior of crude oil is determined by the relationship between shear stress and shear rate, typically characterized by experimental rheometry. A linear relationship indicates Newtonian fluid behavior, while a nonlinear relationship signifies non-Newtonian behavior. Several models have been suggested to describe the rheological behavior of crude oils, including the Herschel-Bulkley, power law, Bingham, and Casson models [6]. Barskaya et al. [7] demonstrate in their study that, despite two crude oils having identical concentrations of resins, asphaltenes, and solid paraffins, they exhibit distinct rheological behaviors at low shear rates. The chemical composition of the high molecular weight components, namely asphaltenes and solid paraffins, was analyzed and revealed no significant differences in their composition. The study identifies that the differing rheological behaviors are attributed to variations in the content of saturated and aromatic hydrocarbons. An increase in mono- and bi-aromatic hydrocarbon content leads to an enhanced non-

Newtonian behavior, which is attributed to the formation of coagulated structures within the crude oil. The authors conclude that these findings should be considered when predicting crude oil viscosity for the development of oil recovery and transportation technologies. Ilyin and Strelets [8] investigated the rheological properties of eight different types of crude oils, including light, heavy, waxy, and extra-heavy oils, using a RheoStress 600 rotational rheometer. Their study demonstrated that the viscosity of crude oils is influenced by their composition, temperature, and the applied shear stress. The authors concluded that the rheological behavior of crude oils is primarily determined by their inherent characteristics.

The purpose of this article is to provide a comprehensive analysis of the rheological behavior of Algerian crude oils, focusing on key aspects such as steady-state rheology, yield stress, and thixotropy. Through a series of experimental investigations, the relationship between viscosity, shear stress, and shear rate at various temperatures is explored, offering valuable insights into the flow characteristics of these crude oils under different conditions. Furthermore, the impact of temperature on viscosity and shear stress at variable shear rates is examined to better understand the thermal sensitivity of these fluids. The article aims to shed light on the yield stress behavior of Algerian crude oils, highlighting their ability to resist flow under low-shear conditions. Additionally, the study addresses the thixotropic properties of these oils, which are essential for understanding their behavior during processing and transportation. By providing a detailed exploration of these key rheological parameters, the article contributes to a deeper understanding of the flow properties of Algerian crude oils, with implications for both the oil industry and the development of improved handling and processing techniques.

RESULTS AND DISCUSSION

Viscosity and shear stress vs. shear-rate at different temperatures.

The flow behavior of all crude oil samples was analyzed using the CR mode of the AR-2000 rheometer, focusing on viscosity versus shear rate and shear stress versus shear rate. The results of the rheological tests are presented in Figures 1 and 2, which illustrate the variation of viscosity and shear stress with shear rate over a temperature range of 20°C and 30°C.

The flow curves demonstrate the non-Newtonian pseudoplastic behavior of the crude oil samples across the entire temperature range. Specifically, the curves indicate a lack of flow when the applied shear stress is below a critical threshold, referred to as the yield point. Moreover, the flow curves exhibit consistent trends across all test temperatures, characterized

by a gradual increase in shear stress as the shear rate rises. Experimental observations also reveal that as temperature increases, both viscosity and shear stress decrease, with a corresponding reduction in yield stress.

The experimental data presented in Figures 1-2a demonstrate that the apparent viscosity of the crude oil samples exhibits shear rate dependence.

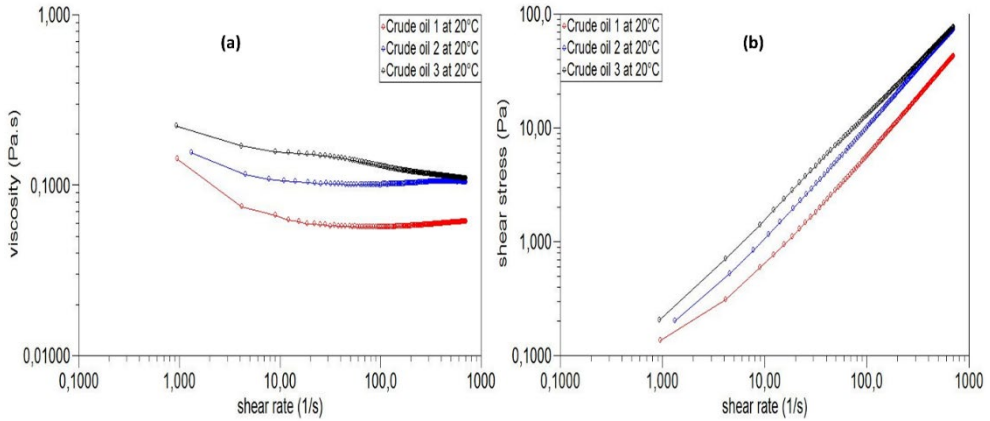


Figure 1. Flow curves of crude oils at a temperature of 20 °C: (a) viscosity vs. shear rate, (b) shear stress vs. shear rate.

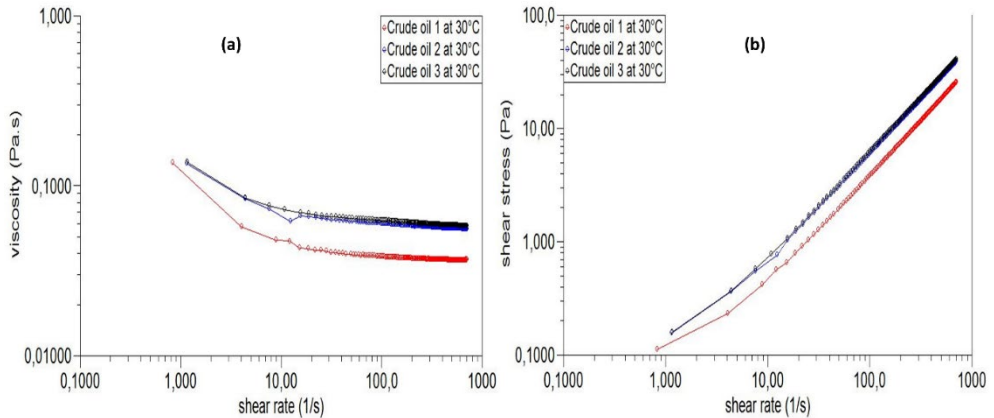


Figure 2. Flow curves of crude oils at a temperature of 30 °C: (a) viscosity vs. shear rate, (b) shear stress vs. shear rate.

The behavior can be categorized into two distinct regions: the first region, observed at low shear rates, is characterized by a significant decrease in viscosity, while the second region, observed at high shear rates, shows a stabilization of apparent viscosity, remaining constant as the heavier components undergo irreversible dissipation at elevated shear rates. Additionally, the viscosity is found to be more sensitive to temperature variations at high shear rates. Notably, a pronounced viscosity reduction is observed between 20°C and 30°C within the test temperature range. The results further indicate that the viscosity decreases more rapidly at lower shear rates and temperatures compared to higher shear rates and temperatures. This effect is particularly evident in crude oil sample 3, which exhibits slightly higher density and heavier components relative to the other samples. These findings are consistent with the results reported by several researchers [9-11] for different crude oil types.

The composition of crude oil samples plays a crucial role in understanding their rheological behavior. Temperature is a key factor influencing the viscosity of heavier constituents in crude oils, such as asphaltenes and resins, with significant effects typically observed within the temperature range of 20 to 30°C. The reduction in viscosity at higher temperatures can be attributed to the thermal influence on the chemical structure of these heavy components. Specifically, the elevated temperature disrupts the ordered structures of the heavy constituents, leading to a substantial and irreversible reduction in viscosity [12-13]. Additionally, the molecular chains present in crude oil samples contribute to viscosity changes. As the shear rate increases, the viscosity of crude oils decreases due to the detangling, stretching, and reorientation of chain-like molecules, which align parallel to the applied force [14].

A modeling analysis was conducted to identify an appropriate rheological model that best fits the experimental measurements. Four distinct rheological models were evaluated in this study, as described by equations 1-4: the Bingham model, the Casson model, the power law model, and the Herschel-Bulkley model.

$$\tau = \tau_0 + \mu\dot{\gamma} \quad (1)$$

$$\sqrt{\tau} = \sqrt{\tau_0} + \sqrt{\mu\dot{\gamma}} \quad (2)$$

$$\tau = K\dot{\gamma}^n \quad (3)$$

$$\tau = \tau_0 + K\dot{\gamma}^n \quad (4)$$

Where: τ is shear stress (Pa); τ_0 is apparent yield stress (Pa); μ is apparent viscosity (Pa. s); K is the consistency index (Pa.sⁿ); $\dot{\gamma}$ is shear rate (s⁻¹) and n is the flow behavior index.

The rheological models previously outlined were employed to fit the shear stress data corresponding to various shear rates for each crude oil sample analyzed in this study. The predicted shear stress values from the

rheological models and the experimentally measured shear stress are utilized to estimate statistical parameters in terms of error. To assess the accuracy of the rheological models, the standard error (SE), a statistical metric, is calculated as follows [15]:

$$SE = \left[\frac{\left[\frac{\sum_{i=1}^n (x_m - x_c)^2}{n - 2} \right]^{\frac{1}{2}}}{X_m^{max} - X_m^{min}} \right] \times 1000 \tag{5}$$

The term x_m represents the measured value, x_c denotes the calculated value, and n refers to the total number of data points.

Table 1. Standard error values of shear stress for various rheological models.

Crude oil	Temperature, °C	Bingham (Eq.1)	Casson (Eq.2)	Power law (Eq.3)	Herschel-Bulkley (Eq.4)
1	20	8.637	10.86	1.418	0.892
	30	1.374	1.396	1.969	1.272
2	20	3.319	4.056	3.103	3.229
	30	2.654	0.9615	1.514	1.202
3	20	6.745	2.117	1.638	1.464
	30	2.615	0.9282	1.485	1.182

Based on the results from the modeling study presented in Table 1, and considering the minimal standard errors, it can be concluded that the Herschel-Bulkley model best describes the flow behavior of crude oil 1 across a known range of shear rates and temperatures. For a temperature of 30°C, the Casson model accurately describes the similar flow behavior of crude oils 2 and 3. However, at 20°C, the power law and Herschel-Bulkley models provide the best fits for crude oils 2 and 3, respectively.

Viscosity and shear stress vs. temperature with variable shear rate.

The relationship between apparent viscosity and shear stress of crude oils as a function of temperature at various shear rates, in order to observe their non-Newtonian behavior, is presented in Table 2. Pressure drop refers to the loss of flow energy caused by the friction between the fluid and the internal pipe walls. Lower viscosity leads to a reduced pressure drop,

whereas higher viscosity results in a significant pressure drop and greater dissipation of fluid flow energy. Shear stress is strongly influenced by the viscosity of the crude oil and serves as a measure of the resistance to flow near the pipe walls, where frictional forces occur [16].

Table 2. Influence of temperature on the rheological properties of crude oils at varying shear rates.

		Temperature, °C					
		20°C		30°C		50°C	
Type	Shear rate, S ⁻¹	Viscosity, mPa.s	Shear stress, Pa	Viscosity, mPa.s	Shear stress, Pa	Viscosity, mPa.s	Shear stress, Pa
Crude oil 1	100	56.92	5.61	38.39	3.778	17.74	1.754
	200	57.68	11.41	37.37	7.386	17.33	3.433
	300	58.68	17.52	36.9	11.01	17.21	5.143
	400	59.45	23.65	36.65	14.57	17.17	6.835
	500	60.26	30.04	36.55	18.22	17.13	8.547
	600	60.73	36.3	36.52	21.83	17.23	10.31
	700	61.18	42.73	36.62	25.58	17.31	12.1
Crude oil 2	100	99.34	9.826	60.18	5.943	24.5	2.415
	200	102.8	20.37	58.27	11.53	23.82	4.711
	300	104.5	31.24	57.15	17.07	23.63	7.054
	400	105.1	41.84	56.48	22.48	23.49	9.344
	500	105	52.22	56.14	28	23.43	11.68
	600	104.7	62.61	55.98	33.47	23.52	14.06
	700	103.9	72.6	55.84	39.02	23.56	16.46
Crude oil 3	100	129.7	12.77	62.61	6.182	25.59	2.518
	200	120	23.73	60.62	12	24.9	4.921
	300	116.3	34.71	59.45	17.76	24.6	7.342
	400	113.8	45.25	58.77	23.39	24.55	9.759
	500	111.9	55.81	58.52	29.19	24.57	12.25
	600	110.5	66.07	58.22	34.81	24.52	14.66
	700	109.1	76.21	58.1	40.6	24.57	17.16

The crude oils exhibited the greatest sensitivity to heat treatment in the temperature range of 20°C to 50°C. Within this range, a sharp decrease in both apparent viscosity and shear stress was observed, indicating significant changes in the flow properties.

To evaluate the enhancement in the flow behavior of crude oils, specifically in terms of viscosity and shear stress reduction, the Average Degree of Reduction (DAR) is defined. This can be determined using the following equation:

$$(DAR)\% = \frac{1}{n} \sum_{i=1}^n \left[\frac{\text{initial value} - \text{final value}}{\text{initial value}} \right] \times 100 \quad (6)$$

Table 3. Percentage reduction in viscosity and shear stress of crude oils with increasing temperature.

		Temperature, °C					
		20°C - 30°C		30°C - 50°C		20°C - 50°C	
Type	Shear rate, S ⁻¹	% Viscosity reduction	% Shear stress reduction	% Viscosity reduction	% Shear stress reduction	% Viscosity reduction	% Shear stress reduction
Crude oil 1	100	32.55	32.66	53.79	53.57	68.83	68.73
	200	35.21	35.27	53.63	53.52	69.95	69.91
	300	37.12	37.16	53.36	53.29	70.67	70.64
	400	38.35	38.40	53.15	53.09	71.12	71.10
	500	39.35	39.35	53.13	53.09	71.57	71.55
	600	39.86	39.86	52.82	52.77	71.63	71.60
	700	40.14	40.14	52.73	52.70	71.71	71.68
Crude oil 2	100	39.42	39.52	59.29	59.36	75.34	75.42
	200	43.32	43.40	59.12	59.14	76.83	76.87
	300	45.31	45.36	58.65	58.68	77.39	77.42
	400	46.26	46.27	58.41	58.43	77.65	77.67
	500	46.53	46.38	58.27	58.29	77.69	77.63
	600	46.53	46.54	57.98	57.99	77.54	77.54
	700	46.26	46.25	57.81	57.82	77.32	77.33
Crude oil 3	100	51.73	51.59	59.13	59.27	80.27	80.28
	200	49.48	49.43	58.92	58.99	79.25	79.26
	300	48.88	48.83	58.62	58.66	78.85	78.85
	400	48.36	48.31	58.23	58.28	78.43	78.43
	500	47.70	47.70	58.01	58.03	78.04	78.05
	600	47.31	47.31	57.88	57.89	77.81	77.81
	700	46.75	46.73	57.71	57.73	77.48	77.48

The results presented in Table 3 show that increasing the temperature from 20°C to 50°C resulted in an average reduction in the initial viscosity and shear stress between the flowing fluid and the pipe wall for crude oils 1, 2,

and 3 by approximately 71%, 77%, and 79%, respectively, thereby enhancing transportability. When the temperature was increased from 20°C to 30°C, the reductions were 38%, 45%, and 49%, respectively. From 30°C to 50°C, the reductions were 53%, 59%, and 58%, respectively. The reduction in viscosity is primarily attributed to the temperature-induced decrease in the viscosity of higher molecular weight components, such as wax and asphaltenes, which contributes to a lower viscosity of the entire crude oil mixture. Additionally, the elevation in temperature enhances the Brownian motion of particles, further disrupting the ordered structures of these higher molecular weight components, thereby facilitating a reduction in overall viscosity.

Yield stress

The yield stress is defined as the critical stress threshold beyond which a material transitions from solid-like behavior to fluid-like behavior. Below this threshold, the material exhibits elastic deformation that is directly proportional to the applied stress, following a linear relationship. When the applied stress exceeds the yield stress, the material undergoes irreversible deformation, leading to the initiation of flow [3, 17].

Yield stress measurements of crude oil samples were performed at various temperatures using an AR-2000 Rheometer. This experimental approach enables precise determination of the yield stress by graphically or numerically extrapolating the shear stress versus shear rate (flow curves) to zero shear rate.

Table 4. Yield stress and hysteresis area measurements of crude oils as a function of temperature.

Crude oil	Temperature, °C	Yield stress, Pa	Hysteresis area, Pa/s
Crude oil 1	20	0.135	1375
	30	0.112	212
	50	0.102	117.4
Crude oil 2	20	0.202	2504
	30	0.155	334
	50	0.104	155
Crude oil 3	20	0.210	2975
	30	0.160	345.4
	50	0.097	154.4

Table 4 illustrates the variation in yield stress as a function of temperature for the crude oils. It is evident that the yield stress, which is necessary to initiate flow, decreases with an increase in temperature. For crude oil 1, the yield stress decreased by 24.4% (from 0.135 Pa to 0.102 Pa) as the temperature increased from 20°C to 50°C. Similarly, in the same temperature range, the yield stress for crude oil 2 and crude oil 3 decreased by 48.5% (from 0.202 Pa to 0.104 Pa) and 54% (from 0.210 Pa to 0.1 Pa), respectively. These observations suggest a significant reduction in apparent yield stress with increasing temperature, indicating a decrease in the energy required for the crude oils to flow. This behavior implies that higher temperatures reduce the internal friction, facilitating the flow of the crude oil samples.

Thixotropy behavior

Solutions exhibiting microstructure typically demonstrate thixotropic behavior, characterized by reversible changes between different microstructural states. These changes are governed by the interplay between flow-induced breakdown, buildup from nonflow collisions, and Brownian motion. These mechanisms collectively influence the viscosity of the solution, with each process requiring a certain amount of time to transition between states under applied shear. The thixotropic behavior is commonly quantified by measuring the hysteresis loop, which represents the area between the ascending and descending curves of the rheogram. This area, referred to as the thixotropic area, serves as a key parameter for evaluating thixotropy [18,19,5]. To fully dismantle the thixotropic structure of the crude oil samples, multiple cycles of up and down shear may be necessary to determine the appropriate duration for each cycle. Experimental tests were conducted on the crude oil samples using cycle durations of 100, 200, and 300 seconds for both the up and down shear phases. The shear rate was gradually increased from 0 to 700 s⁻¹ over the specified duration and then immediately decreased from 700 to 0 s⁻¹ over an equal time period. The hysteresis area was calculated for each cycle. The test utilizing a 300-second duration for both the up and down shear cycles (from 0 to 700 s⁻¹ and from 700 to 0 s⁻¹, respectively) was sufficient to ensure complete breakdown of the crude oil structure.

The objective of this study is to examine the thixotropic behavior of crude oil samples. Thixotropy measurements were performed using the CR-mode, with the shear rate incrementally increased from 0 to 700 s⁻¹. The shear stresses and corresponding shear rates were recorded to construct the up-curve of the flow curve. To generate the down-curve, the shear rate was progressively reduced from 700 to 0 s⁻¹. Each cycle had a duration of 300 seconds. For non-thixotropic materials, the down-curve closely mirrors

the up-curve. However, for thixotropic materials, the down-curve deviates from the up-curve, creating a hysteresis loop. The area of this loop, denoted as A (in Pa/s), serves as an indicator of thixotropy, providing a measure of the energy per unit volume required to disrupt the thixotropic structure.

Figure 3 illustrates the thixotropic behavior of the crude oils at various temperatures, highlighting the hysteresis phenomenon. The region between the upward and downward curves quantifies the thixotropic effect. This area was measured for each crude oil at the different temperatures tested and is reported as a function of temperature in Table 4. The data, presented in both the figure and table, indicate a significant reduction in thixotropic behavior, with values decreasing from 1375, 2504, and 2975 Pa/s to 117.4, 155, and 154.40 Pa/s for crude oils 1, 2, and 3, respectively, across the temperature range of 20–50 °C. The results indicate that increased temperature reduces the energy required to break bonds, thereby enhancing flow within the pipeline.

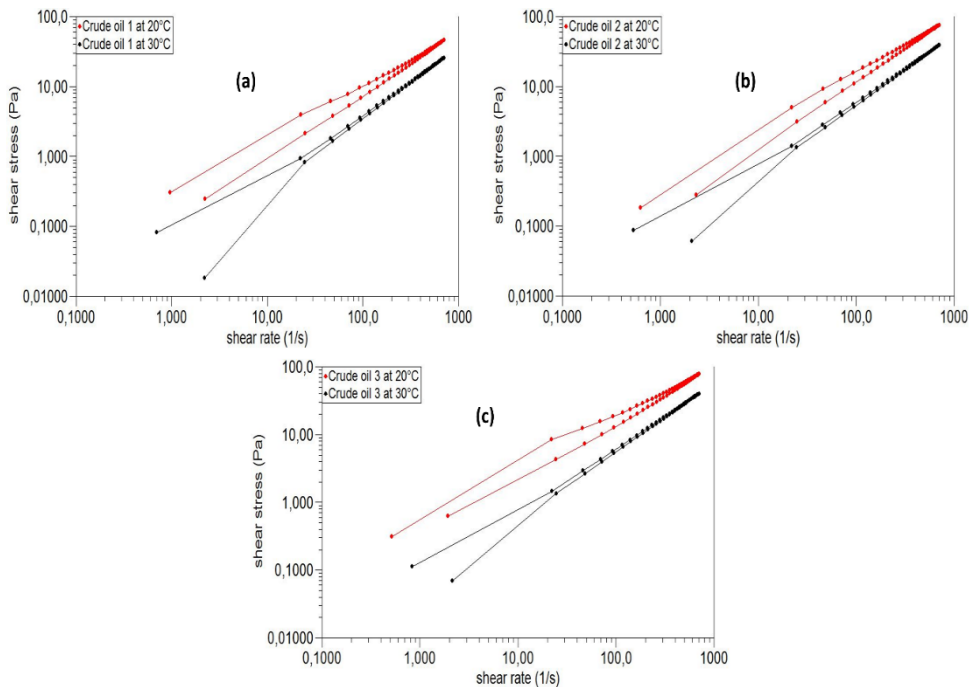


Figure 3. Thixotropic behavior of crude oils at temperatures of 20°C and 30°C.

When a thixotropic structural material is introduced into a viscometer, its microstructure initially consists of large flocs when at rest. As the shear rate is gradually increased, and sufficient time is allowed, the floc size continuously diminishes. At high shear rates, the flocs disintegrate into their individual components. This disaggregation process occurs over a specific period. Conversely, if the shear rate is suddenly reduced, the individual particles begin to colloid and flocculate, progressively forming larger flocs until they reach a size consistent with the new shear conditions. This reassembly process also unfolds over time but at a rate distinct from the breakdown process [18,5].

CONCLUSIONS

In conclusion, the rheological analysis of the three Algerian crude oil samples revealed consistent non-Newtonian pseudoplastic behavior across all tested temperatures, with significant influence from temperature and shear rate on the oils' flow properties. As temperature increased, both the viscosity and yield stress decreased, facilitating easier flow and reducing the internal friction within the crude oils. The apparent viscosity of the crude oils demonstrated shear rate dependence, with the highest sensitivity to temperature observed in the 20°C to 30°C range. Additionally, the study highlighted the distinct rheological behaviors of the samples, with crude oil 3 exhibiting a stronger response due to its heavier components.

The modeling results indicated that different models best describe the flow behavior of the crude oils under various conditions, with the Herschel-Bulkley model accurately capturing the flow of crude oil 1, while the Casson and power law models were most appropriate for crude oils 2 and 3 under certain temperature conditions. Notably, temperature had a pronounced effect on viscosity reduction, with the most significant decreases observed between 20°C and 50°C, improving the transportability of the crude oils. The yield stress also decreased significantly with temperature, further reducing the energy required for flow initiation.

Moreover, the crude oils exhibited thixotropic behavior, which was notably reduced at higher temperatures, suggesting that increased temperatures not only lowered viscosity but also decreased the energy needed to break internal bonds, thus enhancing the flow within pipelines. These findings are crucial for understanding the flow behavior of Algerian crude oils under varying temperature conditions and optimizing their transportation and processing.

EXPERIMENTAL SECTION

Crude oil samples were obtained from multiple oil fields situated in the Tin Fouye Tabankort/South Algeria region (TFT). These samples were labeled as 1, 2, and 3 for identification purposes. The key properties of the crude oil samples are presented in Table 5. The flow behavior of these samples was evaluated using an AR-2000 rheometer [20-23] equipped with a Couette geometry (14 mm diameter) at different temperatures (20, 30 and 50°C). Data acquisition and analysis were conducted using software from TA Instruments (Rheology Advantage Data Analysis Program). The rheometer utilized cylindrical and Couette geometries with a 14 mm diameter and a 1 mm gap between the upper and lower plates. This configuration offers a large surface area, ensuring precise measurements even at very low viscosities. Prior to testing, all samples underwent pre-shear for 30 seconds at a shear rate of 100 s⁻¹ to ensure proper homogenization [24]. The samples were allowed to rest for one minute before initiating the measurement process. Shear rates ranging from 0 to 700 s⁻¹ were applied during the tests.

Table 5. Properties of the crude oil samples utilized in this study.

Sample	Density, 15°C	Gravity, °API	Asphaltenes, wt %	Resins, wt %
1	0.830	39	0.58	6.50
2	0.840	37	0.62	7.10
3	0.850	35	0.70	7.50

REFERENCES

1. B. Elarbe; I. Elganidi; N. Ridzuan; N. Abdullah; K. Yusoh; *Mater. Today Proc.*, **2021**, 42, 201-210.
2. F. Souas; A. Safri; A. Benmounah; *Pet. Sci. Technol.*, **2020**, 38, 849-857.
3. M. Meriem-Benziane; S.A. Abdul-Wahab; M. Benaicha; M. Belhadri; *Fuel.*, **2012**, 95, 97-107.
4. R. Kumar; S. Banerjee; A. Banik; T.K. Bandyopadhyay; T.K. Naiya; *Pet. Sci. Technol.*, **2017**, 35, 615-624.
5. M.T. Ghannam; S.W. Hasan; B. Abu-Jdayil; N. Esmail; *J. Petrol. Sci. Eng.*, **2012**, 81,122-128.
6. S. Sharma; V. Mahto; V.P. Sharma; A. Saxena; *Pet. Sci. Technol.*, **2016**, 34, 523-530.
7. E.E. Barskaya; E.S. Okhotnikova; Y.M. Ganeeva; T.N. Yusupova; *Pet. Sci. Technol.*, **2022**, 41,159-175.

8. S.O. Ilyin; L.A. Strelets; *Energ Fuel.*, **2018**, 32, 268-278.
9. D.E. Djemiat; A. Safri; A. Benmounah; B. Safi; *J. Petrol. Sci. Eng.*, **2015**, 133,184-191.
10. S.M. Al-Zahrani; T.F. Al-Fariss; *Chem. Eng. Process. Intens.*, **1998**, 37, 433-437.
11. M.A. Farah; R.C. Oliveira; J.N. Caldas; K. Rajagopal; *J. Petrol. Sci. Eng.*, **2005**, 48, 169-184.
12. M.T. Ghannam; N. Esmail; *Pet. Sci. Technol.*, **2006**, 24, 985-999.
13. M.R. Khan; *Energy sources.*, **1996**, 18, 385-391.
14. S.W. Hasan; M.T. Ghannam; N. Esmail; *Fuel.*, **2010**, 89,1095-1100.
15. K. Benyounes; *SN Appl. Sci.*, **2019**, 1,1-8.
16. R.I. Ibrahim; M.K. Oudah; A.F. Hassan; *J. Petrol. Sci. Eng.*, **2017**, 156,356-365.
17. R. Kumar; S. Mohapatra; A. Mandal; T.K. Naiya; *J. Pet. Sci. Res.*, **2014**, 3, 90-99.
18. H.A. Barnes; *J. Non-newton. Fluid Mech.*, **1997**, 70,1-33.
19. J. Mewis; *J. Non-newton. Fluid Mech.*, **1979**,6,1-20.
20. F. Souas; A. Safri; A. Benmounah; D.E. Djemiat; *Pet. Sci. Technol.*, **2018**, 36, 1093-1099.
21. F. Souas; A. Safri; A. Benmounah; D.E. Djemiat; *Pet. Sci. Technol.*, **2018**, 36, 1757-1763.
22. F. Souas; A. Safri; A. Benmounah; *Pet. Sci. Technol.*, **2019**, 37, 443-451.
23. F. Souas; *Pet. Res.*, **2022**, 7, 536-544.
24. Y. Al-Roomi; R. George; A. Elgibaly; A. Elkamel; *J. Petrol. Sci. Eng.*, **2004**, 42, 235-243.